Field Inspections and Monitoring of Continuous Deck Slabs on Prestressed Concrete Bridges for Development of Refined Details

by

Brandon Richard Lundstrum

A thesis submitted to the Graduate Faculty of
Auburn University
in partial fulfillment of the
requirements for the Degree of
Master of Science

Auburn, Alabama
May 10, 2025

Keywords: bridges, continuous, deck, slab,
cracking, thermal, shrinking

Approved by

Matthew T. Yarnold, Committee Chair, Associate Professor, Department of Civil and Environmental Engineering and Director of Advanced Structural Engineering Laboratory
Anton K. Schindler, Professor, Department of Civil and Environmental Engineering and Director of Highway Research Center
Robert W. Barnes, Professor, Department of Civil and Environmental Engineering

Abstract

Expansion joints are used in bridges to allow for the unrestrained movement of the superstructure. However, due to the need for frequent maintenance, continuous deck details have been developed to replace them. This study evaluated the current detail Alabama Department of Transportation (ALDOT) uses to make the deck slab continuous at pier bent locations (termed closed joints) in prestressed girder bridges instead of using expansion joints (termed open joints). The study inspected five bridges across Alabama to assess the performance of the in-service detail. The inspected bridges varied in properties, including the span and overall lengths, skew angles, girder types, ages, and environments. Based on visual observations, the study found that the factor that most affected the visual performance of the deck was the detailing and tooling of the construction joint. The main damage observed at these closed joints was due to traffic wear and did not cause structural concern. To evaluate the behavior of and the demands on the closed-joint detail further, the study then monitored a bridge for a year. The behavior of both open and closed joints were monitored. The demands and movements at the girder ends were captured during this period, with a focus on the effects of thermal demands. The measured rotations from the monitored bents were similar in magnitude regardless of the detail used for the joint, indicating little to no rotational restraint was provided at the closed joint. The rotations measured from field monitoring indicated that using the AASHTO design values for rotation from thermal gradients will work for future design. For recommending values for future design, demands from live load and time-dependent effects were superimposed using guidance from AASHTO.

Table of Contents

Abstract 2

Table of Contents 3

List of Tables 6

List of Figures 7

Chapter 1: Introduction 13
- 1.1. Introduction 13
- 1.2. Research Objectives 14
- 1.3. Research Approach 16
- 1.4. Terminology 17

Chapter 2: Literature Review 19
- 2.1. Overview 19
- 2.2. Behavior of Closed-Joint Bridges 19
- 2.3. Design of Closed-Joint Bridges 31
  - 2.3.1. Analysis Methods 31
  - 2.3.2. Materials 36
  - 2.3.3. Link-Slab Configuration 38
- 2.4. Field Instrumentation and Monitoring 40
- 2.5. Standard Practices 43

Chapter 3: Field Inspections 47
- 3.1. Introduction 47
- 3.2. Selected Bridges 47
- 3.3. Observations 53
- 3.4. Conclusions 57

Chapter 4: Field Monitoring 58
- 4.1. Introduction 58
  - 4.1.1. Scope 58
  - 4.1.2. Bridge Selection 59

4.2. Bridge Description 60
4.3. Monitoring Setup 67
4.4. Theoretical Basis 75
4.5. Monitoring Results 80
4.5.1. Zeroing Rotations and Displacements 80
4.5.2. Challenges in Monitoring 82
4.5.3. Data Plotting and Comparisons 82
4.6. Conclusions 98

Chapter 5: Closed-Joint Demands 100
5.1. Introduction 100
5.2. General Assumptions and Properties 100
5.3. Live-Load Demands 101
5.4. Time-Dependent Effects 102
5.5. Combined Load Effects 105

Chapter 6: Conclusions and Recommendations 108

References 109

Appendix A: Field Inspection Reports 113
A.1. I-85 over Co Rd 54 (LEE-1) 114
A.2. I-85 over SR-51 (LEE-2) 118
A.3. Co Rd 10 over I-85 (LEE-3) 121
A.4. I-20 over Co Rd 49 (CLB-1) 125
A.5. Co Rd 39 over I-10 (MOB-1) 130
A.6. US-11 over Sucarnoochee River (SUM-1) 136

Appendix B: Prestressed Girder Details 140

Appendix C: CRBasic Codes 147
C.1. Bent 7 Code 147
C.2. Bent 8 Code 148
C.3. Bent 9 Code 149

Appendix D: Monthly Graphs 150
D.1. Girder Rotations 150
D.1.1. Single End Rotations 150
D.1.2. Total Rotation Across Joint 156
D.2. Girder-End Displacements 162
D.2.1. Open Joint (OJ) 162
D.2.2. Closed Joint (CJ) 167
D.3. End Temperatures (from Bent 8) 173
D.3.1. Temperature Gradient 174

Appendix E: Closed-Joint Demand Calculations 180
E.1. Geometries and Material Properties 180
E.2. Rotations from Temperature Gradient using AASHTO 3.12.3 and 4.6.6 181
E.3. Rotations from HL-93 Loading using AASHTO 3.6.1.2 and 3.6.1.3 182
E.4. Rotations from Time-Dependent Effects using AASHTO 5.9.3.4 183

List of Tables

Table 2-1. Closed-joint bridges investigated (Wolde-Tinsae et al., 1988) 20

Table 2-2. Details of in-service closed-joint bridges analyzed for parametric study (Thippeswamy, 1996).. 23

Table 2-3. Variables and ranges utilized in parametric study (Canales, 2019) 30

Table 2-4. Bridges selected for field inspection (Aktan et al., 2008) 32

Table 2-5. Experiment parameters for sub-assembly evaluation (Stringer and Burgueño, 2012) 34

Table 2-6. Full-scale bridge model properties (Stringer and Burgueño, 2012) 34

Table 3-1: Summary of details for inspected bridges 53

Table 4-1: Temperature gradient design values (AASHTO, 2024) 76

Table 4-2: Percent difference between measured and calculated rotation ranges 98

List of Figures

Figure 1-1: Expansion joint in bridge deck.......... 13

Figure 1-2: Current ALDOT closed-joint detail (ALDOT, 2020).......... 15

Figure 1-3: Current ALDOT closed-joint detail: Detail 'B' (ALDOT, 2020).......... 15

Figure 1-4: Temperature gradient sign convention.......... 18

Figure 1-5: Curvature sign convention.......... 18

Figure 1-6: Rotation and strain sign convention.......... 18

Figure 2-1. Typical closed-joint bridge deck details by state DOTs (Caner and Zia, 1998).......... 21

Figure 2-2. Section of link slab utilized in the bridge (Wing and Kowalsky, 2005).......... 24

Figure 2-3. Plan view of current continuous bridge deck (SR 46 Over Oconee River) (Snedeker et al., 2011).......... 26

Figure 2-4. Section view at construction joint of current continuous bridge deck (SR 46 Over Oconee River) (Snedeker et al., 2011).......... 26

Figure 2-5. Plan view of modified continuous deck detail (Snedeker et al., 2011).......... 27

Figure 2-6. Section view of modified continuous deck detail (Snedeker et al., 2011).......... 27

Figure 2-7. Dial gauge system diagram and bridge installation (Davidson et al., 2012).......... 28

Figure 2-8. DEMEC points at construction joint (Davidson et al., 2012).......... 28

Figure 2-9. Wax plate for tracking the motion of the bridge (Davidson et al., 2012).......... 29

Figure 2-10. Proposed link-slab details (Aktan et al., 2008).......... 33

Figure 2-11. Proposed link-slab details (Ulku et al., 2009).......... 33

Figure 2-12. Debonded link slab system studied (Au et al., 2013).......... 35

Figure 2-13. Lap reinforcement configurations (Charuchaimontri et al., 2008).......... 38

Figure 2-14: New Zealand design thermal gradient from Priestley (1978).......... 41

Figure 2-15: General layout of instrumentation at girder ends (Birley et al., 2025).......... 43

Figure 2-16: Example of integral abutment detail (Trados, 2016).......... 45

Figure 2-17: Florida Department of Transportation details for continuous slab over joint between simple spans (Trados, 2016) 45

Figure 2-18: Link-slab detail used by the Virginia Department of Transportation to eliminate open joints in rehabilitation projects (Trados, 2016) 46

Figure 3-1: Locations of bridges inspected (map adapted from ArcGIS) 48

Figure 3-2: Elevation view of I-85 bridge over Co Rd 54 (LEE-1) 49

Figure 3-3: Elevation view of the I-85 bridge over SR-51 (LEE-2) 50

Figure 3-4: Elevation view of the Co Rd 10 bridge over I-85 (LEE-3) 50

Figure 3-5: Elevation view of the Co Rd 39 bridge over I-10 (MOB-1) 51

Figure 3-6: Elevation view of the I-20 bridge over Co Rd 49 (CLB-1) 51

Figure 3-7: Elevation view of the US-11 bridge over Sucarnoochee River (SUM-1) 52

Figure 3-8: Typical spalling observed at closed joint 54

Figure 3-9: Spalling and cracking observed at the freshly constructed closed joint (LEE-2) 55

Figure 3-10: Full-depth edge beam with cracking observed (I-20 over Co Rd 49) 56

Figure 3-11: Full-depth edge beam with significant concrete breakout (Co Rd 39 over I-10) 56

Figure 4-1: Elevation view of US-11 over Sucarnoochee River 61

Figure 4-2: Diagram of deck build-up and girder camber 62

Figure 4-3: Typical superstructure half cross section for spans adjacent to monitored bents 63

Figure 4-4: Bent 7 girder ends and expansion bearings 64

Figure 4-5: Bent 8 girder ends and expansion bearings 65

Figure 4-6: AASHTO type girder clip angle for fixed bearing (Bent 9) 66

Figure 4-7: Anchor bolt and well detail for fixed bearing (Bent 9) 66

Figure 4-8: Bent 9 girder ends and fixed bearings 67

Figure 4-9: Field monitoring instrumentation plan 68

Figure 4-10: Field monitoring data acquisition system (DAQ) plan 68

Figure 4-11: Sensor placement on girder ends 69

Figure 4-12: Thermocouple installation positions 71

Figure 4-13: Inclinometer installation position (Bent 7 displayed) 72

Figure 4-14: Crackmeter installation position (Bent 9 displayed) 73

Figure 4-15: Diagram for measured data 74

Figure 4-16: Solar radiation zones for the United States (AASHTO, 2024) 76

Figure 4-17: AASHTO (2024) temperature gradient in concrete and steel structures 76

Figure 4-18: New Zealand design thermal gradient from Priestley (1978) 78

Figure 4-19: Locations of thermocouples and key points on temperature gradient 79

Figure 4-20: Girder-end temperature differences in April 2024 showing zeroing time 81

Figure 4-21: Girder-end temperature differences in December 2023 showing zeroing time 81

Figure 4-22: Rotation comparison for occurrence of largest negative rotations 84

Figure 4-23: Rotation comparison for occurrence of hottest temperatures 85

Figure 4-24: Open- and closed-joint displacement for occurrence of hottest temperatures 86

Figure 4-25: Rotation comparison for occurrence of largest positive rotations 87

Figure 4-26: Rotation comparison for occurrence of largest temperature difference (singular day) 88

Figure 4-27: Rotation comparison for occurrence of largest temperature difference (consistently over multiple days) 89

Figure 4-28: Rotation comparison for occurrence of coldest temperatures 90

Figure 4-29: Open- and closed-joint displacement for occurrence of coldest temperatures 91

Figure 4-30: Difference between positive rotation peaks over one year 92

Figure 4-31: Difference between negative rotation peaks over one year 93

Figure 4-32: Peak rotation ranges from December 2023 to March 2024 94

Figure 4-33: Peak rotation ranges from April 2024 to July 2024 95

Figure 4-34: Peak rotation ranges from August 2024 to November 2024 95

Figure 4-35: Maximum total range in rotation across girder ends from various methods of calculations ... 97

Figure 5-1: Diagram for rotation due to concrete creep ... 103

Figure 5-2: Diagram for rotation due to differential concrete shrinkage ... 104

Figure 5-3: Diagram for rotation due to steel relaxation (Nawy, 2009) ... 105

Figure B-1: AASHTO Type II Prestressed Girder (LEE-1) ... 140

Figure B-2: AASHTO Type II Modified Prestressed Girder (LEE-1) ... 140

Figure B-3: AASHTO Type I Modified (III) Prestressed Girder (LEE-2) ... 141

Figure B-4: AASHTO Type I Modified (BT+) Prestressed Girder (LEE-2) ... 141

Figure B-5: Modified BT-54 Prestressed Girder (LEE-3) ... 142

Figure B-6: Type BT-63 Prestressed Girder (MOB-1) ... 143

Figure B-7: Type BT-54 Prestressed Girder (CLB-1) ... 144

Figure B-8: AASHTO Type III Prestressed Girder (SUM-1) ... 145

Figure B-9: AASHTO Type I Prestressed Girder (SUM-1) ... 145

Figure B-10: Type BT-72 Prestressed Girder (SUM-1) ... 146

Figure D-1: Average rotation and temperature during December 2023 ... 150

Figure D-2: Average rotation and temperature during January 2024 ... 150

Figure D-3: Average rotation and temperature during February 2024 ... 151

Figure D-4: Average rotation and temperature during March 2024 ... 151

Figure D-5: Average rotation and temperature during April 2024 ... 152

Figure D-6: Average rotation and temperature during May 2024 ... 152

Figure D-7: Average rotation and temperature during June 2024 ... 153

Figure D-8: Average rotation and temperature during July 2024 ... 153

Figure D-9: Average rotation and temperature during August 2024 ... 154

Figure D-10: Average rotation and temperature during September 2024 ... 154

Figure D-11: Average rotation and temperature during October 2024 ... 155

Figure D-12: Average rotation and temperature during November 2024 155

Figure D-13: Average total rotation across joint and temperature during December 2023 156

Figure D-14: Average total rotation across joint and temperature during January 2024 156

Figure D-15: Average total rotation across joint and temperature during February 2024 157

Figure D-16: Average total rotation across joint and temperature during March 2024 157

Figure D-17: Average total rotation across joint and temperature during April 2024 158

Figure D-18: Average total rotation across joint and temperature during May 2024 158

Figure D-19: Average total rotation across joint and temperature during June 2024 159

Figure D-20: Average total rotation across joint and temperature during July 2024 159

Figure D-21: Average total rotation across joint and temperature during August 2024 160

Figure D-22: Average total rotation across joint and temperature during September 2024 160

Figure D-23: Average total rotation across joint and temperature during October 2024 161

Figure D-24: Average total rotation across joint and temperature during November 2024 161

Figure D-25: Average OJ displacement and temperature during December 2023 162

Figure D-26: Average OJ displacement and temperature during January 2024 162

Figure D-27: Average OJ displacement and temperature during April 2024 163

Figure D-28: Average OJ displacement and temperature during May 2024 163

Figure D-29: Average OJ displacement and temperature during June 2024 164

Figure D-30: Average OJ displacement and temperature during July 2024 164

Figure D-31: Average OJ displacement and temperature during August 2024 165

Figure D-32: Average OJ displacement and temperature during September 2024 165

Figure D-33: Average OJ displacement and temperature during October 2024 166

Figure D-34: Average OJ displacement and temperature during November 2024 166

Figure D-35: Average CJ displacement and temperature during December 2023 167

Figure D-36: Average CJ displacement and temperature during January 2024 167

Figure D-37: Average CJ displacement and temperature during February 2024 168

Figure D-38: Average CJ displacement and temperature during March 2024 168

Figure D-39: Average CJ displacement and temperature during April 2024 169

Figure D-40: Average CJ displacement and temperature during May 2024 169

Figure D-41: Average CJ displacement and temperature during June 2024 170

Figure D-42: Average CJ displacement and temperature during July 2024 170

Figure D-43: Average CJ displacement and temperature during August 2024 171

Figure D-44: Average CJ displacement and temperature during September 2024 171

Figure D-45: Average CJ displacement and temperature during October 2024......................... 172

Figure D-46: Average CJ displacement and temperature during November 2024..................... 172

Figure D-47: Girder-end temperature over 12-month monitoring period 173

Figure D-48: Girder-end gradient during December 2023 174

Figure D-49: Girder-end gradient during January 2024 174

Figure D-50: Girder-end gradient during February 2024 175

Figure D-51: Girder-end gradient during March 2024 175

Figure D-52: Girder-end gradient during April 2024 176

Figure D-53: Girder-end gradient during May 2024 176

Figure D-54: Girder-end gradient during June 2024 177

Figure D-55: Girder-end gradient during July 2024 177

Figure D-56: Girder-end gradient during August 2024 178

Figure D-57: Girder-end gradient during September 2024.. 178

Figure D-58: Girder-end gradient during October 2024.. 179

Figure D-59: Girder-end gradient during November 2024.. 179

Chapter 1: Introduction

1.1. Introduction

Bridges have historically been designed with deck slab expansion joints to accommodate the movement of the superstructure, mainly when adjacent spans displace relative to one another at the pier bents. Figure 1-1 displays a typical expansion joint constructed in a bridge deck. This movement can be attributed to demands such as traffic live loads, thermal gradients, and time-dependent effects (i.e., creep, shrinkage, and relaxation). These expansion joints need to be regularly maintained. If not, debris can intrude into the expansion joint, decreasing its ability to allow deck movement as it was designed. This restraint on movement can lead to a buildup of stress in the superstructure, lowering its structural capacity. Unmaintained expansion joints could also allow water or other deteriorating chemicals to pass through the joint and cause corrosion problems below the deck.

Figure 1-1: Expansion joint in bridge deck

One solution to stop the intrusion of debris and water is by implementing a continuous deck at these joints, sometimes referred to as a “closed joint,” whereas an expansion joint is referred to as an “open joint”. When these closed joints perform well, they typically require little to no maintenance, just regular inspection with the rest of the bridge. The deck being continuous effectively “seals” the gap at the joint, removing the possibility of debris buildup within the joint or leakage through the gaps.

The removal of the expansion joint restrains the movement that was once free to occur. The closed joint must accommodate the stresses that result from the superstructure movement at these joints, the magnitude of which is influenced by a variety of factors, the main sources of which are its location, geometry, and materials present in the superstructure. Standards have been developed by the American Association of State Highway and Transportation Officials (AASHTO) to guide the design, but this is more of a broad overview and more specific guidance is needed from state to state. The Alabama Department of Transportation (ALDOT) has been constructing prestressed concrete girder bridges with closed joints, but this detail was borrowed from other Departments of Transportation (DOTs). Research was conducted to develop a detail that could help with the ease of construction, improve performance, and be a more efficient design.

1.2. Research Objectives

The primary objective of this research study is to perform an evaluation of the current closed-joint detail in use by ALDOT. This detail is illustrated in Figure 1-2 and Figure 1-3. The main components of this detail are the continuity of the deck over the joint, a grooved construction joint with a silicone joint seal, the presence of an edge beam, and a bond breaker (premade bituminous filler) within the edge beam.

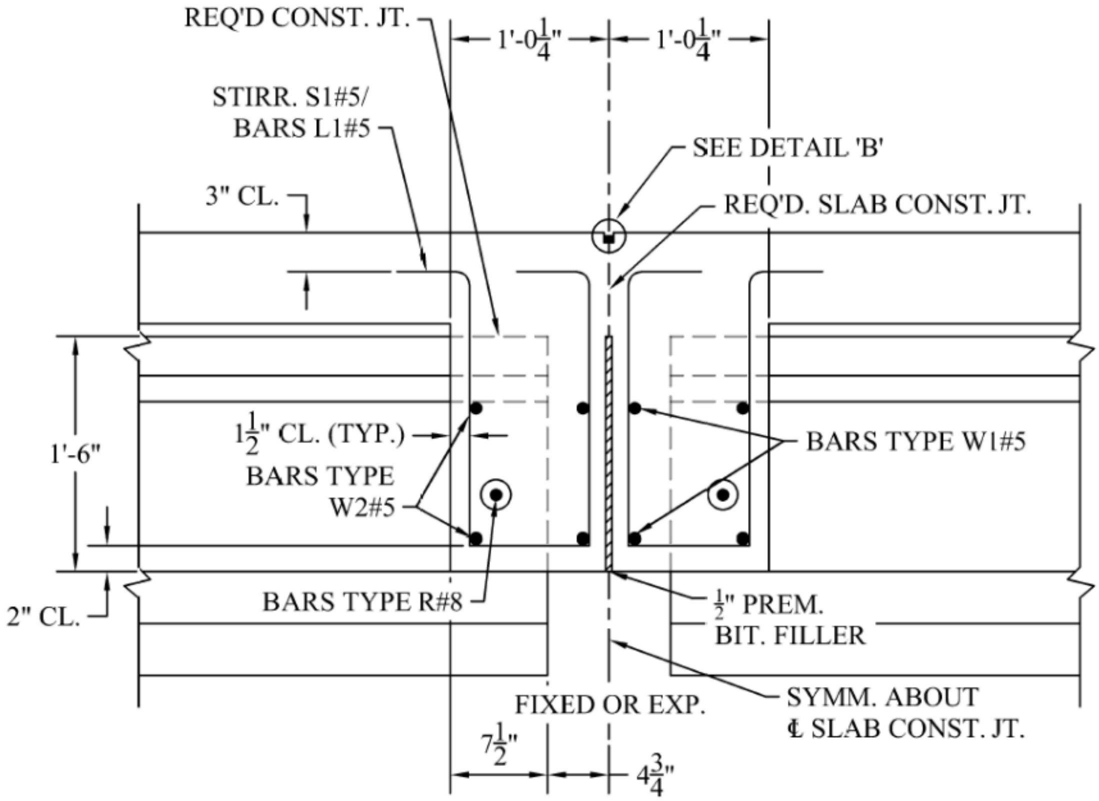

Figure 1-2: Current ALDOT closed-joint detail (ALDOT, 2020)

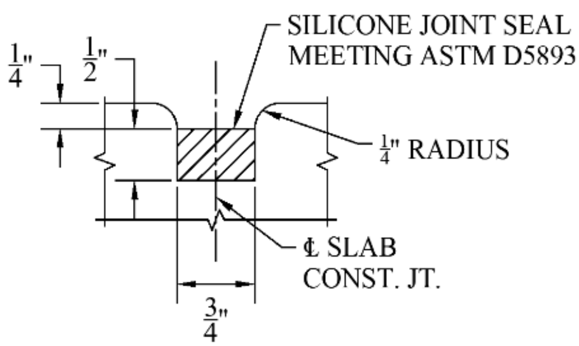

Figure 1-3: Current ALDOT closed-joint detail: Detail ‘B’ (ALDOT, 2020)

Through this evaluation of the current detail for closed joints, the aim is to identify improvements that can be made in the constructability of closed joints as well as note any structural defects that result from the performance of the current detail. To comprehensively evaluate the current detail for closed joints, the influence of factors will need to be qualified in reference to their effect on the behavior of closed joints. These factors include overall bridge length, span length, skew angle, bearing fixities/types, location of the bridge (effects from climate such as cold weather conditions or proximity to saltwater), and age.

With the influence of the factors affecting the closed joint identified, the behavior will then need to be quantified. This quantification should include the magnitude of the superstructure movements, which can include the girder-end rotation, expansion and contraction of girder ends, strain in the deck, etc. The magnitudes of these deformations can then be used to aid full-scale testing in a laboratory setting, but this is outside the scope of the covered in this thesis.

1.3. Research Approach

To evaluate the current closed-joint detail and its performance in service, field inspections were conducted across the state of Alabama. This study observed the performance of the closed-joint detail across a variety of ages and locations (aiming to capture behavior under different climates present in Alabama). These inspections identified any visible signs of distress that were attributed to the closed joint. This phase of the project investigated what aspects of the bridge to focus on for the next phase of the project, field monitoring, and what exact behavior to capture during the monitoring. The details of the field inspection phase of the study are discussed in Chapter 3: Field Inspections.

To better understand the behavior of closed joints in bridges, the field monitoring phase of the project monitored an in-service bridge over a whole year. By monitoring over a year, the thermal effects from both hot weather (summer) and cold weather (winter) were captured. The scope of the monitoring recorded the rotation and displacement of the ends of the girders at the joints. Monitoring an open joint on the same bridge provided a baseline for the movements being captured at the closed joints. This allowed for a direct comparison of demand between the two cases, providing a sound basis for the quantification of the demands that the closed joint was subjected to. The details of the field monitoring phase of the study are discussed in Chapter 4:Field Monitoring.

Because the bridge was in-service, the monitoring focused on the demand from thermal gradients, so the temperature across the girder ends were captured along with the movements. Other demands from traffic loading or time-dependent effects were superimposed with the thermal movements through performing a numerical study. The details of this numerical study are discussed in Chapter 5: Closed-Joint Demands.

1.4. Terminology

Throughout this study, the terminology used to describe the type of joint used in the deck will follow ALDOT's terminology. The term "closed joint" is used to describe when the deck is built continuously over the joint without an expansion joint. Several literature reviews also use the term "link slab," which typically refers to a debonded design for the joint and falls under the closed-joint terminology, which can be both debonded or bonded. The term "open joint" is used to refer to expansion joints. This system is not to be confused with terminology from the AASHTO LRFD Bridge Design Specifications that also uses "open" and "closed" joints. These terms both refer to types of expansion joints, describing their properties of being designed as physically open or closed.

A sign convention was also established when referring to the movements of the girder ends at the joints. The sign conventions in AASHTO LRFD provide a convention for the temperature gradients, but no basis is given for the rotations of the girder ends. For thermal effects, the temperature gradient that is developed in the superstructure can either be positive or negative (see Figure 1-4), with the higher temperature at the top for the positive gradient and at the bottom for the negative gradient. When subject to the positive temperature gradient, this causes the span to "hog up" and be in negative curvature (see Figure 1-5). This curvature along adjacent spans results in the tops of the girder ends rotating towards each other and subjecting the deck to compression. This rotation, then, is negative (see Figure 1-6) and most commonly occurs when the sun is rising and heating the deck surface. Conversely, when the spans are subjected to the negative temperature gradient, this results in the girder spans going into positive curvature and rotating the tops of the girder ends away from each other. This movement develops tension in the deck (if the deck joint cannot open freely) and is a negative rotation. This rotation occurs from thermal loads at the coldest time of day and the temperatures below the deck are warmer than the top. This rotation also commonly comes from gravity and live loads applied to the deck.

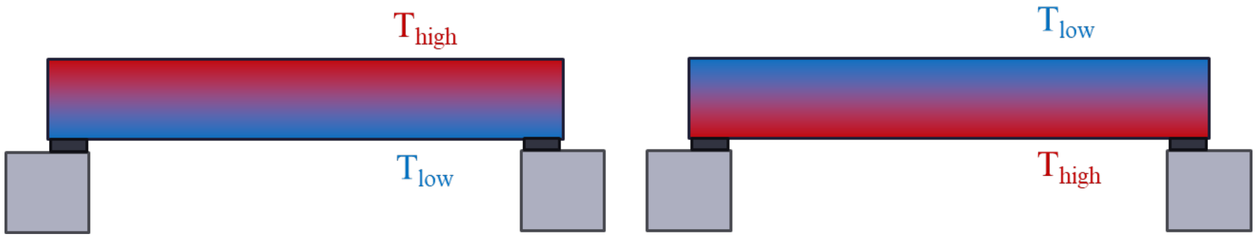

(a) Positive Temperature Gradient (b) Negative Temperature Gradient

Figure 1-4: Temperature gradient sign convention

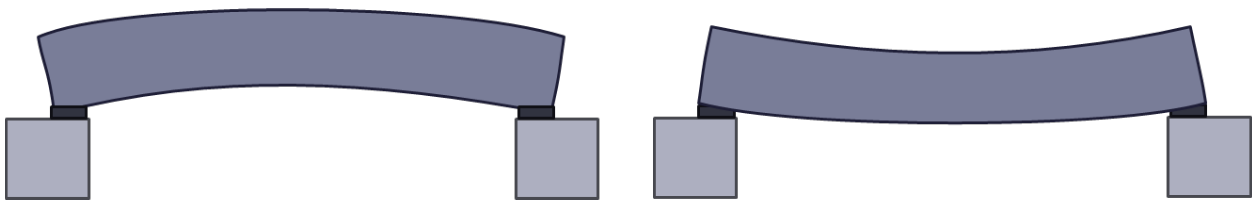

(a) Negative Curvature (b) Positive Curvature

Figure 1-5: Curvature sign convention

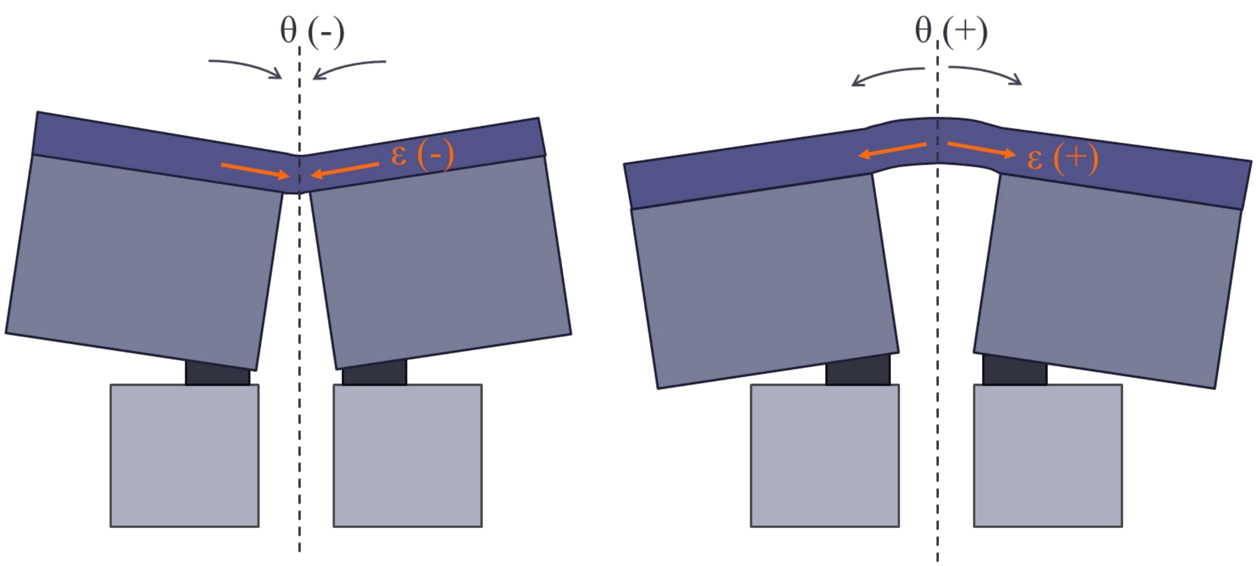

(a) Negative Rotation in Girder and Negative Strain in Deck

(b) Positive Rotation in Girder and Positive Strain in Deck

Figure 1-6: Rotation and strain sign convention

Chapter 2: Literature Review

2.1. Overview

When a concrete bridge deck is subjected to thermal loads, this causes expansion, contraction, and rotation of the bridge deck. Expansion joints have been employed to reduce cracking and thermal loads experienced in bridge concrete deck slabs by allowing unrestrained translation and rotation. For them to be effective in this goal, expansion joints need to be regularly maintained, but they are often not. Debris can get into and clog these joints and reduce their ability to allow unrestrained movement of the bridge concrete deck slabs, negatively impacting their performance. Chemicals and water can also get through these joints and lead to corrosion issues. Joint seals can be used to combat this problem, but they deteriorate over time and can be subject to poor levels of maintenance. The overall cost of expansion joints, then, is high due to their lifetime maintenance needs and durability issues that can result from improper maintenance.

When designing or retrofitting bridges for better performance, eliminating expansion joints and making the deck continuous over the joint has been investigated by many researchers and implemented in many projects. The structural needs that would be required of these structures have been investigated, and the performance of the structure could be affected by factors such as span length, skew angle, support type, girder type, girder dimensions, and stiffness of the structure and its elements. To make the deck continuous, the closed joints are often constructed using link slabs, which can either be bonded to or debonded from the girders, where the benefits and drawbacks of using each system have been investigated. Several bridges throughout Alabama use continuous deck details in their plans, but this detail is not standardized when considering when or where it should be used or how to detail the closed joint itself.

2.2. Behavior of Closed-Joint Bridges

As bridges were constructed with continuous decks, more data and cases became available to monitor their behavior and assess the viability of closed joints versus using open joints. The demands that these bridge elements would be subjected to were evaluated for different span lengths, number of spans, and girder types. From these evaluations, researchers aimed to better quantify the behavior of closed-joint bridges and determine the limits to which they can be used effectively.

Wolde-Tinsae et al. (1988) investigated the performance of closed-joint bridges by performing on-site inspections, design reviews, and discussions with the designers and maintenance personnel about multiple closed-joint bridges in selected states across the United States. Problems encountered with the bridges concerning the abutments, approach slabs, wingwalls, and approach fill were also assessed in this study. The bridges that were investigated in this study to analyze the corrective measures that have been used by state highway departments to improve the performance of these bridges are shown in Table 2-1.

Table 2-1. Closed-joint bridges investigated (Wolde-Tinsae et al., 1988)

Bridge	State	Length	Girder Type
South Fork Putah Creek Bridge	California	572 ft 6 spans	RC Box Girders
San Juan Road Overcrossing	California	440 ft 4 spans	RC Box Girders
Holston River Bridge	Tennessee	2,696 ft 29 spans	PC Box-Beam Girders
US Route 129 South Interchange	Tennessee	400 ft 2 spans	Continuous Rolled Steel Beams
Route 9W over Coeyman's Creek	New York	107 ft 1 span	PC Box Girder

Wolde-Tinsae et al. (1988) found in this study that the bridges were performing as intended and the removal of open joints had not resulted in major structural distress or affected the serviceability of the structure. However, some states had encountered issues in the approach slab and backfill areas for the longer closed-joint bridges, noticing problems with settlement, resulting in bumps at the bridge ends.

Caner and Zia (1998) investigated the behavior of link slabs connecting two adjacent simple-span girders using both steel and prestressed concrete girders. The goal of this study was to propose a method for designing a link slab for closed-joint bridges. The study also considered the typical designs of link slabs that state Departments of Transportation (DOTs) use to aid in the investigation. Figure 2-1 gives an example of typical designs of continuous decks by Texas and Florida DOTs.

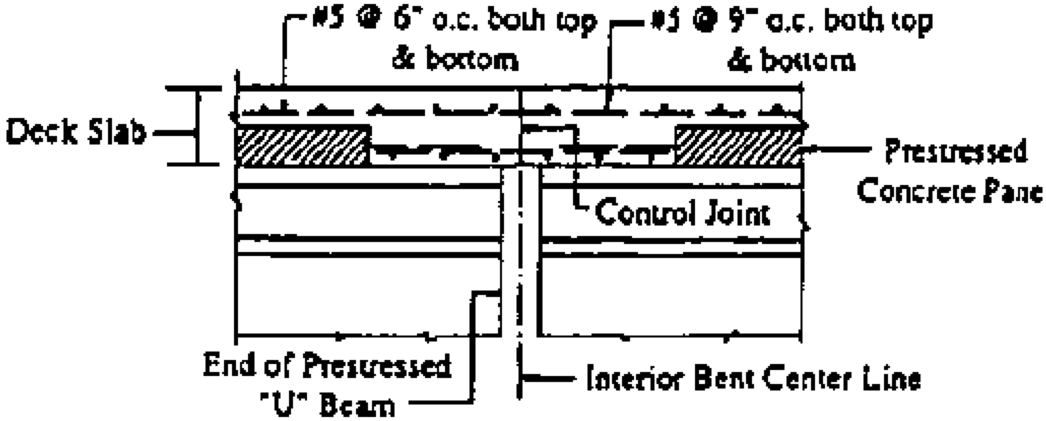

(a) Texas

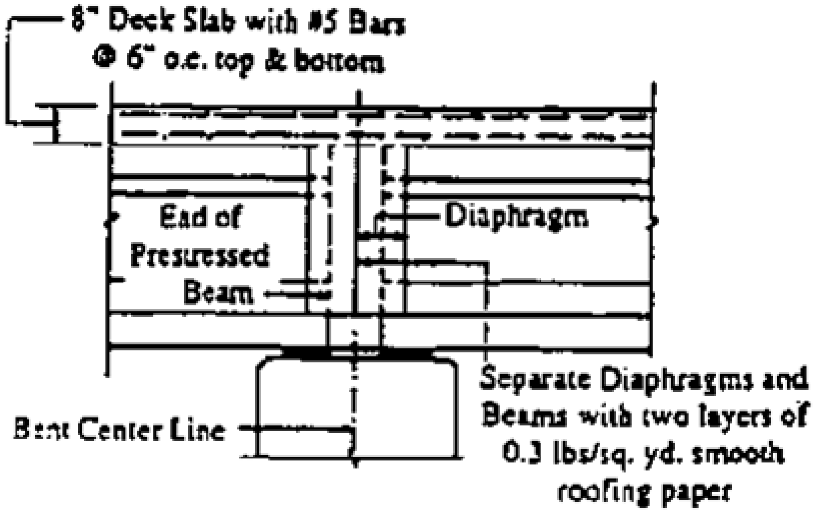

(b) Florida

Figure 2-1. Typical closed-joint bridge deck details by state DOTs (Caner and Zia, 1998)

The strains within the elastic range in the girders and link-slab reinforcement of the bridges observed by Caner and Zia (1998) were not affected by the type of support conditions. The composite girders also behaved similarly to that of simply supported girders due to the low stiffness of the link slab. The forces that were observed in the link slab in this study resulted from bending stress rather than tensile stress. It was concluded that the girder can be designed independently for each span as simply supported due to negligible continuity provided by the link slab.

El-Safty (1994b) investigated bridges with continuous decks with partial debonding from the ends of the girders. Effects from the variation of girder types were analyzed for both steel and prestressed concrete girders, along with the effects from the variation of time-dependent material properties and temperatures. Various support conditions, steel reinforcement ratios in the deck, and a variation in loading arrangements were also investigated regarding their effects on the behavior of the link slab. Analysis was also performed to determine the optimal length of a link slab, as well as the optimum debonded length, to connect simply supported girders by testing a specimen in a laboratory setting. In this study, it was found that the response and stiffness of the deck on a closed-joint bridge with partially debonded link slabs are affected by the boundary conditions and loading arrangement of the structure. The response of the link slab was observed to improve when the partially debonded beams have hinge-type supports, with the stiffness being comparable to that of a fully continuous beam under service loads. El-Safty (1994b) observed that increasing the steel in the connection element improves the response and ultimate load; however, this also increases the risk of deck failure by the crushing of the concrete. When the connection was subjected to tensile forces when experiencing symmetrical loading with a hinge on either side, the capacity of the link slab was seen to improve. Failure due to reinforcement in the connection element yielding would result in the beam behaving as if it were simply supported. Creep effects were observed to increase capacity, with more observed for debonded than bonded link slabs. Effects observed from temperature variation did not differ based on whether the continuous deck was bonded or debonded.

Thippeswamy (1996) collected and analyzed information about closed-joint bridges that were subjected to varying load conditions, combinations, and foundation types. One of the goals of the study was to observe the long-term performance of closed-joint bridges, considering creep, shrinkage, and settlement, and investigate the strength, stiffness, and performance of existing closed-joint bridges. Five bridges were chosen as part of a parametric study, which can be seen in Table 2-2, with the system dimensions, loads/load combinations, material properties, and boundary conditions being used to classify the parameters of the study.

Table 2-2. Details of in-service closed-joint bridges analyzed for parametric study (Thippeswamy, 1996)

Name of the Bridge	Location of the Bridge	Bridge Details
Short Creek Bridge	Brooke and Ohio Co., WV	Span: 110'; Total width: 50'-6"; # of Stringers and spacing: 6, 106"; Skew Angle: 70°; Abutment height: 98"; Piles: Single row of HP 12x53; Pile orientation: Strong axis bending; Design live load: HS 25-44; Concrete modulus: 3,605 ksi (superstructure), 3,122 ksi (substructure)
South Saturn Parkway Bridge	Maury Co., TN	Spans: 132.5' – 117.5'; Total width: 50'; # of Stringers and spacing: 6, 120"; Skew Angle: 78°; Abutment height: 88"; Piles: Single row of HP 10x42; Pile orientation: Strong axis bending; Design live load: HS 20-44; Concrete modulus: 3,120 ksi (superstructure and substructure)
Lone Tree Road Bridge	Black Hawk Co., IA	Spans: 114' – 114'; Total width: 40'; # of Stringers and spacing: 5, 112"; Skew Angle: 81°; Abutment height: 96"; Piles: Single row of HP 10x42; Pile orientation: Weak axis bending; Design live load: HS 20-44; Concrete modulus: 3,372 ksi (superstructure and substructure)
Bridge Over Creek	Jones Co., SD	Spans: 68' – 87'– 68'; Total width: 38'; # of Stringers and spacing: 5, 102"; Skew Angle: 90°; Abutment height: 73.5"; Piles: Single row of HP 10x42; Pile orientation: Weak axis bending; Design live load: HS 20-44; Concrete modulus: 3,605 ksi (superstructure and substructure)
Bridge Over Little Kanawha River	Upshur Co., WV	Spans: 45' – 60'– 45'; Total width: 28'; # of Stringers and spacing: 4, 96"; Skew Angle: 70°; Abutment height: 77.2"; Piles: Single row of HP 10x42; Pile orientation: Weak axis bending; Design live load: HS 25-44; Concrete modulus: 3,824 ksi (superstructure), 3,122 ksi (substructure)

Note: The superstructure for all bridges is comprised of concrete slab composite with steel stringers

Wing and Kowalsky (2005) assessed the performance of the first closed-joint bridge using link slabs in North Carolina to validate the design assumptions and amend the design concept. The most important assumption that needed to be checked in this study was that the girders on bridges with link slabs could be assumed to be simply supported for dead and live loads. For this, a full-scale live load test and long-term monitoring of the bridge were performed, in which the bridge was subjected to seasonal- and service-level loading. An analytical model of the bridge was also developed to predict the performance of the closed-joint bridge. The link-slab detail that they used in the bridge can be seen in Figure 2-2.

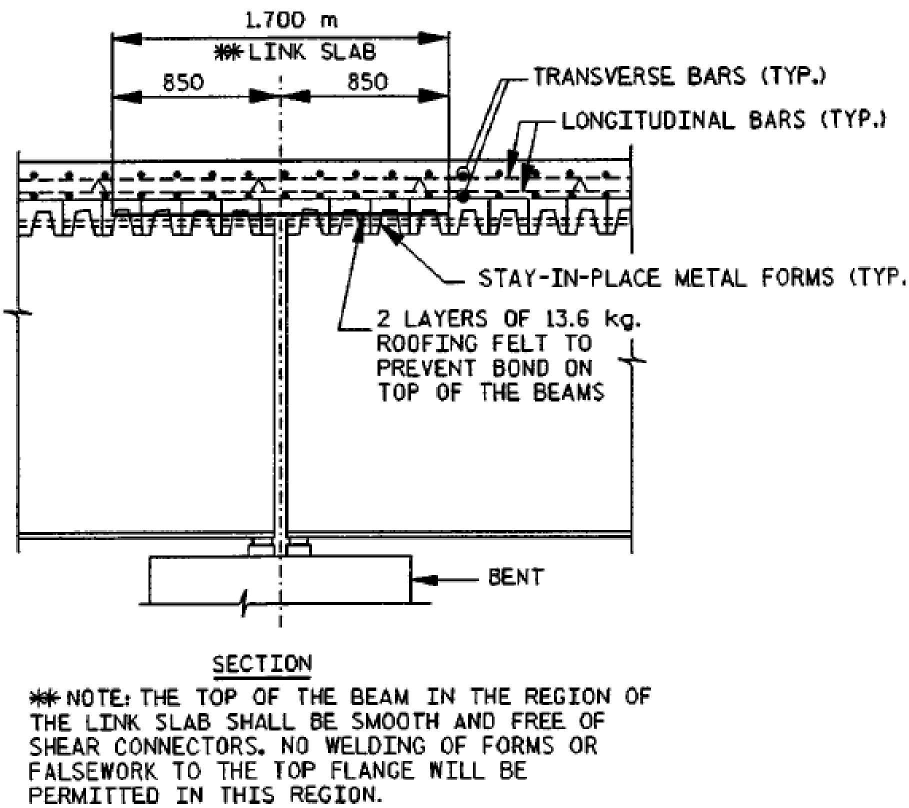

Figure 2-2. Section of link slab utilized in the bridge (Wing and Kowalsky, 2005)

It was observed by Wing and Kowalsky (2005) that traffic loads induced low rotation in the link slab while thermal loads induced rotations that were greater. From this, it was concluded that the assumption of the link-slab girders being simply supported was valid and conservative. The crack in the link slab was larger than the design criteria but has thus far not been observed to impact the service of the bridge. The proposed design approach, where the reinforcement is sized based on rotational demand and crack control, is said to allow the engineer to easily create design charts for various structural configurations.

Snedeker et al. (2011) evaluated the performance history of continuous-deck details in Georgia. The study determined which details work the best, why they worked well for each of their applications, and then recommended optimal lengths for continuous bridges using these details. The current practices with continuous decks by the Georgia Department of Transportation (GDOT) were collected and summarized to fully understand the performance history, as well as collecting maintenance reports and field evaluations. The movement of bridges due to thermal strains, creep and shrinkage, and structural loads were measured to evaluate the demands from the continuous-deck details.

After completing the study, no major in-service issues were found with the current continuous-deck detail, with only small amounts of leaks and cracking being observed. However, the study found there was difficulty in the construction of the joint, consuming time and labor, especially in skewed bridges. After evaluating the current practices throughout the United States, Snedeker et al. (2011) concluded that most designs are satisfactory but still can be improved, especially at the abutments of these bridges. Using beam theory to analyze the forces in the continuous deck, it was determined that due to the high amount of strain induced, there is not a realistic number of reinforcing bars to prevent cracking. Performing a rigid-body mechanics analysis, it was found that the girders experienced end rotation and longitudinal movement, reducing the tension force across the construction joint. A new design was recommended at the construction joints for continuous decks, with the original detail as shown in Figure 2-3 and Figure 2-4 and then the modified details are shown in Figure 2-5 and Figure 2-6.

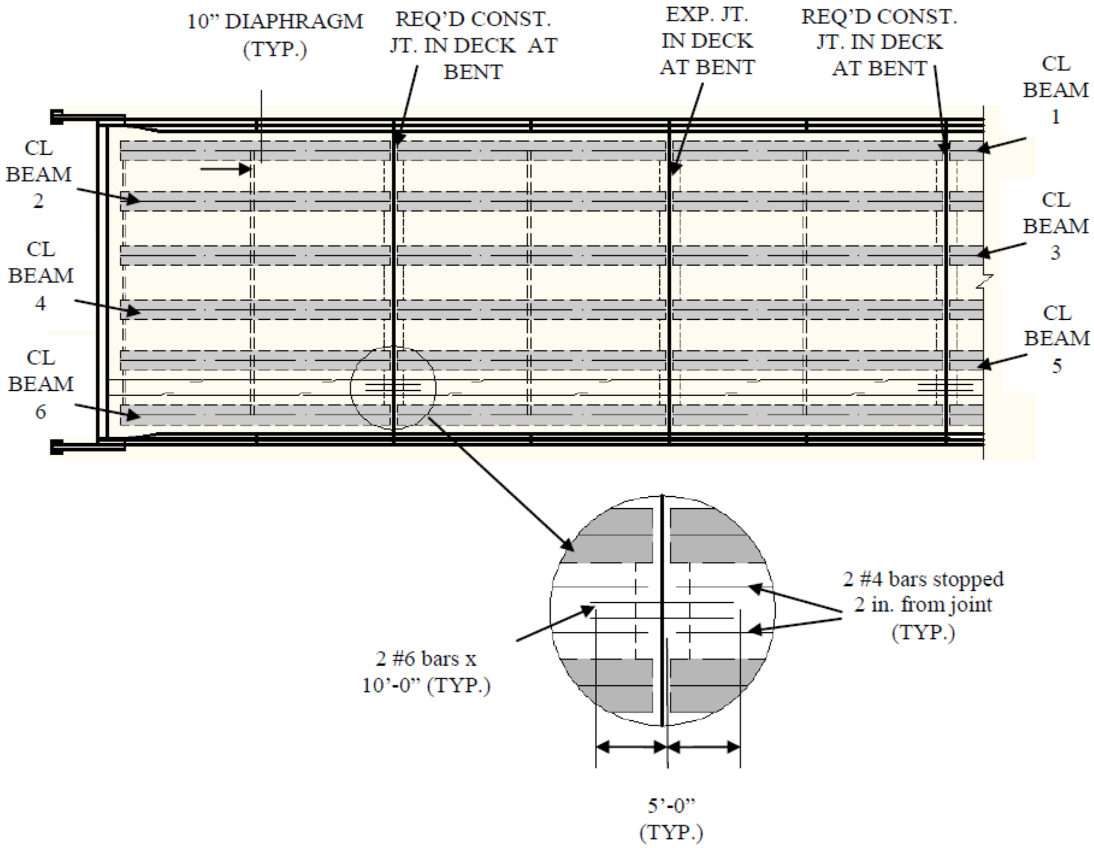

Figure 2-3. Plan view of current continuous bridge deck (SR 46 Over Oconee River) (Snedeker et al., 2011)

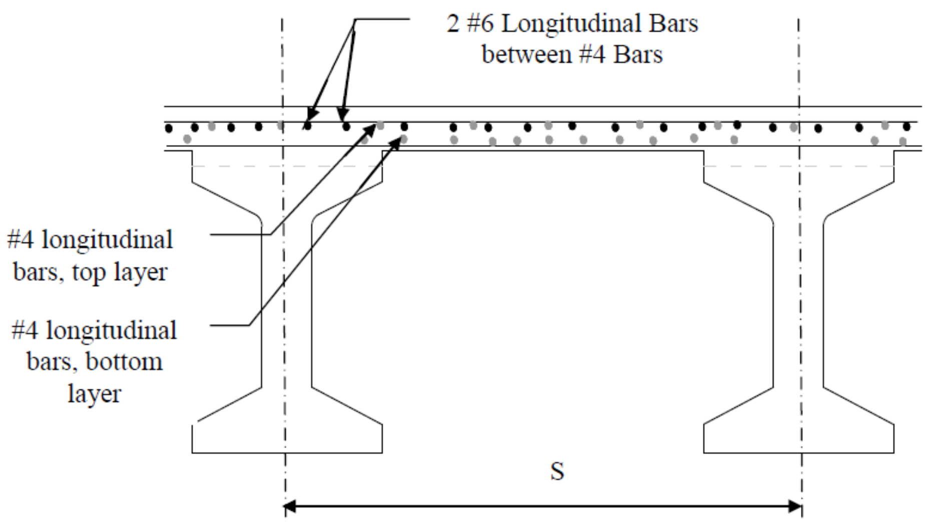

Figure 2-4. Section view at construction joint of current continuous bridge deck (SR 46 Over Oconee River) (Snedeker et al., 2011)

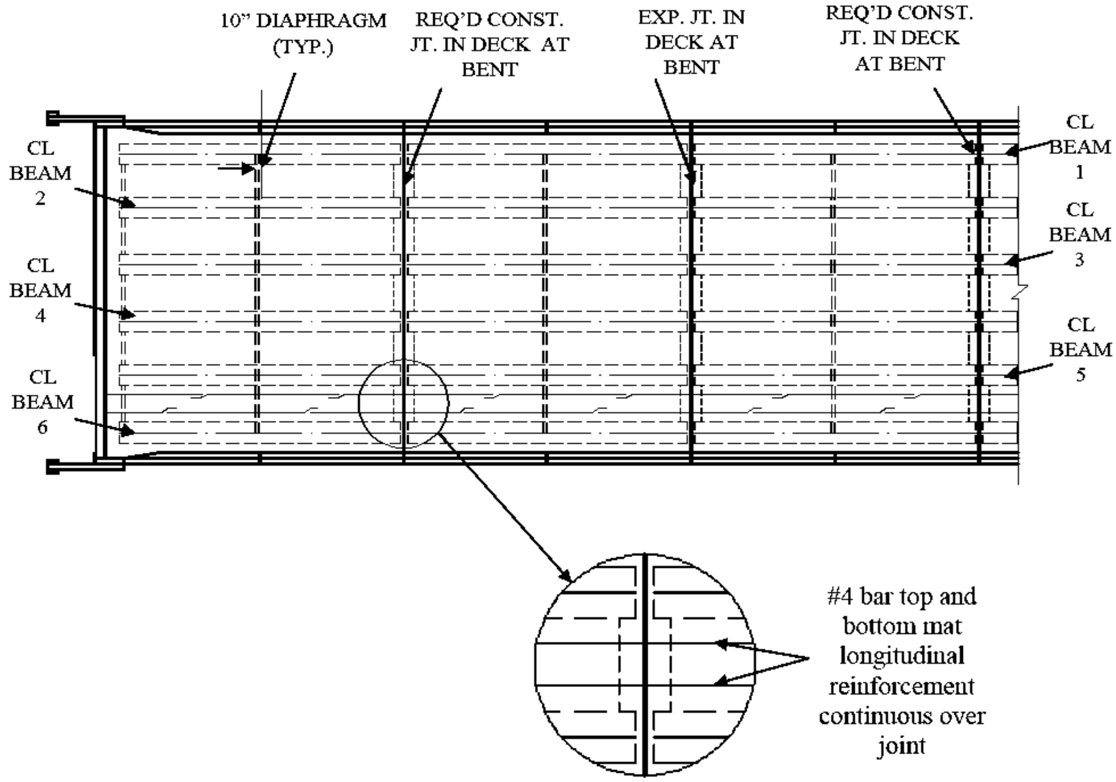

Figure 2-5. Plan view of modified continuous deck detail (Snedeker et al., 2011)

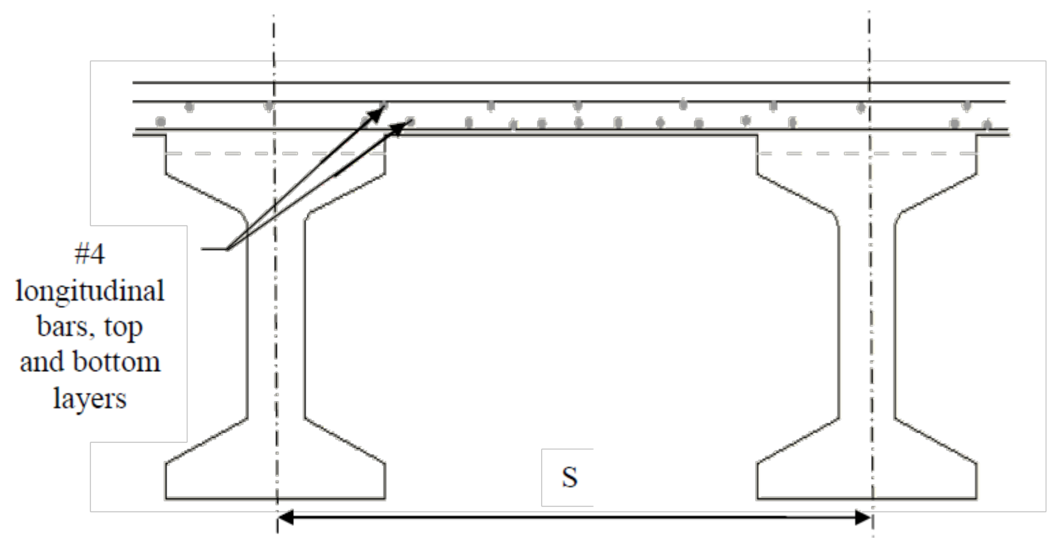

Figure 2-6. Section view of modified continuous deck detail (Snedeker et al., 2011)

Following the study performed by Snedeker et al. (2011), Davidson et al. (2012) then performed a field monitoring study. This involved five bridges being instrumented in Georgia to observe movement at the open and closed joints. This field monitoring was performed to provide more insight into the demands that would be placed upon the continuous deck detail. The bridges were instrumented to primarily observe the performance due to thermal loads. Dial gauges were used to measure longitudinal movement (Figure 2-7) and Demountable Mechanical Strain Gauge (DEMEC) points to measure expansion and contraction at the bridge joints (Figure 2-8). Wax plates were used to track the overall range of motion at the joints, the system shown in Figure 2-9.

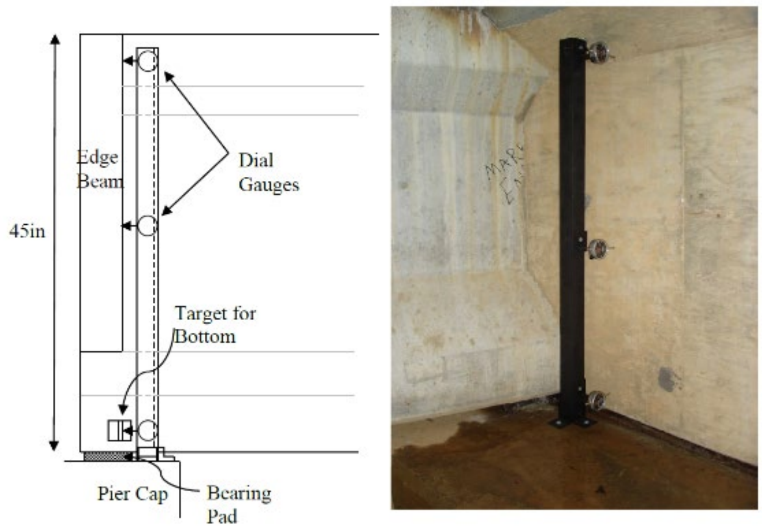

Figure 2-7. Dial gauge system diagram and bridge installation (Davidson et al., 2012)

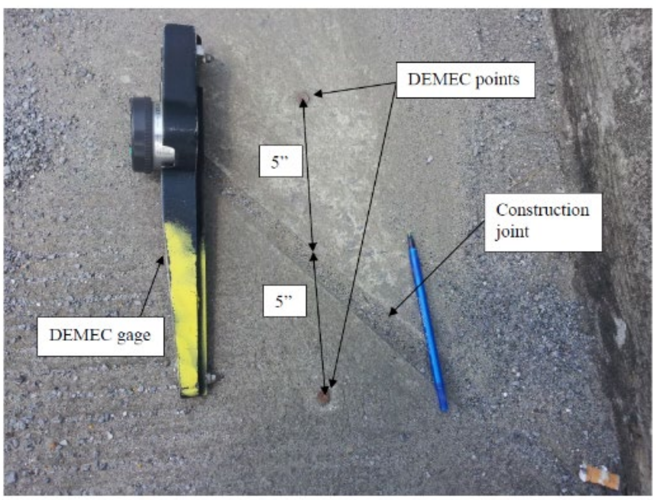

Figure 2-8. DEMEC points at construction joint (Davidson et al., 2012)

Figure 2-9. Wax plate for tracking the motion of the bridge (Davidson et al., 2012)

After performing the field study, Davidson et al. (2012) recommended that the maximum length of a bridge should be 400 ft when using the Evazote joint design at the abutment as the length is limited by the deformation capacity of the closed joints. They also gave recommendations for the best practices when constructing the joints to allow for the best performance and minimize leaking and cracking.

Canales (2019) performed a study to understand the relationship that the performance of a link slab has as part of a continuous-deck bridge while considering the varying degrees of stiffness and structural loading conditions. The force that a link slab is subjected to, the reactions in the supports, and the interactions between the two were analyzed with a parametric study, looking at the effect different variables had. The parameters investigated are shown in Table 2-3. To further investigate the performance of link slabs, a field study was performed on a bridge with link slabs in different configurations, which also considered live-load testing and long-term health monitoring.

Table 2-3. Variables and ranges utilized in parametric study (Canales, 2019)

<table>
<tr><th colspan="7">Variants</th></tr>
<tr><td>Number of Spans</td><td colspan="3">2</td><td colspan="3">3</td></tr>
<tr><td>Total Length</td><td colspan="2">100ft; 150ft</td><td colspan="2">150ft; 225ft</td><td colspan="2">200ft; 300ft</td></tr>
<tr><td>Span Length Ratio (β)</td><td colspan="2">0.5</td><td colspan="2">0.7</td><td colspan="2">1</td></tr>
<tr><td>Girder Spacing</td><td colspan="2">6ft</td><td colspan="2">7ft</td><td colspan="2">8ft</td></tr>
<tr><td>Support</td><td colspan="3">Bearing Pad Supports – Fixed</td><td colspan="3">Bearing Pad Supports – Floating</td></tr>
<tr><td>Temperature</td><td colspan="2">0°F</td><td colspan="2">36°F</td><td colspan="2">73°F</td></tr>
</table>

A weak relationship was observed between the composite section axial and rotation stiffness and the tension force that develops in the link slab, whereas the support stiffness has the greatest influence on link-slab performance. It was found that the idealized support conditions may overestimate the role of the link slab. The stiffness of the girder was not found to have a direct influence on the tension force, but the temperature can have a considerable influence on the force in the link slab. Canales (2019) observed that most of the displacement of the girder ends comes from thermal loading. Increasing the restraint that is imposed by the supports increased the width of cracks that develop on the tensioned face. The formation of these cracks was also found to be directly affected by temperature gradients. Increasing the restraint was also found to result in larger forces in the link slab due to the restriction of girder-end movements. Effects on the deck from the live-load tests were less than the effects observed from thermal loads on the deck section.

Summary

Through all the varying conclusions reached across different aspects of a closed-joint bridge's behavior, the main conclusion reached in most of the studies was that the stiffness of the closed joint can be negligible compared to the girders. This results in the girder ends of closed-joint bridges being observed by researchers to rotate as if an open joint were present, behaving as individual simply supported spans. The main factor that contributed to the movement of the girder ends was loading from thermal gradients, where live loads had a smaller effect on these demands. This increased movement, then, creates a need for crack control at these locations, which could be handled by tooled construction joints or saw-cut joints.

2.3. Design of Closed-Joint Bridges

With more research available on the range of behavior that a closed-joint bridge could exhibit, studies also looked at how to incorporate the closed joints in their bridge design with simpler and more effective procedures. To be able to develop these programs and ensure they truly work, more analysis was required in laboratory settings to determine the effects of the components in the closed joint on the overall bridge. Research also included investigating the effects of new material designs for concrete and reinforcement, as well as arrangements of reinforcement within the closed joint.

2.3.1. Analysis Methods

Caner (1996) worked to improve the program developed by El-Safty (1994a) to be able to provide better predictions or develop a new method of analysis to validate test results. This task was accomplished using two separate test programs, the first being one that was developed by Gastal (1986) and then modified by El-Safty (1994a), which was referred to as the JBDS program in the paper. The second program that was developed to validate the test results after the JBDS program failed to accurately predict results was referred to as the JBDL program. The research aimed to analyze the shrinkage, creep, and thermal changes for closed-joint bridges and then develop design criteria for closed-joint bridge decks that are on simple-span girders.

After results were obtained from testing, Caner (1996) concluded that each girder in the bridge can be designed as a simply supported member due to the lower stiffness of the link slab, creating negligible continuity. Bending and cracking effects were determined to be the governing factors in link-slab design due to girder deformation under live load impact. The proposed design method developed as part of the study accurately predicted the test results, and the link-slab behavior was observed to be independent of the types of supports under live load testing. When designed for live loads, the link slab was found to be satisfactory for handling loads from thermal and time-dependent effects. It was recommended that two layers of reinforcement should be used to provide better crack control.

In their study, Okeil and El-Safty (2005) focused on the integration of continuity into only the deck of the structure (partially continuous) using link slabs. They presented a simplified method for analyzing these types of bridges as part of the study. A parametric study was also conducted for a two-span bridge to validate the design parameters for closed-joint bridges. From these studies, the link slabs that span over hinge supports were predicted to experience larger tension forces as compared to support conditions with less fixity (rollers). For practical reinforcement ratios, the continuity moment experienced was observed to be 9-22% of the fully continuous system for roller supports and 50-91% for hinged supports. For the positive moment experienced at midspan, it was found that the moments were 94-98% of the simply supported system for roller supports and 77-90% for hinged supports. For Okeil and El-Safty (2005), the hinged support case was a worst-case scenario, so any movement in these supports was said to reduce the forces experienced in the structure.

Aktan et al. (2008) identified distresses in closed-joint bridges in their study through field inspection, looking at the link slab, abutments, pier caps, open joints at the sleeper slab, and bearings. Finite element models of several components and combinations were developed to better understand the behavior of these components due to varying factors. Bridges in Michigan that were selected as part of this analysis are shown in Table 2-4.

Table 2-4. Bridges selected for field inspection (Aktan et al., 2008)

No	Bridge ID	Year Built	Region	County	Feature Intersected	Facility	Main Spans	Max Span (ft)	Length (ft)	Skew (Deg.)	Girder Type
1	S04-1 of 63174+	2001	Metro	Oakland	13 Mile Road	I-75 NB	3	63	141	0	PC++
2	S04-2 of 63174+	2001	Metro	Oakland	13 Mile Road	I-75 SB	3	63	141	0	PC
3	S08 of 41027	1964	Grand	Kent	Monroe	I-196 EB M-21	3	72	179	Varies	ST*
4	B01 of 10042	2003	North	Benzie	Betsie River	M-115	3	50	150	20	ST
5	S12-3 of 25042**	1969	Bay	Genesee	I-75	I-69 EB	4	70	210	20	PC
6	S12-4 of 25042**	1969	Bay	Genesee	I-75	I-69 WB	4	70	210	20	PC
7	S12-7 of 25042**	1969	Bay	Genesee	I-75	I-69 Ramp E	4	70	210	20	PC
8	S12-8 of 25042**	1960	Bay	Genesee	I-75	I-69 Ramp F	4	70	210	20	PC

+ Identical bridges; ++ Prestressed concrete girders; * Steel girders; ** Identical bridges

Aktan et al. (2008) observed that the current detail could be improved by eliminating the continuity of the top reinforcement of the link slab. This modification is shown in Figure 2-10. They also recommended that future details for closed-joint bridge decks that have construction joints with continuous bottom reinforcement where deck sliding over the backwall or backwall sliding over the abutment are incorporated.

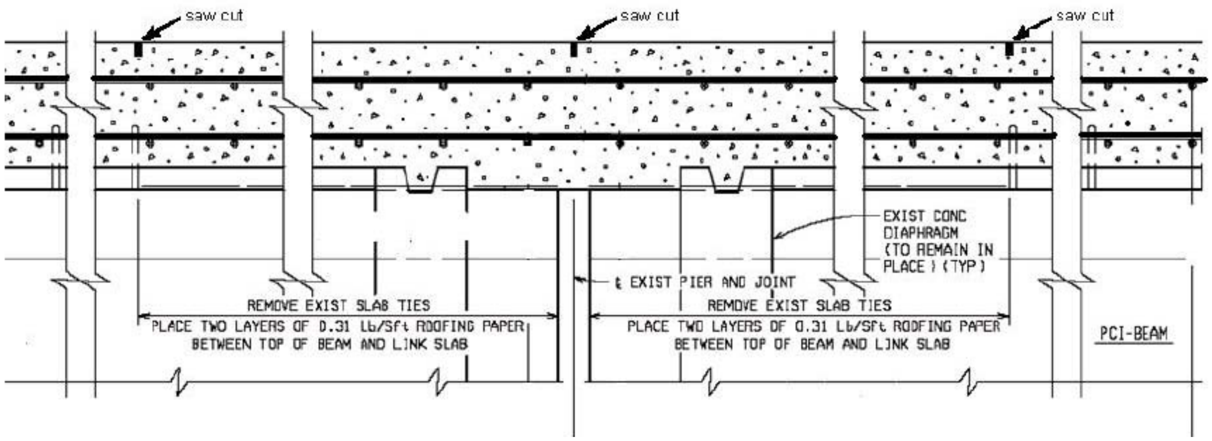

Note: Both reinforcement layers are continuous with three saw cuts

Figure 2-10. Proposed link-slab details (Aktan et al., 2008)

Ulku et al. (2009) performed a finite element investigation into the behavior of link slabs to recommend better details for their design, providing an example of their method for designing a link slab at the end of the paper. Through this investigation, it was recommended to set the debonding length as 5% of the span length due to the moments observed to develop at the link slab decreasing with an increase in debonded length. Because of the effects of thermal loading, Ulku et al. (2009) also recommended using both top and bottom reinforcement along with a saw cut over the pier centerline for crack management. The proposed link-slab detail is shown in Figure 2-11, which follows closely with the detail proposed by Aktan et al. (2008).

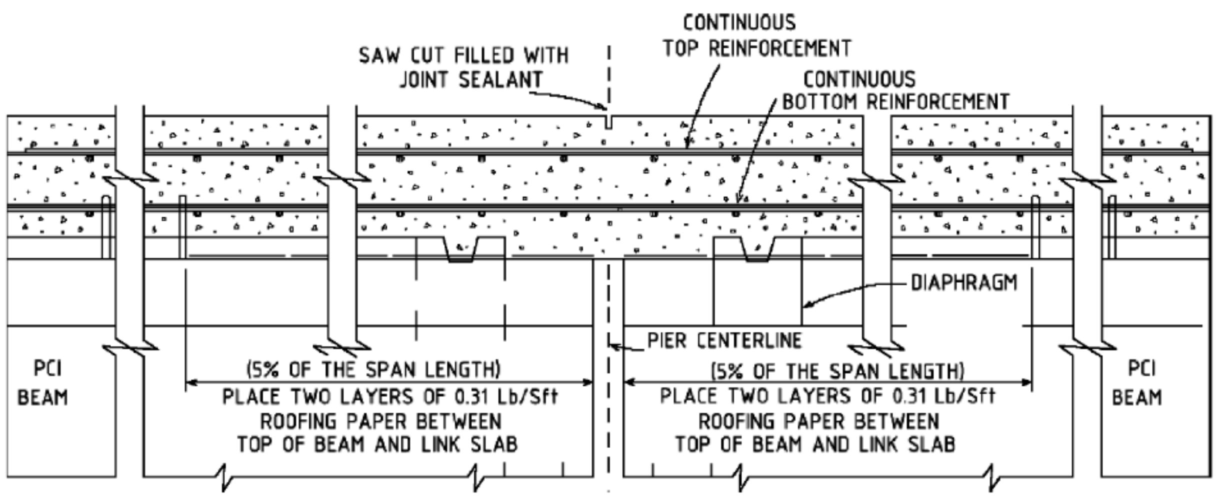

Figure 2-11. Proposed link-slab details (Ulku et al., 2009)

Stringer and Burgueño (2012) performed inspections on several closed-joint bridges in Michigan that were determined to be suffering from deck cracking. From this inspection, parameters and conditions were identified to aid in modeling this distress and develop a prototype system for evaluation. The behavior of the closed-joint bridge was evaluated by running experiments on four test-unit systems, which were used to validate the computer model, with the parameters of these test units shown in Table 2-5. A parametric study was also conducted on full-scale bridge models, one with concrete girders and the other with steel girders. The parameters of each model are listed in Table 2-6.

Table 2-5. Experiment parameters for sub-assembly evaluation (Stringer and Burgueño, 2012)

Test No.	Girder Type	Diaphragm Type	Shear Connectors	Reinforcement Detail	Concrete Mix	*Unique Parameter*
1	Steel	C-Channel	Studs-Density 1	Detail 1	Standard	*Standard Design*
2	Steel	C-Channel	Studs-Density 2	Detail 1	Standard	*Shear Connector Density*
3	Steel	X-Bracing	Studs-Density 1	Detail 2	Standard	*Diaphragm Type and Reinforcement Density*
4	Steel	C-Channel	Studs-Density 1	Detail 1	Optimized	*Concrete Mix*

Table 2-6. Full-scale bridge model properties (Stringer and Burgueño, 2012)

Parameter	Concrete Spread Box Beam	Steel Girder
Beam/Girder Type	60” Prestressed Concrete Box Beam	39” Continuous Plate Girders
Beam/Girder Spacing	90” on center	5’-5 1/2” on center
Beam/Girder Support Conditions	Simply Supported on Elastomeric Bearings	Rocker Bearings at abutments, fixed at the central pier
Number of Spans	4	2
Bridge Length	322’-6”	260’-0”
Bridge Width	58’-8”	85’-11”
Abutment Type	Fully Integral, with piles oriented in weak axis bending	Fully Integral, with rigid piles oriented in strong axis bending
Skew Angle	0°	22°

For both the steel and concrete girder bridges, the observed behavior concerning shrinkage cracking was similar to one another, and their performance was not observed to be noticeably better than the other. For bridges with larger spans, and therefore more negative moments around the piers, higher inelastic strain values and more cracking were observed in the specimens. The amount of cracking and the magnitudes of the shrinkage loads were said to be more influenced by the mixture design when compared to changing the other bridge design parameters. The amount of reinforcement was also not observed to have a considerable influence on the amount of cracking in the bridge deck. Increasing the skew angle, however, lowered the bridge's performance and resulted in more deck cracking observed near the abutment region. The models developed by Stringer and Burgueño (2012) showed that providing less restraint will result in less cracking, and that minimizing shear connectors would be ideal. Changing the amount of reinforcement had a minimal effect on performance, so it was recommended that the current design that the Michigan Department of Transportation (MDOT) used be maintained.

Au et al. (2013) performed an experimental study for the Ministry of Transportation of Ontario (MTO) on the debonded link slab (DLS) system to observe its structural behavior, with Figure 2-12 depicting the details of this system. This study involved using scaled models and applying a repetitive loading cycle to simulate traffic loads and observing the system's long-term performance. Behavioral load tests were also conducted on a recently rehabilitated structure using the DLS system.

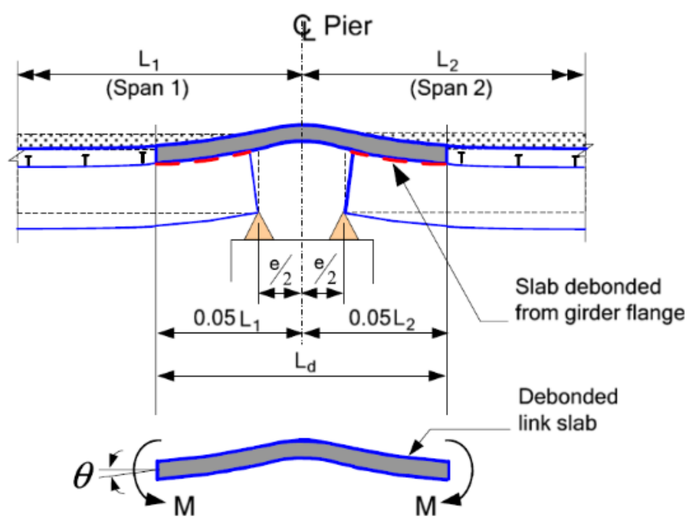

Figure 2-12. Debonded link slab system studied (Au et al., 2013)

The test data from field tests performed lined up with the experimental laboratory tests and models, with measured deflections being consistently smaller than theoretical values. Au et al. (2013) observed that the link slab was able to provide partial continuity in the deck at the pier supports. The rotations were reduced at the girder ends, the vertical displacements of the girder were smaller, and smaller positive moments were observed in the spans. The procedure that was proposed by Caner and Zia (1998) was modified by the researchers to be able to account for displacement between the link slab and the girder, with a new equation being derived and presented by Au and Lam (2011).

Gergess (2019) investigated the behavior of link slabs bonded to precast, prestressed girders varying in length and type. From this analysis, a methodology was developed to be able to calculate the shear and bending moments in the link slab. Parameters that influenced the shear and flexural stiffness of the link slab were identified (length of link slab, deck thickness, concrete strength, amount of reinforcement) and a closed-form solution was created based on these parameters. A parametric study was then conducted to investigate how these parameters affect the structural response. The study determined that the ratio of the link slab moment to the girder simple-span moment varies from 0.22-0.09 for a uniform load and 0.14-0.07 for a distributed load for an AASHTO Type IV girder. It was also observed that by increasing the dimension of the open joint, reducing the steel ratio, and increasing the girder strength, the above ratios will be reduced. Gergess (2019) recommended using $0.75\rho_b$ for the steel ratio for Type II to IV girders and limiting the steel ratio to $0.55\rho_b$ for Type V and $0.40\rho_b$ for Type VI in the link slab.

2.3.2. Materials

Saber and Aleti (2012) conducted laboratory testing to study the behavior and strength of closed-joint bridge decks in Louisiana reinforced with FRP grids under static loading, recording and measuring the loads, deflections, strains, and capacity of the FRP link-slab specimens. Finite element models were also developed as part of this study to further investigate the behavior of closed-joint bridges with link slabs. Two models were developed to compare against one another, one with open joints over the support and the other with closed joints.

From the study, Saber and Aleti (2012) observed that the ductility provided by the FRP grid reinforcement was able to accommodate deformations experienced in the bridge deck, caused by girder deflection, concrete shrinkage, and thermal loading. They concluded that the results indicated that using FRP link slabs would allow for structural needs to be addressed, lower the flexural stiffness of the link slab, and provide adequate durability of the link slab. From these conclusions, the researchers recommended that this design be used in new construction projects and that these techniques be considered when repairing and retrofitting bridge decks.

Hou et al. (2018) performed several experiments to explore the mechanisms involved in using Ultra-High Ductility Cementitious Composites (UHDCC) in the design of link slabs in China to improve their performance under fatigue effects. For this, uniaxial tension and compressive tests were conducted to observe the fatigue properties of plain UHDCC. From these tests, Hou et al. (2018) observed that plain beams composed of UHDCC have acceptable fatigue behavior under high stresses. To determine the static and fatigue capacity of a UHDCC link slab, a four-point bending test was conducted. Higher deformation was observed in the UHDCC link slabs, but outperformed link slabs composed of standard concrete in fatigue, which could be attributed to the tensile-hardening behavior of UHDCC. They also observed that the UHDCC helped with the energy dissipation from fatigue vibrations, reducing the energy input intensity.

The goal of Accelerated Bridge Construction (ABC) is to provide bridge designs and construction methods that allow for quick construction and create durable and long-lasting bridges. Shafei et al. (2018) conducted an experimental study on Fiber Reinforced Concrete (FRC) beam specimens to determine optimum amounts of synthetic concrete fibers in cast-in-place link slabs to enhance the durability, constructability, and overall effectiveness of this connection. The mixture designs from the experimental study were then evaluated for link slab performance under uniaxial tension to test for cracking behavior, rebar deformation, and global deformation. These results were then also compared against the performance of a specimen composed of ultra-high performance concrete (UHPC). To observe the stresses that developed in the specimens, half-depth link slabs were created under varying support conditions. Observations made on crack initiation and propagation at ultimate loading were used to help determine the suitability of using FRC for link slabs for ABC applications.

After performing the experiments and analysis, the support conditions were observed by Shafei et al. (2018)to have a major effect on the strains and stresses experienced in the link slab, with the Hinge-Roller-Roller-Hinge (HRRH) case being the lower bound case and the RHHR case being the upper bound. The strains in the bonded region of the link slab in both the steel and concrete were lower than ones observed in the debonded region, meaning bonded link slabs were more effective in transferring stresses, along with a more linear stress distribution in the bonded region in this study. Shafei et al. (2018) concluded that the FRC material for the link slabs demonstrated its effectiveness due to small crack widths and consolidation of small cracks being observed in the debonded region.

2.3.3. Link-Slab Configuration

Charuchaimontri et al. (2008) performed a laboratory study in Thailand that considered the behavior of long link slabs with various lap reinforcement details by measuring the axial deformations, end rotations, end translations, and modified span loading with fixed-end supports. Three full-scale tests were performed, each with a different configuration of lap reinforcement, shown in Figure 2-13.

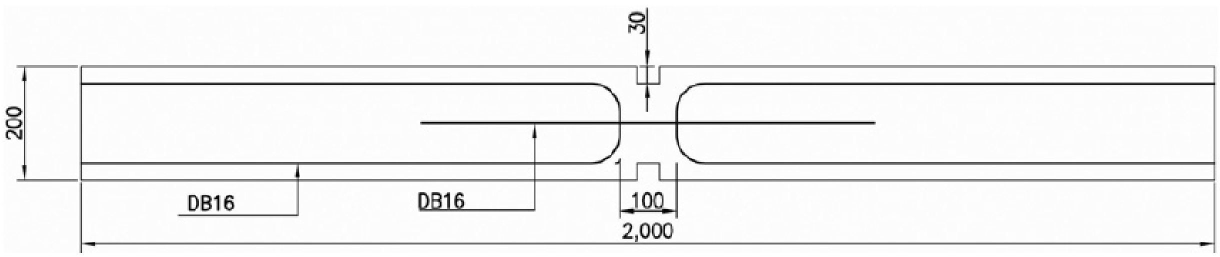

(a) Mid-span hinge (LS_000).

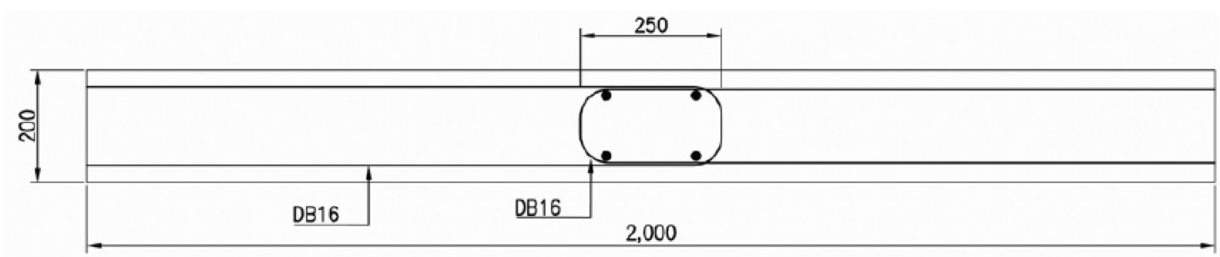

(b) Semi continuous (LS_025).

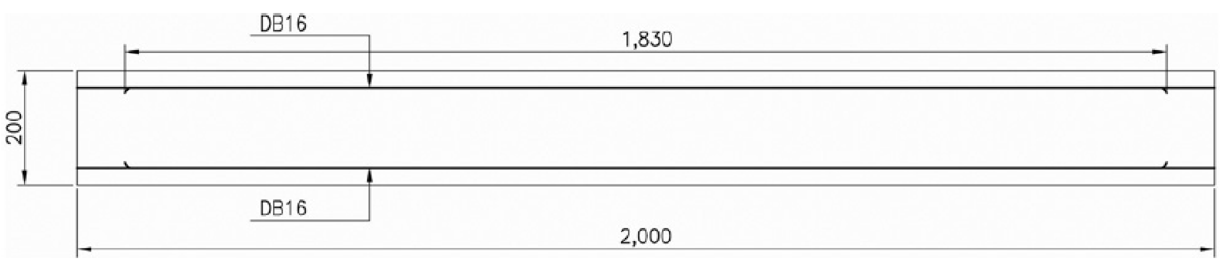

(c) Fully continuous (LS_183).

Note: Dimensions shown are in millimeters

Figure 2-13. Lap reinforcement configurations (Charuchaimontri et al., 2008)

The crack distribution and widths were observed to be significantly affected by the reinforcement of the link slab. The mid-span hinge (L.S.000) arrangement was observed to behave as two cantilevers with a compressive force at the top surface of each side. The failure occurred when a horizontal crack formed at the top of the mid-span section (due to compression) and inclined cracks formed at the supports. The semi-continuous (L.S.025) arrangement functioned as a continuous slab until a flexural shear crack occurred due to the insufficient splice of reinforcement not allowing the positive moment to fully develop. For the continuous (L.S.183) arrangement, the positive moment was able to fully develop, resulting in a crushing of the concrete or crack splitting at failure.

Reyes and Robertson (2011) performed laboratory testing in the state of Hawaii three different link slab configurations: 1) cast-in-place (CIP), 2) precast and dowelled horizontally and vertically, and 3) precast and dowelled only vertically. The suitability of each was determined to be implemented into local and national highways. Several parameters were determined to characterize the suitability of the link slab. The displacement of the gap should be nearly equal to the displacement of the unbonded section, which would indicate if the unbonded section was behaving elastically. The link slab should remain elastic and retain its compressive capacity. The tension failure of the link slab should occur further on from expected loads. Finally, uniform micro-cracking over entire debonded section of the link slab should be observed. The researchers observed in this study that the CIP link slab provided suitable continuity at the ends of the high-performance fiber-reinforced cementitious composite (HPFRCC) section. However, the effectiveness of the link slab in compression was reduced, so a pre-cracked link slab was recommended. When time is a consideration during the construction process, it is recommended not to use HPFRCC concrete due to the long time needed to reach optimal strength. For precast slabs, Reyes and Robertson (2011) recommended that vertical dowels be installed at an angle and use a combination of vertical and horizontal dowels to make the bond more effective.

Summary

From the research conducted investigating the factors that affect how bridges with closed joints are designed, a common consensus was that each span could be designed as an individual simply supported span, mainly when considering effects from live load. For the reinforcement that is present at the closed joint in the deck, providing continuous top and bottom reinforcement was found to result in the best performance. This reinforcement layout's main contribution is improving crack width control at these locations. Using different materials for the link slabs in bridges resulted in better fatigue resistance and smaller crack widths, depending on the material used. The effectiveness of these options depends on the constructability and cost of materials versus the increase in lifespan.

2.4. Field Instrumentation and Monitoring

Monitoring the behavior of bridges constructed in the field can provide useful data to understand the full effect of designing bridges with closed joints. These bridge decks are subjected to a wide range of environmental conditions and are more physically affected by the rest of the structure, something that is often not fully captured by laboratory testing. The instrumentation installed on these bridges, then, needs to be able to fully capture the wide range of movements and responses to properly analyze these closed joints.

Kowalsky and Wing (2003) instrumented a closed-joint bridge to observe its behavior due to live, random, and thermal loading. For the live-load tests, a truck loaded with gravel to impose maximum positive and negative moments on the bridge was used. Then, using two LVDTs of a known distance apart, the rotation from the load was determined. From this live load testing, the researchers noticed fine cracks in the link slab. This was stated to be normal under everyday service loads, with crack width sizes of 0.08 in (2 mm) and located 0.79 in (2 cm) apart. Comparing the results from testing and a simply supported model that was developed, the rotations and deformations were similar, and the deformations between the link slab and girders were said to be compatible with each other. This meant the assumptions for design and analysis were valid for live-load analysis. For the link-slab rotation due to several loading conditions, the rotations due to overload were observed to be the most severe (comparing service, overload, and thermal demands). A simplified design procedure was investigated in this paper as well. These produced design charts that the steel reinforcement can be obtained from the desired crack width and rotation.

French et al. (2012) completed a large study on instrumenting, monitoring, and modeling the newly constructed I-35W bridge. This bridge did not employ the use of closed joints, but the methods taken to instrument and monitor the bridge are still of value to this research project. Several different types of instrumentation were used to monitor the bridge, which included static (vibrating wire strain gauges, thermistors) and dynamic (accelerometers, linear potentiometers, resistive strain gauges) sensors as well as a corrosion monitoring system. This project began in tandem with the construction of the bridge, so samples of the concrete used in the bridge were able to be taken for analysis of the in-place properties, which included the compressive strength, modulus of elasticity, tensile strength, shrinkage and creep, and coefficient of thermal expansion. Finite element models were used to validate the measured data in the field. This allowed the researchers to compare the performance of the bridge to design standards and create a tool through which the performance of a bridge can be predicted.

To induce known loading onto the bridge, French et al. (2012) used trucks of known weight. This established a baseline response of the bridge for known static and dynamic loading. Using the data measured from these tests, the finite element models created for investigating the behavior of the bridge were able to be validated. One set of these tests was performed before the bridge opening (2008), and the other after two years of the bridge being open to traffic (2010). For the thermal effects on the bridge, the study defined a positive thermal gradient as the top temperatures being higher than web temperatures. Differences were observed between the linear potentiometer data and estimates that only assumed axial expansion showed that "axial expansion due to the thermal gradients, rotation of the boundary conditions, and time-dependent effects will need to be accounted for to better predict the structural expansion."

From the instrumentation and monitoring, the study concluded that environmental variations were found to have a larger impact on global bridge behavior than truck tests. The measured temperature gradient for the bridge was found to best match the gradient from Priestley (1978), seen in Figure 2-14, which was scaled to the temperature zone defined by AASHTO (2010). The study concluded that thermal gradient effects can only be considered structurally when considering service-level behavior.

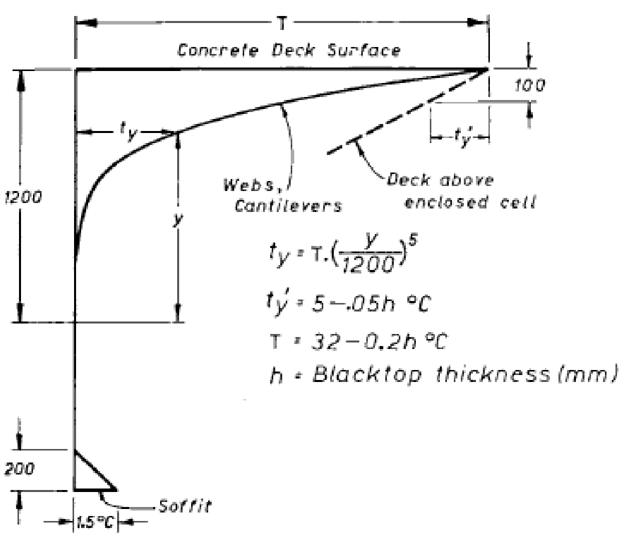

Figure 2-14: New Zealand design thermal gradient from Priestley (1978)

Chen et al. (2015) focused on reusing instruments through each stage of the bridge's life, from construction to completion to monitoring. The study focuses primarily on prestressed concrete box girder bridges, but the study is still a good reference for what parts of a bridge to focus on when monitoring and provides good strategies for instrumentation. For the bridge behavior, instrumentation measured strain, deflection/rotation, support displacement, and acceleration/velocity. To monitor the bridge over its lifecycle and signs of physical damage/losses, instrumentation was installed to observe corrosion, crack sizes, and prestress losses. The external causes of loading conditions were also recorded by using traffic cameras, measuring the temperature, and utilizing available weather stations.

Ziaei et al. (2022) monitored a curved integral abutment bridge with closed joints supported by steel girders having over 100 ft span lengths. The focus of the instrumentation installed on the bridge was at the abutments. This project ran in tandem with the construction of the bridge, so instrumentation was able to be installed before bridge completion and could therefore capture a larger range of behavior than other bridge monitoring projects. From this study, it was concluded that the amount of curvature in the bridge does not affect the linearity of the relationship between the bridge length to the longitudinal displacements, but the bridge having more curvature does display larger lateral displacements. The maximum stress at the pile-abutment connection generally displays a linear relationship with bridge length. The types of bearings at intermediate piers have a high influence over lateral displacements.

Birley et al. (2025) performed a study that aimed to provide recommendations for the improvement of the current link-slab details used by the Texas Department of Transportation (TxDOT), known as "poor boy joints." This was done both through field inspections and monitoring as well as performing full-scale experiments within a laboratory setting. The field work aimed to evaluate what is currently in place and its effectiveness, which consisted of field inspections and evaluation of eight (8) different in-place bridges and field monitoring of five (5) different in-place bridges for one week. The study also collected inspection reports to better understand the performance of the details in service across the state of Texas. In relation to the bridge movements that were focused on in the field monitoring, the system was comprised of displacement gauges installed at the top and bottom of the girder as well as a strain gauge on the underside of the deck spanning the joint. These gauges also provided temperature readings for calculating the temperature gradient across the section. The diagram of this layout is shown in

Figure 2-15. The rotation of the girder ends was calculated from the differential movement between the two displacement gauges.

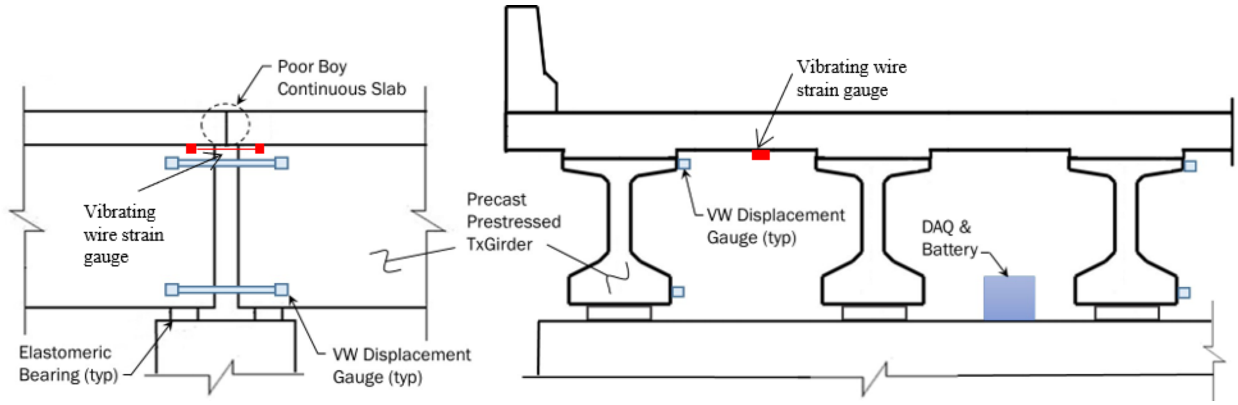

Figure 2-15: General layout of instrumentation at girder ends (Birley et al., 2025)

From the field monitoring, Birley et al. (2025) found that the rotations where this detail was used were smaller in magnitude than locations monitored with expansion joints. This indicated that the poor boy detail provides continuity that results in a reduction in girder-end rotation. The rotations that were monitored from live loads were found to be smaller in magnitude than the thermal rotations, highlighting the importance of quantifying the thermal demands that bridges will be subjected to.

Summary

The static responses to applied loads on the bridges that were monitored in prior studies were the rotations and displacements at the ends of the girders. Dynamic responses typically included acceleration and strain at and across the joints (open and closed). More comprehensive information about a bridge's behavior can be captured by installing instrumentation as the bridge is constructed, providing useful data as the bridge experiences loads throughout its life cycle. The response at the abutment of the bridges was also a heavy focus for closed-joint bridges, places that can experience settlement issues, and high-load responses. These field studies were compared with computer models developed to better understand the data recorded.

2.5. Standard Practices

As more research has given guidance and recommendations on how to use closed joints in bridge design, many state agencies have developed methods for themselves to use closed joints in their bridges. The effectiveness of their designs depends on what environmental conditions the bridges are typically exposed to and how much experience the state has with employing closed-joint designs. Reviewing what agencies have used and seeing what issues may arise in the field can be effective in guiding the development of an improved closed-joint design for ALDOT.

Eriksson (2001) reviewed the state of the art of precast/prestressed integral bridges and their limitations in several different areas. For the length of the bridges, they concluded that this creates concern with passive pressure effects, stresses in the piles, and the capacity of joints to carry the movement from the larger structure. Some state departments had implemented a restriction of 300 ft for steel superstructures and 600 ft for prestressed concrete superstructures, but Tennessee has been successfully able to implement continuous decks in larger span lengths. Looking at the geometry of the bridge, curved bridges imposed a harder challenge for continuous joints to handle, with only six states able to use integral construction for curved bridges. The skew angles of the integral bridges have been up to 40°. Tennessee, however, has been able to implement a skew angle up to 70°. The paper also recommended that pile foundations are not used where rock is closer than 10 ft to the bottom to allow the abutment piles to be flexible, with the New York State Department of Transportation (NYSDOT) specifying 20 ft penetration into suitable soils. Integral bridges had mostly been found to have piles as foundations, with a few cases that used spread footings.

Trados (2016) reviewed what details are used for eliminating open joints in bridges over multiple DOTs, looking at details for the abutments, bearings, and piers. For the details at abutments, Midwest states employ an integral abutment detail where steel girders are directly welded to HP Piles at the abutments. If the abutment was subject to excessive stress or deflections due to thermal effects, semi-integral (turn-down) details have been used. An example of this detail is shown in Figure 2-16. Some owners have recommendations that are not affected by the span length up to a 45-degree skew angle.

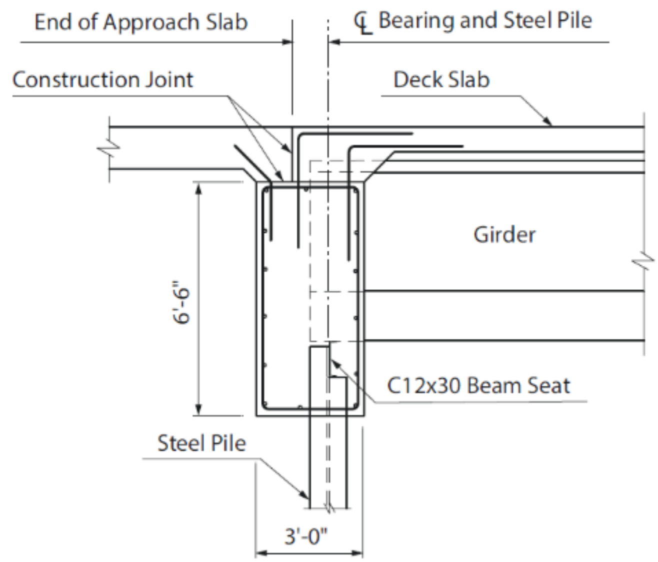

Figure 2-16: Example of integral abutment detail (Trados, 2016)

Looking at the pier details for simple span beams with continuous deck slabs, most bridges in Florida and Texas were built where the deck is continuous over the joint without end diaphragms or debonding shown in the details. An example of a typical detail can be seen in Figure 2-17. These details also include callouts for a saw-cut or tooled construction joint.

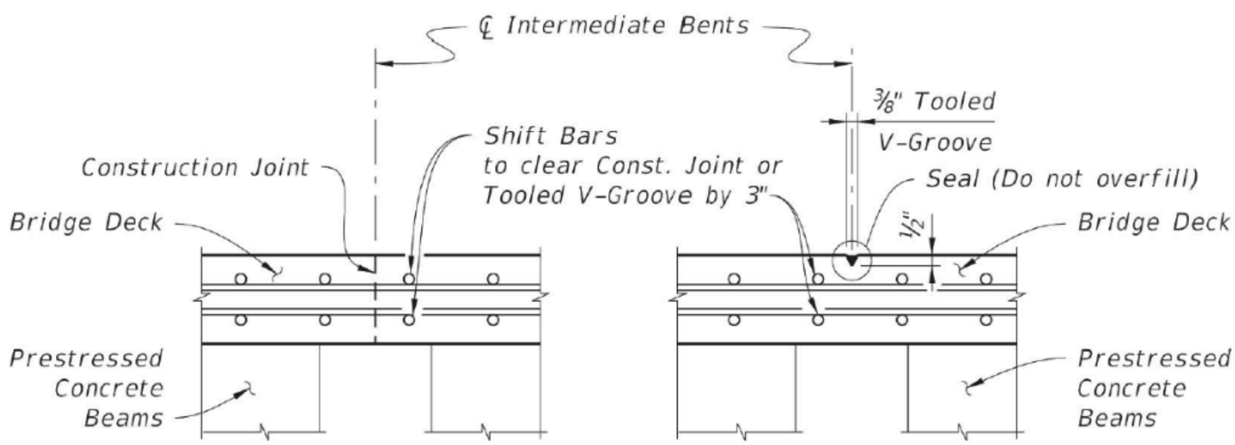

Figure 2-17: Florida Department of Transportation details for continuous slab over joint between simple spans (Trados, 2016)

The case with simple span beams with link slabs was also investigated, where the bridge deck is continuous over the joint with a length of the deck debonded from the girders around the joint. Typically, a groove is specified to be formed to control cracking. This type of detail was found to be common in the south and southwest. An example of the detail for retrofitting this type of continuous joint used in Virginia can be found in Figure 2-18.

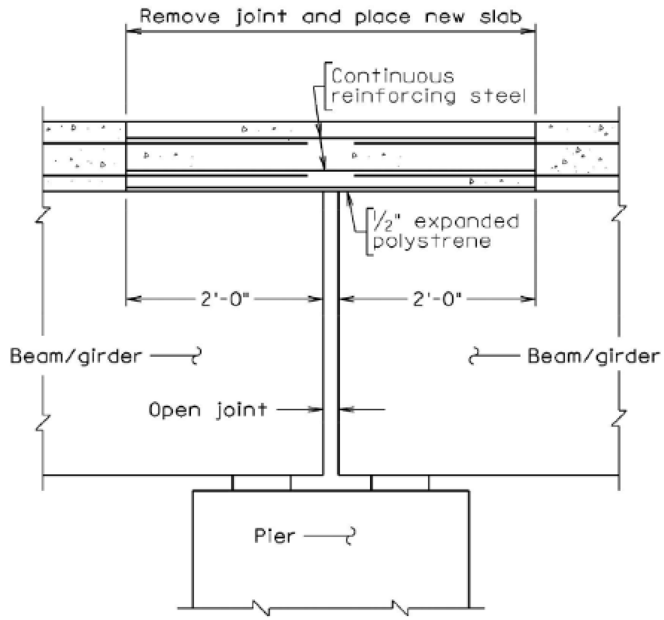

Figure 2-18: Link-slab detail used by the Virginia Department of Transportation to eliminate open joints in rehabilitation projects (Trados, 2016)

This study found that eliminating open joints is an effective method for reconstructing bridge decks, resulting in reduced maintenance, and leading to a longer lifespan. The consensus from the DOTs investigated was that open joints have been successfully eliminated on bridge sections up to 650 ft.

Chapter 3: Field Inspections

3.1. Introduction

Field inspections of closed joints were performed to determine the performance of the detail ALDOT has been using for bridges currently in service. These inspections aimed to identify any presence of structural concerns at the closed joint. Performing inspections across a variety of bridges with different lengths, skew angles, numbers of spans, etc., can provide cases, if any, where the closed joint is more appropriate to utilize in a bridge design than others based on its observed performance. Information obtained in these inspections can be used to determine the best aspects of the closed joint to focus on during the field monitoring phase of this project.

The scope of these inspections was limited to bridges within the state of Alabama that were built using some version of the ALDOT closed-joint detail, inspecting the top of the deck for signs of wear and cracking, and underneath the deck for cracking and any other possible deterioration. To aid in determining which bridges had closed joints, ALDOT provided a list of bridges that they knew utilized this detail. The provided list ended up being more than 20 bridges, while the project was limited to performing five field inspections.

To further narrow this list, several more criteria were applied to obtain the necessary information to properly evaluate the closed joint and the factors that affect its behavior. The selected bridges were required to be in varying locations to observe the effects of various environmental conditions, such as being regularly exposed to chlorides. The inspections required that the underside of the deck be accessed relatively easily, so bridges over a long span of water or 30+ ft in the air were not considered for final selection. The bridges had to have relatively large spans (80+ ft) as short spans would not impose large enough movements to significantly impact the performance of the closed joint. The bridges also needed to be across different ages in their lifespan, from newly constructed to 20 years or more into their service life.

3.2. Selected Bridges

The bridges that were selected for inspection are displayed in Figure 3-1 at their approximate locations.

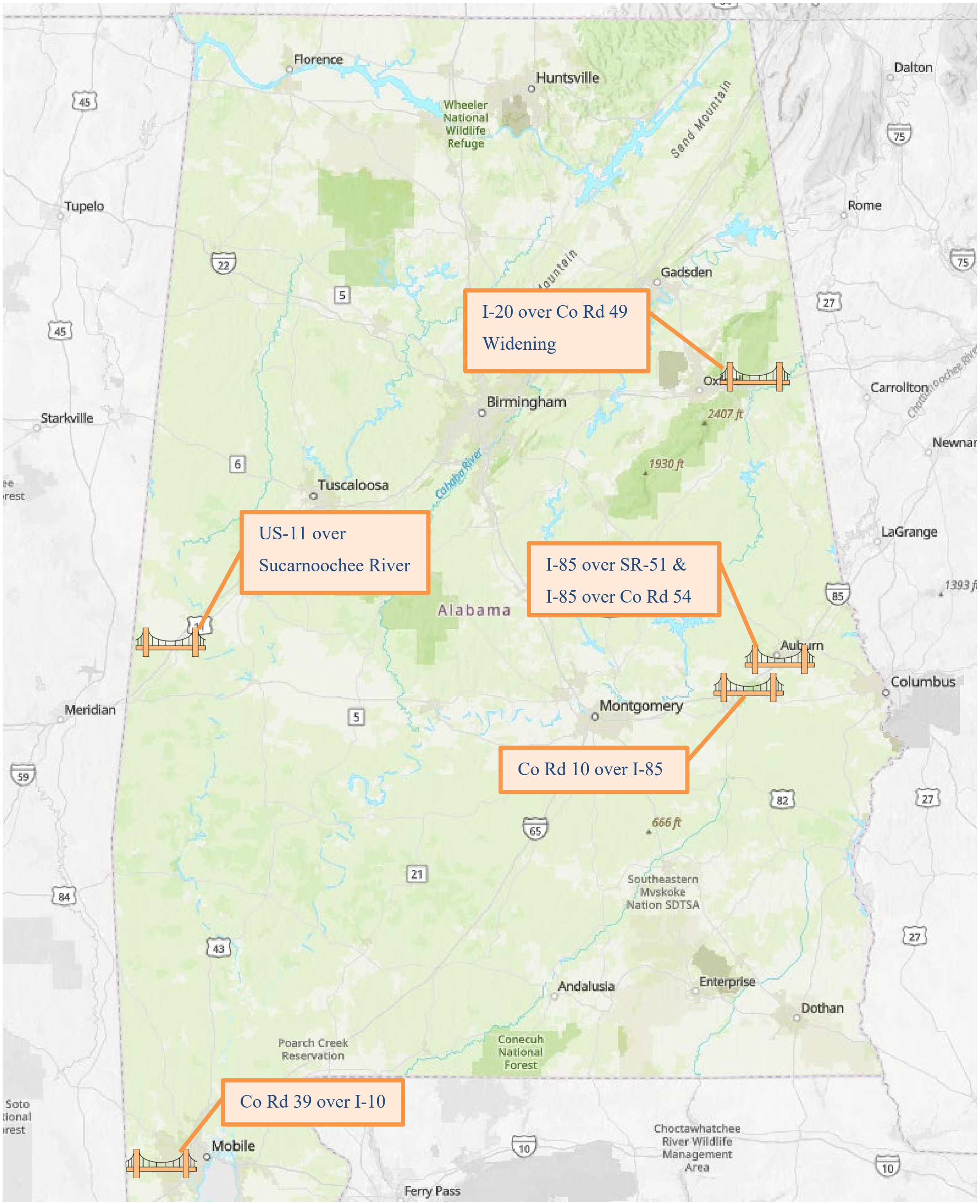

Figure 3-1: Locations of bridges inspected (map adapted from ArcGIS)

The first bridge (called LEE-1) that was inspected was I-85 over Co Rd 54 (LEE-1) in Lee County on August 9, 2023, as seen in Figure 3-2. This bridge was constructed as part of a larger project for bridge replacements in Opelika and finished construction earlier that year, with the first phase of construction happening in 2021. LEE-1 has three spans with a center span of 80 ft and adjacent spans of 50 ft, making an overall length of 180 ft. The bridge is at a skew angle of 30.6° and a grade of -1.53%. The center span is supported by AASHTO Type II Modified Girders with regular AASHTO Type II Girders on the adjacent spans. Diagrams of the type of prestressed girders can be found in Appendix B: Prestressed Girder Details. The deck is continuous over the length of the bridge, putting the closed joints at Bents 2 and 3.

Figure 3-2: Elevation view of I-85 bridge over Co Rd 54 (LEE-1)

The next bridge (called LEE-2) inspected was I-85 over SR-51 on the same day as LEE-1, as seen in Figure 3-3. This bridge was built as a part of the same project for bridge replacements in Opelika and had the final phase of deck placement on July 24, 2023, with the first phase of construction happening in December 2022. This allowed for the inspection of freshly placed closed joints. LEE-2 is like LEE-1 in that it also has three spans with a center span of 80 ft, but instead has adjacent spans of 55 ft, making an overall length of 190 ft. The bridge is at a skew angle of 18.7° and a grade of +0.76%. The center span is supported by AASHTO Type I Modified (BT+) Girders with AASHTO Type I Modified (III) Girders on the adjacent spans (see Appendix B: Prestressed Girder Details for the modifications made on girders). Like LEE-1, LEE-2 is continuous over the entire length, with closed joints in the deck at Bents 2 and 3.

Figure 3-3: Elevation view of the I-85 bridge over SR-51 (LEE-2)

The bridge (called LEE-3) on Co Rd 10 over I-85 was then inspected on November 28, 2023, as shown in Figure 3-4. Construction on LEE-3 was finished in 2010. This bridge has two equal span lengths of 140 ft, with an overall length of 280 ft. The bridge is at a skew angle of 17.5°. The spans are supported by Modified BT-54 Girders. The deck is continuous over the entire length, making Bent 2 the closed joint.

Figure 3-4: Elevation view of the Co Rd 10 bridge over I-85 (LEE-3)

The bridge (called MOB-1) on Co Rd 39 over I-10 was inspected on December 6, 2023, as seen in Figure 3-5, by an ALDOT Bridge Inspector, providing photos and inspection notes. The location is near the Gulf Coast and is therefore exposed to chlorides from the saltwater. Construction on MOB-1 was finished in 2005, making it about 20-years old. MOB-1 has four spans with center spans of 100 ft and adjacent spans of 120 ft, making an overall length of 440 ft. The bridge is at a skew angle of 1.6°. The spans are supported by BT-63 Girders. The deck is continuous for the two middle spans (for a continuous length of 200 ft), with Bent 3 being a closed joint.

Figure 3-5: Elevation view of the Co Rd 39 bridge over I-10 (MOB-1)

The bridge inspected (called CLB-1) next was I-20 over Co Rd 49 on December 12, 2023, as seen in Figure 3-6, specifically the portion constructed to widen the bridge. Construction on CLB-1 was finished as part of the widening project in 2012. CLB-1 has three spans with a center span of 100 ft and adjacent spans of 81 ft 5 in., with an overall length of 262 ft 10 in. The bridge is at a skew angle of 14.6°. The spans are supported by BT-54 Girders. The deck is continuous for the two middle spans (for a continuous length of 200 ft), with Bent 3 being a closed joint.

Figure 3-6: Elevation view of the I-20 bridge over Co Rd 49 (CLB-1)

The final bridge (called SUM-1) that was inspected was US-11 over Sucarnoochee River on April 16, 2024, as seen in Figure 3-7. The construction of the bridge finished in 2003, making it 21-years old, which makes it the bridge that had been in service the longest out of the bridges inspected. SUM-1 also has the longest overall span length and number of spans, with 11 spans totaling 855 ft. The 1st and last spans are 45 ft (supported by AASHTO Type I Girders), the 3rd span is 125 ft (supported by BT-72 Girders), and the rest are 80 ft spans with AASHTO Type III Girders. SUM-1 has no skew. The bridge has two continuous deck sections, Spans 4-6 (240 ft total) and Spans 7-10 (320 ft total). The inspection for this bridge was limited to Bents 7, 8, and 9 since these were the joints being monitored for the field monitoring portion. Refer to Chapter 4: Field Monitoring for a more in-depth description of this bridge and its joints.

Figure 3-7: Elevation view of the US-11 bridge over Sucarnoochee River (SUM-1)

Table 3-1: Summary of details for inspected bridges

BIN	Identifier	Name	Overall Length	Number of Spans	Prestressed Concrete Girder Type
021511	LEE-1	I-85 over Co Rd 54 (Long St)	180’-0”	3	AASHTO Type II
021513	LEE-2	I-85 over SR-51 (Marvyn Pkwy)	190’-0”	3	AASHTO Type I
020356	LEE-3	Co Rd 10 (Beehive Rd) over I-85	280’-0”	2	BT-54
020425 & 020423	CLB-1	I-20 over Co Rd 49	262’-10”	3	BT-54 Bulb Tee
018396 & 018397	MOB-1	Co Rd 39 over I-10	440’-0”	4	BT-63 Bulb Tee
017888	SUM-1	US-11 over Sucarnoochee River	855’-0”	11	AASHTO Type III (Inspected Spans)

3.3. Observations

The main damage to the surface observed consistently over all the closed joints on the inspected bridges was spalling around this joint. An example of the typical spalling observed is shown in Figure 3-8. More photos of the spalling across the inspected bridges can be found in Appendix A: Field Inspection Reports in the figures following the bridge summaries. This spalling, however, was not observed to indicate any more severe signs of distress related to the closed joint.

Figure 3-8: Typical spalling observed at closed joint

One difference that was noticed for LEE-2 as compared to the other bridges inspected was the detail used for the construction joint. The current detail uses a curved edge along with joint sealant, as shown in Figure 1-3. However, no joint sealant or curved edge was observed for the closed joint at LEE-2. Cracks were observed running along the joint with spalling in the deck that had only been in service for just under a year (placed in Construction Phase I).

Figure 3-9: Spalling and cracking observed at the freshly constructed closed joint (LEE-2)

Another common sign of distress noticed during the inspections was observed at the full-depth edge beams under the joints, shown in Figure 3-10 and Figure 3-11, at LEE-3 and MOB-1 respectively. Large cracks were observed at the base of these full-depth edge beams while no cracking was observed at edge beams that were not full-depth. For MOB-1, this cracking extended to a large concrete breakout that was observed. While this was not seen to affect the structural performance of the joint or the rest of the superstructure, this could be unsightly to the public and could lead to a source of further deterioration into its service life.

Figure 3-10: Full-depth edge beam with cracking observed (I-20 over Co Rd 49)

Figure 3-11: Full-depth edge beam with significant concrete breakout (Co Rd 39 over I-10)

3.4. Conclusions

The major factor that was observed in the field inspections that most affected the visual performance of the deck was the type of construction joint used at the closed joints. The closed joints that were tooled (rounded edges with joint sealer) had fewer signs of damage when compared to saw-cut closed joints. Along with having the proper detailing for having a durable closed joint, another source of error comes in the construction process, specifically if they are improperly implemented (such as being saw-cut when the detail calls for a tooled construction joint).

Relating to the proper design of the surface at the closed joint, out of the bridges inspected, the damage observed at closed joints was mainly related to traffic wear rather than structural performance. Spalling was observed on most of the closed joints, with some major enough to cause concern. The issue of the spalling of the concrete along the closed joint is related to traffic wear over the joint and the quality of the construction joint. A tooled joint that has been rounded seems to result in improved performance.

With the bridges inspected, the edge beams seem to be a constructability challenge when being used as part of the closed-joint detail. However, the presence of the edge beam does not seem to affect the structural performance at the closed joint. Full-depth edge beams were observed to crack more. Again, these problems are limited to the edge beam itself and were not seen to affect the closed joint in the deck.

For further studies conducted in this field, inspections should be performed near the Gulf Coast to capture more effects on saltwater corrosion for Alabama bridges. Also, performing inspections in northern Alabama could provide more information on how the closed joint performs under cold weather effects and in exposure to deicing salts (more chloride exposure effects). The ways that this study could inspect bridges were limited to bridges with relatively easy access to the underside of the bridge. Further studies that can inspect bridges that span waterways or have larger heights could lend to a more diverse group of bridges.

Chapter 4: Field Monitoring

4.1. Introduction

4.1.1. Scope

To better understand the movements that the closed joint is subjected to in the field, field monitoring was performed in this study to determine the behavior of this structural detail in service. The main goal of the field monitoring was to be able to quantify the actual demands on a bridge and its joints due to thermal demands. The movements in the superstructure that apply the most demand to the closed joint are the rotations of the beam ends, which apply axial force and bending moment to the link slab. The field monitoring was able to quantify the changes in the behavior of the closed joint that result from hot weather conditions (summer) and compare them against cold weather conditions (winter).

Along with monitoring responses from the ambient temperature that the bridge is subjected to, the difference of this measured temperature across the superstructure was also focused on. This temperature difference was expected to be the most important aspect to focus on since this creates a temperature gradient across the bridge cross section that is the main cause of girder rotation. This temperature gradient changes curvature along the span due to the differential expansion or contraction of the concrete. Since monitoring was performed over a whole year, the large temperature differences that the bridge typically experienced were recorded, with the largest differences occurring when temperature shifts in the weather were more prominent (i.e., in the fall and spring).

The scope of the field monitoring was limited to observation over a whole year to capture the effects and differences that accompanied the changes in weather over one year. For the behaviors of the in-service closed-joint detail, the study was limited to monitoring only in-service bridges. This meant that the monitoring was not able to begin during the construction of the bridge, so there was no instrumentation installed before concrete was placed, such as strain gauges in the deck concrete or on the reinforcing steel.

The behavior of the bridge that was monitored included both open- and closed-joint movements. By having the information on how both open and closed joints behaved over a year, a direct comparison of movements between the types of joints was able to be performed rather than having to make assumptions on how the open joint behaved. The open joints were expected to experience more movement due to the nature of the constructed expansion joint in the deck, which was designed to allow the deck to expand and contract longitudinally without any constraint. This observation was limited to only the joints and girder ends of the bridge, so no instrumentation was present within the span such as the vertical displacement of the girders at midspan. The types of superstructure movements and their sources that were recorded were limited to only non-destructive installation of instruments which prevented the embedment of sensors through drilling into the superstructure concrete.

The field observation was limited to measuring demands only from deformations due to thermal demands and did not directly observe deformations that result from applied live load. A system could have been installed that recorded dynamic responses at the girder ends with higher data collection rates and more precise sensors. However, the larger uncertainty in this study was the demands that temperature changes impose on the closed joint. The importance of measuring these thermal effects is supported by observations from French et al. (2012) and Birley et al. (2025) as discussed in Chapter 2: Literature Review. Also, without strain gauges or load sensors in the deck, there would not be a way to directly or verifiably record the size or weight of the vehicle that induced the dynamic responses from live load. Experiments have been run by taking a vehicle of known size and weight to induce movement at a known time (Kowalsky and Wing, 2003), but this option is outside the scope of this study. Instead, the demands that come from live loads were calculated and superimposed to these measured demands in Chapter 5: Closed-Joint Demands.

4.1.2. Bridge Selection

Several criteria were considered to select a bridge for monitoring that would be best suited for collecting the necessary data. The scope of the project limits the location of the bridge to be within the state of Alabama, so the ALDOT detail for closed joints can be observed. Travel distance to the bridge did not impose too much of a constraint on considerations since most points within Alabama could have been reached within 4 hours or less from Auburn, AL. The span lengths that make up the bridge were one of the most important factors in terms of the bridge's geometry. The spans needed to be long enough to produce appreciable movements at the joints under observation to impose sufficient demand. The total amount of spans or length of the bridge should not have a large impact on this movement, only the portion of the bridge that is a continuous deck.

For installation purposes, the underside of the bridge needed to be easily accessible, which included not spanning a large waterway that would have no land underneath to set up ladders to climb up to the girder ends. Under the same logic, the underside of the bridge cannot be high up, which will prevent the use of conventional ladders. The area beneath the bridge could not have too much brush or clearing needed that would inhibit the transportation of instrumentation and power to the monitoring site. The location could also not be located too close to a highly populated area where the risk of tampering with the equipment could become an issue.

The service age of the bridge was also considered in the selection of bridges to be monitored. The bridge being well into its service life allowed rapid changes that would have occurred in its early service life to be settled by the time the monitoring was performed, allowing for a more constant overall behavior. This includes deformations due time-dependent deformations such as concrete creep and shrinkage, which occurs rapidly and levels out as time progresses.

4.2. Bridge Description

The bridge to perform the field monitoring was selected to be the US-11 Bridge over the Sucarnoochee River and Relief in Sumter County. Field inspections were performed on this bridge after its selection. The results from this inspection can be found in Chapter 3: Field Inspections. Figure 4-1 displays the selected bridge in elevation view, with the monitored bents labeled (discussed later in this section). This bridge was constructed as a replacement for an existing bridge.

Figure 4-1: Elevation view of US-11 over Sucarnoochee River

The bridge is made of 11 spans, totaling a length of 855 ft. All but three of the spans are 80 ft simple spans and are supported by AASHTO Type III prestressed concrete (PC) girders. The first and last spans are 45 ft simple spans and are supported by AASHTO Type I PC girders. The third span in the bridge crosses the Sucarnoochee River, making it the longest length at 125 ft and is supported by BT-72 PC girders. Appendix B: Prestressed Girder Details contains details for the dimensions of the girder types present within this bridge. The bridge contains two segments of continuous deck which utilize ALDOT's closed-joint detail. The first segment is a total of 240 ft long, comprised of spans 4, 5, and 6 (Bents 5 and 6 having closed joints) and the second segment is 320 ft long, comprised of spans 7, 8, 9, and 10 (Bents 8, 9, and 10 having closed joints). One of the goals of the field monitoring was to be able to collect data on the behavior of both closed and open joints to directly compare the demands that are present. For this, instrumentation was installed on Bents 7, 8, and 9. Further description of the bridge will be focused on the geometry of the spans adjacent to these bents.

The bridge was constructed with an 8” gap at 70°F between the girder ends, which makes the total length of each girder 79’-4”. The bearings for each girder are 2 ft apart at each bent, which results in an effective span length of 78 ft. The superstructure is supported by six girder lines spaced at 7 ft on center. All the monitored joints contain an edge beam that is approximately 33” in depth and 24” wide. The 7” deck is constructed with a 3” build-up (haunch) between the top of the girder and bottom of the deck to account for the camber of the girder. This build-up decreases closer to midspan, and the as-designed shape of this change can be seen in Figure 4-2.

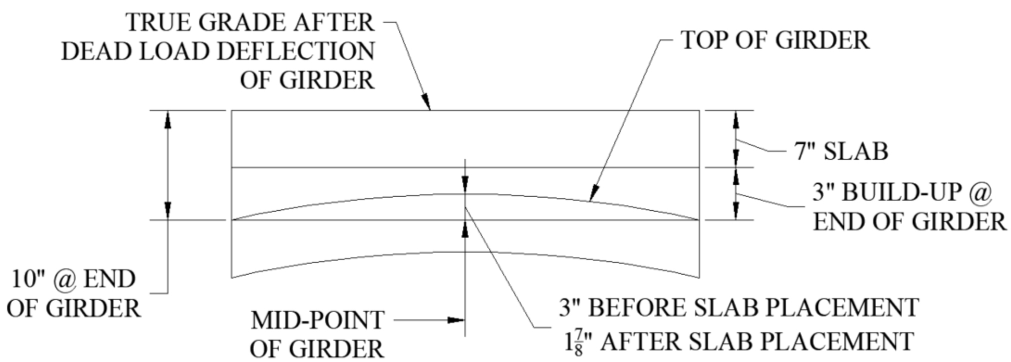

Figure 4-2: Diagram of deck build-up and girder camber

For the reinforcing steel within the deck, the transverse bars are #5s spaced at 6” on the top and bottom, with 2” cover on the top and 1” cover on the bottom. For the longitudinal steel, #4s are spaced at approximately 17” on top which are present in the entire span. Within 12 ft on each side of the closed joints (Bents 8 and 9), additional #6s are evenly spaced between the #4 bars on top. A more comprehensive description of the geometry and layout of the superstructure can be found in Figure 4-3 along with details on the reinforcement located in the bottom of the deck.

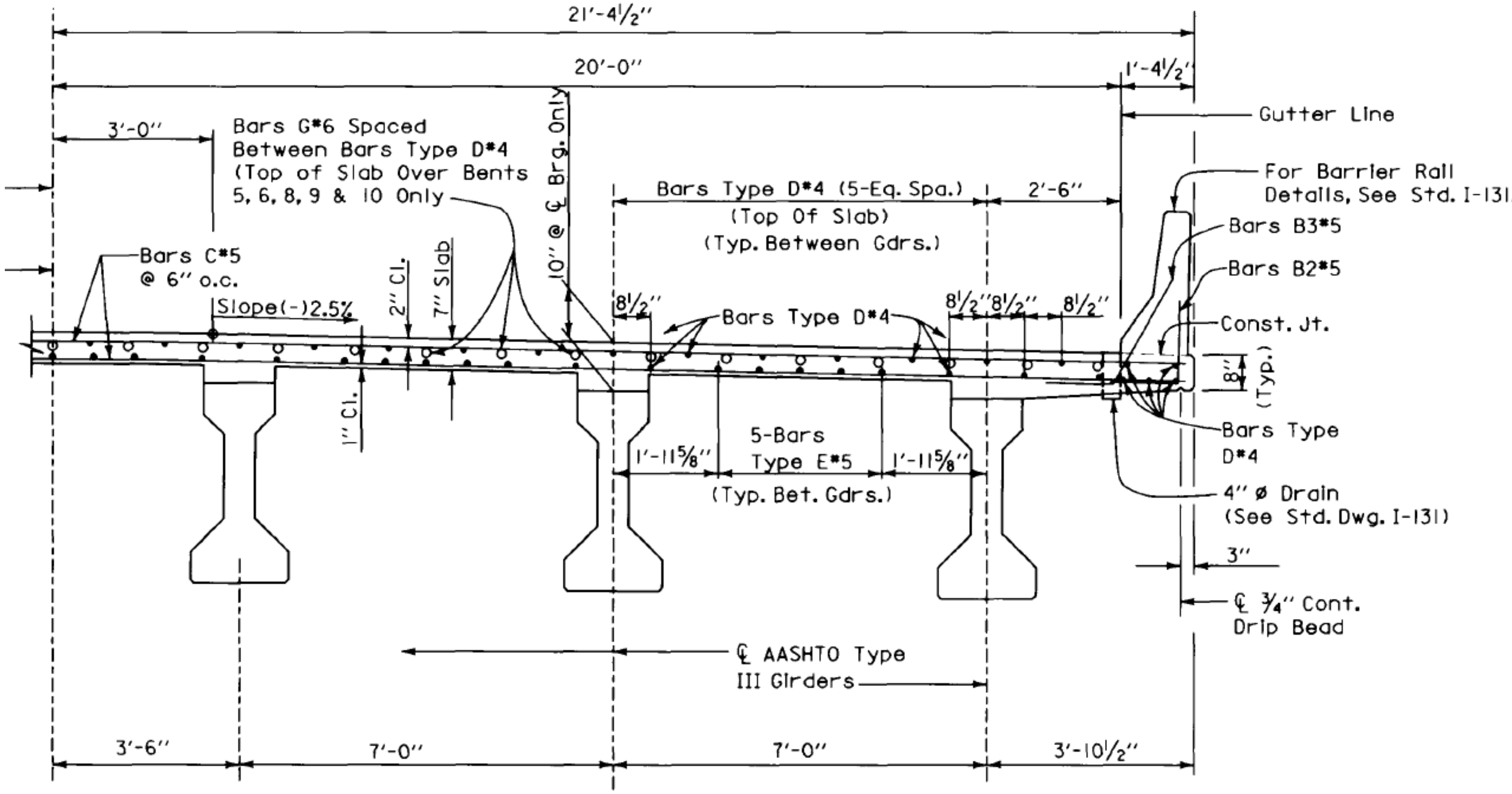

Figure 4-3: Typical superstructure half cross section for spans adjacent to monitored bents

Bent 7 was the chosen bent to monitor to collect data on the behavior of an open joint. The girders at this bent rest on expansion bearings, which are detailed as Type 2 elastomeric bearings. These bearings are 1 ⅝” x 10” x 1’-8 ½” with 3-12 galvanized steel plates embedded within them. There is no connection angle present for these bearings. The expansion joint in the deck was detailed to have a 1.5” width at a temperature of 70°F. The gap between the girder ends was detailed to be 8”, and measurements taken during field visits measured the gap at 8.75” (10 am on April 16th, 2024). The temperature measured with the thermocouples (located at Bent 8) was 74.0°F on the surface of the middle of the girder (the total temperature difference across girder height was 2.9°F). This middle temperature was assumed to be the uniform temperature applied to the superstructure (based on the AASHTO temperature gradient). Figure 4-4 displays the girder ends and the expansion bearings.

Figure 4-4: Bent 7 girder ends and expansion bearings

Bent 8 was chosen to monitor the behavior of the closed-joint detail in service. The girders at this bent rest on expansion bearings (like Bent 7), which are detailed as Type 2 elastomeric bearings. These bearings are 1” x 10” x 1’-8 ½” with 2-12 galvanized steel plates embedded within them. There is no connection angle present for these bearings. The gap between the girder ends was detailed to be 8”, and measurements taken during field visits measured the gap at 8.75” (11 am on April 16th, 2024). The temperature measured with the thermocouples (located at Bent 8) was 75.5°F on the surface of the middle of the girder (the total temperature difference across girder height was 1.9°F). Figure 4-5 displays the girder ends and the expansion bearings.

Figure 4-5: Bent 8 girder ends and expansion bearings

Bent 9 was selected as a second closed joint to monitor, to supplement data collected from Bent 8. The girders at this bent are attached to fixed bearings, which are detailed as Type 2 elastomeric bearings. Like Bent 8, these bearings are 1” x 10” x 1’-8 ½” with 2-12 galvanized steel plates embedded within them. Unlike Bent 8 however, there is a connection angle present. This angle is an L6” x 6” x ½” that is 12” in length and are attached to the bent with anchor bolts. Figure 4-6 and Figure 4-7 display the details for the angle and the location of its holes as well as the anchoring dimensions for the fixed bearing. The gap between the girder ends was detailed to be 8”, and measurements taken during field visits measured the gap at 8.50” (8:30 am on April 16th, 2024). The temperature measured with the thermocouples (located at Bent 8) was 73.3°F on the surface of the middle of the girder (the total temperature difference across girder height was 4.3°F). Figure 4-8 displays the girder ends and the fixed bearings.

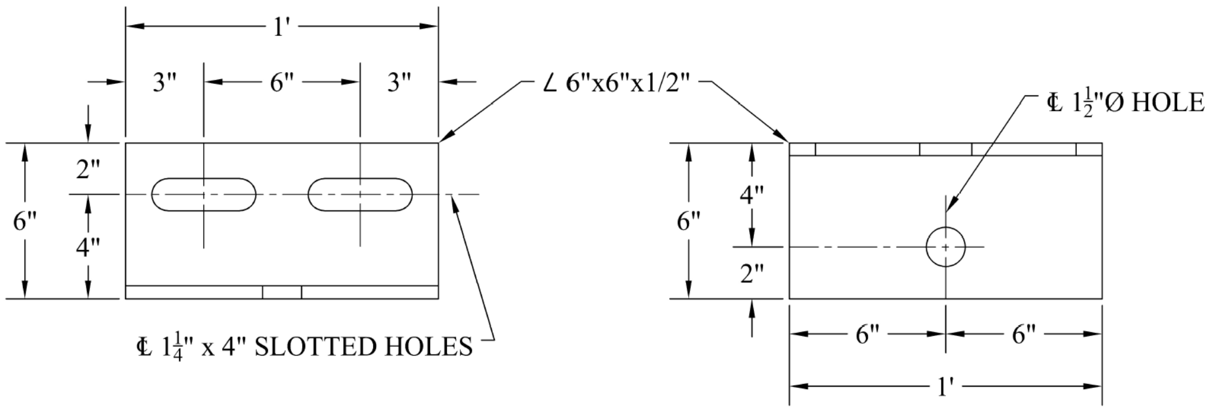

Figure 4-6: AASHTO type girder clip angle for fixed bearing (Bent 9)

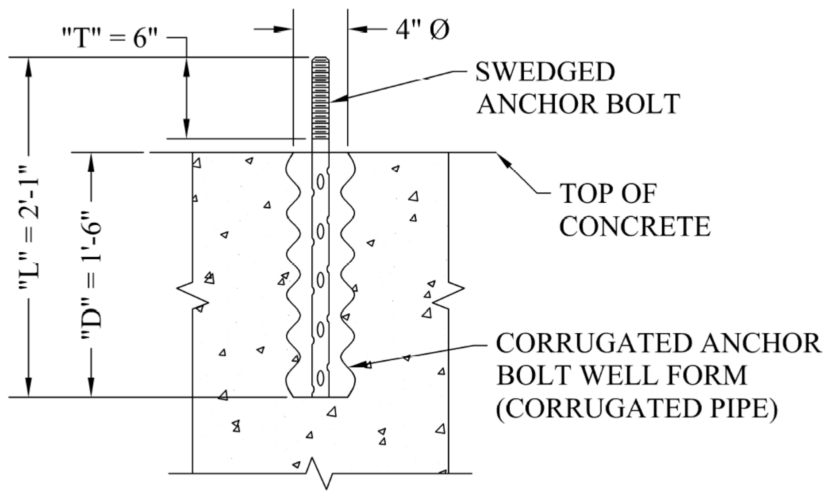

Figure 4-7: Anchor bolt and well detail for fixed bearing (Bent 9)

Figure 4-8: Bent 9 girder ends and fixed bearings

4.3. Monitoring Setup

The main movements that occur at the closed joints below the deck surface are the rotation and displacement of the girder ends. Birley et al. (2025) monitored these movements through the installation of two displacement sensors, calculating the angle of rotation from the difference in displacements. The presence of the edge beam at the bents removes the ability to install a sensor that connects the girder ends in the webs, so inclinometers were chosen instead to measure the girder-end rotation directly. To capture the displacement of the girder due to uniform temperature changes, crackmeters were installed on the bottom flanges of the girders out of the way of the edge beam. The third type of instrumentation chosen was thermocouples to measure the temperature across the cross section to allow for the calculation of the demand imposed by differential temperatures. Because the installation of the instruments was required to be as nondestructive as possible, these thermocouples were surface mounted onto the girders.

These instruments were installed on girder lines 4 and 5, which were on the interior of the bridge. This lowered the influence of uneven loading that would typically be experienced on girder lines on the edge of bridges (girder lines 1 and 6 for this bridge). Figure 4-9 displays the layout of the instrumentation across the three bents monitored.

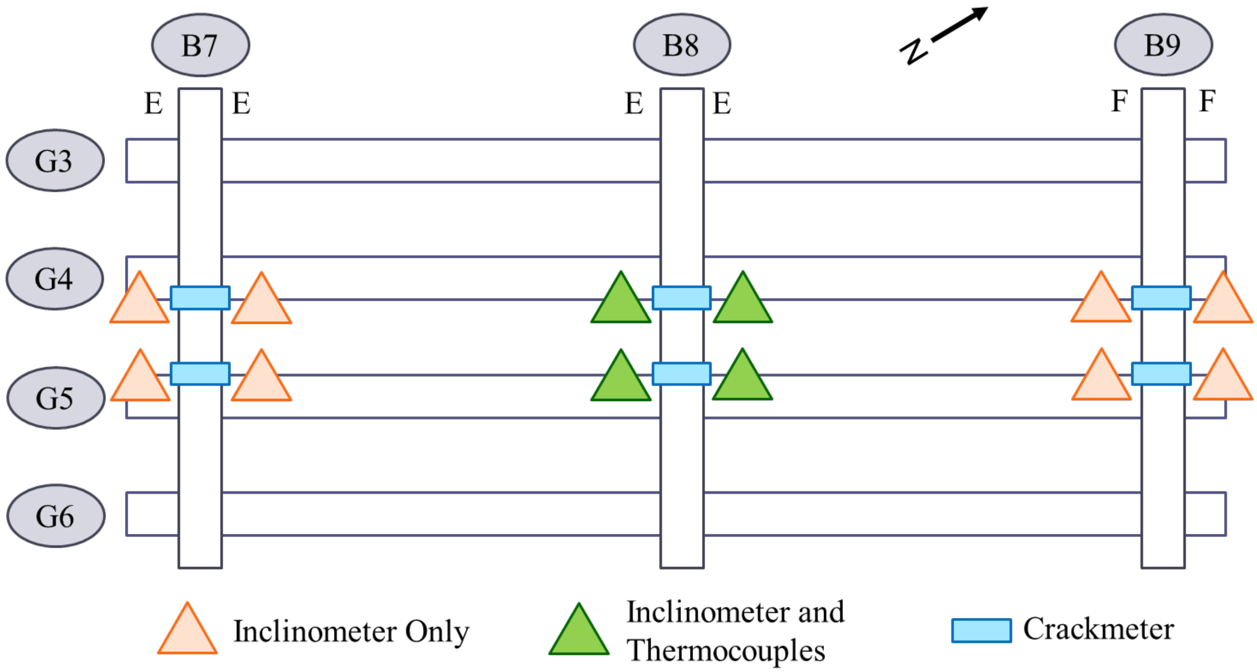

Figure 4-9: Field monitoring instrumentation plan

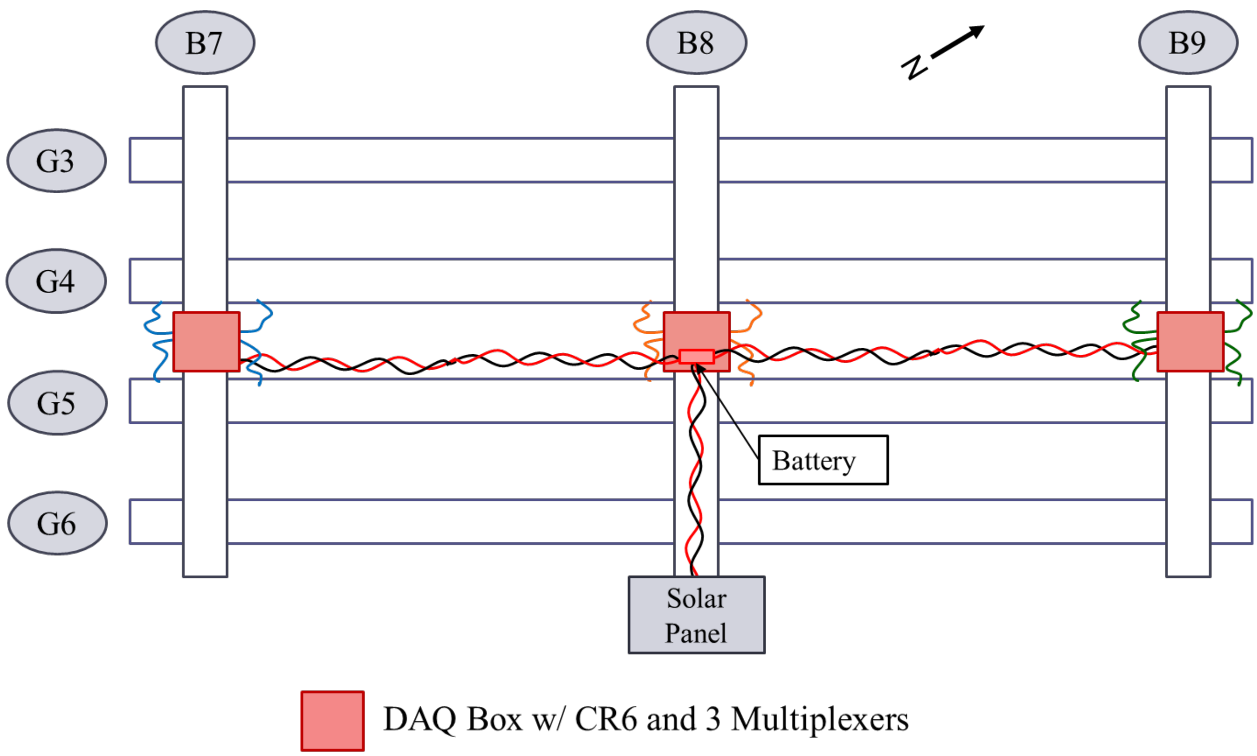

Figure 4-10: Field monitoring data acquisition system (DAQ) plan

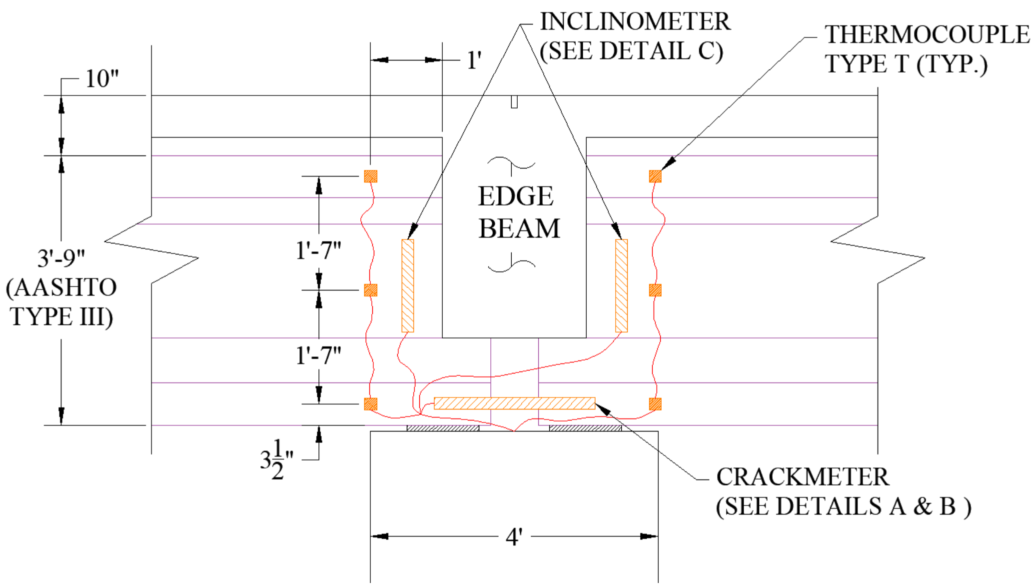

(a) Overall view, typical thermocouple locations

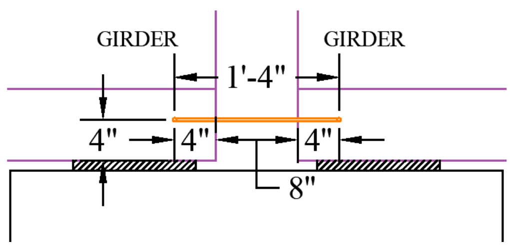

(b) Detail A, Typical 50 mm (2”) crackmeter location

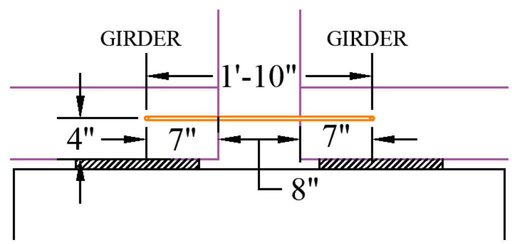

(c) Detail B, Typical 100 mm (4”) crackmeter location

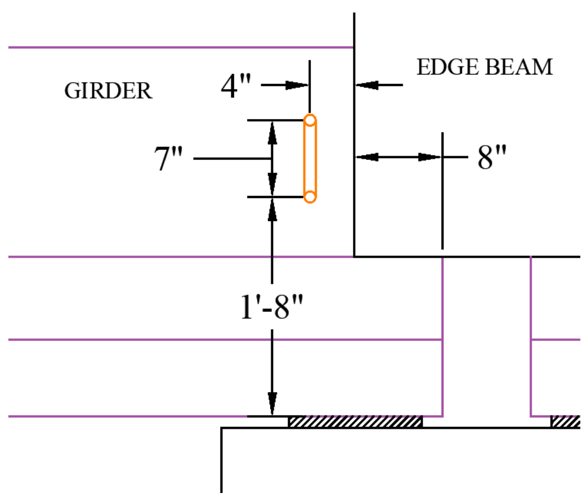

(d) Detail C, Typical inclinometer location

Figure 4-11: Sensor placement on girder ends

The thermocouples used were Type T, which are repeatable under a temperature range from -454°F to 700°F. The metals used to measure the temperature for Type T are Copper (+) and Constantan (55% Copper and 45% Nickel) (-). The accuracy of the sensor is the greater of ± 1.0°C and ± 0.75% (TEMPSENS, 2020). To capture the temperature gradients that develop across the girder over a year, three thermocouples were installed per location on the bridge on the top, middle, and bottom of the girder. Because the bridge is in service and traffic would put the sensors at risk of damage, no temperature data was able to be recorded in or on the deck. These locations on the girder can be seen in Figure 4-12.

The tape that was being used to attach the thermocouples to the concrete surface did not adhere as well as expected. Because of this, the decision was made to only install the thermocouples on Bent 8 since it was the main closed-joint detail that was being monitored. Bent 9 was the secondary closed joint to verify the data collected at Bent 8. Bent 7 was the open-joint detail to directly compare data from Bent 8. The temperatures recorded were assumed to be consistent 80 ft each way from Bent 8, so the thermocouple data was used for all three bents and their temperature differences.

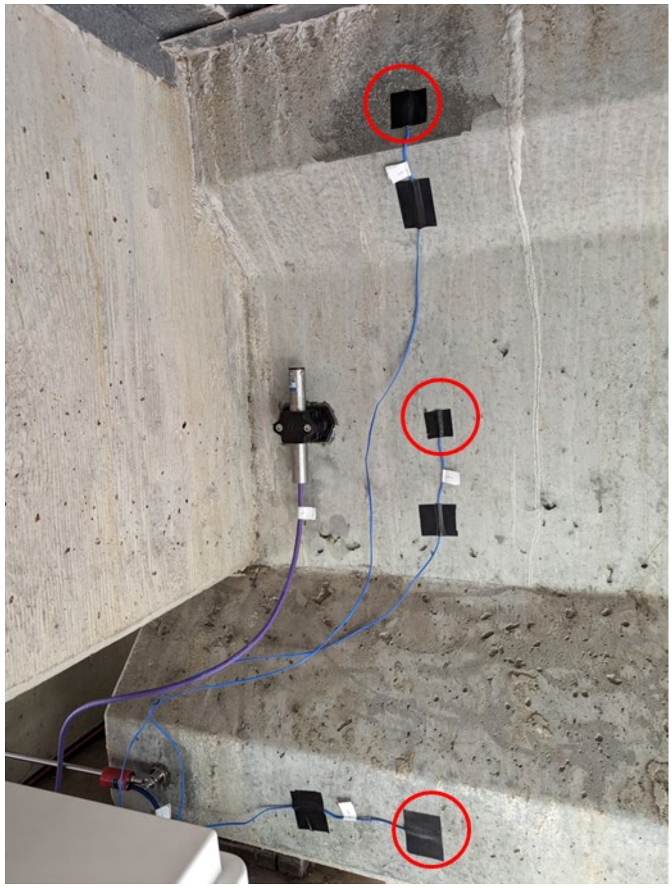

Figure 4-12: Thermocouple installation positions

The inclinometers used were Geokon Model 6190 Tilt Sensors that had a calibrated rotation range of ± 30°. The resolution of the sensors was ± 0.00025° (4.36 x 10^{-6} rad) and a precision of ± 0.0075° (1.31 x 10^{-4} rad). To capture the rotation at the end of the girder, they were positioned as close as possible to the bearing where the point of rotation was assumed to happen. The presence of the edge beam and size of the mounting equipment hindered the efforts to place the inclinometer directly in line with the bearings, but they were able to be positioned within 1 ft of the girder end which was presumed to have minimal effect on the change in rotation observed. The typical setup of the inclinometers can be seen in Figure 4-13.

Due to the mounts and the inclinometers not having a notch or clear way of identifying exactly 90 degrees for the sensor readings, the inclinometers were not able to read exactly perpendicular to the girders they were installed on. It was assumed that no out-of-plane rotation would occur since the inclinometers were installed on interior girders, so no out-of-plane forces or heat distribution would be present. Because of this assumption, any rotation measured was assumed to be in-plane, and the total magnitude was the change in rotation since the inclinometer records two sets of rotations in axes oriented 90° to one another.

Figure 4-13: Inclinometer installation position (Bent 7 displayed)

The crackmeters used to measure displacement were Geokon Model 4420 Vibrating Wire Crackmeters. Because the open joint (Bent 7) was expected to experience larger displacements, two ranges of crackmeters were used. The crackmeters at Bent 7 had a 4” total range, while the crackmeters at Bent 8 and 9 (closed joints) had a total range of 2”. The crackmeters had a resolution of 0.025% Full Scale Range (FSR) (0.001” for 4” crackmeters and 0.0005” for 2” crackmeters). These sensors were installed in the center of the bottom flange of the girder to capture the longitudinal displacements of the girder ends.

The low placement of the sensors is due to the presence of the edge beam, so the crackmeters were predicted to measure movement from both the longitudinal expansion of the girders and displacement due to the rotation due to temperature gradients. The crackmeters on Bent 9 had to be placed higher on the flange due to the location of the angles to create the fixed bearing, but not much difference was predicted to result from the slight increase in height. The installation of the crackmeters on Bent 9 is shown in Figure 4-14, which is typical for all bents besides the height of the crackmeter.

Figure 4-14: Crackmeter installation position (Bent 9 displayed)

Figure 4-15 shows a simplified diagram that displays the girder-end movements being measured. The edge beam is not shown for simplicity. θ_g is the change in rotation of the girder end, measured by the inclinometers and zeroed at a date with little to no thermal influence. Positive rotations are rotations that cause the top of the girder surface to "open up" and widen the gap between the top of the girders, inducing tension in the deck. Negative rotations, then, are when the top of the girder surfaces rotate toward each other, inducing compression in the deck. ΔL is the displacement measured at the girder ends, where a widening gap would result in positive values and a closing gap would result in negative values.

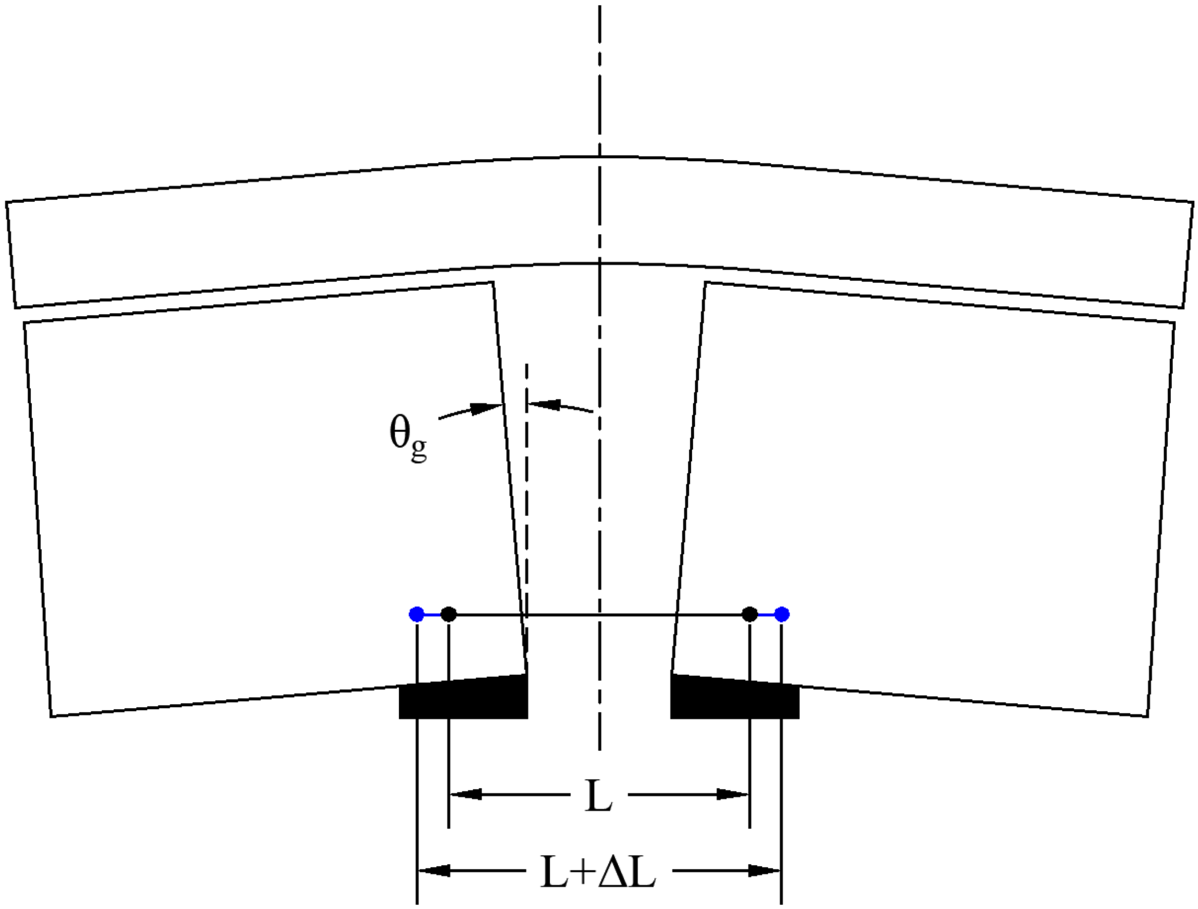

Figure 4-15: Diagram for measured data

The Data Acquisition System (DAQ) was comprised of three Campbell Scientific AM16/32B Relay Multiplexers and one Campbell Scientific CR6 Measurement and Control Datalogger for each bent. Multiple multiplexers were used for each bent due to the difference in communication methods with each type of instrumentation. The crackmeters were measured with differential voltages, so the multiplexer the crackmeters were wired into needed to be on 4x16 mode. The inclinometers were MEMS sensors which meant that these sensors transmitted signal codes, so they needed to be read by the COMM ports on the CR6 with the multiplexer on 2x32 mode. The Type T Thermocouples needed to use the same material wire to connect into the CR6 with the multiplexer on 2x32 mode. Using a CR6 for each bent allowed for the number of wires spanning the 80 ft gap to be reduced. This reduced the possibility of noise due to long wire lengths.

To have a steady supply of power to the DAQ, a solar panel was installed on the east side of Bent 8 for an optimal amount of sunlight. This location was chosen based on visual inspections during prior field visits. This solar panel fed power into a battery on Bent 8, which then distributed power to the rest of the DAQ across the spans. Grounding wires were run across spans, culminating at Bent 8, and then connected to a copper rod planted into the ground to provide sufficient grounding for the DAQ.

A remote connection was able to be established using a cellular modem connected to the DAQ network, which allowed for data to be collected whenever an internet connection was available. The data ended up being collected every two weeks, so the amount of data downloaded was not too much. The collection times were not spread too far apart so regular "check-ups" could be performed, making sure no sensors stopped working. The code used to collect and record the data can be found in Appendix C: CRBasic Codes. The remote connection for the DAQ was only able to be connected to Bents 7 and 8 due to the limited amount of communication ports on the CR6. The data from Bent 9 was then only collected approximately every four months, which is when the field visits occurred, and when the final takedown happened (three collection dates).

4.4. Theoretical Basis

As the field monitoring observed demands from typical service loading, a theoretical basis had to be established to relate the behavior of the closed joint in the field to the demands that the joints were designed for. The main movement that needed to be quantified was the rotation at the girder ends, specifically the total rotation across the joint, θ_T, as the closed joint is subjected to the rotation from both girder ends. The two temperature gradients considered for determining the movements from thermal loading were from the 10th edition of AASHTO LRFD Bridge Design Manual (2024) and the New Zealand design gradient from Priestley (1978).

AASHTO (2024) divides the US into solar radiation zones (Figure 4-16), each of which is assigned design differential temperatures (Table 4-1) at points across the superstructure cross section. As Alabama lies within Zone 3, T_1 was taken as 41°F and T_2 as 11°F. According to AASHTO (2024), T_3 should be taken as 0°F unless a site-specific study was conducted to show otherwise. As the superstructure was concrete and exceeded 16" in depth, A was taken as 12". The temperature gradient that these values were applied to can be seen in Figure 4-17. The coefficient of thermal expansion of the concrete was taken as 6.0×10^{-6} in/in/°F (AASHTO 2024 5.4.2.2). The modulus of elasticity of the concrete was calculated with AASHTO 2024 Eq. 5.4.2.4-1 (See Section 5.2. General Assumptions and Properties or E.1. Geometries and Material Properties).

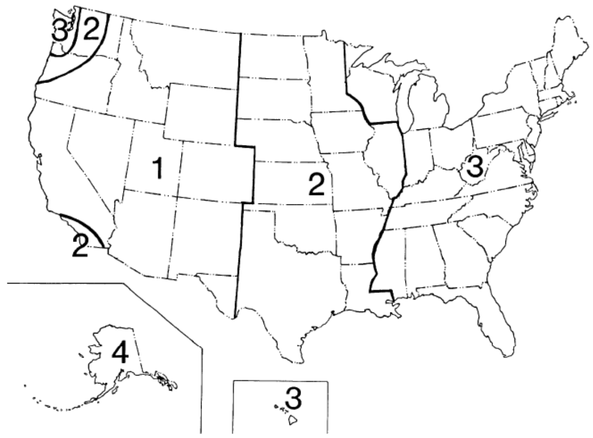

Figure 4-16: Solar radiation zones for the United States (AASHTO, 2024)

Table 4-1: Temperature gradient design values (AASHTO, 2024)

Zone	T_1 (°F)	T_2 (°F)
1	54	14
2	46	12
3	41	11
4	38	9

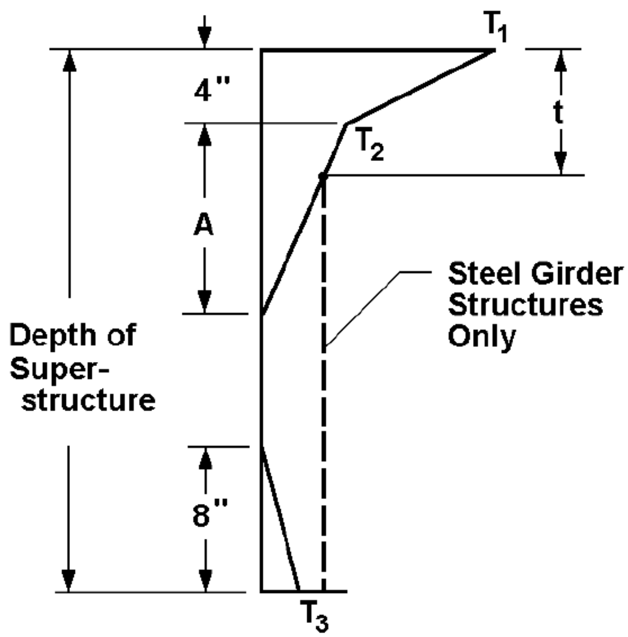

Figure 4-17: AASHTO (2024) temperature gradient in concrete and steel structures

Equation 4-1 was used to calculate the curvature from the temperature gradient that was developed (AASHTO 2024 Eq. C4.6.6-3), with the temperature being assumed to be constant over the width of the cross section. Equation 4-2 assumes the curvature is constant over the entire span to calculate the rotation at one girder end. For the case being analyzed, adjacent spans are the same so θ_T can be found by summing θ_g from both sides. This process is used for all temperature gradients developed, including the AASHTO and New Zealand Design Gradient. The calculations for the cross-sectional properties and the rotation due to these design values can be found in Appendix E: Closed-Joint Demand Calculations.

$$\phi = \frac{\alpha}{I} \int \int (T_G * z)\, dw\ dz \qquad \text{Equation 4-1}$$

$$\theta_g = \phi * \frac{L}{2} \qquad \text{Equation 4-2}$$

The total end rotation across the joint due to the design temperature gradient specified by AASHTO (2024), $\theta_{T,AASHTO}$, was calculated to be -2.78 x 10^{-3} rad. for the positive temperature gradient. The negative rotation is due to the previously mentioned sign convention, where the positive temperature difference induces negative curvature along the length of the girders. To determine the design rotation for a negative temperature difference, the positive design temperature is to be multiplied by -0.30 for plain concrete decks, as stated by AASHTO (2024). This results in 0.83 x 10^{-3} rad. for the negative temperature gradient.

The New Zealand temperature gradient (Priestley, 1978) is shown in Figure 4-18. As there is no blacktop present on the deck, the difference in temperature at the top of the gradient (equivalent to T_1 for AASHTO (2024)) was taken as 32°C (57.6°F) since h = 0 mm. Relative temperature units are used instead of absolute temperatures since the points on the temperature gradient have the uniform temperature subtracted out. For the differential temperature equivalent to T_3, 1.5°C (2.7°F) was used, which falls within the limits of taking a maximum of 5°F set by AASHTO (2024). The calculations for the rotations due to values specified in the New Zealand design temperature gradient can be found in Appendix E: Closed-Joint Demand Calculations.

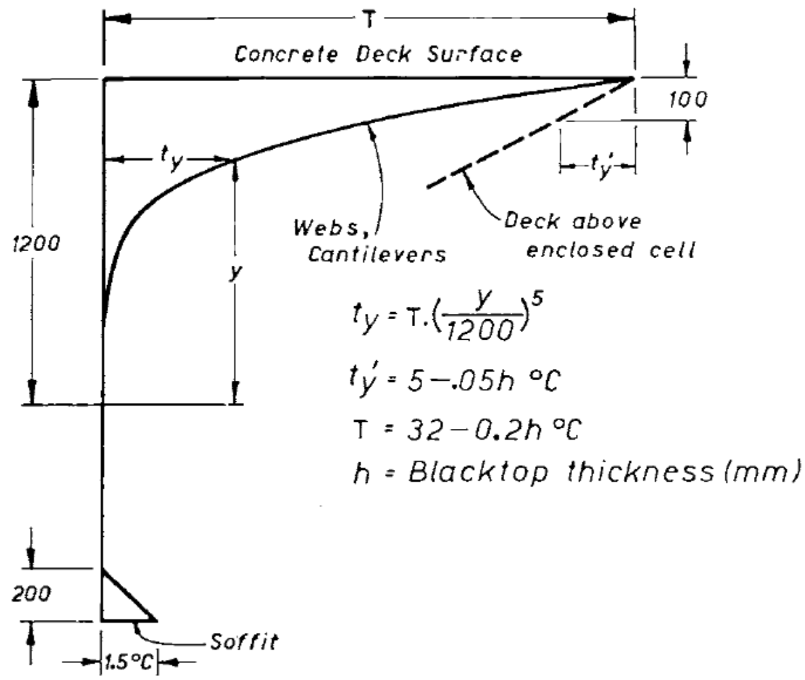

Figure 4-18: New Zealand design thermal gradient from Priestley (1978)

The total end rotation across the joint due to the design temperature gradient specified by AASHTO (2024), $\theta_{T,NZ}$, was calculated to be -5.68 x 10^{-3} rad. for the positive temperature gradient. The negative rotation is due to the previously mentioned sign convention, where the positive temperature difference induces negative curvature along the length of the girders. To determine the design rotation for a negative temperature difference, the positive design temperature is to be multiplied by -0.30 using guidance from AASHTO (2024) since there were no recommendations given by the New Zealand design gradient (Priestley, 1978). This results in 1.70 x 10^{-3} rad. for the negative temperature gradient.

To capture the thermal demand on the cross section, the temperature gradient developed needed to be estimated using the measured temperature at the thermocouple locations. The location of these thermocouples can be seen on the left side of Figure 4-19. The AASHTO (2024) design gradient could not be practically used for the conversion of measured temperatures to a field temperature gradient. Because of the lengths of the curves specified for the AASHTO (2024) design gradient, the top curve would be zero only 3.5" below the location of the top thermocouple. Fitting the curve to the measured temperature, then, would mean that the slope would be more sensitive to small changes in temperature difference and would lead to over/under predictions in the gradient magnitude. Along with this, the top section of the curve lies completely within the 7" bridge deck. Without any temperature values recorded in or on deck, there was no accurate way to realistically fit the top curve to thermocouple data without greatly overestimating this value.

Instead, the New Zealand design gradient was used to create the field temperature gradients. The top curve is only one section (rather than two for the AASHTO (2024) gradient curve) so the gradient can be fit to one temperature point measured in the field. This was the more practical way of calculating the temperature difference at the top of the deck using temperature recorded beneath the deck surface, especially since the point lies about 34” from the zero point of the top curve for the New Zealand gradient. Figure 4-19 displays the key locations and curves of the New Zealand gradient and their distances from the measured temperature locations for curve fitting. The top of the gradient is a power five curve and was fit to the calculated temperature difference (Equation 4-3) using Equation 4-5. The bottom of the New Zealand gradient is similar to that of the AASHTO (2024) gradient, being a linear curve, and was fit to the bottom temperature difference (Equation 4-4) with Equation 4-6.

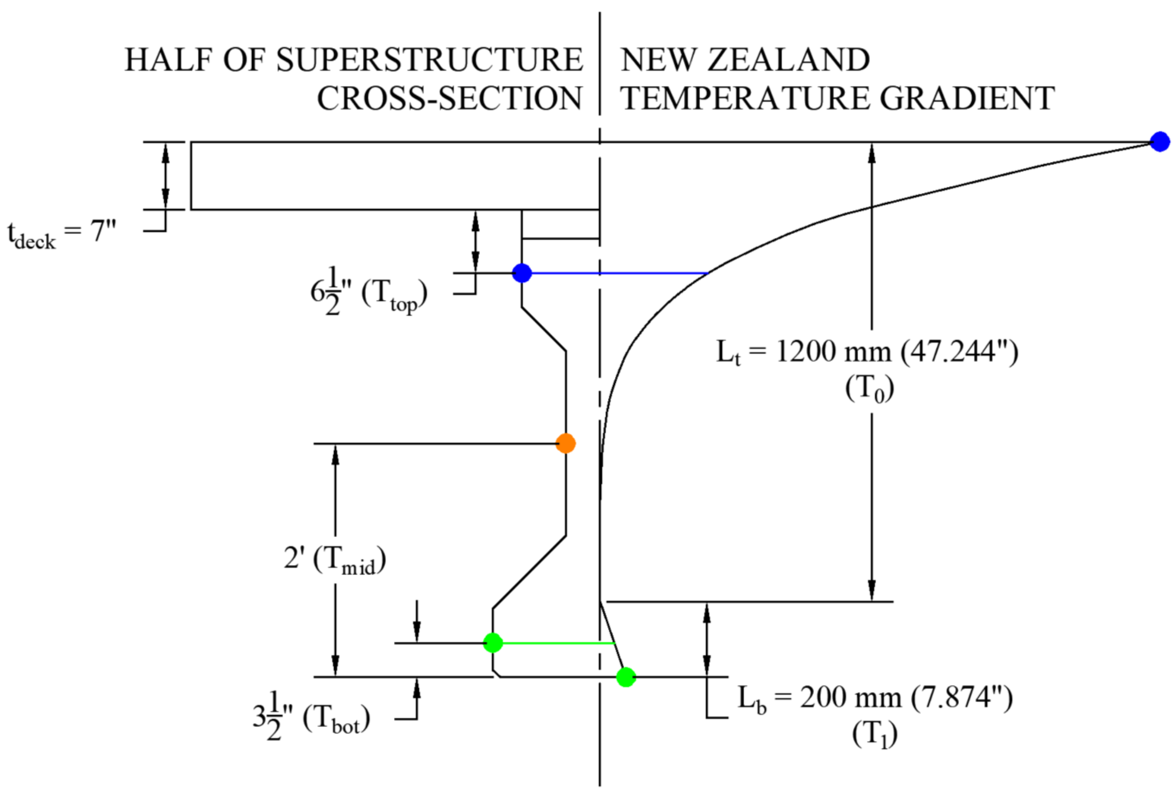

Figure 4-19: Locations of thermocouples and key points on temperature gradient

$$\Delta T_{top} = T_{top} - T_{mid} \qquad \text{Equation 4-3}$$

$$\Delta T_{bot} = T_{mid} - T_{bot} \qquad \text{Equation 4-4}$$

$$T_0 = \Delta T_{top} * \left(\frac{L_t - (H_c - L_t)}{L_t - (t_{deck} + 6.5")}\right)^5 \qquad \text{Equation 4-5}$$

$$T_1 = L_b * \left(\frac{-\Delta T_{bot}}{L_b - 3.5"}\right) \qquad \text{Equation 4-6}$$

4.5. Monitoring Results

The measured temperatures, displacements, and rotations were processed and are discussed within this section. This data provides values that represent the in-service demands that the closed joint is typically exposed to, at least for the three bents on the one bridge monitored over the one-year period. The recorded values are compared with calculated design values from AASHTO (2024) which can be applicable to future designs. For reference, Bent 7 is an open joint with expansion bearings, as detailed by ALDOT. Bent 8 and 9 are closed joints where Bent 8 has expansion bearings and Bent 9 has fixed bearings. A more detailed description of these bents and their differences can be found in Section 4.2. Bridge Description.

4.5.1. Zeroing Rotations and Displacements

Because the sensors were installed on the bridge after its construction and in-service, it was impossible to know the initial positions of the girder ends or the positions when exposed to no applied thermal loads. The "zero position" was instead estimated by taking the readings from the sensors on a day where there had been small differences in temperatures over a relatively long period. This could be a string of overcast days where the temperature remains constant, allowing the bridge to return to its undeformed shape (with respect to thermal loads). The best "zeroing time" from the year of data collected ended up being on April 11, 2024, at midnight. The one exception to using this zeroing time were the crackmeters on Bent 7 since they detached from the girders in January 2024 and were not reattached until April 25, 2024. The next best time to use for zeroing was when the crackmeters were still in service and experienced a period of low temperature differences was on December 25, 2023. The temperature differences over these months are shown in Figure 4-20 and Figure 4-21 with the periods of low temperature differences highlighted.

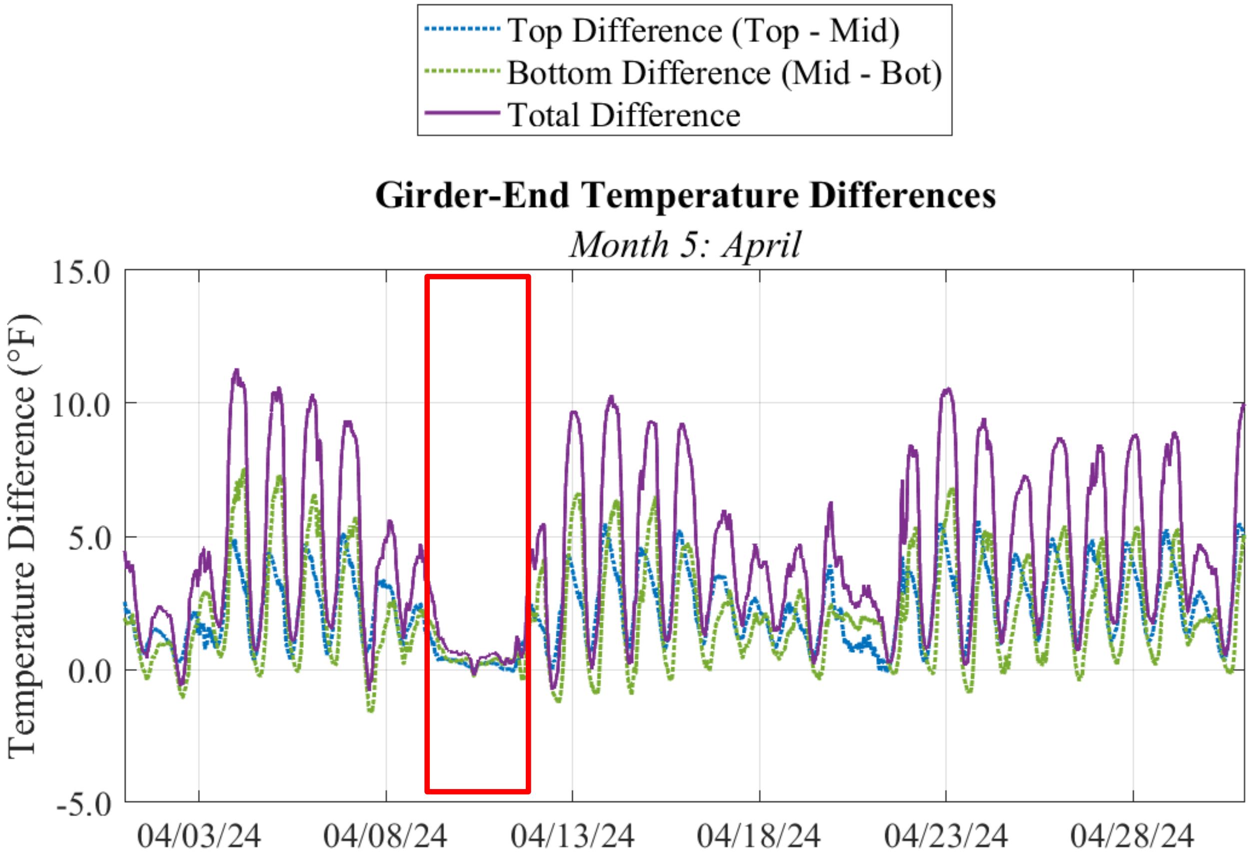

Figure 4-20: Girder-end temperature differences in April 2024 showing zeroing time

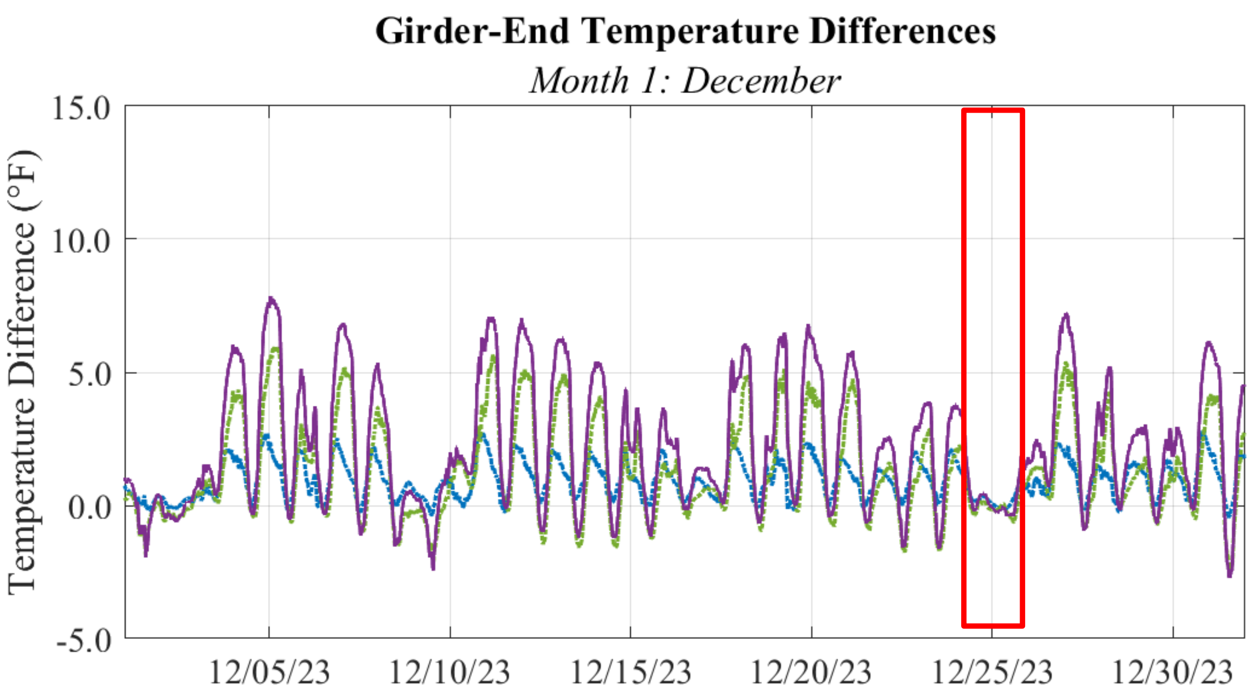

Figure 4-21: Girder-end temperature differences in December 2023 showing zeroing time

4.5.2. Challenges in Monitoring

Before the results are shown, the gaps in the data collection need to be addressed. This is because there were several errors that occurred with sensors going out of service during the field monitoring. As mentioned earlier, the crackmeters on Bent 7 began outputting a large amount of displacement consistently starting on January 24, 2024. During the field visit to collect data from Bent 9 on April 25, 2024, it was found that the mounts had detached from the girder ends. The mounts were able to be reattached during this visit, but this resulted in a loss of data for Bent 7 displacement over these three months. Like Bent 7, the crackmeters on Bent 8 began exhibiting erroneous values starting on July 3, 2024. These mounts were found to be detached from the girder ends during the second field visit for the collection of data from Bent 9. These mounts were also able to be reattached with only a little less than two months of data lost.

Opposed to sensors breaking during their operation, the thermocouple (all on Bent 8) on the bottom of the northwest girder (girder line 4) did not output values starting at installation. This could have been due to a faulty port on the multiplexer or improper wiring. Since there were three other thermocouples installed at the same position on the other girder ends, it was decided to leave this sensor out of the data processing. The thermocouple at the top of the southwest girder (girder line 4) had uncharacteristically high readings at inconsistent intervals, which may have been due to improper contact with the ports it was wired into on the multiplexer. With similar reasoning for the bottom northwest thermocouple, this sensor's data was taken out of the temperature averages to simplify data analysis as opposed to selectively using data from this sensor whenever it recorded reasonable values.

4.5.3. Data Plotting and Comparisons

For the graphs that display movements over time, the days are labeled on the x-axis at midnight (00:00). Unless stated otherwise, the orange, green, and blue lines are values at Bents 7, 8, and 9, respectively, and are plotted with the purple lines representing values from measured temperature and temperature differences. The entirety of the monitored movements and temperatures over the monitored year are displayed in Appendix D: Monthly Graphs within their respective section. The data is displayed by month to present details by day that would be lost in overall plots.

The girder-end rotations and displacements displayed cyclic behavior, with peaks reached in the early and late mornings of each day. For the girder-end rotations, the negative peaks occurred around 06:00, depending on the time of the year, heating up the top of the bridge. The positive rotation peaks occurred around 14:00, depending on the time of the year, which was when the temperature below the bridge began to be warmer than above as the sun started lowering. The sign convention used for these rotations that occur can be seen in Figure 1-6. This behavior was consistent across all three of the monitored bents.

Figure 4-22 displays the total measured rotations across the joint (θ_T), rotations calculated from measured temperatures, and temperature differences during the week when the largest negative rotation between the girder ends was recorded by the inclinometers. This occurred at Bent 7 with a value of -2.43 x 10^{-3} radians in the afternoon of April 22, 2024. The peak occurring in the spring was expected, as spring weather results in larger temperature gradients due to temperatures having larger fluctuations. One observation of note for the peaks during this time is that the positive peaks for each day are all below zero. This means that, compared to the rotation of the bridge at the zeroing time that was chosen (midnight of April 11, 2024), the bridge was in a state of constant negative rotation and did not cycle out of this state for a few days after this peak rotation. This peak value does approach the negative rotation value calculated by the AASHTO (2024) gradient and design temperatures (see Section 4.4) but remains smaller than this value. The shape of the rotations calculated from measured temperatures does exhibit a similar shape to that of the measured rotations but is slightly offset and with larger values than what was observed. Along with the largest negative rotations observed, Bent 7 had the largest difference in peak rotations (between negative and positive). This occurred on April 22nd as well, between the peak positive rotation late at night and the peak negative rotation in the afternoon. This value is effectively the largest amplitude observed for the daily cycles of girder-end rotation that Bent 7 is subjected to by thermal demands.

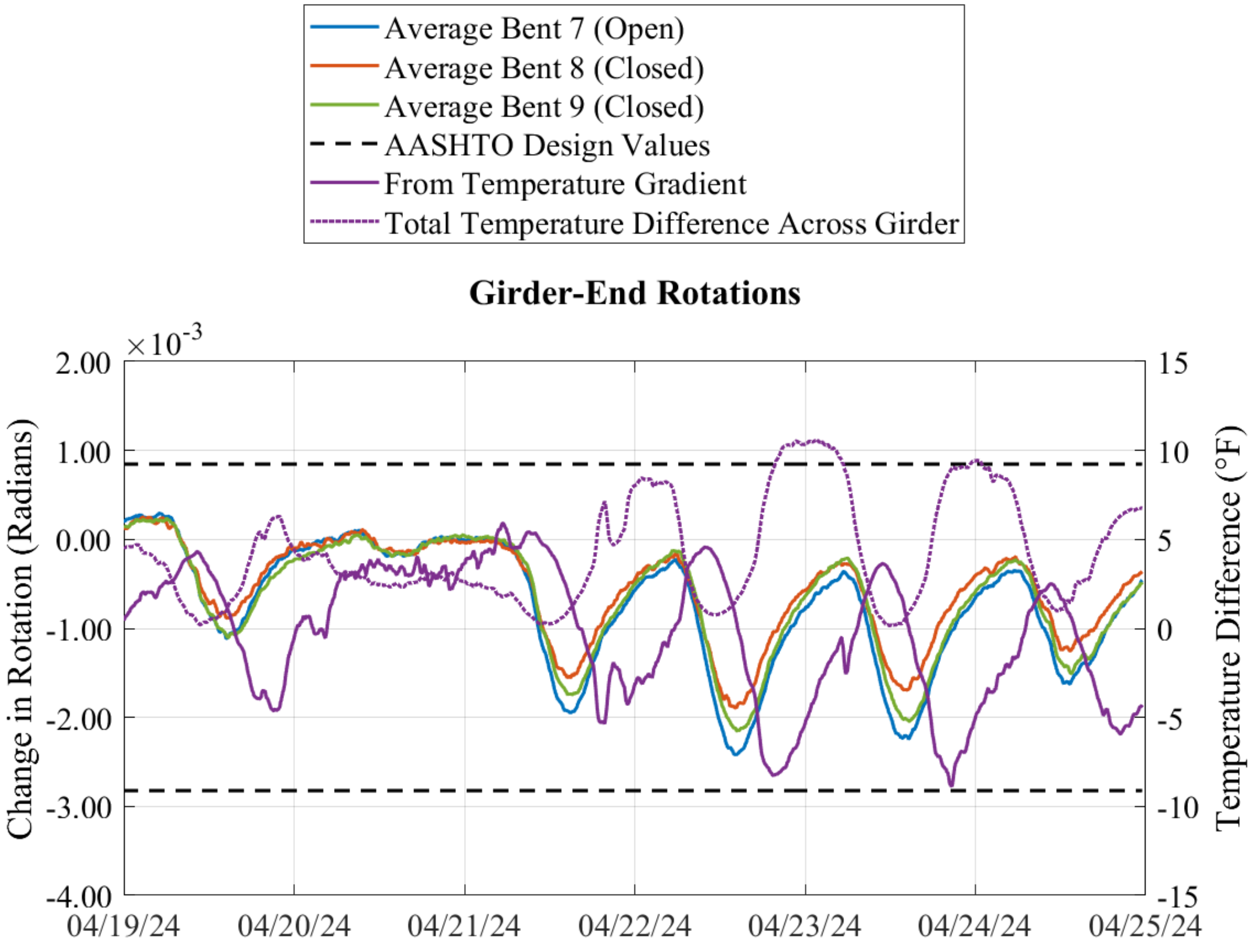

Figure 4-22: Rotation comparison for occurrence of largest negative rotations

The time of the year that subjected the bridge to the hottest temperatures was at the beginning of August. Figure 4-23 shows the girder-end rotations measured by the inclinometers along with the rotations calculated using the temperatures measured by the thermocouples during the period of maximum temperature values recorded. During this time, the peak positive rotations measured approached the AASHTO (2024)design value for positive rotation due to a negative gradient (see Section 4.4) but remained smaller than the design value. This consistent large rotation throughout this period can be attributed to the temperatures beneath the bridge at night being warm enough to result in appreciable positive curvature across the spans. The rotation cycles in hot weather have consistent amplitudes and peaks between each day.

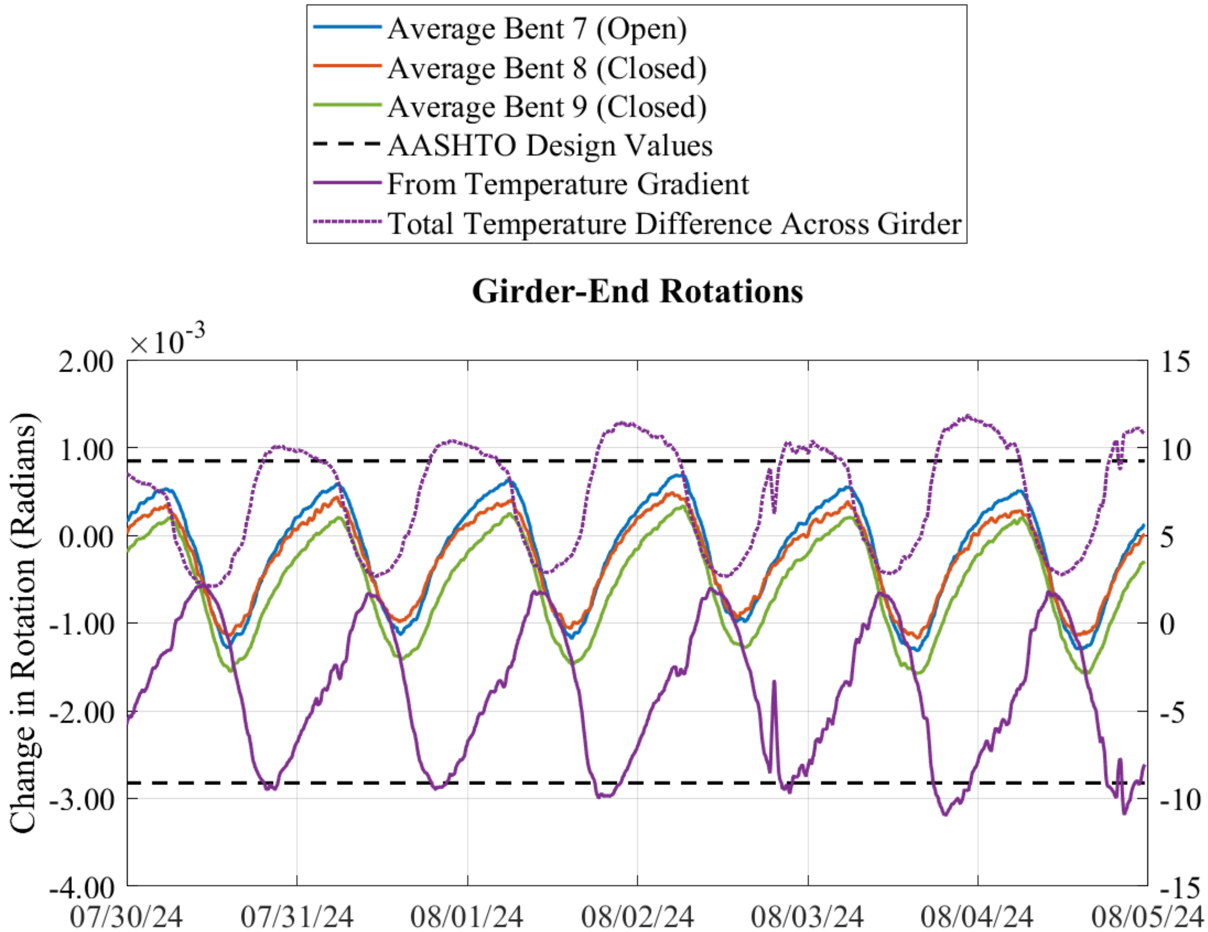

Figure 4-23: Rotation comparison for occurrence of hottest temperatures

Figure 4-24 displays the girder-end displacements measured at the open-joint (Bent 7) and at both closed-joint locations (Bent 8 and 9) when the bridge is subject to high temperatures. As shown earlier in Figure 4-11, these displacements are measured at the bottom flange of the girder ends. The open joint was observed to have a constant, large negative displacement, approaching 0.25” of displacement during this time. This aligns with the expectations for larger negative displacements under hot temperatures as the concrete in the superstructure expands, closing the gap between the girders. On the other hand, the closed joints had a small amount of displacement as compared to the open joint, having cycles with magnitudes of 0.1”. Because of the smaller magnitude, the cycle in displacement observed can be attributed to the rotation of the girders rather than axial expansion and contraction of the girders exposed to uniform temperature. The displacements of Bent 8 and 9 are almost on top of each other, which indicates that the bearing types classified by ALDOT (fixed versus expansion) do not have a significant impact on the displacement behavior of these closed joints.

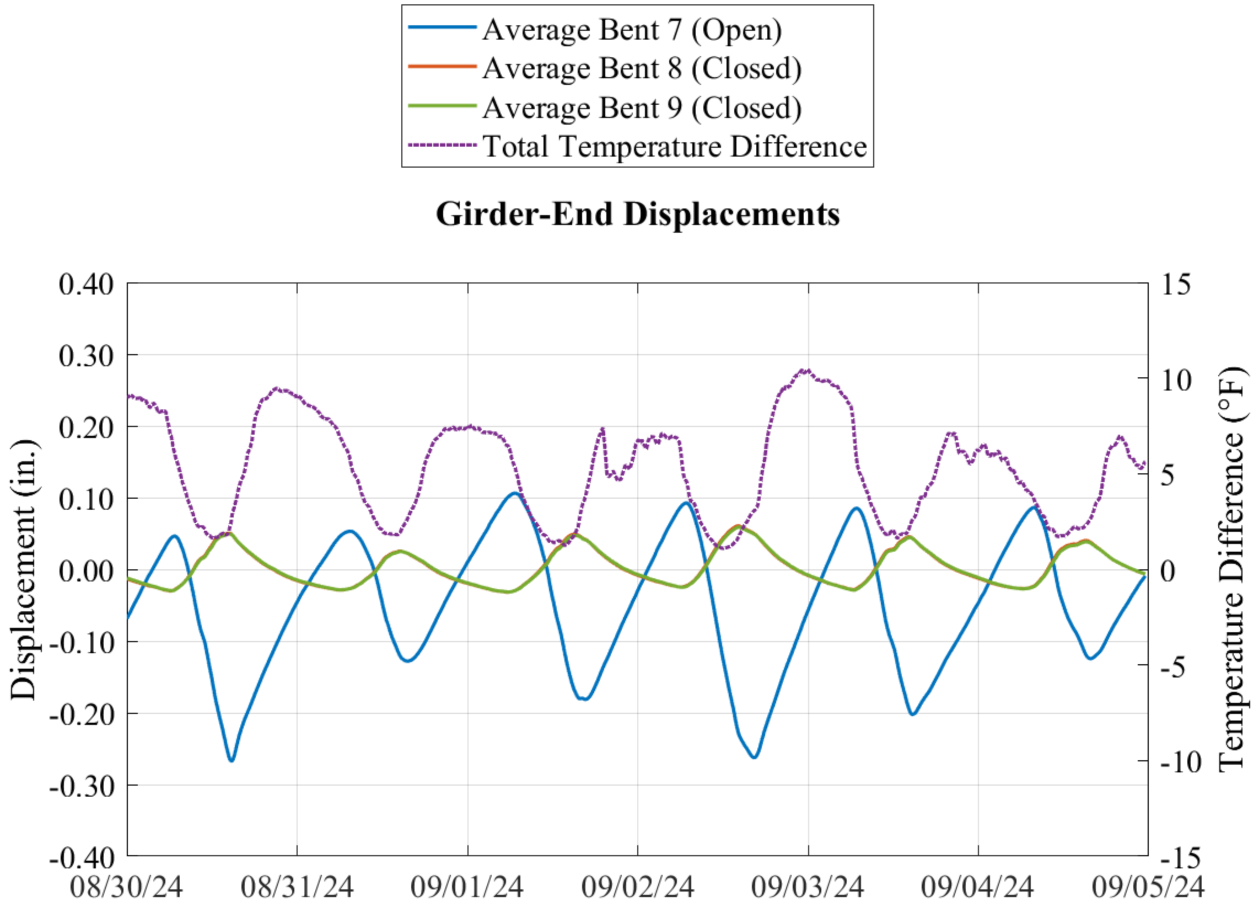

Figure 4-24: Open- and closed-joint displacement for occurrence of hottest temperatures

Figure 4-25 displays the measured rotations, rotations calculated from measured temperatures, and temperature differences during the week when the largest positive rotation between the girder ends was recorded by the inclinometers. This occurred at Bent 7 with a value of 1.12 x 10^{-3} radians in the early morning of September 1, 2024. The peak occurring in the fall was expected as fall weather results in larger temperature gradients due to temperatures having larger fluctuations. This peak value, along with several days surrounding this peak, is slightly larger than the positive rotation value calculated by the AASHTO (2024) design gradient and design values (see Section 4.4). These measured rotations only cross over the design value by about 0.00015 radians, with the maximum only 0.00028 radians above this value. One aspect of note is that this maximum value is reached by the open joint, not the closed joints. The maximum rotation of the closed joint does approach the design value but never exceeds it.

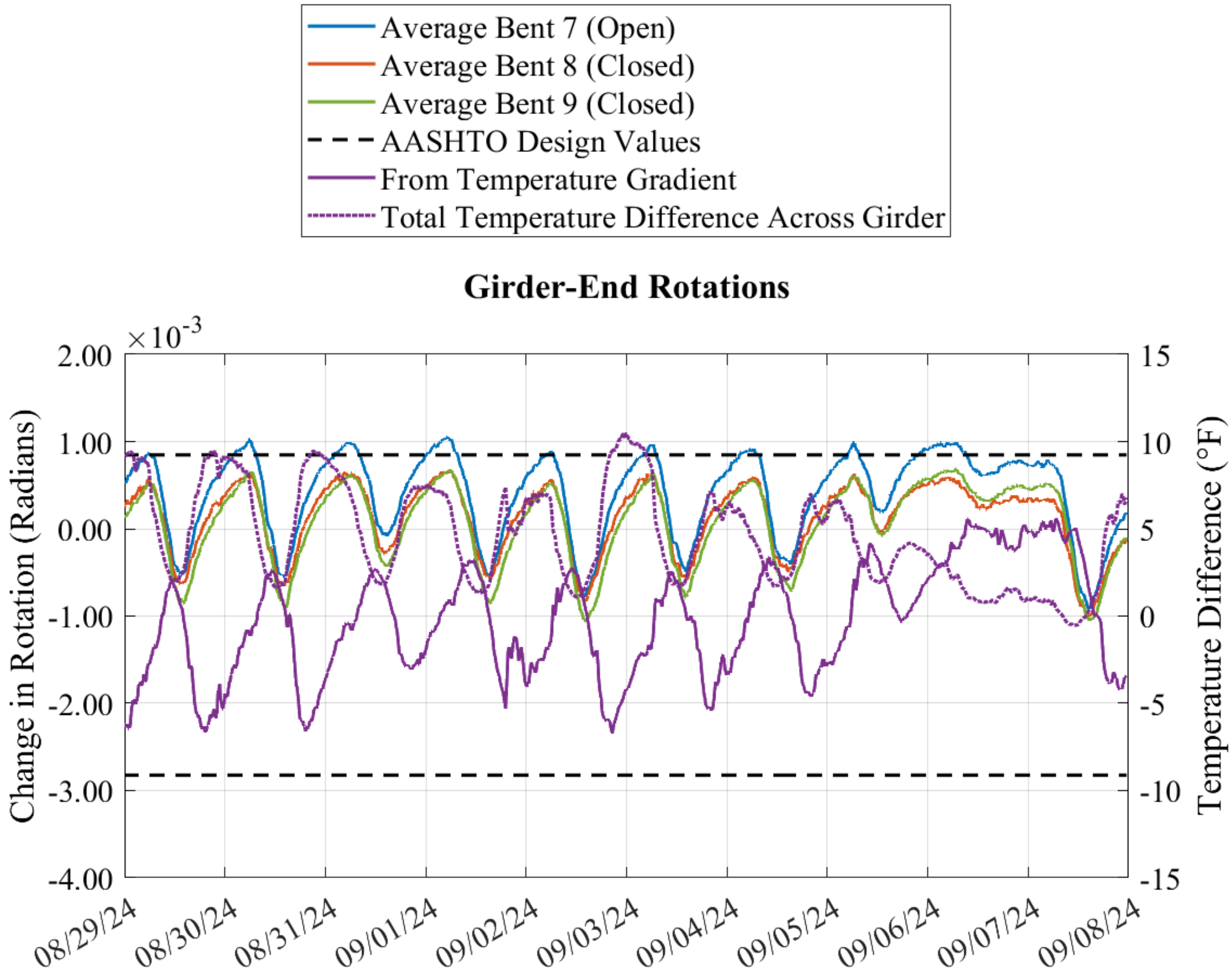

Figure 4-25: Rotation comparison for occurrence of largest positive rotations

One aspect to note about the cycles in temperature differences and the rotations calculated from these differences displayed in these plots is the offset between the measured rotation peaks and the measured temperature difference peaks. Theoretically, the maximum rotation (per daily cycle) across the girder ends happens when the temperature gradient is at the largest value. However, the temperature difference cycles, as well as the rotation calculated from the measured temperatures, occur approximately 6.33 hours (380 minutes) after the measured rotation cycles. This could be due to the rate of heat dissipation through the superstructure, where the deck is immediately heated by the sun, but the girders are heated more slowly through air temperature and heat diffusion from the deck, so the installed thermocouples attached to the surface of the girder recorded the delayed temperatures.

Figure 4-26 and Figure 4-27 display the measured rotations and temperature differences for the rotation across the girder ends over the periods where the largest temperature differences occurred. The rotation cycles observed when the largest temperature differences occur have large daily amplitudes, as seen on May 29th for the largest difference on a singular day. This large amplitude is seen consistently in Figure 4-27, with the largest difference between peak rotations for Bent 9 occurring on June 10th with a magnitude of 2.09 x 10^{-3} radians. The largest daily amplitude observed for Bent 8 with a magnitude of 1.75 x 10^{-3} radians occurred on May 13th, which was just larger than the magnitudes seen in Figure 4-26. The cycles over this period are large and consistent because the temperature differences are consistently high between night and day. As compared to the measured rotations that had the largest negative rotation (Figure 4-22), these cycles are larger in magnitude, but their daily zero position is higher, which prevents the negative rotation values from being larger than the peak rotations observed earlier in the spring.

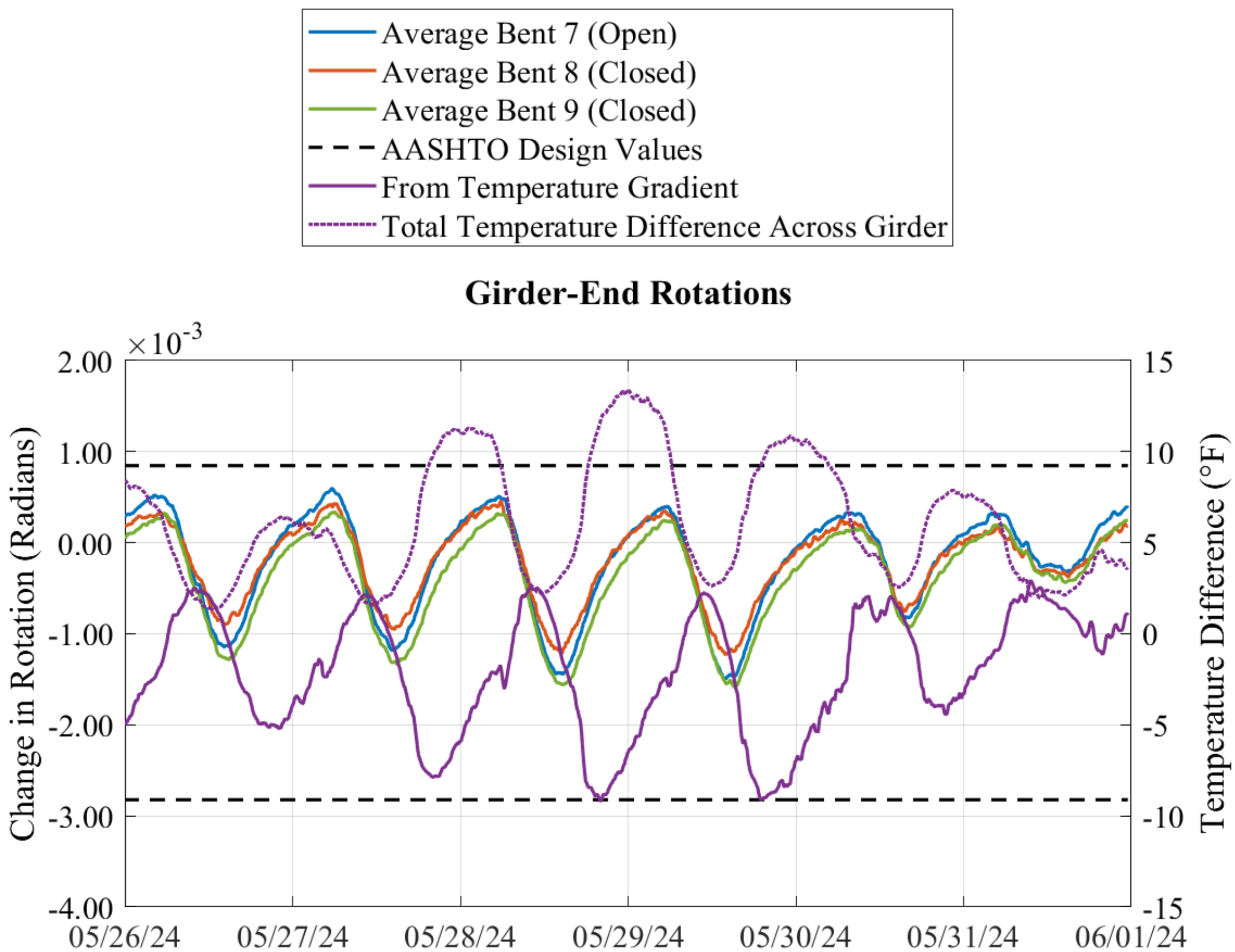

Figure 4-26: Rotation comparison for occurrence of largest temperature difference (singular day)

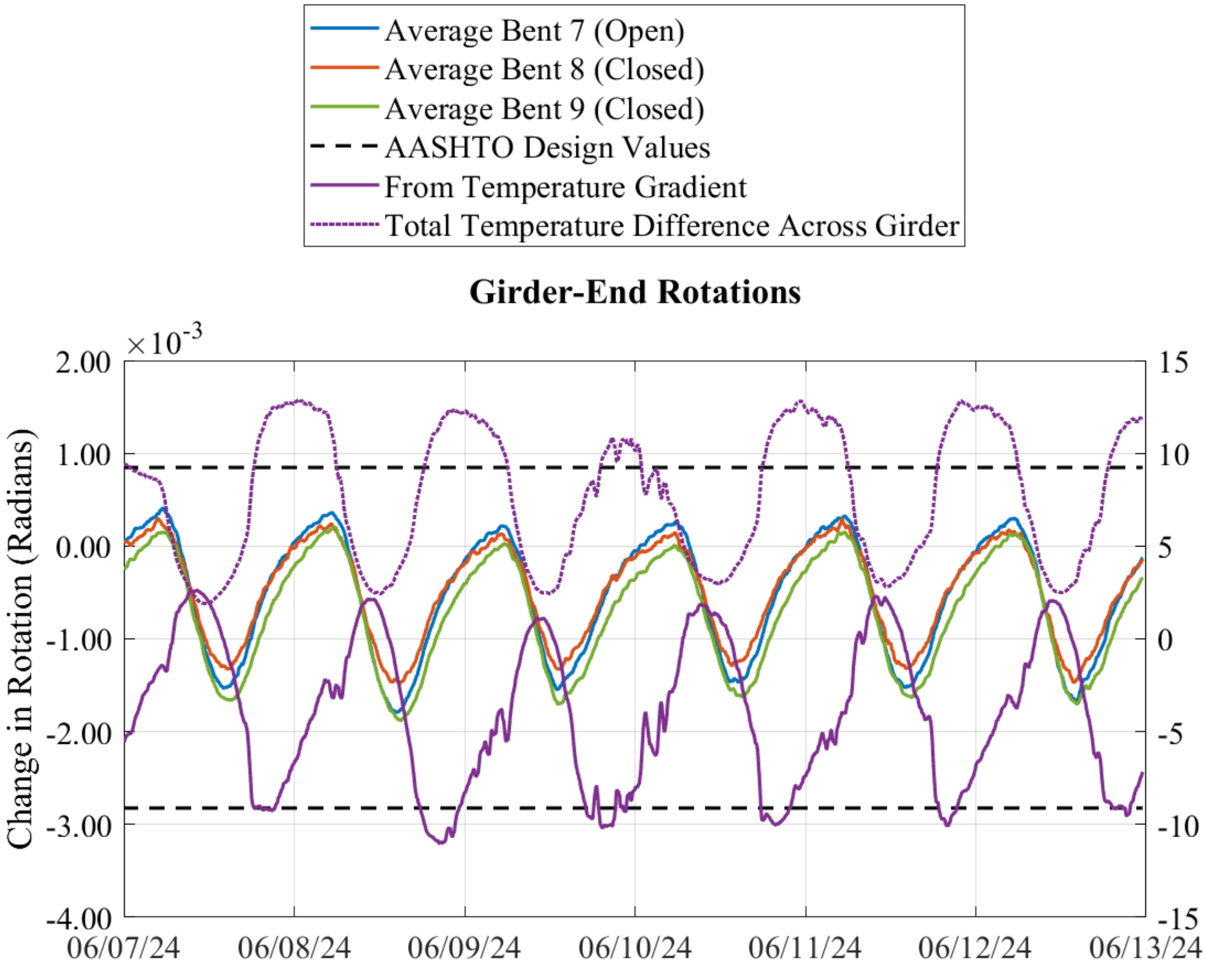

Figure 4-27: Rotation comparison for occurrence of largest temperature difference (consistently over multiple days)

The lowest temperatures that the bridge was subjected to over the monitored year occurred in mid-January when temperatures dropped below freezing. Figure 4-28 displays the measured rotations and temperature differences at the girder ends during this period. The amplitude of the daily rotation cycles during this period was relatively small but also less inconsistent compared to warmer temperatures. The zero point for each of the daily cycles shifts down enough during this time to result in a peak negative rotation of about -2 x 10^{-3} radians with a temperature difference of 2.5°F where the largest negative rotation reached (-2.43 x 10^{-3} radians) was when temperature differences were nearing 10°F (see Figure 4-22).

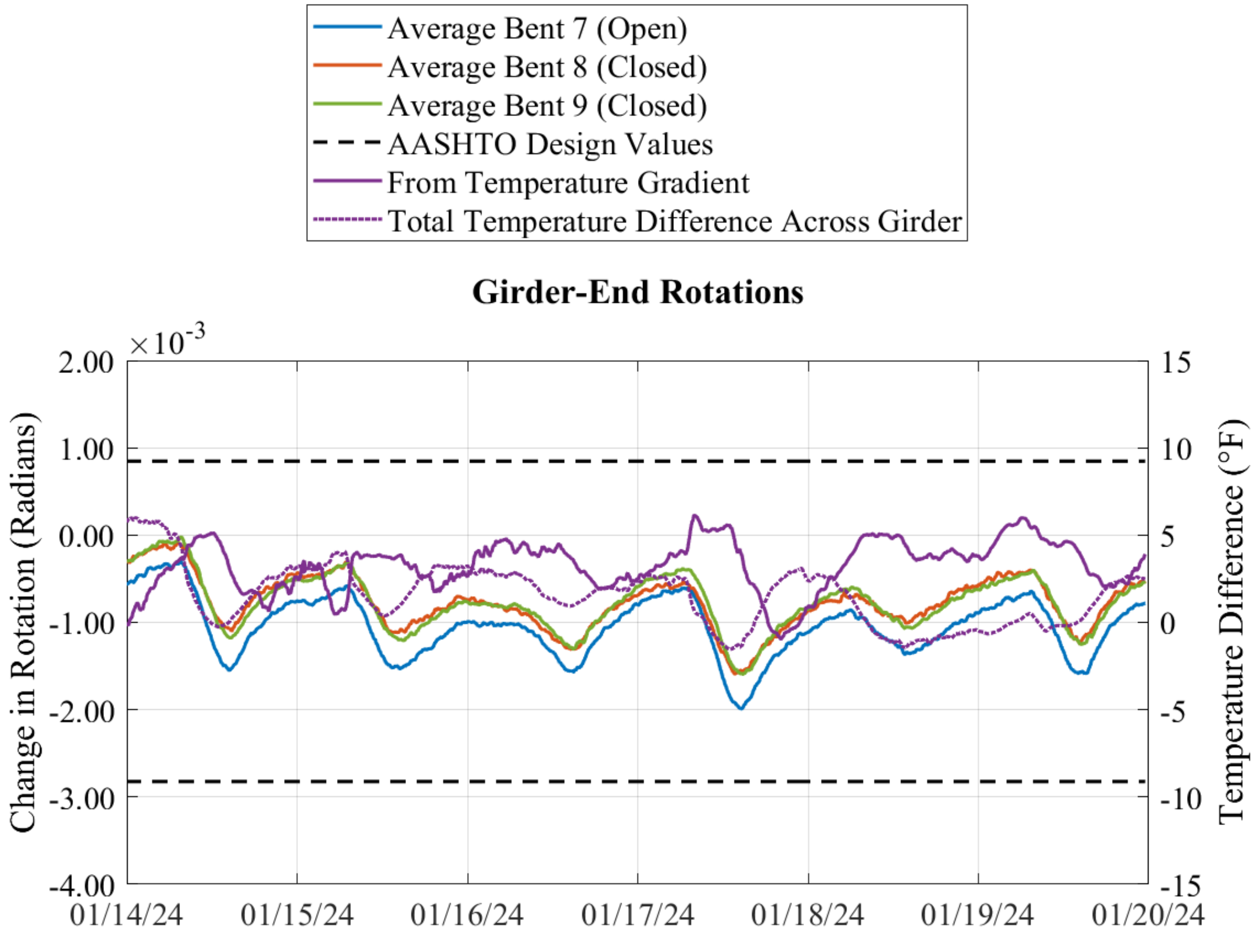

Figure 4-28: Rotation comparison for occurrence of coldest temperatures

Figure 4-29 displays the girder-end displacements measured at the open joint (Bent 7) and at both closed-joint locations (Bent 8 and 9) when the bridge is subject to low temperatures. As shown earlier in Figure 4-11, these displacements are measured at the bottom flange of the girder ends. The open joint was observed to have constant, large positive displacement, approaching 0.5" of positive displacement. This aligns with the expectations for larger displacements under cold temperatures as the concrete in the superstructure shrinks, opening the gap between the girders more. On the other hand, the closed joints had a small amount of displacement as compared to the open joint. Because of the smaller magnitude, the cycle in displacement observed is most likely attributed to the rotation of the girders rather than axial expansion and contraction. The rotations of Bent 8 and 9 are almost on top of each other, similar to the behavior in hot weather (Figure 4-24), displaying the same displacement behavior regardless of bearing type.

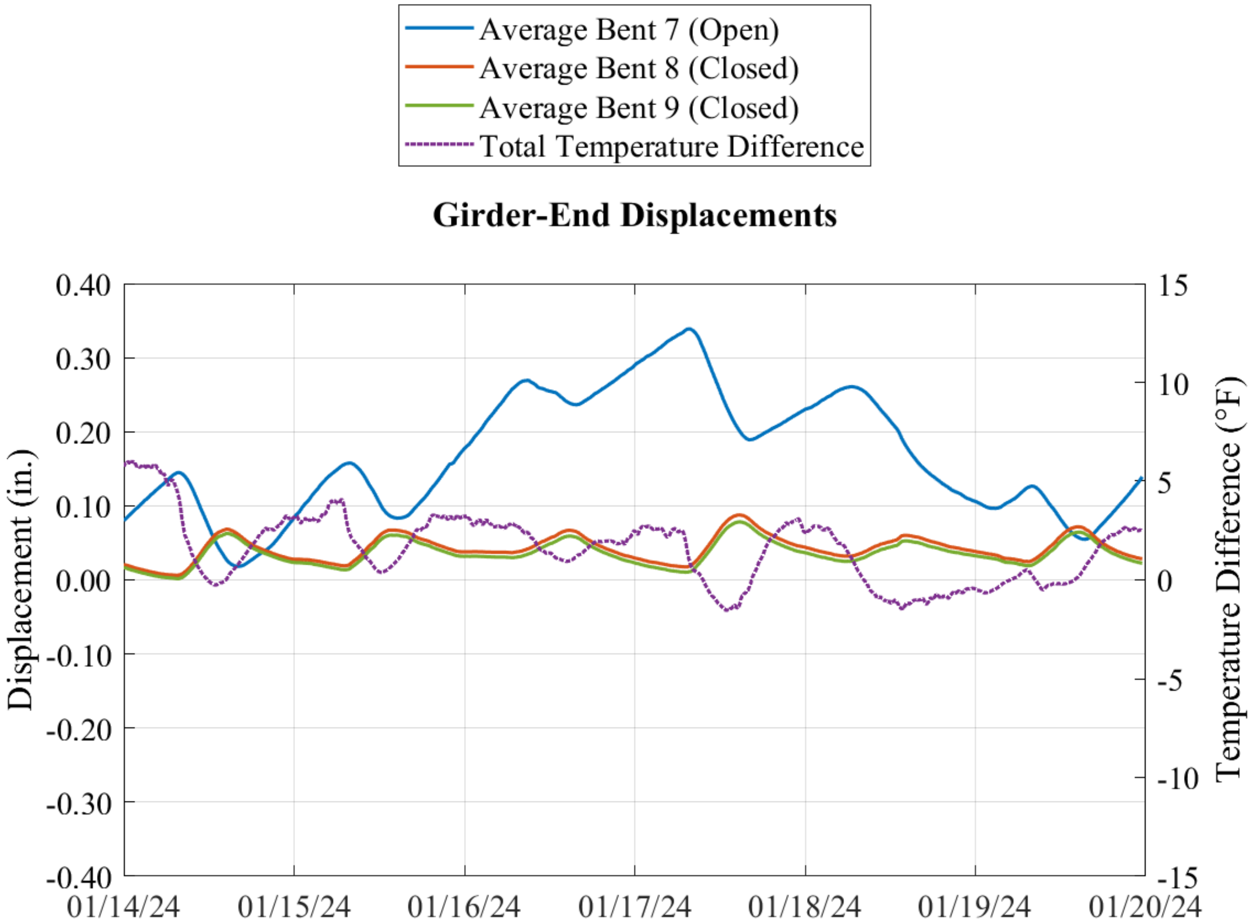

Figure 4-29: Open- and closed-joint displacement for occurrence of coldest temperatures

The magnitudes of the girder-end rotations were observed to be consistent across the bents, with the plots over the whole year exhibiting similar shapes in cycles regardless of the joint being open or closed. This consistency is displayed in Figure 4-30 for the positive peaks and in Figure 4-31 for the negative peaks from each day. From these values, no reasonable difference could be found between the rotations to conclude a major difference in rotation behavior between closed and open joints. The differences in positive and negative rotations between open and closed joints (Bent 7 versus 8 and Bent 7 versus 9) generally follow the same upward trend as the weather changes throughout the year. The trend is consistent between positive and negative peaks, indicating that the differences between rotations are due to a shifting zero for the cycles rather than differences in behavior between open and closed joints. This shift in zero may be due to the nature of the conditions at the open joint because the difference between the two closed joints (8-9) remains relatively close to zero for both negative and positive peak differences. However, since the amplitude of the cycles is consistent between open and closed joints, this should not affect the demand at the girder ends.

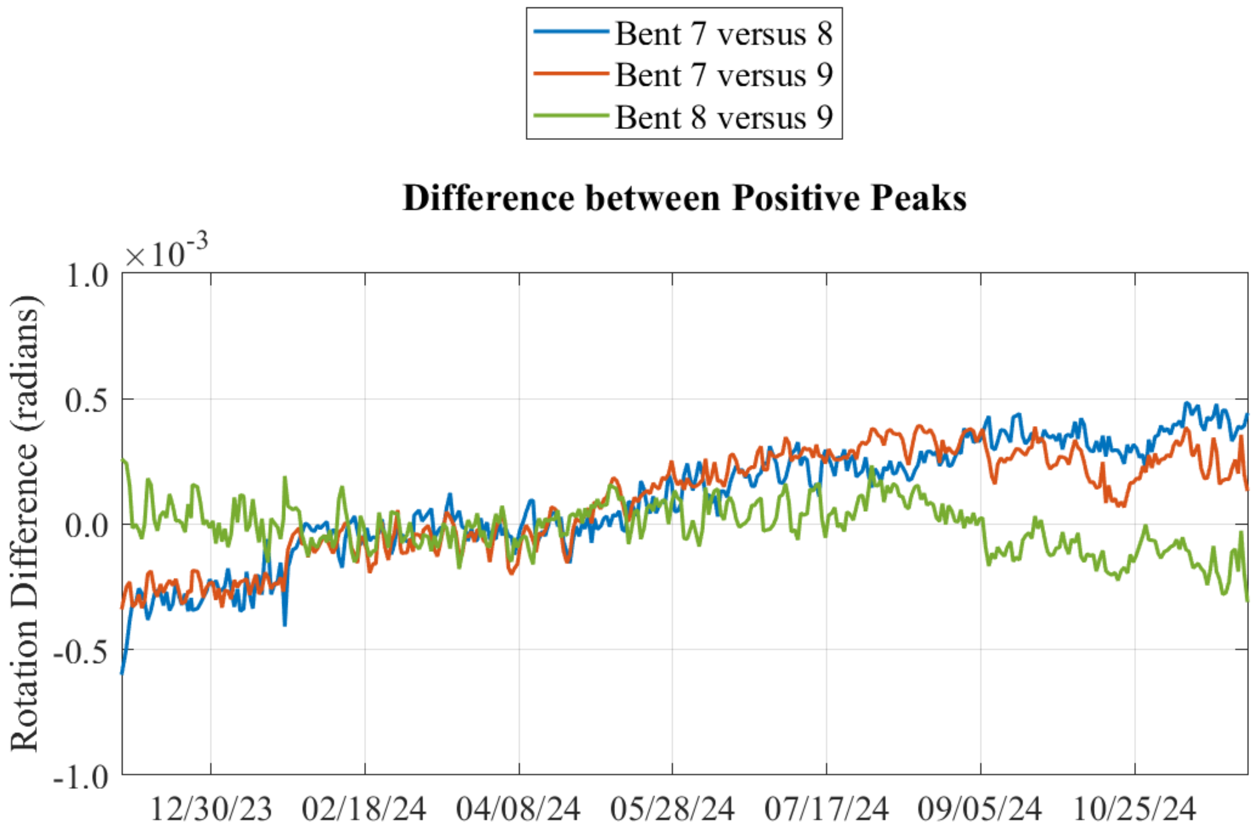

Figure 4-30: Difference between positive rotation peaks over one year

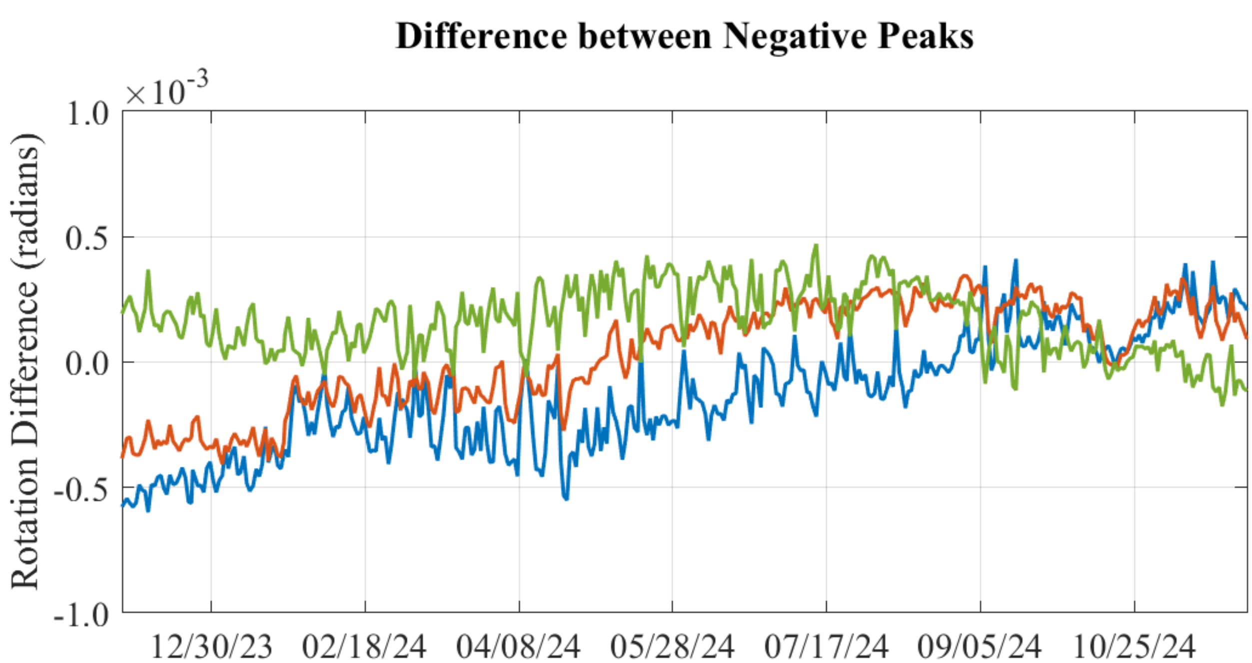

Figure 4-31: Difference between negative rotation peaks over one year

To compare the overall rotational demand by month at each bent, the peak positive and negative measured rotations were plotted for each month along with the rotation calculated from the measured temperature. Figure 4-32 displays December to March, Figure 4-33 displays April to July, and Figure 4-34 displays August to November. The striped sections of the bar plots represent the range for negative rotations over that month, while the solid sections are the positive rotation ranges. It is not possible to know the true zero for the girders since no observations or monitoring were performed at the placement of the bridge. Because of this, the bars could shift up or down depending on the chosen zero point, which in the case of this study was in April. Further studies or observations could be performed to determine a zeroing point based on multiple years of data collection, but this is outside the scope of this study.

Looking at the rotations calculated from the field measured temperatures using the New Zealand gradient, the upper peak rotations, essentially the daily positive rotations, were never calculated to be above zero for the summer months. This can be attributed to the temperatures at the bottom of the girder never being recorded to be larger than the middle temperature and the middle temperature never being larger than the top temperature. The thermocouples may not accurately represent the temperatures within the girder or the superstructure, as well as being impacted by ambient temperatures. Along with the same logic, this may also be responsible for the peak negative rotations calculated from temperature having larger magnitudes than the actual measured rotations (Figure 4-33 and Figure 4-34). These calculated values from measured surface temperature are better suited to be a theoretical blend between the New Zealand design gradient and the direct values measured in the field rather than being a direct prediction of the rotations of the in-service bridge. However, the peak rotations do display closer predicted values with the measured rotations in the winter (Figure 4-32) for both negative and positive rotations. Along with this same point, through all the figures covered previously with both the measured rotations and rotations calculated from measured temperatures, the daily amplitudes are similar and the difference between the two being an offset in the daily zeroing point.

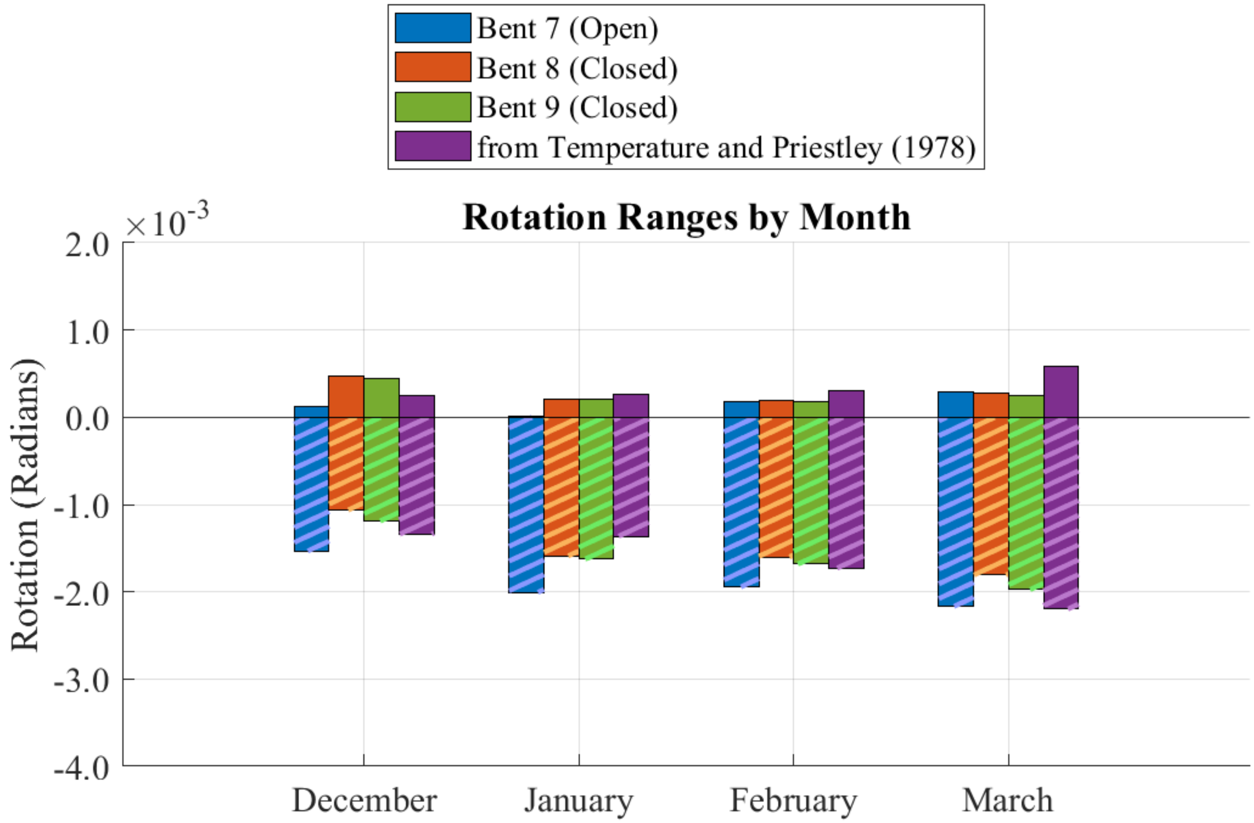

Figure 4-32: Peak rotation ranges from December 2023 to March 2024

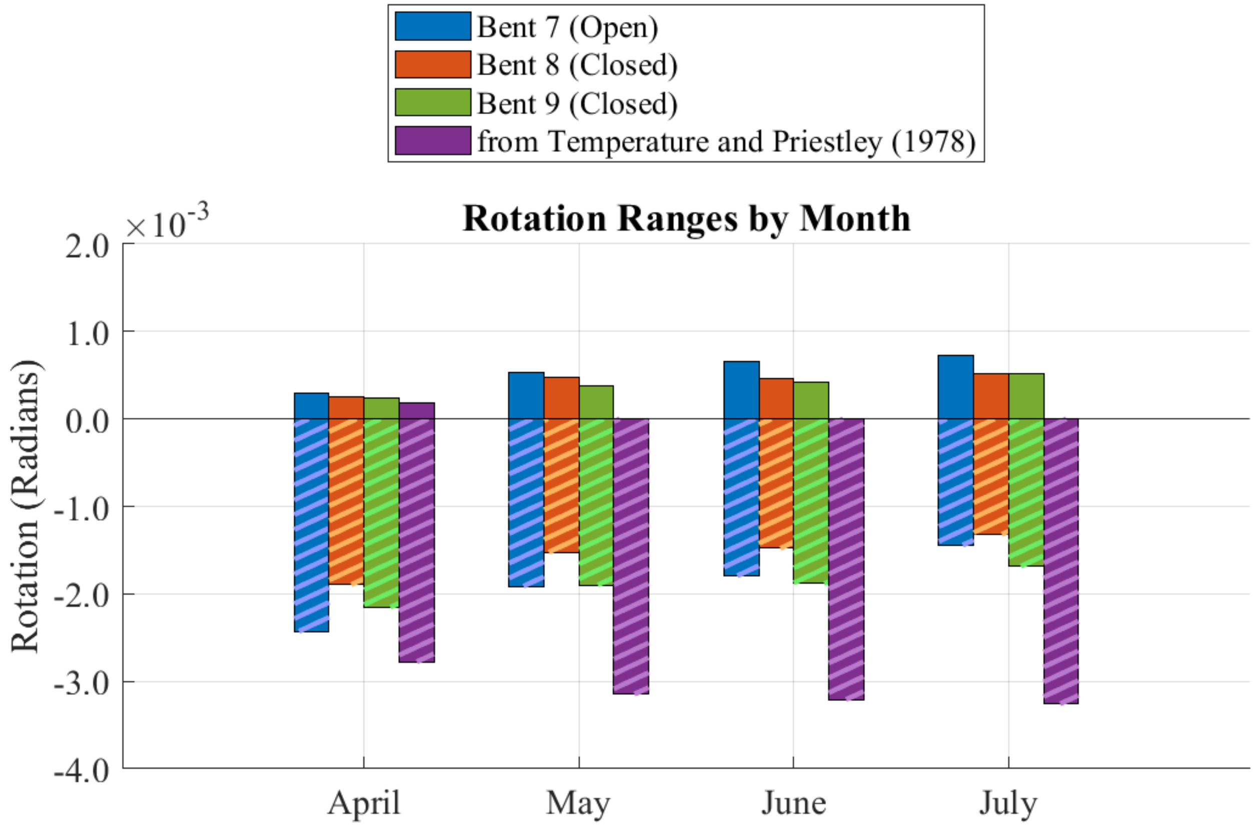

Figure 4-33: Peak rotation ranges from April 2024 to July 2024

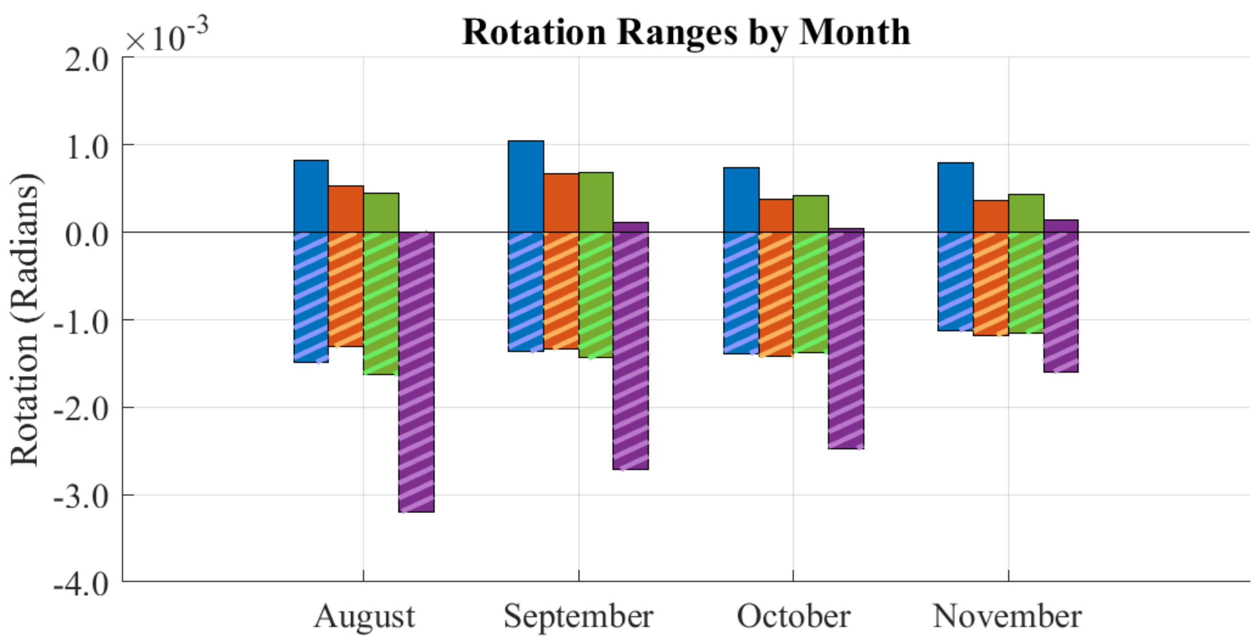

Figure 4-34: Peak rotation ranges from August 2024 to November 2024

Figure 4-35 compares the maximum positive and negative rotations between the girder ends from different sources of measurements and calculations. The measured rotations from the inclinometers are labeled as “Peak Field Rotation” and are the sum of the rotation on each side of the joint for each girder line. The rotation calculated from the measured girder-end temperatures using the New Zealand gradient is labeled as “Peak Field Temperature.” The design rotations using the recommended design temperatures and gradient from AASHTO (2024) (Figure 4-17) along with the New Zealand design gradient (Figure 4-18) are also displayed with their respective labels. The graph is arranged by increasing positive rotation values because these will be the rotations that will be inducing tension into the closed joint and deck.

The negative measured rotations are smaller than all the methods of predicting the rotations, which are expected for the three design methods since the recommended design temperatures for the gradients are chosen to represent the largest gradient the bridge could realistically experience. Since the thermocouples for the measured temperatures were exposed to ambient air temperatures, the temperatures tended towards larger positive gradients, resulting in larger calculated negative rotations and smaller positive rotations, which is not exactly indicative of what the whole superstructure cross section was experiencing. The negative rotations for AASHTO (2024) design are slightly higher in magnitude than measured rotations, but the design positive rotation is slightly lower by approximately the same magnitude. This difference may be due to a zeroing difference for the measured rotations, as discussed earlier, and the bar could be shifted depending on the observed zeroing value. As seen in Table 4-2, the AASHTO (2024) design gradient using the AASHTO (2024) design temperatures has the smallest percent difference when looking at both positive and negative measured rotations.

The New Zealand design gradient has the largest design rotation for both positive and negative values, which is due to the large temperature difference design values recommended, specifically at the deck surface (57.6°F). Referring to Figure 4-16 and Table 4-1, the New Zealand value for the temperature difference is closer to the design value recommended by AASHTO (2024) for Zone 1 (54°F), which encompasses mostly the west of the United States, where Alabama falls into Zone 3. To account for this difference in climate, the design temperatures given for Zone 3 (which includes 0°F at the bottom of the girder) were used with the shape of the New Zealand gradient (x^5 curve) to produce the rotations for the “NZ Gradient w/ AASHTO Temps.” This method of calculation produces negative rotations that are still much larger than the measured rotations but are reduced from the original New Zealand design rotations by about 30%. The positive rotation calculated from this method has the smallest percent difference for positive rotations compared to the other methods of rotation prediction.

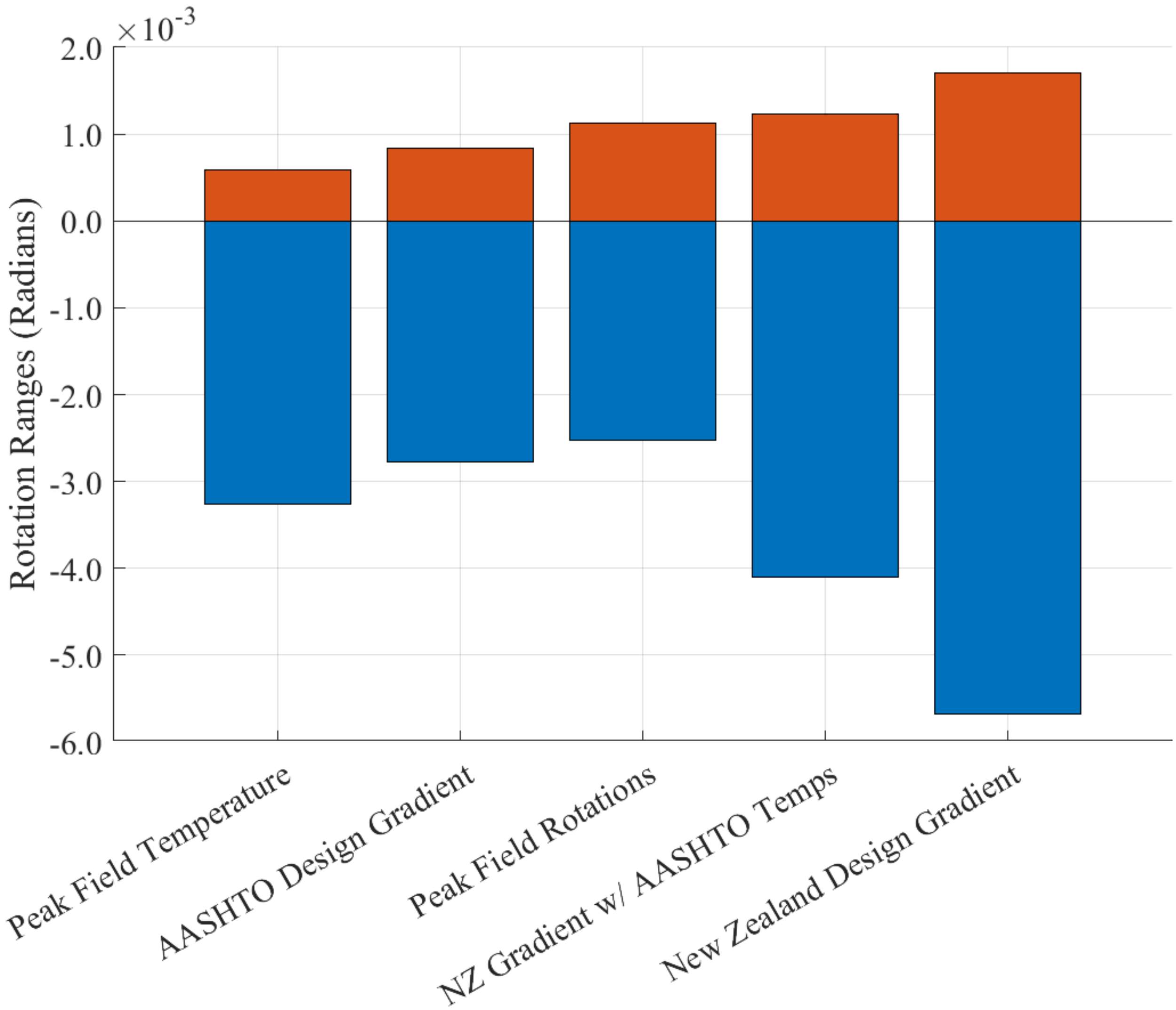

Figure 4-35: Maximum total range in rotation across girder ends from various methods of calculations

Table 4-2: Percent difference between measured and calculated rotation ranges

	Field Temperature	AASHTO Gradient and Temperatures	NZ Gradient and AASHTO Temperatures	NZ Gradient and Temperatures
Positive Rotation	-48.0%	-25.7%	9.86%	52.2%
Negative Rotation	28.8%	9.70%	62.1%	124%
Average	38.4%	17.7%	36.0%	88.1%

4.6. Conclusions

Throughout the entire year observed, the displacements measured at both closed joints (Bents 8 and 9) were consistent. The average difference between the displacements, excluding the period in which the crackmeters on Bent 8 broke off from the girder, was 8.8% of the average amplitude of the displacement cycles (0.05”) with a difference of 0.0044”. The only difference between Bents 8 and 9 was the bearings for the girders, which were expansion and fixed, respectively, as defined by ALDOT. The expansion bearing details have the girder only resting on a neoprene pad, while the fixed bearing also includes an angle attaching the girder to the bent cap. The small difference between displacements means that the bearings of the girders, specifically for the expansion versus fixed types, do not have a significant impact on the behavior of the girder ends and thus the demand on the closed joint.

The measured girder-end rotations at all three of the monitored bents were similar in magnitude, regardless of the detail used for the deck joint. This similarity was consistent for both the positive and negative rotation of the girder ends experiencing both cold and hot weather conditions. From this, the study can conclude that the closed-joint detail restrains a negligible amount of rotational movement at the girder ends as compared to an open joint. The deck and closed-joint detail do not have enough stiffness to restrain the rotation of the girders from thermal demands.

The largest values that were recorded from directly measured rotation by the installed inclinometers were roughly equal to AASHTO (2024) design values for both positive and negative rotations. The AASHTO (2024) negative rotation was 9.7% larger in magnitude than the measured rotation, but negative rotation produces compression, so a smaller value is more conservative for design. The AASHTO (2024) positive rotation was smaller than the measured rotation by 0.29 x 10^{-3} radians, which would be less conservative due to positive rotation inducing tension into the deck. However, this difference is small and would not lead to large differences in design. The values produced by using the AASHTO (2024) design gradient work well for design, at least for the one bridge for which field monitoring was performed for one year.

For future studies, better attachment methods for thermocouples are recommended to easily monitor multiple bents, instead of one, to capture any temperature fluctuations across the spans that may occur. This could include drilling into the concrete and embedding the sensors rather than surface mounting them (if allowed by the owner). By embedding the sensors, this may also remove the influence of air temperature on temperature calculation and record the temperature of the girder concrete more accurately. A more precise method of mounting the inclinometers so they read perfectly parallel to the girder line is also recommended. This would remove the need to assume that no out-of-plane rotation was occurring if the inclinometers were installed 90° to the girder.

By installing strain gauges on or near the deck surface, the movement of the deck surface could be recorded directly instead of estimating this movement with the rotation and displacement of the girder ends. If the gauges were installed within the deck surface, this would allow for monitoring to begin during construction and continue into service. This would provide a more accurate value for the position of the bridge when there is no demand applied to it rather than estimating the value from low thermal gradients captured. Also, looking at the data collected, using larger dataloggers that can handle more connections would allow all the bents to transmit data remotely instead of not being able to monitor one for months at a time.

Chapter 5: Closed-Joint Demands

5.1. Introduction

To capture the overall demands at the closed joints, a numerical study was conducted. Closed joints are subjected to axial force and bending moments when the adjacent girders undergo loads that result in girder-end rotations and displacements in the deck, which will be the demands that are focused on and calculated in this numerical study. Fieldwork was performed (see Chapter 4: Field Monitoring) that was able to capture the effects on the closed joints from thermal demands, but this numerical study accounts for the other sources of demands and deformations that were not captured in this field study. The other main sources of loads that produce rotation at the girder ends are live loads and deformations due to time-dependent effects, which will be the focus of this numerical study. The self-weight of the bridge also produces an initial rotation at the end of the girder, but this rotation will have occurred by the time the closed joint is placed and cured, so no forces are developed in-service due to dead load. The same principle goes for time-dependent effects that occur before deck placement, so these effects will only develop forces in the closed joint after deck placement. This numerical study focuses on the case of the bridge that was instrumented for the field monitoring study to superimpose the demands and be more applicable to other cases.

5.2. General Assumptions and Properties

The US-11 Bridge over the Sucarnoochee River and Relief geometry used for determining the section properties came from the ALDOT design plans, the description of which can be found in Chapter 4:. The section properties of the girder were taken from the standard table for AASHTO girder shapes. A diagram of the section can be found in Appendix B: Prestressed Girder Details for the corresponding size.

For the material properties used, the plans stated that "The concrete in the AASHTO girders shall have a minimum of 5,000 psi compressive strength prior to receiving prestressing force and a minimum 28-day compressive strength of 6,000 psi," so a f'_{ci} of 5 ksi and a f'_c of 6 ksi was used for the prestressed girders. The plans stated that "Bridge Superstructure Concrete, Class 'A'" shall be used for the deck concrete. The Standard Specification for Highway Design (2002) for ALDOT defined this type of concrete as having a minimum 28-day compressive strength of 4 ksi, so this value was used for the f'_c of the deck. The coefficient of thermal expansion of the concrete was taken as 6.0 x 10^{-6} in/in/°F (AASHTO 2024 5.4.2.2). Taken from AASHTO 5.4.2, Equation 5-1 was used to calculate the modulus of elasticity (E) of the concrete.

$$E = 120{,}000 K_1 w_c^{2.0} {f'_c}^{0.33} \qquad \text{Equation 5-1}$$

Where: K_1 = correction factor for source of aggregate to be taken as 1.0 unless determined by physical test, and as approved by the Owner

w_c = unit weight of concrete (kcf)

f'_c = compressive strength of concrete for use in design (ksi)

For composite calculations, a deck-to-girder modular ratio was used to transform the section properties of the deck concrete into equivalent girder concrete. To simplify calculations, the girder was assumed to be straight (no camber) and be offset by 3" from the deck (with deck concrete filling this gap). Assumptions and properties used for calculating movements from thermal loading are discussed in Section 4.4. Theoretical Basis.

5.3. Live-Load Demands

As the deck is continuous across several simple spans, the largest demand from live-load applications would be one that produces the maximum negative moment effect at the piers. AASHTO 3.6.3.3 – Application of Design Vehicular Live Loads recommends "For negative moment between points of contraflexure under a uniform load on all spans, and for reaction at all interior supports of multi-span structures regardless of superstructure continuity, 90 percent of the effect of the design lane load on all spans combined with 90 percent of the effect of two design trucks spaced a minimum of 50.0 ft between the lead axle of one truck and the rear axle of the other truck. The distance between the 32.0-kip axles of each truck shall be taken as 14.0 ft. The two design trucks shall be placed in adjacent spans to produce maximum force effects."

As the distance from the center of the pier to the support of the girder is 1.0 ft, the first truck was placed where the rear axle was 24 ft from the end of the span, and the second truck was placed where the front axle was 24 ft behind the end of the second span. Assuming simple supported spans, the total rotation across the joint (rotation of both beam ends) from the application of the HL-93 truck was calculated to be 1.67 x 10^{-3} radians for the back truck and 1.53 x 10^{-3} radians of rotation for the front truck, including the girder distribution factor. The application of the lane load across both spans resulted in 1.20 x 10^{-3} radians of total rotation, including the girder distribution factor. In total, including the 90% effect recommended by AASHTO, the rotation from live load application was calculated to be 3.97 x 10^{-3} radians (0.23 deg). The calculations for this demand can be seen in Section E.3. Rotations from HL-93 Loading using AASHTO 3.6.1.2 and 3.6.1.3.

5.4. Time-Dependent Effects

The three sources of time-dependent effects for the bridge superstructure are (1) the creep of the girder concrete, (2) the differential shrinkage of the girder and deck concrete, and (3) the relaxation of the steel. Because any losses that occur before deck placement cannot develop stress into the closed joint, the deformation at the closed joint only comes from effects from deck placement to the final time being analyzed. Guidance from ALDOT's Structural Design Manual was used for calculating these losses with equations from AASHTO 5.9.3.4. – Refined Estimate of Time-Dependent Losses. The expected strengths that are recommended by ALDOT (2020) are based on work performed by Mante et al. (2022). The assumptions and properties recommended by ALDOT (2020) are:

- Time at strand release: 0.75 days
- Time from release of strands to placement of the bridge deck: 120 days
- Relative humidity: 75%
- Final age: 27,500 days
- Concrete strengths (using expected concrete strengths):
    - At prestress transfer, f_{ci}^*:
      For 4 ksi $\leq f_{ci}' \leq$ 5 ksi, $f_{ci}^* = f_{ci}' + 1.95$ ksi
      For 5 ksi $\leq f_{ci}' \leq$ 9 ksi, $f_{ci}^* = 0.9f_{ci}' + 2.45$ ksi
    - At 28 days, f_c^*:
      For $f_{ci}' \leq$ 9 ksi, $f_c^* = 1.3f_{ci}' + 3.5$ ksi

With these assumptions, the time-dependent effects from each of the three sources considered were able to be calculated for the girders. The calculations can be found in Section E.4. Rotations from Time-Dependent Effects using AASHTO 5.9.3.4. For the effects due to the creep of the concrete, equations and guidance from AASHTO (2024) 5.9.3.4.3b – Creep of Girder Concrete was used to calculate the creep coefficient and strain after deck placement. To compute the rotation from this strain, it was assumed that this strain occurs at the center of the steel strands and Equation 5-4 is used to calculate this rotation (see Figure 5-1 for variables used). This is the total rotation over the closed joint from both girder ends, assuming both spans are equal.

$$\theta_{T,CR} = 2\left(\frac{\epsilon_{creep} * \frac{L}{2}}{D_{creep}}\right) \qquad \text{Equation 5-2}$$

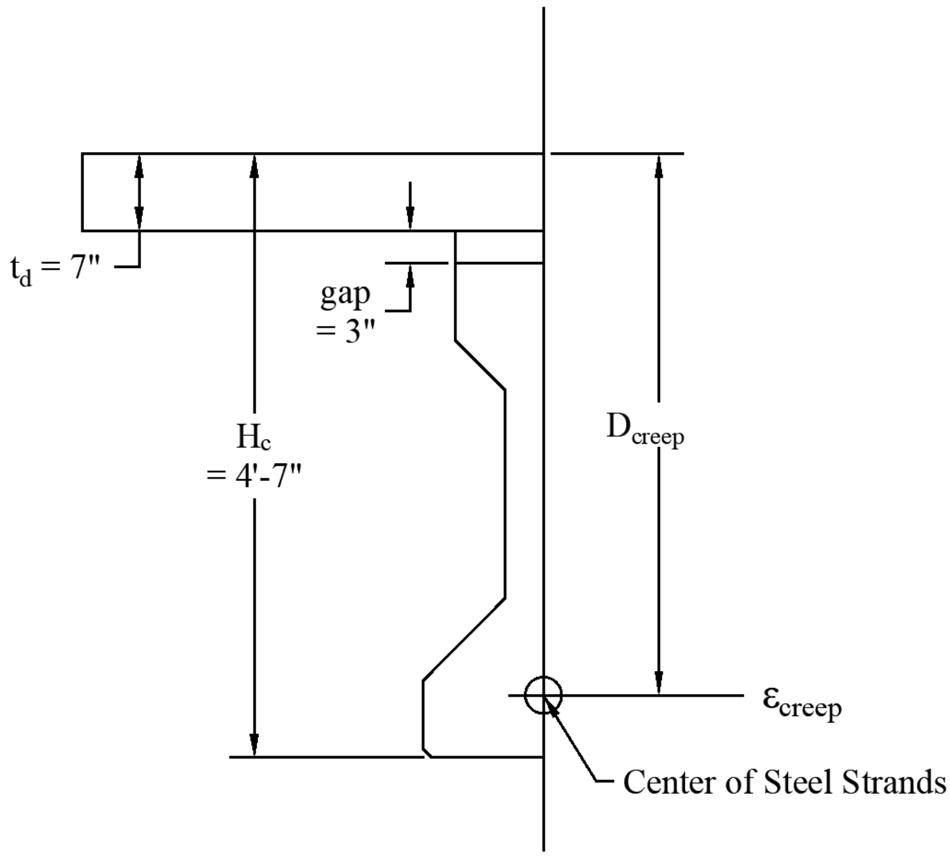

Figure 5-1: Diagram for rotation due to concrete creep

For the effects due to the differential shrinkage of the concrete, equations and guidance from AASHTO (2024) 5.9.3.4.3a – Shrinkage of Girder Concrete and 5.9.3.4.3d – Shrinkage of Deck Concrete was used to calculate the shrinkage strain in both the girder and deck after deck placement. To compute the rotation from these strains, it was assumed that they occur at the center of gravity of the respective elements and Equation 5-3 is used to calculate this rotation (see Figure 5-2 for variables used). This is the total rotation over the closed joint from both girder ends, assuming both spans are equal. The shrinkage of the concrete also causes axial displacement in the deck, which can be calculated from the uniform strain across the superstructure, taken as the shrinkage strain in the girder (ε_{gdf}) and can simply calculate the axial displacement by multiplying it by the length of the girder (assuming equal adjacent spans).

$$\theta_{T,CS} = 2\left(\frac{(\epsilon_{ddf} - \epsilon_{gdf}) * \frac{L}{2}}{D_{shrink}}\right) \qquad \text{Equation 5-3}$$

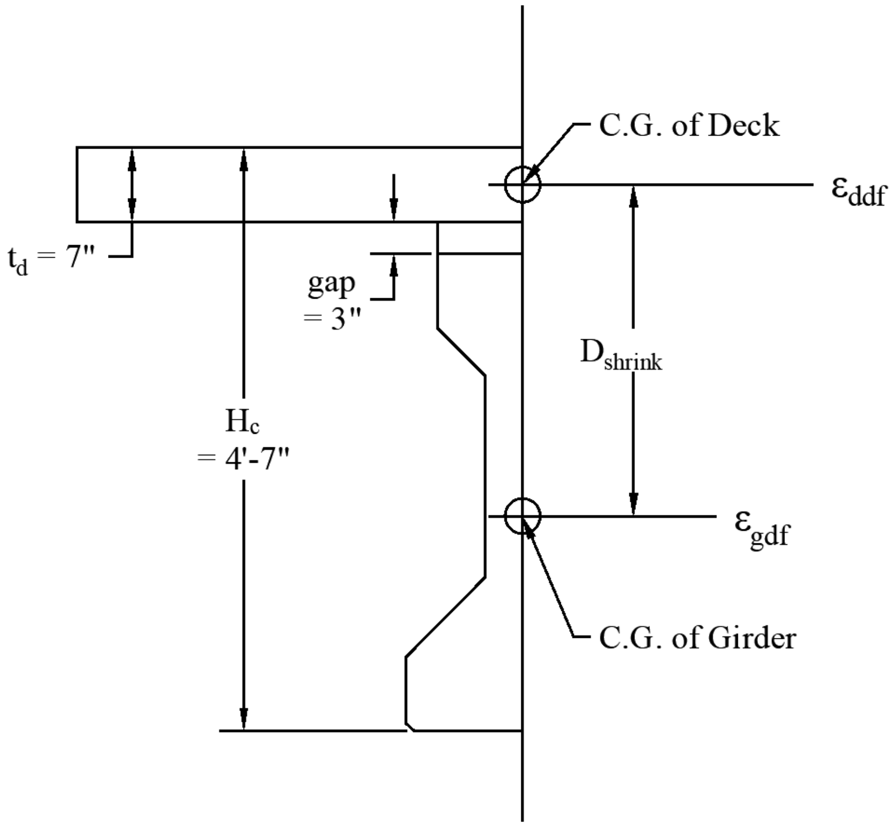

Figure 5-2: Diagram for rotation due to differential concrete shrinkage

For the effects due to the relaxation of the steel in the girder, guidance from AASHTO (2024) 5.9.3.4.3c – Relaxation of Prestressing Strands was used to determine the prestress loss in the steel strands after deck placement. To compute the rotation from this prestress loss, guidance and equations from Nawy (2009). Equation 5-4 is used to calculate this rotation (see Figure 5-3 for variables used). This is the total rotation over the closed joint from both girder ends, assuming both spans are equal.

$$\theta_{T,SR} = 2\left(\frac{Pe_c}{EI} * \frac{L}{2}\right) \qquad \text{Equation 5-4}$$

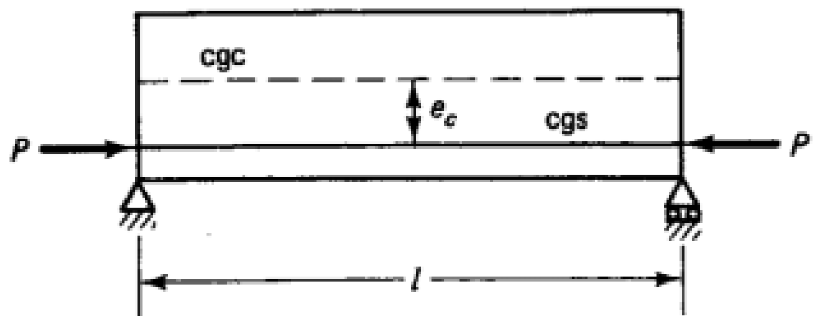

Figure 5-3: Diagram for rotation due to steel relaxation (Nawy, 2009)

After performing these calculations, the rotation due to the creep of the concrete is -1.30 x 10^{-3} radians, due to the shrinkage of the girder concrete is 0.06 x 10^{-3} radians, and due to the relaxation of the steel is 0.08 x 10^{-3} radians. The total rotation that the closed joint experiences (due to time-dependent effects after deck placement) is -1.14 x 10^{-3} radians (-0.07 deg). The axial displacement due to time-dependent effects after deck placements (from concrete shrinkage) was calculated to be 0.23 in.

5.5. Combined Load Effects

To superimpose the demand from the three sources of movement at the girder ends, the direction and frequency of the demands need to be classified and consistently combined. The thermal demand on the bridge superstructure mainly comes from the differential temperature across the cross section created by the rising and setting of the sun and associated changes in ambient temperatures. The peaks of this demand occur daily, the magnitude of which is variable day by day. The worst-case scenario for the rotation at the closed joint is when the deck is cast in hot weather, making the zero-point for the thermal rotations the bottom of the negative peaks. This exposes the closed joint to positive rotation over the whole range of thermal movements.

The rotation that live load induces is cyclic as the truck moves over the joint. The frequency that the bridge experiences this demand may be more inconsistent but is more dynamic and quicker than thermal demands. Like the worst case for thermal effects, the zero point of the live-load cycles lies at the troughs of the cycles since loads from trucks only apply a downwards force, so the live load induces a maximum positive rotation in simply supported girders.

The direction of the rotation that results from time-dependent effects depends on the effect under evaluation. For the creep of the concrete, the negative strain at the center of the strands creates an increase in negative curvature, resulting in negative rotation at the girder ends. For concrete shrinkage, assuming the deck shrinkage is more than the girder shrinkage, this leads to positive rotation at the girder ends. The relaxation of the steel also induces positive curvature and rotation for the girders. These losses begin rapidly after girder concrete placement but slowly level out over time and gradually approach a maximum value.

The load combination factors from AASHTO Table 3.4.1-1 were used to superimpose and combine the rotations from the different demand types. AASHTO 3.4.1 specifies four different combinations for service limit states. The Service I limit state relates to the normal operational use of the bridge with all loads taken at their nominal values. The Service II limit state is intended to be used to control the yielding of steel structures and slip of slip-critical structures due to vehicular live load, which does not apply to this case. The limit state for Service III is meant for longitudinal analysis relating to flexural tension and principal tension in the webs of prestressed concrete superstructures, which does not apply to this case. The limit state for Service IV only relates to tension in prestressed concrete columns, which does not apply to this case. The Service I limit state was the only combination used to calculate an overall rotational demand at the girder ends for closed joints. The load factors and the combination of the demands for the Service I limit state are shown in Equation 5-5. The value of the load factor for the temperature gradient was given by to be 0.50 since it was a service limit state where live load was considered.

$$Service\ I = \gamma_{TG}(TG) + 1.00(LL) + 1.00(CR + SH + PS) \qquad \text{Equation 5-5}$$

Where:

TG = 3.61 x 10^{-3} rad., force effects due to temperature gradient

γ_{TG} = 0.50, load factor for temperature gradient

LL = 3.97 x 10^{-3} rad., vehicular live load effects

CR = -1.30 x 10^{-3} rad., force effects due to creep

SH = 0.06 x 10^{-3} rad., force effects due to shrinkage

PS = 0.08 x 10^{-3} rad., force effects due to relaxation

The service rotation, using the values discussed above, is calculated to be 4.64 x 10^{-3} rad (0.27 deg). For future designs considering the demands on closed joints, the study recommends using the Service I limit states with demands from Thermal, Live Load, and Time-Dependent Effects (i.e., concrete creep, concrete shrinkage, and steel relaxation).

The rotations due to force effects calculated as part of this numerical study are recommended to be used in future studies, specifically for lab testing attempting to replicate the in-service demands the closed joint experiences in the field. The maximum rotation observed in the field was 1.12×10^{-3} radians of positive rotation and -2.43×10^{-3} of negative rotation for a maximum rotation range of 3.55×10^{-3} radians. By running this numerical study, the maximum service rotation increases by 131% when considering all the sources of rotational demand rather than just thermal for the case of this bridge. This worst case considers the positive rotation from thermal as it induces tension into the closed joint where the negative rotation would relieve the tension seen in the joint.

The uniform thermal loading is also a source of axial displacement. The calculation of this displacement uses Equation 5-6 (AASHTO (2024) Eq. 3.12.3-1) and assumes equal span lengths on both sides of the closed joint.

$$\Delta_T = \alpha * L * \left(T_{MaxDesign} - T_{MinDesign}\right) \qquad \text{Equation 5-6}$$

The displacement due to the design temperatures from AASHTO was calculated to be 0.46 in. Using the Service I limit state (Equation 5-7) results in a total displacement of 0.78 in.

$$Service\ I = \gamma_{TU}(TG) + 1.00(SH) \qquad \text{Equation 5-7}$$

Where:

$TU =$ 0.46 in, force effects due to uniform temperature

$\gamma_{TU} =$ 1.20, load factor for temperature gradient

$SH =$ 0.23 in., force effects due to shrinkage

It is recommended that designs for closed joints should follow a deformation-based approach, using the rotations at the girder ends as the main source of demand imposed onto the closed joints. It can be said that the deck is "along for the ride" when it comes to deformations imposed by the girders and the rest of the superstructure. The AASHTO design values for thermal demands are observed to be fairly accurate and conservative based on the data collected for 1-year at a single bridge location in Alabama and should be considered with the rest of the sources of rotation (i.e., live loading and time-dependent deformations) using the full magnitude of the design thermal rotation range.

Chapter 6: Conclusions and Recommendations

This research study evaluated the current detail for closed joints in use by ALDOT for prestressed girder bridges. Through performing field inspections on bridges that use this detail, the study concluded that the type and quality of the construction joint used for the closed-joint detail were the major factors that affected the visual performance of the closed joint in the deck. The damage that was observed in these inspections at the closed joints was related to wear from traffic. Another aspect of the closed-joint detail that the field inspections investigated was the role of the edge beam in the performance of the joint and the bridge overall. These inspections concluded that they do not play a structural role for the joint and tend to experience a large amount of cracking when they are full-depth.

The study then performed a year-long field monitoring operation to gain further insight into the demands and behaviors that the closed joint is subjected to. Through this monitoring, the rotation of the girder ends at the open and closed joints were observed to be nearly identical. This similar behavior means that the closed-joint detail does not restrain much more rotation than the open joint and its demands on the joint come from the deformation of the girder ends. The maximum values that were directly from the measured rotation were roughly equal to design values that were obtained from using the AASHTO temperature gradient in Section 3, Loads and Load Factors, with these values being recommended and working well for future design when considering thermal effects.

Because the field monitoring only recorded the response of the bridge from thermal loading, the study also performed calculations to superimpose the deformation from multiple demand sources. When considering the effects of live loads, the guidance from AASHTO 3.6.1.3, Application of Design Vehicular Live Loads, was used, considering the deck as structurally continuous and generating the maximum negative moment possible. When considering the effects from time-dependent losses in the prestressed girder, the initial assumptions were made with guidance from ALDOT's Structural Design Manual. These assumptions were then used along with AASHTO 5.9.3.4, Refined Estimate of Time-Dependent Losses to calculate the deformations at the girder ends that apply the demands into the closed joint. The Service I limit (AASHTO 3.4.1, Load Factors and Load Combinations) state is recommended to combine the deformations from all the demands present at closed joint. For future studies, this method of combining load effects is recommended for laboratory tests benchmarked with field data.

References

AASHTO. (2024). *LRFD Bridge Design Specifications*. American Association of State Highway and Transportation Officials

Aktan, H., Attanayake, U., and Ulku, E. (2008). Combining Link Slab, Deck Sliding over Backwall, and Revising Bearings.

ALDOT. (2020). *Bridge Special Project Drawings*. Alabama Department of Transportation

Au, A., Lam, C., Au, J., and Tharmabala, B. (2013). Eliminating Deck Joints Using Debonded Link Slabs: Research and Field Tests in Ontario. *Journal of Bridge Engineering*, *18*(8), 768-778. https://doi.org/doi:10.1061/(ASCE)BE.1943-5592.0000417

Birley, A. C., Yarnold, M. T., Hurlebaus, S., Pearson, A. N., Krajeck, D. D., and Smith, D. (2025). *Performance and Improvement of Texas Poor Boy Continuous Bridge Deck Details: Final Report* (Publication Number FHWA/TX-25/0-7013-R1) Texas A&M University]. College Station, Texas.

Canales, M. T. J. (2019). *Performance Study of Link Slab Continuity in Prestressed Concrete Bridges* Louisiana State University]. https://digitalcommons.lsu.edu/cgi/viewcontent.cgi?article=6071&context=gradschool_dissertations

Caner, A. (1996). *Analysis and Design of Jointless Bridge Decks Supported by Simple-Span Girders* (Publication Number 9710739) [Ph.D., North Carolina State University]. ProQuest Dissertations & Theses Global. United States -- North Carolina. https://www.proquest.com/docview/304268208?accountid=8421&parentSessionId=LjjrfE1FDZjxmdfsW33VKhDypZg9cnSYpa%2B%2Fosf9iKk%3D

Caner, A., and Zia, P. (1998). Behavior and Design of Link Slabs for Jointless Bridge Decks. *PCI*, *43*(3), 68-80. https://www.pci.org/PCI_Docs/Publications/PCI%20Journal/1998/May-June/Behavior%20and%20Design%20of%20Link%20Slabs%20for%20Jointless%20Bridge%20Decks.pdf

Charuchaimontri, T., Senjuntichai, T., Ožbolt, J., and Limsuwan, E. (2008). Effect of Lap Reinforcement in Link Slabs of Highway Bridges. *Engineering Structures*, *30*(2), 546-560. https://www.sciencedirect.com/science/article/pii/S0141029607001812

Chen, Z., Guo, T., and Yan, S. (2015). Life-Cycle Monitoring of Long-Span PSC Box Girder Bridges through Distributed Sensor Network: Strategies, Methods, and Applications. *Shock and Vibration*, *2015*, 497159. https://doi.org/10.1155/2015/497159

Davidson, E., White, D., and Kahn, L. (2012). Evaluation of Performance and Maximum Length of Continuous Decks in Bridges : Part 2 [Tech Report]. https://rosap.ntl.bts.gov/view/dot/26379

El-Safty. (1994a). Analysis of Jointless Bridge Decks with Partially Debonded Simple Span Beams. *PhD Dessertation, North Carolina State Univ., Raleigh, NC*.

El-Safty. (1994b). *Behavior of Jointless Bridge Decks* (Publication Number 9425459) [Ph.D., North Carolina State University]. ProQuest Dissertations & Theses Global. United States -- North Carolina. https://www.proquest.com/docview/304126844?accountid=8421&parentSessionId=8uUo0oKxQSBTDZtDKUyhLtz8Qnlo1Ku5lgz7sO4gzTY%3D

Eriksson, R. L. (2001). *The State of the Art of Precast/prestressed Integral Bridges*. Precast/Prestressed Concrete Institute Subcommittee on Integral Bridges. https://books.google.com/books?id=vAJFAQAAIAAJ

French, C. W., Shield, C., Stolarski, H. K., Hedegaard, B. D., and Jilk, B. J. (2012). Instrumentation, Monitoring, and Modeling of the I-35W Bridge.

Gastal, F. d. P. S. L. (1986). *Instantaneous and Time-Dependent Response and Strength of Jointless Bridge Beams* http://hdl.handle.net/10183/170152

Gergess, A. N. (2019). Analysis of Bonded Link Slabs in Precast, Prestressed Concrete Girder Bridges. *PCI*, *64*(3), 47-65. https://www.pci.org/PCI_Docs/Publications/PCI%20Journal/2019/May-June/18-0007_Gergess_MJ19.pdf

Hou, M., Hu, K., Yu, J., Dong, S., and Xu, S. (2018). Experimental Study on Ultra-High Ductility Cementitious Composites Applied to Link Slabs for Jointless Bridge Decks. *Composite Structures*, *204*, 167-177. https://doi.org/https://doi.org/10.1016/j.compstruct.2018.07.067

Kowalsky, M. J., and Wing, K. M. (2003). *Analysis of an Instrumented Jointless Bridge*. North Carolina Department of Transportation. https://books.google.com/books?id=8cokAQAAMAAJ

Mante, D. M., Isbiliroglu, L., Hofrichter, A., Barnes, R. W., & Schindler, A. K. (2022). Expected compressive strength in precast, prestressed concrete design: A methodology to analyze regional strength results. *PCI Jorunal*. https://www.pci.org/PCI_Docs/Publications/PCI%20Journal/2022/September-October/21-0027_Mante_SO22.pdf

Nawy, E. G. (2009). *Prestressed Concrete, A Fundamental Approach* (5th Edition Update ed.). Pearson.

Okeil, A. M., and El-Safty, A. (2005). Partial Continuity in Bridge Girders with Jointless Decks. *Practice Periodical on Structural Design and Construction*, *10*(4), 229-238. https://doi.org/doi:10.1061/(ASCE)1084-0680(2005)10:4(229)

Priestley, M. J. N. (1978). Design of Concrete Bridges for Temperature Gradients. *ACI Journal Proceedings*, *75*(5), 209-217. https://doi.org/10.14359/10934

Reyes, J., and Robertson, I. N. (2011). *Precast Link Slabs for Jointless Bridge Decks*.

Saber, A., and Aleti, A. R. (2012). Behavior of FRP Link Slabs in Jointless Bridge Decks. *Advances in Civil Engineering*, *2012*, 452987. https://doi.org/10.1155/2012/452987

Shafei, B., Taylor, P. C., Phares, B. M., Najimi, M., Karim, R., and Hajilar, S. (2018). Material Design and Structural Configuration of Link Slabs for ABC Applications [Tech Report]. https://rosap.ntl.bts.gov/view/dot/42746

Snedeker, K., White, D., and Kahn, L. (2011). Evaluation of Performance and Maximum Length of Continuous Decks in Bridges : Part 1 [Tech Report]. https://rosap.ntl.bts.gov/view/dot/23443

Stringer, D. J., and Burgueño, R. (2012). Identification of Causes and Solution Strategies for Deck Cracking in Jointless Bridges : Research Report [Tech Report]. https://rosap.ntl.bts.gov/view/dot/25400

TEMPSENS. (2020). *Type T Thermocouple*. https://tempsens.com/blog/type-t-thermocouple/

Thippeswamy, H. K. (1996). *Study of Jointless Bridge Behavior and Development of Design Procedures* (Publication Number 9639453) [Ph.D., West Virginia University]. ProQuest Dissertations & Theses Global. United States -- West Virginia. https://www.proquest.com/docview/304281768?accountid=8421&parentSessionId=5qxhqTLNy1CbsewsV0G75ybJK1kzcpza2YKU7FbnMFw%3D

Trados, M. K. (2016). Eliminating Expansion Joints in Bridges. *Aspire*. https://www.aspirebridge.com/magazine/2016Fall/CBT-EliminatingExpansionJoints.pdf

Ulku, E., Attanayake, U., and Aktan, H. (2009). Jointless Bridge Deck with Link Slabs: Design for Durability. *Transportation Research Record*, *2131*(1), 68-78. https://doi.org/10.3141/2131-07

Wing, K. M., and Kowalsky, M. J. (2005). Behavior, Analysis, and Design of an Instrumented Link Slab Bridge. *Journal of Bridge Engineering*, *10*(3), 331-344. https://doi.org/doi:10.1061/(ASCE)1084-0702(2005)10:3(331)

Wolde-Tinsae, A. M., Klinger, J. E., and White, E. J. (1988). Performance of Jointless Bridges. *Journal of Performance of Constructed Facilities*, *2*(2), 111-125. https://doi.org/doi:10.1061/(ASCE)0887-3828(1988)2:2(111)

Ziaei, R., Alhowaidi, Y., Sim, C., Eun, J., Kim, S., and Song, C. R. (2022). Field Monitoring of Joint-Less Curved Integral Abutment Bridge in Nebraska [Tech Report]. https://rosap.ntl.bts.gov/view/dot/67216

Appendix A: Field Inspection Reports

A.1. I-85 over Co Rd 54 (LEE-1)

<table>
<tr><td>BIN:
021511</td><td colspan="2">Project Name:
Bridge Replacements on I-85 over County Road 54 (Long St)</td><td>Skew Angle:
30°</td></tr>
<tr><td>Inspection Date:
8/9/2023</td><td>Final Concrete Pour Date:
Stage I (Center): 11/30/2021
Stage II (SB): 8/17/2022
Stage III (NB): 5/19/2023</td><td>Location:
Lee County
32°37'25.6" N,
85°23'16.6" W</td><td>Overall Length:
180’-0”
Girder Type:
Prestressed Concrete</td></tr>
<tr><td colspan="3">

Figure A-1(a): Elevation view of I-85 over Co Rd 54</td><td>Span 1:
50’-0”
AASHTO Type II
Span 2:
80’-0”
AASHTO Type II (Modified)
Span 3:
50’-0”
AASHTO Type II</td></tr>
<tr><td colspan="4">Comments/Observations:
The closed joints were constructed with a saw cut followed by joint sealer. The tooled joint shown in the plans was not utilized.
Cracking and spalling were observed [shown in Fig. A-1(e) through (i)] at the closed joints. This distress appears to result from heavy traffic wear on the center portion of the deck (Construction Stage I).
Minor transverse cracking was observed at each abutment, originating from gaps in the open joints at these locations.
The rest of the deck exhibited no other noticeable distress.</td></tr>
</table>

Figure A-1(b): Center portion of deck facing Northbound (Construction Stage I)

Figure A-1(c): Abutment expansion joint on Bent 1 (Construction Stage I)

Figure A-1(d): Closed joint at Bent 2 (Construction Stage I)

Figure A-1(e): Cracking and spalling observed on closed joint at Bent 2 (Construction Stage I)

Figure A-1(f): More spalling observed on closed joint at Bent 2 (Construction Stage I)

Figure A-1(g): Closed joint at Bent 3 (Construction Stage I)

Figure A-1(h): Cracking and spalling observed on closed joint at Bent 3 (Construction Stage I)

Figure A-1(i): Spalling observed on open joint at Bent 3 (Construction Stage I)

Figure A-1(j): Abutment open joint at Bent 4 (Construction Stage I)

Figure A-1(k): Underside of bridge (facing Northbound)

Figure A-1(l): Cracking observed on Northbound side of Bent 2

Figure A-1(m): Leakage observed on Southbound side of Bent 2

A.2. I-85 over SR-51 (LEE-2)

<table>
<tr><td>BIN:
021513</td><td colspan="2">Project Name:
Bridge Replacements on I-85 over SR-51
(Marvyn Parkway)</td><td>Skew Angle:
19°</td></tr>
<tr><td rowspan="2">Inspection Date:
8/9/2023</td><td rowspan="2">Final Concrete Pour Date:
Stage I (Center): 2/8/2022
Stage II (SB): 12/13/2022
Stage III (NB): 7/24/2023</td><td rowspan="2">Location:
Lee County
32°37'54.1" N,
85°22'20.1" W</td><td>Overall Length:
190’-0”</td></tr>
<tr><td>Girder Type:
Prestressed Concrete</td></tr>
<tr><td colspan="3">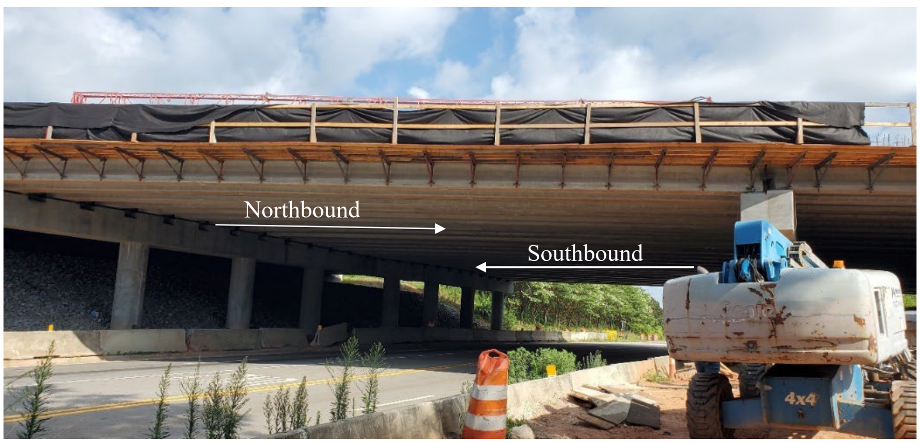

Figure A-2(a): Elevation view of I-85 over SR-51</td><td>Span 1:
55’-0”
AASHTO Type I
(Modified III)
Span 2:
80’-0”
AASHTO Type I
(Modified BT+)
Span 3:
55’-0”
AASHTO Type I
(Modified III)</td></tr>
<tr><td colspan="4">Comments/Observations:

The closed joints were constructed with a saw cut followed by joint sealer. The tooled joint shown in the plans was not utilized.
Cracking and spalling were observed [shown in Fig. A-2(b), (c), (e), and (f)] along the closed joints (continuous joints) for the center (Construction Stage I) deck placement.
Minor cracks were seen in the freshly cast deck for NB (Construction Stage III), which had been cast just over two weeks before the deck observation.
No cracking was observed on the underside of the bridge deck and no other noticeable distress was observed.
</td></tr>
</table>

Figure A-2(b): Spalling at closed joint in center stage at Bent 2 (Construction Stage I)

Figure A-2(c): Cracking at closed joint observed at Bent 2 (Construction Stage III)

Figure A-2(d): Closed joint at Bent 2 (Construction Stage III)

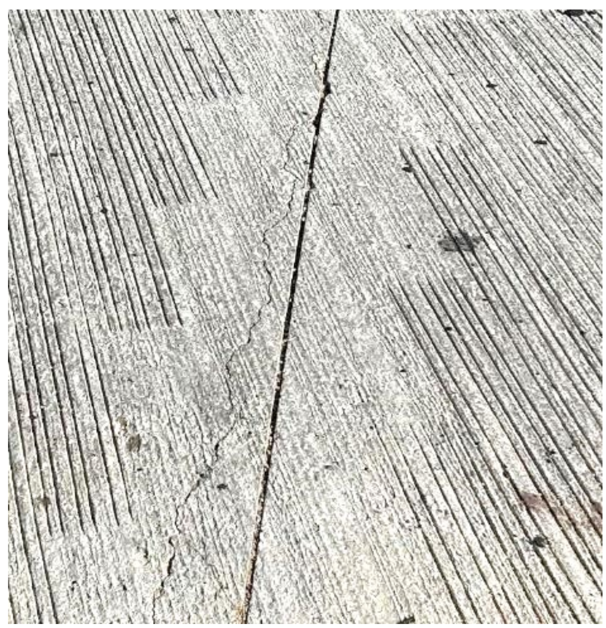

Figure A-2(e): More cracking at closed joint in center stage at Bent 3 (Construction Stage I)

Figure A-2(f): Cracking at closed joint observed at Bent 3 (Construction Stage III)

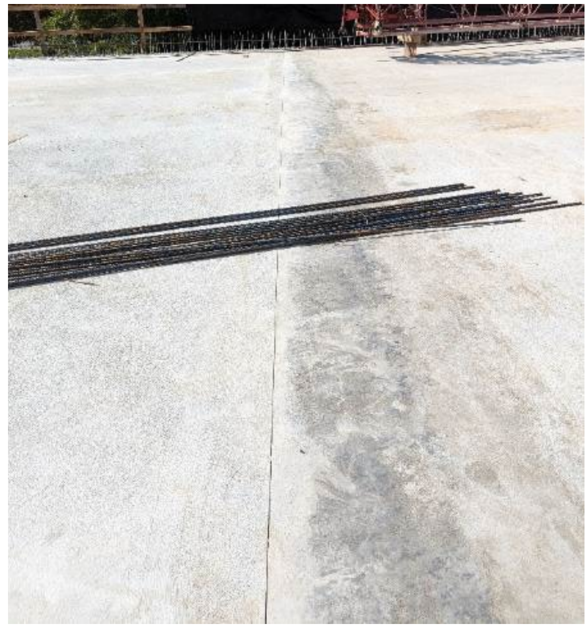

Figure A-2(g): Closed joint at Bent 3 (Construction Stage III)

Figure A-2(h): Underside of bridge at Bent 3

A.3. Co Rd 10 over I-85 (LEE-3)

<table>
<tr><td>BIN:
020356</td><td colspan="2">Project Name:
Bridge on Relocated County Road 10 (Beehive Road) over I-85</td><td>Skew Angle:
17°</td></tr>
<tr><td rowspan="2">Inspection Date:
11/28/2023</td><td rowspan="2">Construction Date:
2012
(from NBI database)</td><td rowspan="2">Location:
Lee County
32°32'51.3" N,
85°31'40.9" W</td><td>Overall Length:
280’-0”</td></tr>
<tr><td>Girder Type:
Prestressed
Concrete</td></tr>
<tr><td colspan="3">

Figure A-3(a): Elevation view of Co Rd 10 over I-85</td><td>Span 1:
140’-0”
Modified BT-54
Span 2:
140’-0”
Modified BT-54</td></tr>
<tr><td colspan="4">Comments/Observations:
• The closed joint [shown in Figures A-3(d), (e), (f), (g), and (h)] was tooled in and filled with a joint sealer as prescribed in the plans.
• Spalling was observed [shown in Figures A-3(f) and (h)] on the closed joint on the bridge deck.
• No other noticeable signs of distress were observed on the bridge deck surface.
• On the underside of the bridge, many cracks were observed [shown in Figures A-3(k) and (l)] in the full-depth edge beam under at the closed joint (continuous joint) on Bent 2 [shown in Figures A-3(k) and (l)].
• Some staining was observed [shown in Figures A-3(j) and (m)] on the sides of the closed joint.</td></tr>
</table>

Figure A-3(b): Abutment open joint at Bent 1

Figure A-3(c): Construction joint in bridge deck between Bents 1 and 2

Figure A-3(d): Closed joint at Bent 2

Figure A-3(e): Close-up of closed joint at Bent 2

Figure A-3(f): Spalling observed at closed joint on Bent 2

Figure A-3(g): Close-up of spalling observed at closed joint on Bent 2

Figure A-3(h): More spalling observed at closed joint on Bent 2

Figure A-3(i): Underside of bridge (facing Eastbound)

Figure A-3(j): Staining observed on Northside of closed joint

Figure A-3(k): Cracking in edge beam at closed joint

Figure A-3(l): Concrete breakout and staining on edge beam for Bent 2

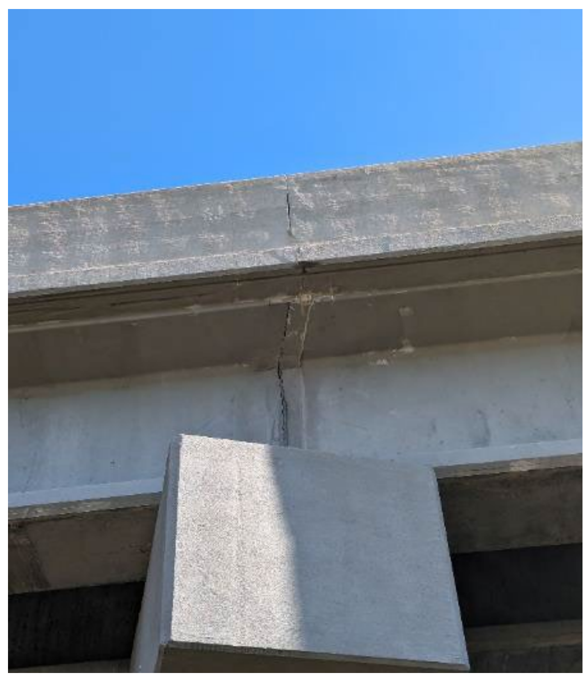

Figure A-3(m): Staining on Southside of closed joint

A.4. I-20 over Co Rd 49 (CLB-1)

<table>
<tr><td>BIN:
Left Lane: 020425
Right Lane: 020423</td><td colspan="2">Project Name:
Dual Bridge Widening on I-20 over County Road 49</td><td>Skew Angle:
15°</td></tr>
<tr><td rowspan="2">Inspection Date:
12/12/2023</td><td rowspan="2">Construction Date:
2013</td><td rowspan="2">Location:
Cleburne County
33°39’13.0” N,
85°24’49.3” W</td><td>Overall Length:
262’-10”</td></tr>
<tr><td>Girder Type:
Prestressed Concrete</td></tr>
<tr><td colspan="3">

Figure A-4(a): Elevation view of I-20 over Co Rd 49</td><td>Span 1:
81’-5”
BT-54 Bulb-Tee
Span 2:
100’-0”
BT-54 Bulb-Tee
Span 3:
81’-5”
BT-54 Bulb-Tee</td></tr>
<tr><td colspan="4">Comments/Observations:
For the inspection, the deck supported by prestressed concrete girders was not able to be accessed due to multiple lanes of heavy traffic.
The closed joint in the deck expansion was constructed purposely to not line up with the construction joint in the existing bridge.
Spalling was observed [shown in Figure A-4(c)] on the closed joint on Bent 2 but no other noticeable signs of distress were observed in the bridge deck.
Cracking and staining were observed [shown in Figures A-4(l) and (m)] on the full-depth edge beams for the closed joint on Bent 3</td></tr>
</table>

Figure A-4(b): Abutment open joint at Bent 1 (Westbound)

Figure A-4(c): Closed joint at Bent 2 (Westbound)

Figure A-4(d): Closed joint at Bent 3 (Westbound)

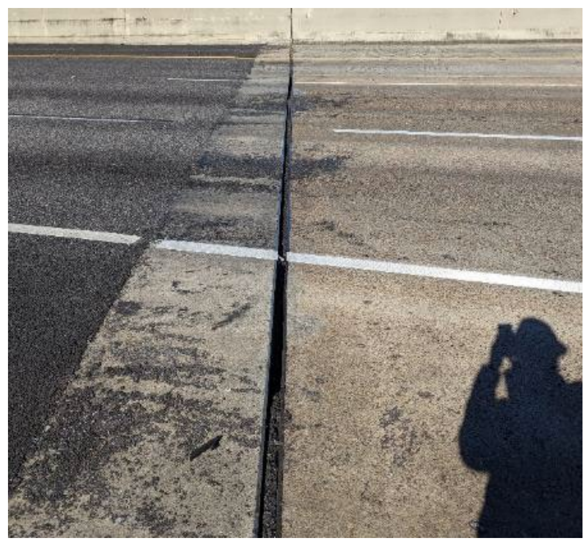

Figure A-4(e): Abutment open joint at Bent 4 (Westbound)

Figure A-4(f): Abutment open joint at Bent 1 (Eastbound)

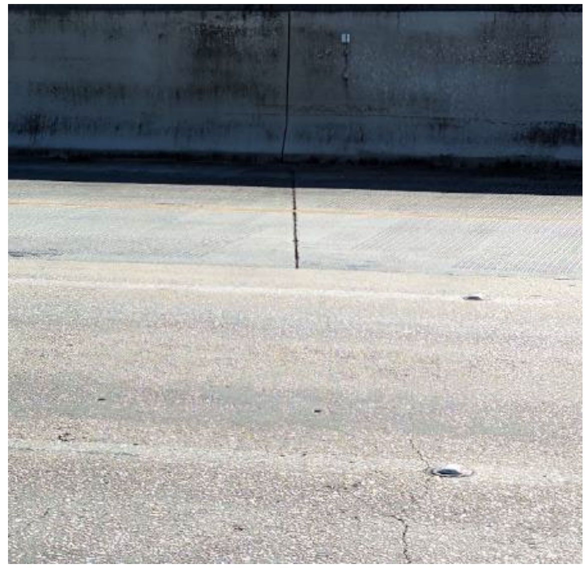

Figure A-4(g): Closed joint at Bent 2 (Eastbound)

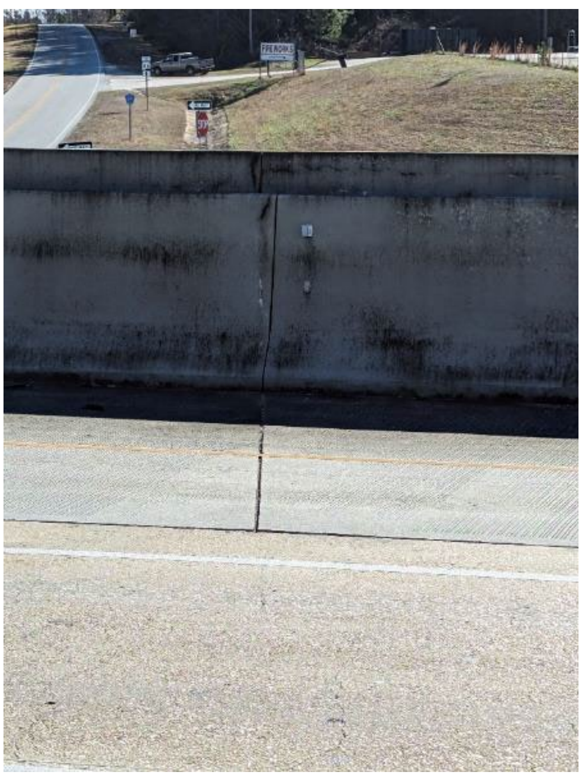

Figure A-4(h): Closed joint at Bent 3 (Eastbound)

Figure A-4(i): Abutment open joint at Bent 4 (Eastbound)

Figure A-4(j): Underside of bridge at Bent 2 (Westbound)

Figure A-4(k): Underside of bridge at Bent 2 (Eastbound)

Figure A-4(l): Edge beam at Bent 2 with cracking and staining

Figure A-4(m): Closed joint on the underside of bridge at Bent 2

Figure A-4(n): Underside of bridge at Bent 3 (Eastbound)

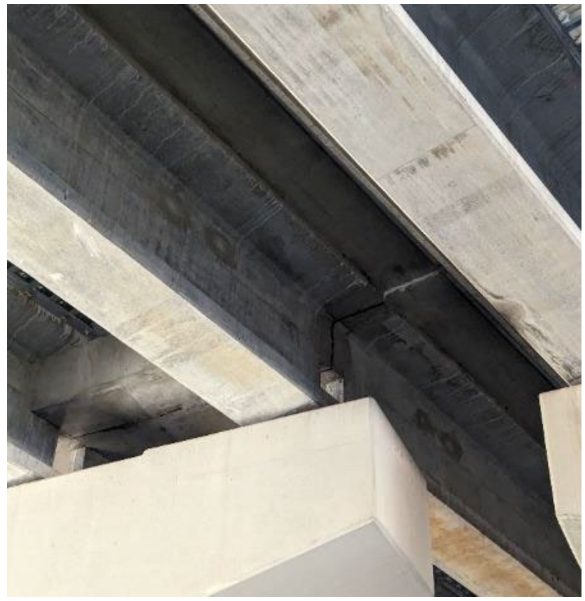

Figure A-4(o): Closed joint on the underside of bridge at Bent 3

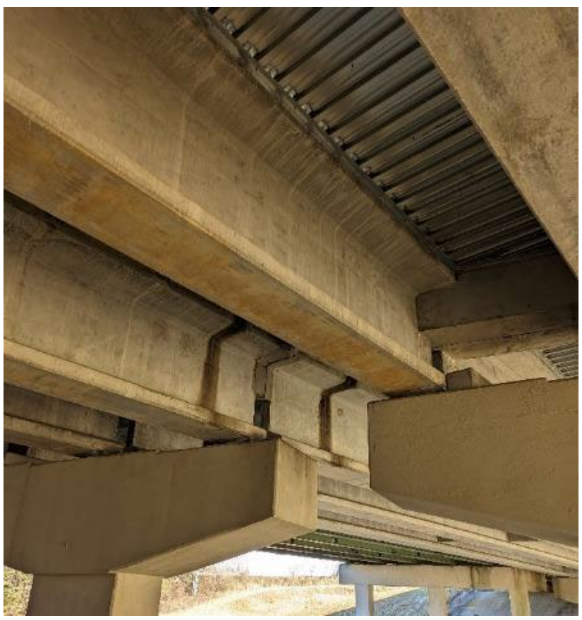

Figure A-4(p): Underside of bridge at Bent 3 (Westbound)

Figure A-4(q): Staining at closed joint edge beam at Bent 3

A.5. Co Rd 39 over I-10 (MOB-1)

<table>
<tr><td>BIN:
Left Lane: 018396
Right Lane: 018397</td><td colspan="2">Project Name:
Dual Bridges on County Road 39 over I-10 North of Bayou La Batre</td><td>Skew Angle:
2°</td></tr>
<tr><td rowspan="2">Inspection Date:
12/6/2023</td><td rowspan="2">Construction Date:
2005
(NBI Database)</td><td rowspan="2">Location:
Mobile County
30°32'14.1" N,
88°14'23.4" W</td><td>Overall Length:
440’-0”</td></tr>
<tr><td>Girder Type:
Prestressed Concrete</td></tr>
<tr><td colspan="3">
Figure A-5(a): Elevation view of Co Rd 39 over I-10</td><td>Span 1:
120’-0”
BT-63 Bulb Tee
Span 2:
100’-0”
BT-63 Bulb Tee
Span 3:
100’-0”
BT-63 Bulb Tee
Span 4:
120’-0”
BT-63 Bulb Tee</td></tr>
<tr><td colspan="4">Comments/Observations:
The inspection was completed by an ALDOT bridge inspector.
The southbound bridge was noted to have significantly more traffic than the northbound bridge.
Significant loss of concrete was observed [Figures A-5(j), (k), (l), (m), and (p)] on the edge beams on Bent 3.
Cracks were observed [shown in Figures A-5(d), (e), and (g)] around the closed joints on both northbound and southbound bridge decks.
Slight wearing was observed [shown in Figures A-5(c) and (h)] around the joint sealer for the closed joint on both southbound and northbound bridges.</td></tr>
</table>

Figure A-5(b): Closed joint at Bent 3 (Southbound)

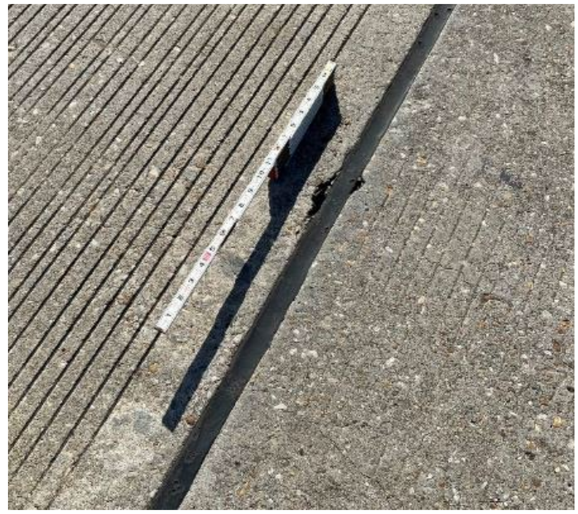

Figure A-5(c): Wearing around closed joint on Bent 3 (Southbound)

Figure A-5(d): Long hairline cracks on closed joint at Bent 3 (Southbound)

Figure A-5(e): Crack perpendicular to closed joint on Bent 3 (Southbound)

Figure A-5(f): Closed joint at Bent 3 (Northbound)

Figure A-5(g): Hairline cracks observed on closed joint at Bent 3 (Northbound)

Figure A-5(h): Wearing around sealant on closed joint at Bent 3 (Northbound)

Figure A-5(i): Underside of bridge at Bent 3 (Southbound)

Figure A-5(j): Concrete breakout on Northside of Bent 3 (Southbound)

Figure A-5(k): Close-up of concrete breakout at Bent 3 (Southbound)

Figure A-5(l): Close-up of more concrete breakout at Bent 3 (Southbound)

Figure A-5(m): Concrete breakout on Southside at Bent 3 (Southbound)

Figure A-5(n): Westside of closed joint on Bent 3 (Southbound)

Figure A-5(o): Underside of bridge at Bent 3 (Northbound)

Figure A-5(p): Concrete breakout on edge beam at Bent 3 (Northbound)

Figure A-5(q): Exposed rebar on Eastside closed joint (Northbound)

Figure A-5(r): Exposed rebar on westside closed joint (Northbound)

A.6. US-11 over Sucarnoochee River (SUM-1)

<table>
<tr><td>BIN:
017888</td><td colspan="2">Project Name:
Bridge Replacement on US-11 over Sucarnoochee River</td><td>Skew Angle:
0°</td></tr>
<tr><td rowspan="2">Inspection Date:
04/16/2024</td><td rowspan="2">Construction Date:
2003
(NBI Database)</td><td rowspan="2">Location:
Sumter County
32°34'25.3" N,
88°11'38.4" W</td><td>Overall Length:
855’-0”</td></tr>
<tr><td>Girder Type:
Prestressed Concrete</td></tr>
<tr><td colspan="3">
Figure A-6(a): Elevation view of US-11 over Sucarnoochee River</td><td>Span 1:
45’-0”
AASHTO Type I
Span 2:
80’-0”
AASHTO Type III
Span 3:
125’-0”
BT-72
Span 4 - 10:
80’-0”
AASHTO Type III
Span 11:
45’-0”
AASHTO Type I</td></tr>
<tr><td colspan="4">Comments/Observations:
The focus of the inspection was on the joints at Bents 7, 8, and 9. These joints are where the girder ends are instrumented for observation.
Small cracks running parallel to the direction of traffic were observed at all joints in similar patterns, but no other noticeable signs of distress were observed on the bridge deck. These cracks all formed about 2 ft from the side of the lane.</td></tr>
</table>

Figure A-6(b): Open joint at north abutment

Figure A-6(c): Closed joint at Bent 9

Figure A-6(d): Close-up of closed joint at Bent 9

Figure A-6(e): Crack observed on closed joint at Bent 9

Figure A-6(f): Closed joint at Bent 8

Figure A-6(g): Crack observed on closed joint at Bent 8

Figure A-6(h): Open joint at Bent 7

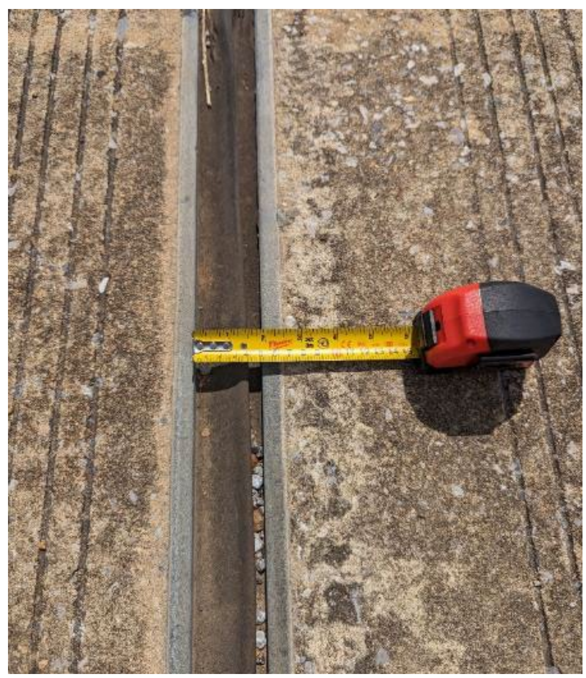

Figure A-6(i): Closeup of open joint at Bent 7

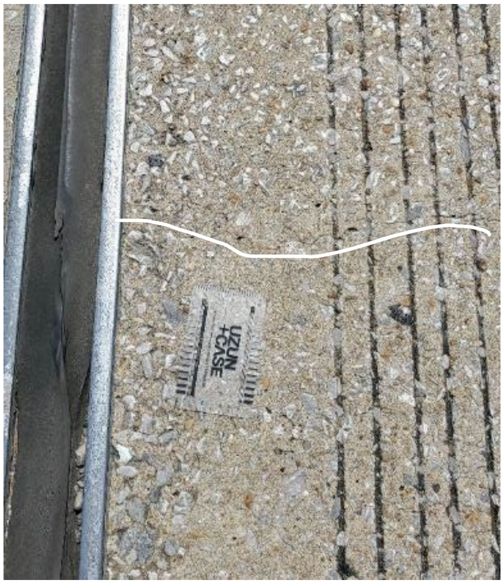

Figure A-6(j): Crack observed at open joint at Bent 7

Appendix B: Prestressed Girder Details

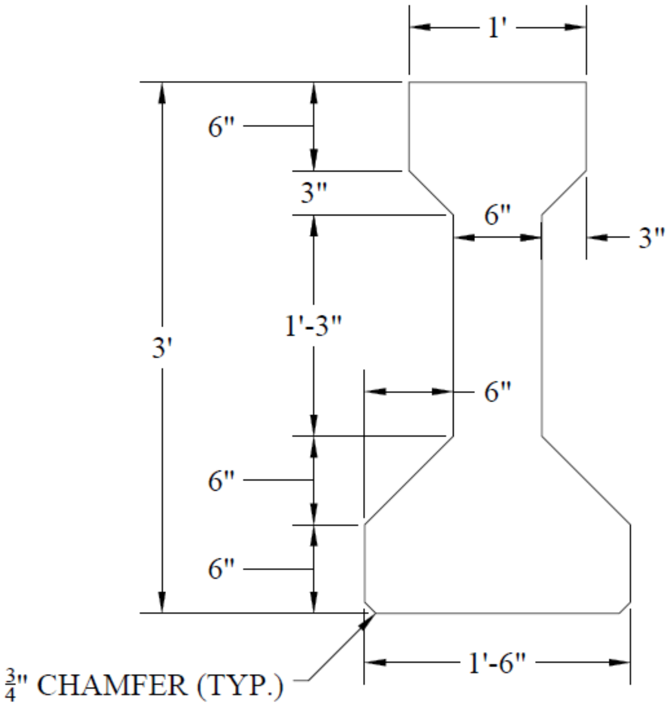

Figure B-1: AASHTO Type II Prestressed Girder (LEE-1)

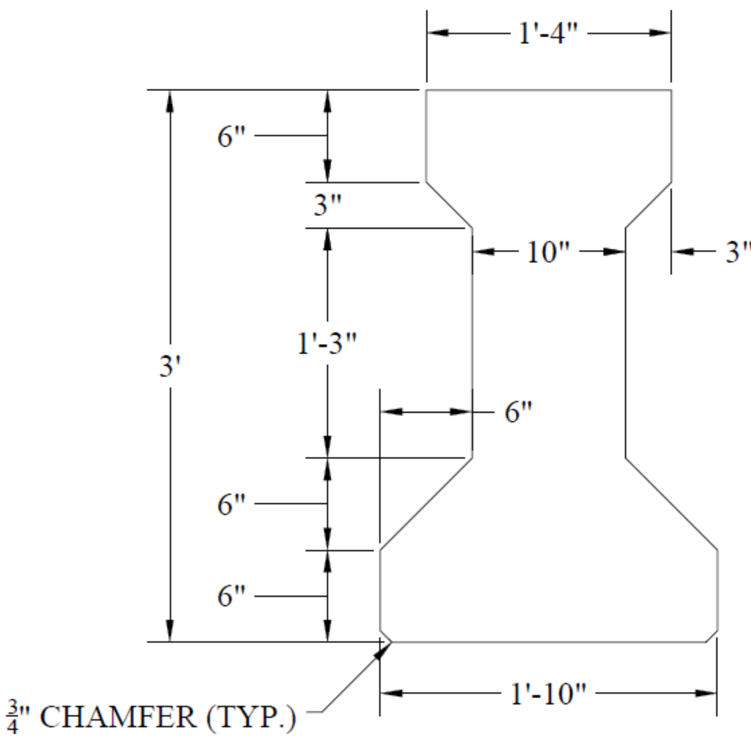

Figure B-2: AASHTO Type II Modified Prestressed Girder (LEE-1)

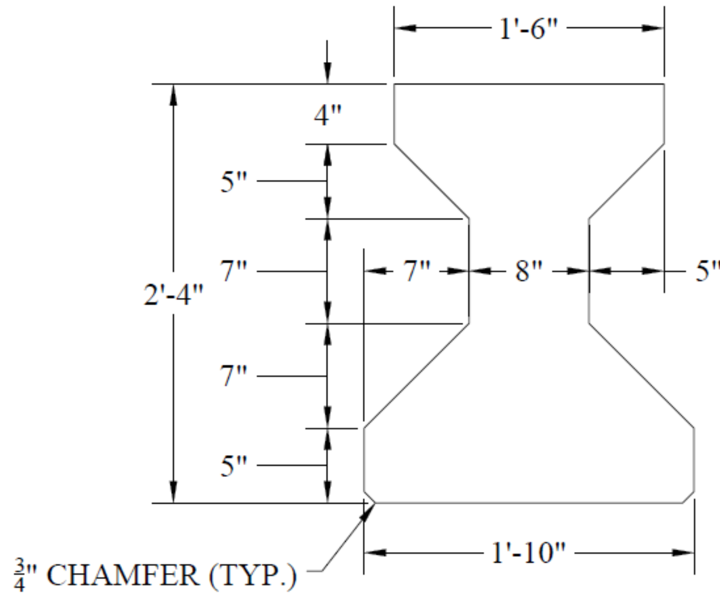

Figure B-3: AASHTO Type I Modified (III) Prestressed Girder (LEE-2)

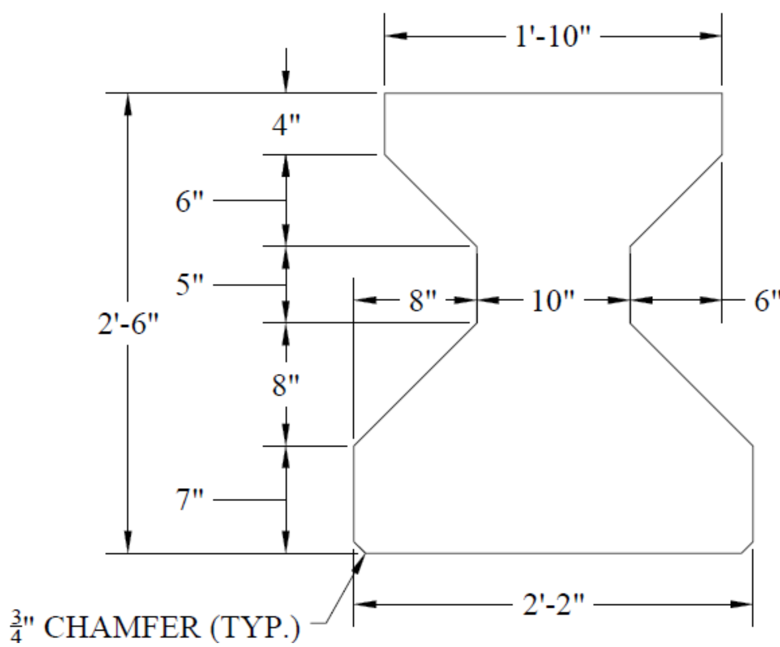

Figure B-4: AASHTO Type I Modified (BT+) Prestressed Girder (LEE-2)

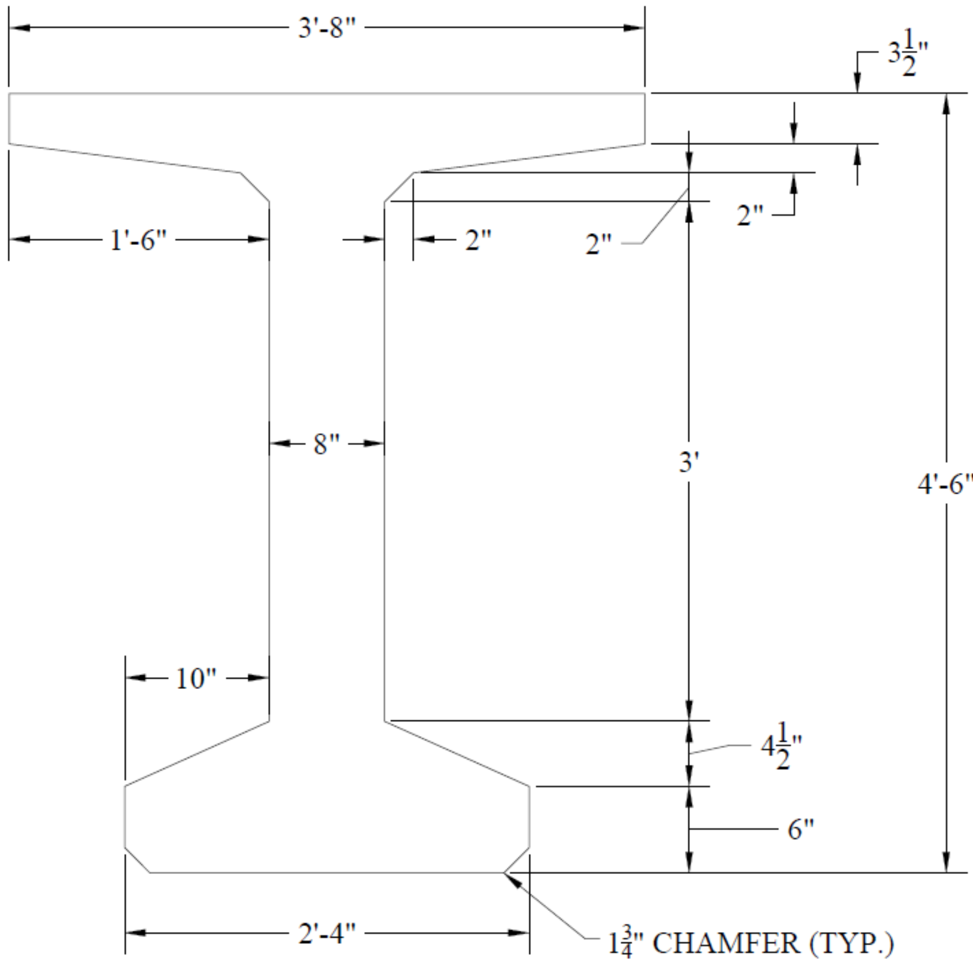

Figure B-5: Modified BT-54 Prestressed Girder (LEE-3)

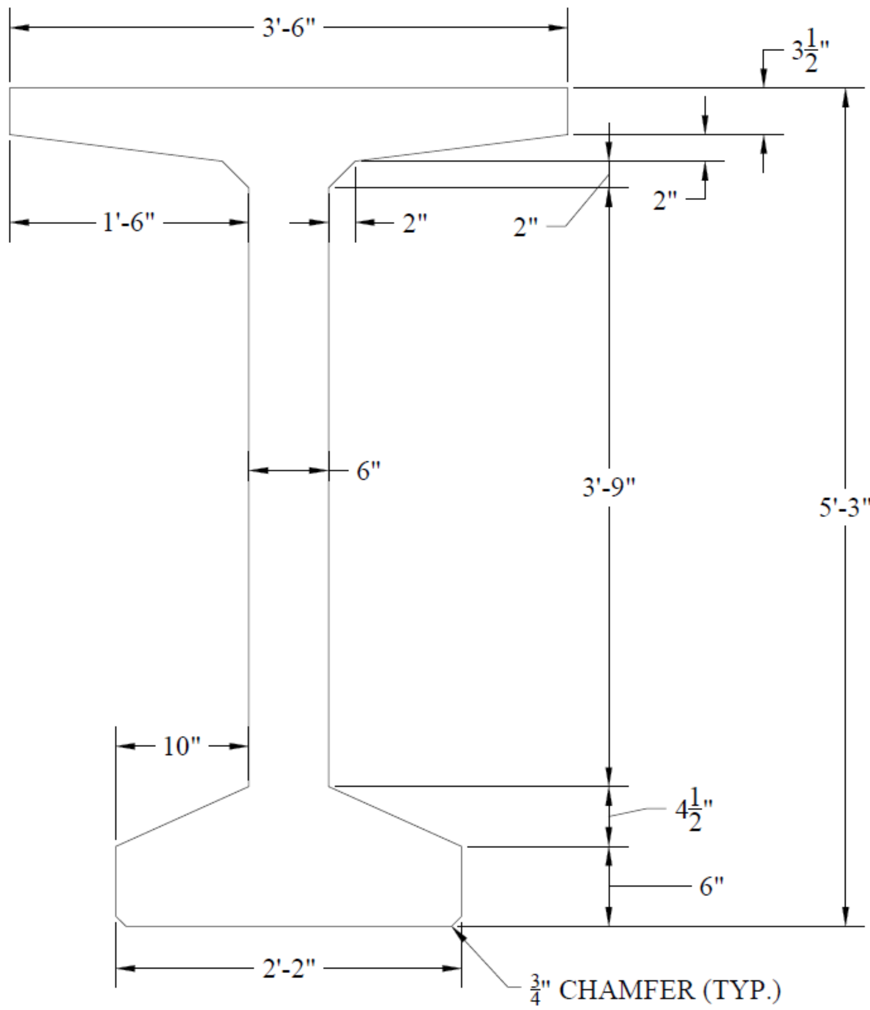

Figure B-6: Type BT-63 Prestressed Girder (MOB-1)

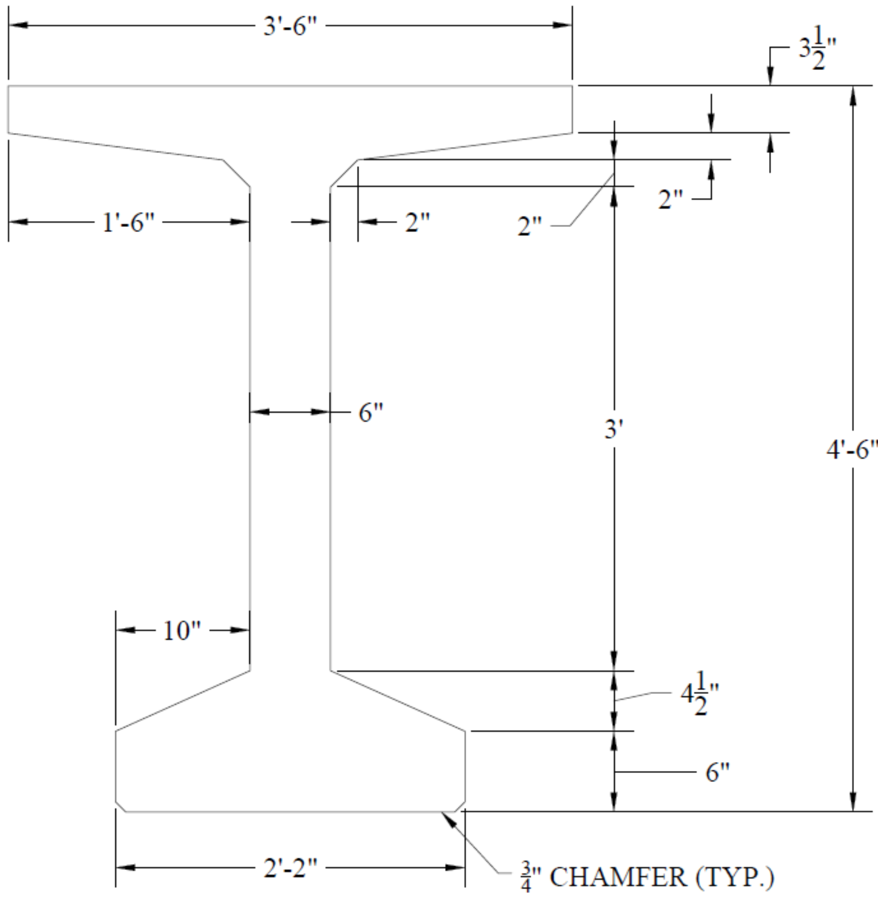

Figure B-7: Type BT-54 Prestressed Girder (CLB-1)

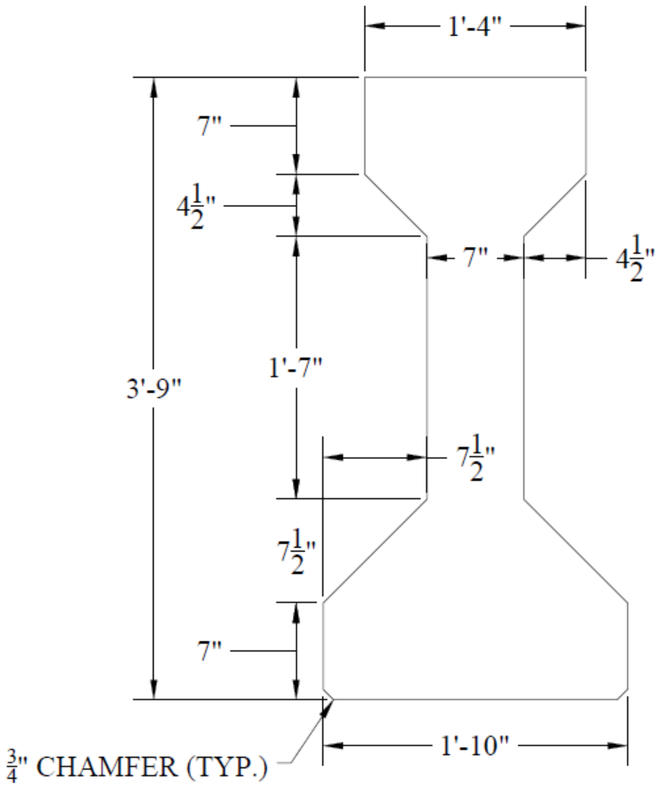

Figure B-8: AASHTO Type III Prestressed Girder (SUM-1)

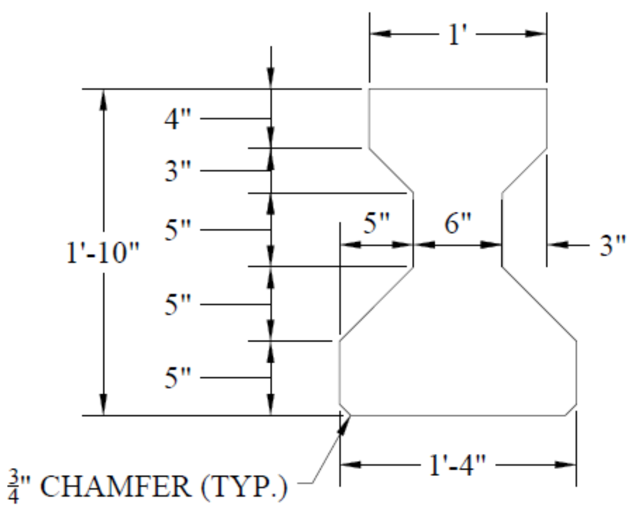

Figure B-9: AASHTO Type I Prestressed Girder (SUM-1)

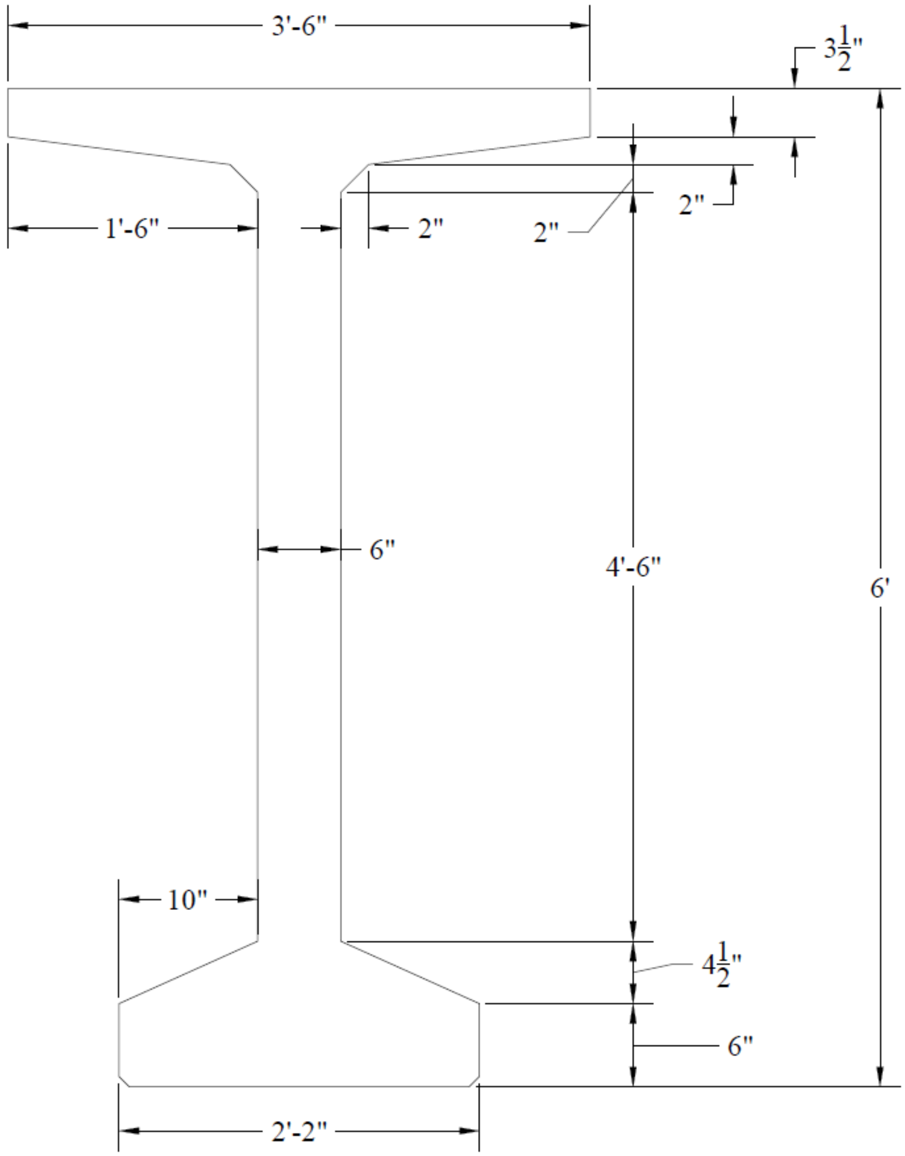

Figure B-10: Type BT-72 Prestressed Girder (SUM-1)

Appendix C: CRBasic Codes

C.1. Bent 7 Code

```
'CR6 Datalogger
'Program: US-11 over Sucarnoochee Bridge Monitoring
'Date Created: 10/17/2023
'Program Author: Brandon Lundstrum
'Sensors:
'  MEMs Tilt Sensors - 8 + 4 (4 per bent, 1 on each end of girder)
'  VW Crackmeters - 6 (2 per bent, 1 between ends of girders)
'    50 mm VW Crackmeters - 4
'    100 mm VW Crackmeters - 2
'  Thermistors - 36 (12 per bent, 3 on each end of girder)
'Data Acquisiton Instruments
'  Bent 7:
'    AM16/32B - 3
'      1 SN: 23509 (Crackmeter) (Anderson)
'      2 SN: 23511 (Thermocoupler) (Anderson)
'      3 SN: 23545 (Inclinometer) (Anderson)
'    CR6 - 1
'        SN: 22934
'  Bent 8:
'    AM16/32B - 3
'      1 SN: 27677 (Crackmeter)
'      2 SN: 27674 (Thermocoupler)
'      3 SN: 34166 (Inclinometer)
'    CR6 - 1
'        SN: 8605
'  Bent 9:
'    AM16/32B - 3
'      1 SN: 23503 (Crackmeter) (Anderson)
'      2 SN: 23510 (Thermocoupler) (Anderson)
'      3 SN: 23545 (Inclinometer) (Anderson)
'    CR6 - 1
'        SN: 8604

'Declare Constants
'for VW Temperature Calculation
  Const A = 1.4051*(10)^(-3)
  Const B = 2.369*(10)^(-4)
  Const C = 1.019*(10)^(-7)

'Declare Private Variables
'VW Crackmeters (1-2 are 100mm, 3-6 are 50mm)
  'SN:                   2305363   2305362   2317924   2317922   2317925   2317923
  'Designation:          G4-B7     G5-B7     G4-B8     G5-B8     G4-B9     G5-B9
  Dim VW_G(6) =         {.0008920, .0008782, .0004502, .0004346, .0004467, .0004455} 'in
  Dim VW_Mult(6) =      {.000398,  .000398,  .000376,  .000376,  .000376,  .000376 }
  Dim VW_B(6) =         {.0864,    .0864,    .328,     .328,     .328,     .328    }
  Dim VW_Digits0(6) =   {2367,     2367,     3599,     3244,     3415,     3391    }
  Dim VW_Temp_0(6) =    {18.53,    18.53,    18.9,     18.9,     18.9,     18.9    }
'MEMs Tilt Sensors
  'SN:                        2274283   2274285   2306833   2306834   2274286   2274281   2274
  'Designation:               G4-B7-N   G4-B7-S   G5-B7-N   G5-B7-S   G4-B8-S   G4-B8-N   G5-B

```

```
'Declare Public Variables
Public i
'Power
  Public BattInfo(4)
  Public Source, VoltIn, ChgReg, BackUp
'VW Crackmeters (2 per Bent)
  Public VW_Results(6)
  Public Freq, Amp, SNRat, NFreq, DRat, TempResist
  Public Digits, K
  Public VW_Temp(2)
  Public VW_Disp(2)
'Thermocouplers (12 per Bent)
  Public SysTemp
'  Public Temp(12)
'MEMs Tilt Sensors (4 per Bent)
  Public ErrorCode(4,4)
  Public MEM_A_Axis(4)
  Public MEM_B_Axis(4)
  Public MEM_Temp(4)

'Define Units
Units VW_Disp() = in
Units VW_Temp() = C
'Units Temp() = C
Units MEM_A_Axis() = degrees
Units MEM_B_Axis() = degrees
Units MEM_Temp() = C

'Define Data Tables
DataTable (Bent_7,1,-1) 'Set table size to # of records, or -1 to autoallocate.
   DataInterval (0,5,min,10)
   'Power
   Sample (1,Source,IEEE4,false)
   Sample (1,VoltIn,IEEE4,false)
  Sample (1,ChgReg,IEEE4,false)
  Sample (1,BackUp,IEEE4,false)
   'VW Crackmeter
   Average (1,VW_Disp(1),IEEE4,False)
   Average (1,VW_Disp(2),IEEE4,False)
   Average (1,VW_Temp(1),IEEE4,False)
   Average (1,VW_Temp(2),IEEE4,False)
   'Thermocouples
'  Average (1,Temp(1),IEEE4,False)
'  Average (1,Temp(2),IEEE4,False)
'  Average (1,Temp(3),IEEE4,False)
'  Average (1,Temp(4),IEEE4,False)
'  Average (1,Temp(5),IEEE4,False)
'  Average (1,Temp(6),IEEE4,False)
'  Average (1,Temp(7),IEEE4,False)
'  Average (1,Temp(8),IEEE4,False)
'  Average (1,Temp(9),IEEE4,False)
'  Average (1,Temp(10),IEEE4,False)
```

```
'  Average (1,Temp(11),IEEE4,False)
'  Average (1,Temp(12),IEEE4,False)
  'MEMS Tiltometers
  Average (1,MEM_A_Axis(1),IEEE4,False)
  Average (1,MEM_A_Axis(2),IEEE4,False)
  Average (1,MEM_A_Axis(3),IEEE4,False)
  Average (1,MEM_A_Axis(4),IEEE4,False)
  Average (1,MEM_B_Axis(1),IEEE4,False)
  Average (1,MEM_B_Axis(2),IEEE4,False)
  Average (1,MEM_B_Axis(3),IEEE4,False)
  Average (1,MEM_B_Axis(4),IEEE4,False)
  Average (1,MEM_Temp(1),IEEE4,False)
  Average (1,MEM_Temp(2),IEEE4,False)
  Average (1,MEM_Temp(3),IEEE4,False)
  Average (1,MEM_Temp(4),IEEE4,False)
EndTable

'Main Program per CR6
BeginProg
  SerialOpen(ComC1,115200,16,0,50,3)
  SerialOpen(ComC3,115200,0,0,0,0)
   Scan (1,min,0,0)
     'Record Power Information
     Battery(BattInfo())
       Source = BattInfo(1)
       VoltIn = BattInfo(2)
       ChgReg = BattInfo(3)
       BackUp = BattInfo(4)
    PanelTemp (SysTemp,60) 'Measure System Temperature
     SW12(SW12_1,1)
     SW12(SW12_2,1)
     'Reading Sensors
      'Crackmeter
     MuxSelect(U2,U1,20,1,1)   'Turn on Multiplexer for Crackmeters on Bent 7
      For i = 1 To 2            'Measure the (up to 2) crackmeters on Bent 7
        VibratingWire(VW_Results(),1,U7,1400,3500,1,0.01,"",60)
       Freq=VW_Results(1)
           Amp=VW_Results(2)
           SNRat=VW_Results(3)
           NFreq=VW_Results(4)
           DRat=VW_Results(5)
           TempResist=VW_Results(6)
           'Calculate digits 'Digits'
           Digits=Freq^2/1000
           'Calculate thermal coefficient 'K'
           K=((Digits*VW_Mult(i))+VW_B(i))*VW_G(i)
           'Calculate Temperature
           VW_Temp(i)=(A + B*LN(TempResist) + C*(LN(TempResist))^3)^(-1) - 273.15
           'Calculate displacement 'Disp'
           VW_Disp(i)=(Digits-VW_Digits0(i))*VW_G(i)+(VW_Temp(i)-VW_Temp_0(i))*K
           'Move to next channel on multiplexer
           PulsePort(U2,5000)
```

```
      Next i
      PortSet(U1,0)             'Turn off multiplexer

      'Thermocoupler
'      MuxSelect(U4,U3,20,1,1) 'Turn on Multiplexer for Thermocouplers on Bent 7
'      For i = 1 To 12          'Measure the (up to 12) thermocouplers on Bent 7
'        TCDiff (Temp(i),1,mV200C,U11,TypeT,SysTemp,False,0,60,1.0,0)
'        Delay(0,0.5,Sec)
'        PulsePort (U4,5000)     'Move to next channel on multiplexer
'      Next i
'      PortSet(U3,0)             'Turn off multiplexer

       'Inclinometer
     MuxSelect(U6,U5,20,1,1)   'Turn on Multiplexer for Inclinometers on Bent 7
      For i = 1 To 4            'Measure the (up to 4) inclinometers on Bent 7
        'Begin communication with inclinometer
        ModbusClient(ErrorCode(1,i),ComC1,115200,1,06,1,&H119,1,2,10,1)
        'Recieving the information about the angle in A and B axises
        ModbusClient(ErrorCode(2,i),ComC1,115200,1,03,MEM_A_Axis(i),&H101,1,10,5,0)
        ModbusClient(ErrorCode(3,i),ComC1,115200,1,03,MEM_B_Axis(i),&H103,1,3,10,0)
        'Receiving the information about the temperature
        ModbusClient(ErrorCode(4,i),ComC1,115200,1,03,MEM_Temp(i),&H107,1,2,10,0)
        PulsePort(U6,5000)      'Move to next channel on multiplexer
      Next i
      PortSet(U5,0)             'Turn off multiplexer
    'Call Output Tables
       CallTable Bent_7
   NextScan
EndProg
```

C.2. Bent 8 Code

```
'CR6 Datalogger
'Program: US-11 over Sucarnoochee Bridge Monitoring
'Date Created: 10/17/2023
'Program Author: Brandon Lundstrum
'Sensors:
'  MEMs Tilt Sensors - 8 + 4 (4 per bent, 1 on each end of girder)
'  VW Crackmeters - 6 (2 per bent, 1 between ends of girders)
'    50 mm VW Crackmeters - 4
'    100 mm VW Crackmeters - 2
'  Thermistors - 36 (12 per bent, 3 on each end of girder)
'Data Acquisiton Instruments
'  Bent 7:
'    AM16/32B - 3
'      1 SN: 23509 (Crackmeter) (Anderson)
'      2 SN: 23511 (Thermocoupler) (Anderson)
'      3 SN: 23545 (Inclinometer) (Anderson)
'    CR6 - 1
'        SN: 22934
'  Bent 8:
'    AM16/32B - 3
'      1 SN: 27677 (Crackmeter)
'      2 SN: 27674 (Thermocoupler)
'      3 SN: 34166 (Inclinometer)
'    CR6 - 1
'        SN: 8605
'  Bent 9:
'    AM16/32B - 3
'      1 SN: 23503 (Crackmeter) (Anderson)
'      2 SN: 23510 (Thermocoupler) (Anderson)
'      3 SN: 23545 (Inclinometer) (Anderson)
'    CR6 - 1
'        SN: 8604

'Declare Constants
'for VW Temperature Calculation
  Const A = 1.4051*(10)^(-3)
  Const B = 2.369*(10)^(-4)
  Const C = 1.019*(10)^(-7)

'Declare Private Variables
'VW Crackmeters (1-2 are 100mm, 3-6 are 50mm)
  'SN:                   2305363   2305362   2317924   2317922   2317925   2317923
  'Designation:          G4-B7     G5-B7     G4-B8     G5-B8     G4-B9     G5-B9
  Dim VW_G(6) =         {.0008920, .0008782, .0004502, .0004346, .0004467, .0004455} 'in
  Dim VW_Mult(6) =      {.000398,  .000398,  .000376,  .000376,  .000376,  .000376 }
  Dim VW_B(6) =         {.0864,    .0864,    .328,     .328,     .328,     .328    }
  Dim VW_Digits0(6) =   {2978,     3147,     2311,     2200,     3415,     3391    }
  Dim VW_Temp_0(6) =    {18.9,     18.9,     18.38,    17.92,    18.9,     18.9    }
'MEMs Tilt Sensors
  'SN:                        2274283  2274285  2306833  2306834  2274286  2274281  2274
  'Designation:               G4-B7-N  G4-B7-S  G5-B7-N  G5-B7-S  G4-B8-S  G4-B8-N  G5-B

```

```
'Declare Public Variables
Public i
Public Bent7_ComResult
'Power
  Public BattInfo(4)
  Public Source, VoltIn, ChgReg, BackUp
'VW Crackmeters
  Public VW_Results(6)
  Public Freq, Amp, SNRat, NFreq, DRat, TempResist
  Public Digits, K
  Public VW_Temp(2)
  Public VW_Disp(2)
'Thermocouplers
  Public SysTemp
  Public Temp(12)
'MEMs Tilt Sensors
  Public ErrorCode(4,4)
  Public MEM_A_Axis(4)
  Public MEM_B_Axis(4)
  Public MEM_Temp(4)

'Define Units
Units Source, VoltIn, ChgReg, BackUp = V
Units VW_Disp() = in
Units VW_Temp(), Temp(), MEM_Temp = C
Units MEM_A_Axis(), MEM_B_Axis() = degrees

'Define Data Tables
DataTable (Bent_7,1,-1) 'Set table size to # of records, or -1 to autoallocate.
   DataInterval (0,5,min,10)
   'Power
   Sample (1,Source,IEEE4,false)
   Sample (1,VoltIn,IEEE4,false)
  Sample (1,ChgReg,IEEE4,false)
  Sample (1,BackUp,IEEE4,false)
   'VW Crackmeter
   Average (1,VW_Disp(1),IEEE4,False)
   Average (1,VW_Disp(2),IEEE4,False)
   Average (1,VW_Temp(1),IEEE4,False)
   Average (1,VW_Temp(2),IEEE4,False)
   'Thermocouples
'  Average (1,Temp(1),IEEE4,False)
'  Average (1,Temp(2),IEEE4,False)
'  Average (1,Temp(3),IEEE4,False)
'  Average (1,Temp(4),IEEE4,False)
'  Average (1,Temp(5),IEEE4,False)
'  Average (1,Temp(6),IEEE4,False)
'  Average (1,Temp(7),IEEE4,False)
'  Average (1,Temp(8),IEEE4,False)
'  Average (1,Temp(9),IEEE4,False)
'  Average (1,Temp(10),IEEE4,False)
'  Average (1,Temp(11),IEEE4,False)
```

```
'  Average (1,Temp(12),IEEE4,False)
  'MEMS Tiltometers
  Average (1,MEM_A_Axis(1),IEEE4,False)
  Average (1,MEM_A_Axis(2),IEEE4,False)
  Average (1,MEM_A_Axis(3),IEEE4,False)
  Average (1,MEM_A_Axis(4),IEEE4,False)
  Average (1,MEM_B_Axis(1),IEEE4,False)
  Average (1,MEM_B_Axis(2),IEEE4,False)
  Average (1,MEM_B_Axis(3),IEEE4,False)
  Average (1,MEM_B_Axis(4),IEEE4,False)
  Average (1,MEM_Temp(1),IEEE4,False)
  Average (1,MEM_Temp(2),IEEE4,False)
  Average (1,MEM_Temp(3),IEEE4,False)
  Average (1,MEM_Temp(4),IEEE4,False)
EndTable

DataTable (Bent_8,1,-1) 'Set table size to # of records, or -1 to autoallocate.
   DataInterval (0,5,min,10)
  'Power
   Sample (1,Source,IEEE4,false)
   Sample (1,VoltIn,IEEE4,false)
  Sample (1,ChgReg,IEEE4,false)
  Sample (1,BackUp,IEEE4,false)
   'VW Crackmeter
   Average (1,VW_Disp(1),IEEE4,False)
   Average (1,VW_Disp(2),IEEE4,False)
   Average (1,VW_Temp(1),IEEE4,False)
   Average (1,VW_Temp(2),IEEE4,False)
   'Thermocouples
  Average (1,Temp(1),IEEE4,False)
  Average (1,Temp(2),IEEE4,False)
  Average (1,Temp(3),IEEE4,False)
  Average (1,Temp(4),IEEE4,False)
  Average (1,Temp(5),IEEE4,False)
  Average (1,Temp(6),IEEE4,False)
  Average (1,Temp(7),IEEE4,False)
  Average (1,Temp(8),IEEE4,False)
  Average (1,Temp(9),IEEE4,False)
  Average (1,Temp(10),IEEE4,False)
  Average (1,Temp(11),IEEE4,False)
  Average (1,Temp(12),IEEE4,False)
  'MEMS Tiltometers
  Average (1,MEM_A_Axis(1),IEEE4,False)
  Average (1,MEM_A_Axis(2),IEEE4,False)
  Average (1,MEM_A_Axis(3),IEEE4,False)
  Average (1,MEM_A_Axis(4),IEEE4,False)
  Average (1,MEM_B_Axis(1),IEEE4,False)
  Average (1,MEM_B_Axis(2),IEEE4,False)
  Average (1,MEM_B_Axis(3),IEEE4,False)
  Average (1,MEM_B_Axis(4),IEEE4,False)
  Average (1,MEM_Temp(1),IEEE4,False)
  Average (1,MEM_Temp(2),IEEE4,False)
```

```
  Average (1,MEM_Temp(3),IEEE4,False)
  Average (1,MEM_Temp(4),IEEE4,False)
EndTable

'Main Program per CR6
BeginProg
  SerialOpen(ComC1,115200,16,0,50,3)
  SerialOpen(ComC3,115200,0,0,0,0)
  Scan (1,min,0,0)
    'Record Power Information
     Battery(BattInfo())
       Source = BattInfo(1)
       VoltIn = BattInfo(2)
       ChgReg = BattInfo(3)
       BackUp = BattInfo(4)
     PanelTemp (SysTemp,60) 'Measure System Temperature
     SW12(SW12_1,1)
     SW12(SW12_2,1)
     'Reading Sensors
      'Crackmeter
     MuxSelect(U2,U1,20,1,1)  'Turn on Multiplexer for Crackmeters on Bent 7
      For i = 1 To 2           'Measure the (up to 2) crackmeters on Bent 7
        VibratingWire(VW_Results(),1,U7,1400,3500,1,0.01,"",60)
       Freq=VW_Results(1)
           Amp=VW_Results(2)
           SNRat=VW_Results(3)
           NFreq=VW_Results(4)
           DRat=VW_Results(5)
           TempResist=VW_Results(6)
           'Calculate digits 'Digits'
           Digits=Freq^2/1000
           'Calculate thermal coefficient 'K'
           K=((Digits*VW_Mult(i+2))+VW_B(i+2))*VW_G(i+2)
           'Calculate Temperature
           VW_Temp(i)=(A + B*LN(TempResist) + C*(LN(TempResist))^3)^(-1) - 273.15
        'Calculate displacement 'Disp'
           VW_Disp(i)=(Digits-VW_Digits0(i+2))*VW_G(i+2)+(VW_Temp(i)-VW_Temp_0(i+2))*K
           'Move to next channel on multiplexer
           PulsePort(U2,5000)
      Next i
      PortSet(U1,0)            'Turn off multiplexer

      'Thermocoupler
      MuxSelect(U4,U3,20,1,1) 'Turn on Multiplexer for Thermocouplers on Bent 7
      For i = 1 To 12          'Measure the (up to 12) thermocouplers on Bent 7
        TCDiff (Temp(i),1,mV200C,U11,TypeT,SysTemp,False,0,60,1.0,0)
        Delay(0,0.5,Sec)
        PulsePort (U4,5000)     'Move to next channel on multiplexer
      Next i
      PortSet(U3,0)            'Turn off multiplexer

       'Inclinometer
```

```
    MuxSelect(U6,U5,20,1,1)  'Turn on Multiplexer for Inclinometers on Bent 7
     For i = 1 To 4           'Measure the (up to 4) inclinometers on Bent 7
       'Begin communication with inclinometer
       ModbusClient(ErrorCode(1),ComC1,115200,1,06,1,&H119,1,2,10,1)
       'Recieving the information about the angle in A and B axises
       ModbusClient(ErrorCode(2),ComC1,115200,1,03,MEM_A_Axis(i),&H101,1,10,5,0)
       ModbusClient(ErrorCode(3),ComC1,115200,1,03,MEM_B_Axis(i),&H103,1,3,10,0)
       'Receiving the information about the temperature
       ModbusClient(ErrorCode(4),ComC1,115200,1,03,MEM_Temp(i),&H107,1,2,10,0)
       PulsePort(U6,5000)      'Move to next channel on multiplexer
     Next i
     PortSet(U5,0)            'Turn off multiplexer
   'Call Output Tables
      CallTable Bent_8

      If TimeIntoInterval (0,5,Min) Then
     GetDataRecord(Bent7_ComResult,ComC3,0,3,000,10,10,32769,Bent_7)
   EndIf

  NextScan
EndProg
```

C.3. Bent 9 Code

```
'CR6 Datalogger
'Program: US-11 over Sucarnoochee Bridge Monitoring
'Date Created: 10/17/2023
'Program Author: Brandon Lundstrum
'Sensors:
'  MEMs Tilt Sensors - 8 + 4 (4 per bent, 1 on each end of girder)
'  VW Crackmeters - 6 (2 per bent, 1 between ends of girders)
'    50 mm VW Crackmeters - 4
'    100 mm VW Crackmeters - 2
'  Thermistors - 36 (12 per bent, 3 on each end of girder)
'Data Acquisiton Instruments
'  Bent 7:
'    AM16/32B - 3
'      1 SN: 23509 (Crackmeter) (Anderson)
'      2 SN: 23511 (Thermocoupler) (Anderson)
'      3 SN: 23545 (Inclinometer) (Anderson)
'    CR6 - 1
'        SN: 22934
'  Bent 8:
'    AM16/32B - 3
'      1 SN: 27677 (Crackmeter)
'      2 SN: 27674 (Thermocoupler)
'      3 SN: 34166 (Inclinometer)
'    CR6 - 1
'        SN: 8605
'  Bent 9:
'    AM16/32B - 3
'      1 SN: 23503 (Crackmeter) (Anderson)
'      2 SN: 23510 (Thermocoupler) (Anderson)
'      3 SN: 23545 (Inclinometer) (Anderson)
'    CR6 - 1
'        SN: 8604

'Declare Constants
'for VW Temperature Calculation
  Const A = 1.4051*(10)^(-3)
  Const B = 2.369*(10)^(-4)
  Const C = 1.019*(10)^(-7)

'Declare Private Variables
'VW Crackmeters (1-2 are 100mm, 3-6 are 50mm)
  'SN:                  2305363   2305362   2317924   2317922   2317925   2317923
  'Designation:         G4-B7     G5-B7     G4-B8     G5-B8     G4-B9     G5-B9
  Dim VW_G(6) =        {.0008920, .0008782, .0004502, .0004346, .0004467, .0004455} 'in
  Dim VW_Mult(6) =     {.000398,  .000398,  .000376,  .000376,  .000376,  .000376 }
  Dim VW_B(6) =        {.0864,    .0864,    .328,     .328,     .328,     .328    }
  Dim VW_Digits0(6) =  {2978,     3147,     3599,     3244,     2145,     2195    }
  Dim VW_Temp_0(6) =   {18.9,     18.9,     18.9,     18.9,     18.18,     18.36    }
'MEMs Tilt Sensors
  'SN:                       2274283  2274285  2306833  2306834  2274286  2274281  2274
  'Designation:              G4-B7-N  G4-B7-S  G5-B7-N  G5-B7-S  G4-B8-S  G4-B8-N  G5-B

```

```
'Declare Public Variables
Public i
'Power
  Public BattInfo(4)
  Public Source, VoltIn, ChgReg, BackUp
'VW Crackmeters
  Public VW_Results(6)
  Public Freq, Amp, SNRat, NFreq, DRat, TempResist
  Public Digits, K
  Public VW_Temp(2)
  Public VW_Disp(2)
'Thermocouplers
  Public SysTemp
'  Public Temp(12)
'MEMs Tilt Sensors
  Public ErrorCode(4,4)
  Public MEM_A_Axis(4)
  Public MEM_B_Axis(4)
  Public MEM_Temp(4)

'Define Units
Units Source, VoltIn, ChgReg, BackUp = V
Units VW_Disp() = in
Units VW_Temp(), MEM_Temp = C
Units MEM_A_Axis(), MEM_B_Axis() = degrees

'Define Data Tables
DataTable (Bent_9,1,-1) 'Set table size to # of records, or -1 to autoallocate.
   DataInterval (0,1,min,10)
   'Power
   Sample (1,Source,IEEE4,false)
   Sample (1,VoltIn,IEEE4,false)
  Sample (1,ChgReg,IEEE4,false)
  Sample (1,BackUp,IEEE4,false)
   'VW Crackmeter
   Average (1,VW_Disp(1),IEEE4,False)
   Average (1,VW_Disp(2),IEEE4,False)
   Average (1,VW_Temp(1),IEEE4,False)
   Average (1,VW_Temp(2),IEEE4,False)
   'Thermocouples
'  Average (1,Temp(1),IEEE4,False)
'  Average (1,Temp(2),IEEE4,False)
'  Average (1,Temp(3),IEEE4,False)
'  Average (1,Temp(4),IEEE4,False)
'  Average (1,Temp(5),IEEE4,False)
'  Average (1,Temp(6),IEEE4,False)
'  Average (1,Temp(7),IEEE4,False)
'  Average (1,Temp(8),IEEE4,False)
'  Average (1,Temp(9),IEEE4,False)
'  Average (1,Temp(10),IEEE4,False)
'  Average (1,Temp(11),IEEE4,False)
'  Average (1,Temp(12),IEEE4,False)
```

```
  'MEMS Tiltometers
  Average (1,MEM_A_Axis(1),IEEE4,False)
  Average (1,MEM_A_Axis(2),IEEE4,False)
  Average (1,MEM_A_Axis(3),IEEE4,False)
  Average (1,MEM_A_Axis(4),IEEE4,False)
  Average (1,MEM_B_Axis(1),IEEE4,False)
  Average (1,MEM_B_Axis(2),IEEE4,False)
  Average (1,MEM_B_Axis(3),IEEE4,False)
  Average (1,MEM_B_Axis(4),IEEE4,False)
  Average (1,MEM_Temp(1),IEEE4,False)
  Average (1,MEM_Temp(2),IEEE4,False)
  Average (1,MEM_Temp(3),IEEE4,False)
  Average (1,MEM_Temp(4),IEEE4,False)
EndTable

'Main Program per CR6
BeginProg
  SerialOpen(ComC1,115200,16,0,50,3)
  SerialOpen(ComC3,115200,0,0,0)
   Scan (1,min,0,0)
     'Record Power Information
     Battery(BattInfo())
       Source = BattInfo(1)
       VoltIn = BattInfo(2)
       ChgReg = BattInfo(3)
       BackUp = BattInfo(4)
     PanelTemp (SysTemp,60) 'Measure System Temperature
     SW12(SW12_1,1)
     SW12(SW12_2,1)
     'Reading Sensors
      'Crackmeter
     MuxSelect(U4,U3,20,1,1)  'Turn on Multiplexer for Crackmeters on Bent 7
      For i = 1 To 2           'Measure the (up to 2) crackmeters on Bent 7
        VibratingWire(VW_Results(),1,U7,1400,3500,1,0.01,"",60)
       Freq=VW_Results(1)
           Amp=VW_Results(2)
           SNRat=VW_Results(3)
           NFreq=VW_Results(4)
           DRat=VW_Results(5)
           TempResist=VW_Results(6)
           'Calculate digits 'Digits'
           Digits=Freq^2/1000
           'Calculate thermal coefficient 'K'
           K=((Digits*VW_Mult(i+4))+VW_B(i+4))*VW_G(i+4)
           'Calculate Temperature
           VW_Temp(i)=(A + B*LN(TempResist) + C*(LN(TempResist))^3)^(-1) - 273.15
           'Calculate displacement 'Disp'
           VW_Disp(i)=(Digits-VW_Digits0(i+4))*VW_G(i+4)+(VW_Temp(i)-VW_Temp_0(i+4))*K
           'Move to next channel on multiplexer
           PulsePort(U4,5000)
      Next i
      PortSet(U3,0)            'Turn off multiplexer
```

```

'       'Thermocoupler
'       MuxSelect(U4,U3,20,1,1) 'Turn on Multiplexer for Thermocouplers on Bent 7
'       For i = 1 To 12         'Measure the (up to 12) thermocouplers on Bent 7
'         TCDiff (Temp(i),1,mV200C,U11,TypeT,SysTemp,False,0,60,1.0,0)
'         Delay(0,0.5,Sec)
'         PulsePort (U4,5000)      'Move to next channel on multiplexer
'       Next i
'       PortSet(U3,0)            'Turn off multiplexer

        'Inclinometer
      MuxSelect(U6,U5,20,1,1)  'Turn on Multiplexer for Inclinometers on Bent 7
       For i = 1 To 4           'Measure the (up to 4) inclinometers on Bent 7
         'Begin communication with inclinometer
         ModbusClient(ErrorCode(1,i),ComC1,115200,1,06,1,&H119,1,2,10,1)
         'Recieving the information about the angle in A and B axises
         ModbusClient(ErrorCode(2,i),ComC1,115200,1,03,MEM_A_Axis(i),&H101,1,10,5,0)
         ModbusClient(ErrorCode(3,i),ComC1,115200,1,03,MEM_B_Axis(i),&H103,1,3,10,0)
         'Receiving the information about the temperature
         ModbusClient(ErrorCode(4,i),ComC1,115200,1,03,MEM_Temp(i),&H107,1,2,10,0)
         PulsePort(U6,5000)      'Move to next channel on multiplexer
       Next i
       PortSet(U5,0)            'Turn off multiplexer

     'Call Output Tables
        CallTable Bent_9
    NextScan
EndProg

```

Appendix D: Monthly Graphs

D.1. Girder Rotations

D.1.1. Single End Rotations

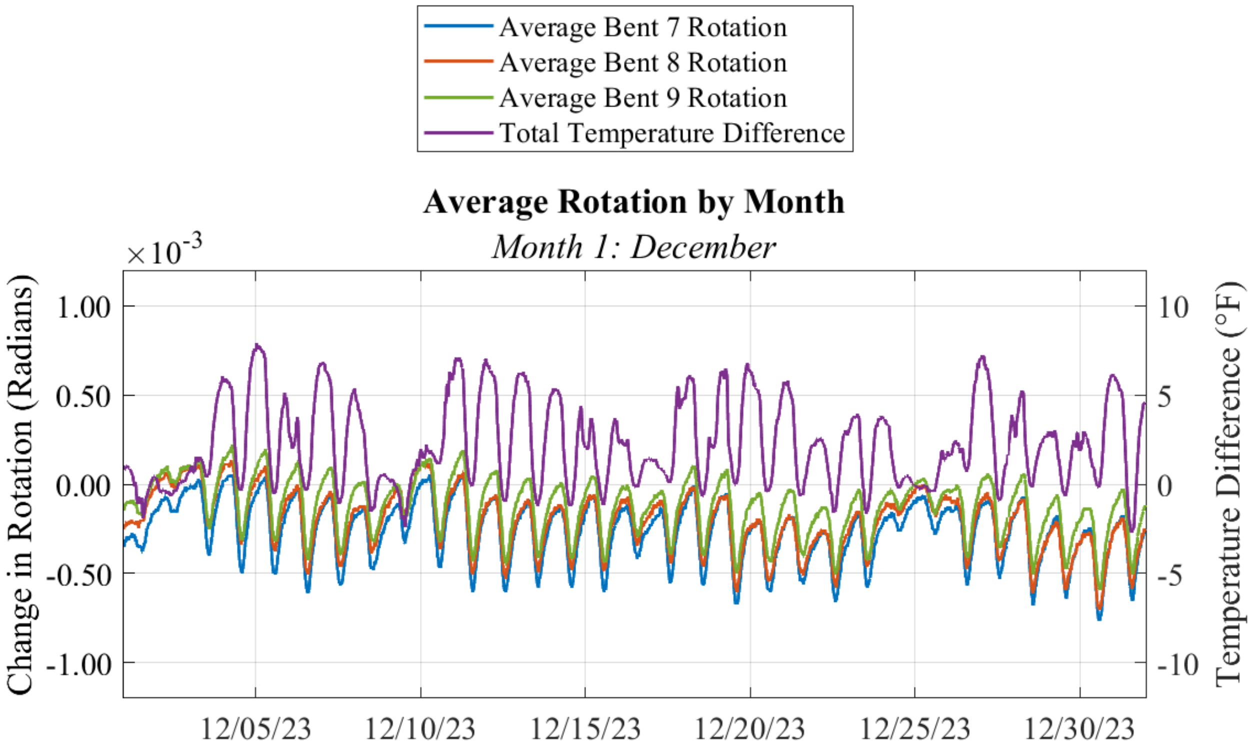

Figure D-1: Average rotation and temperature during December 2023

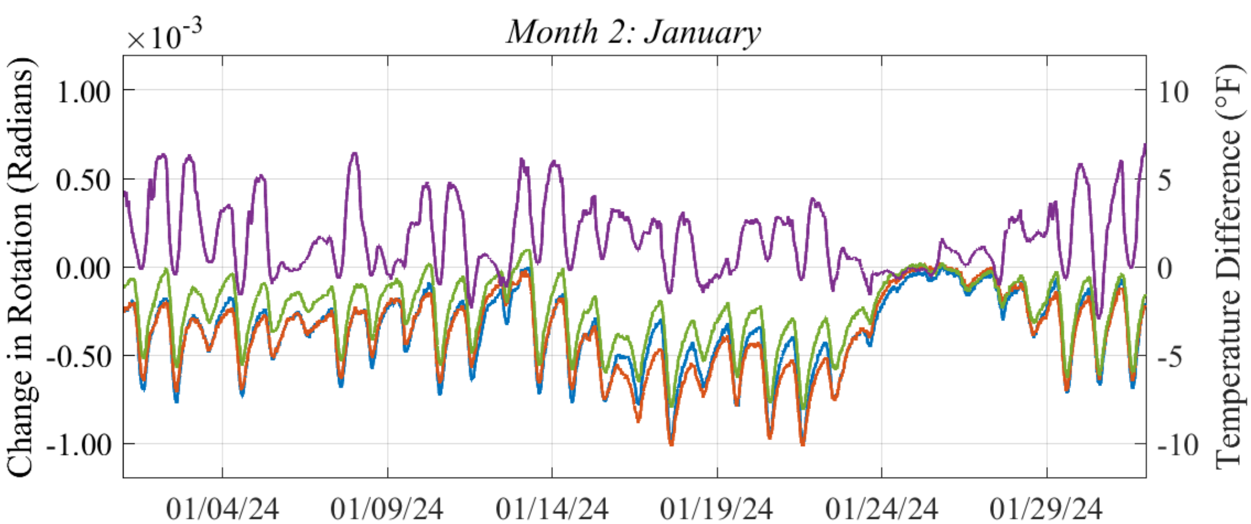

Figure D-2: Average rotation and temperature during January 2024

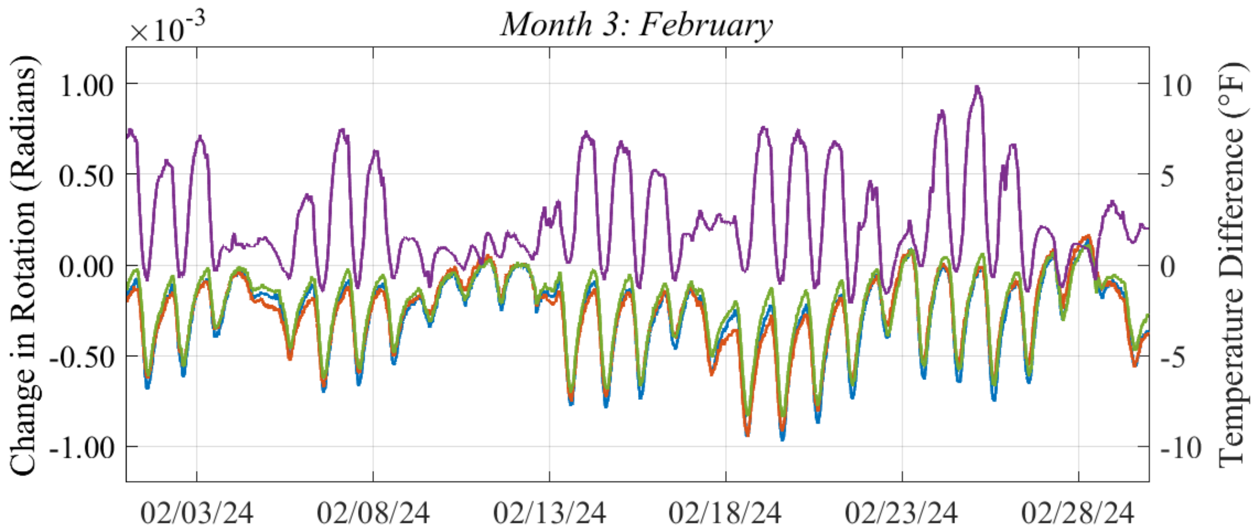

Figure D-3: Average rotation and temperature during February 2024

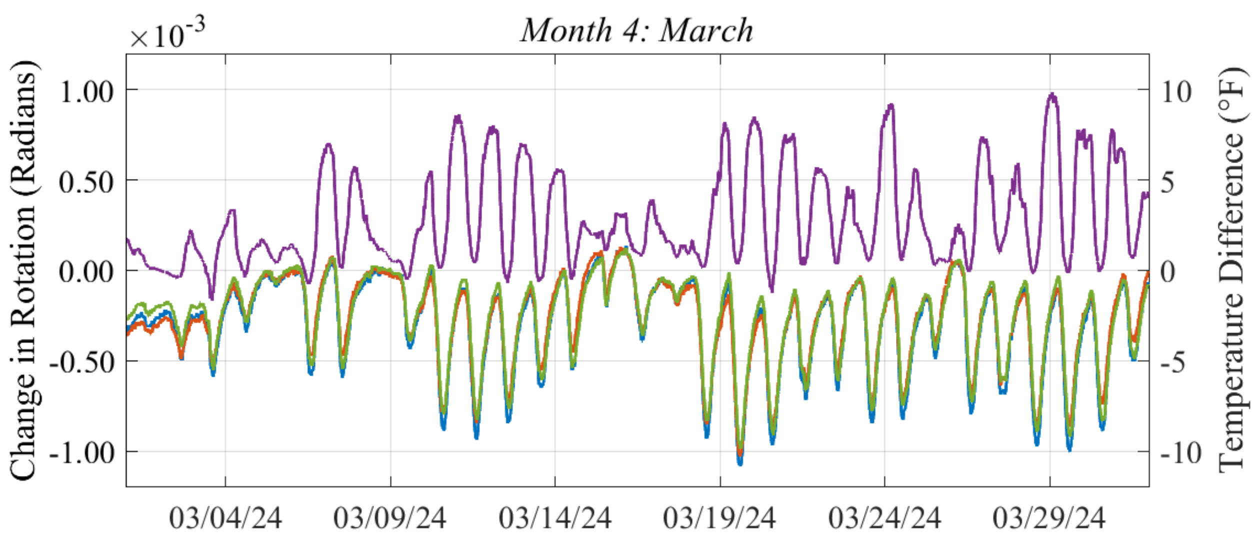

Figure D-4: Average rotation and temperature during March 2024

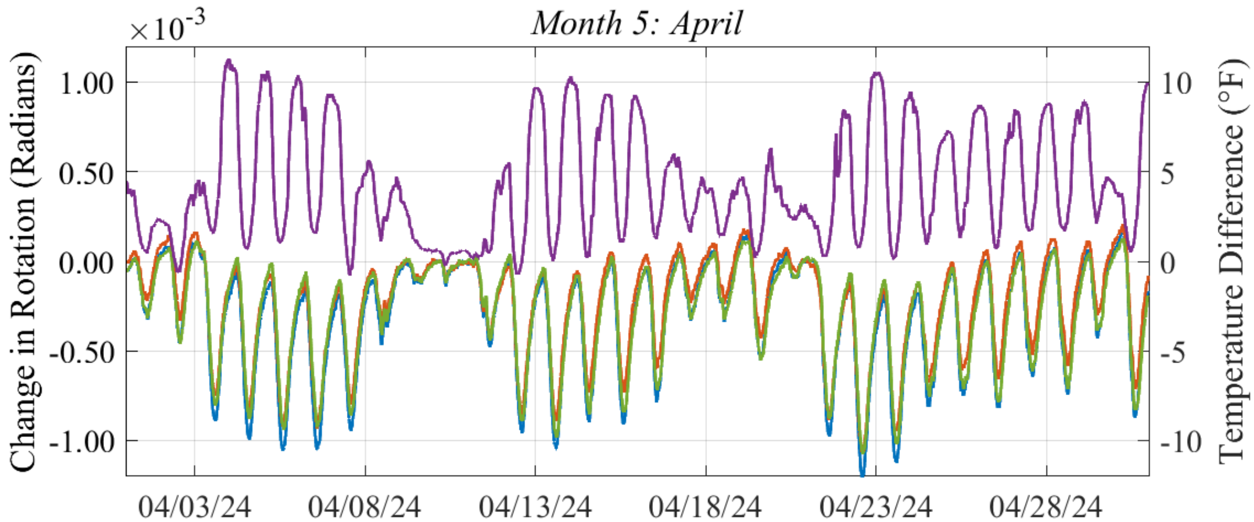

Figure D-5: Average rotation and temperature during April 2024

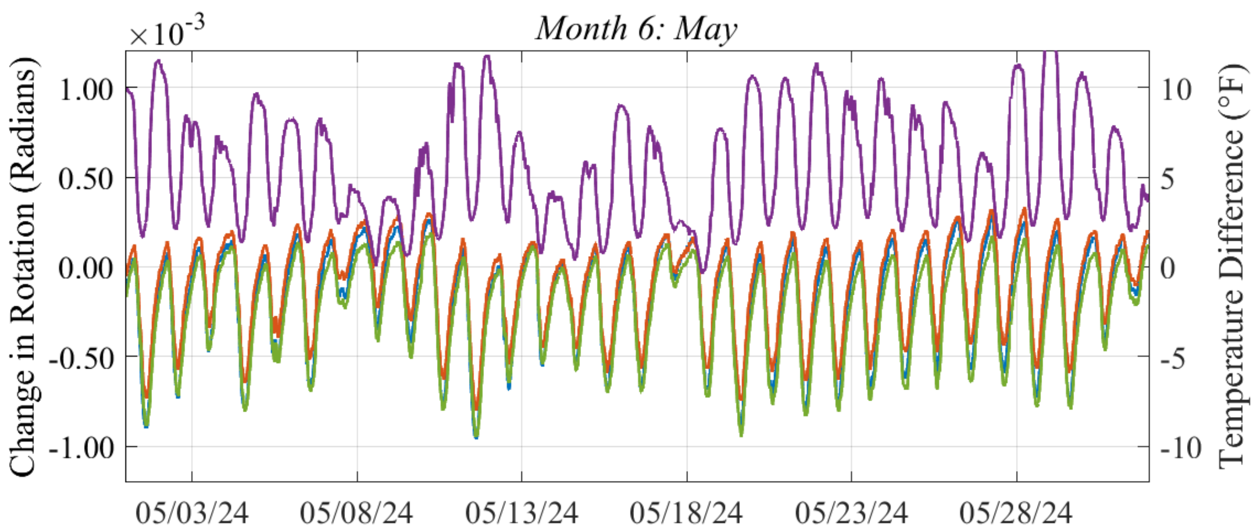

Figure D-6: Average rotation and temperature during May 2024

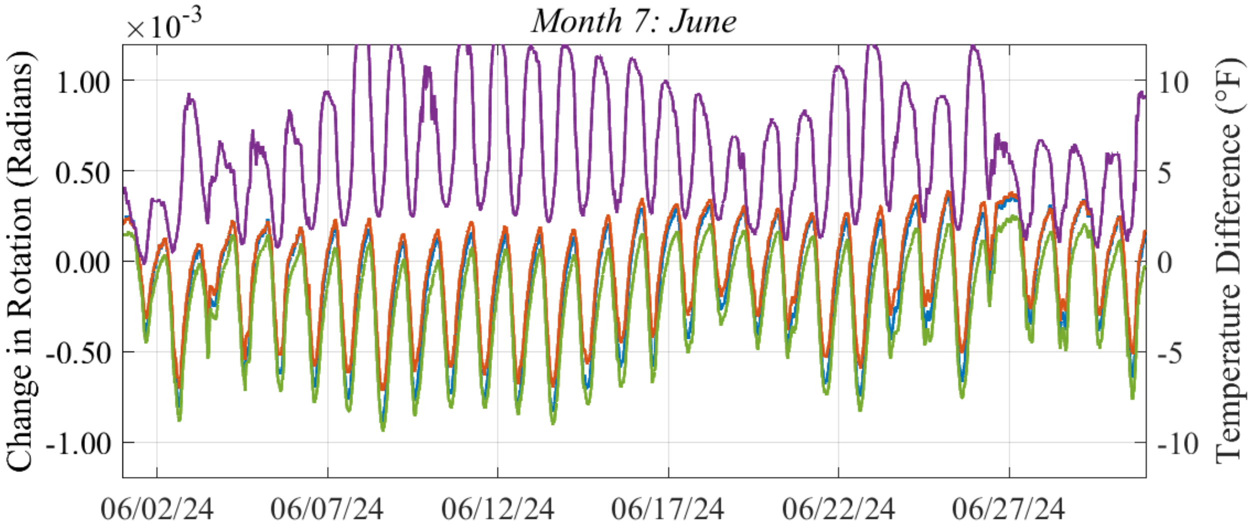

Figure D-7: Average rotation and temperature during June 2024

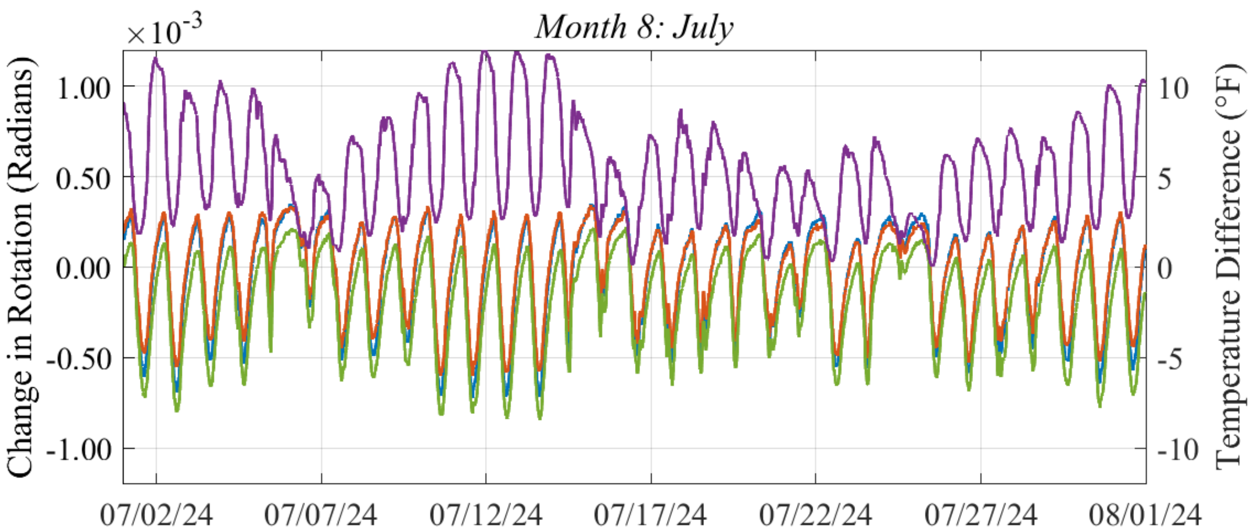

Figure D-8: Average rotation and temperature during July 2024

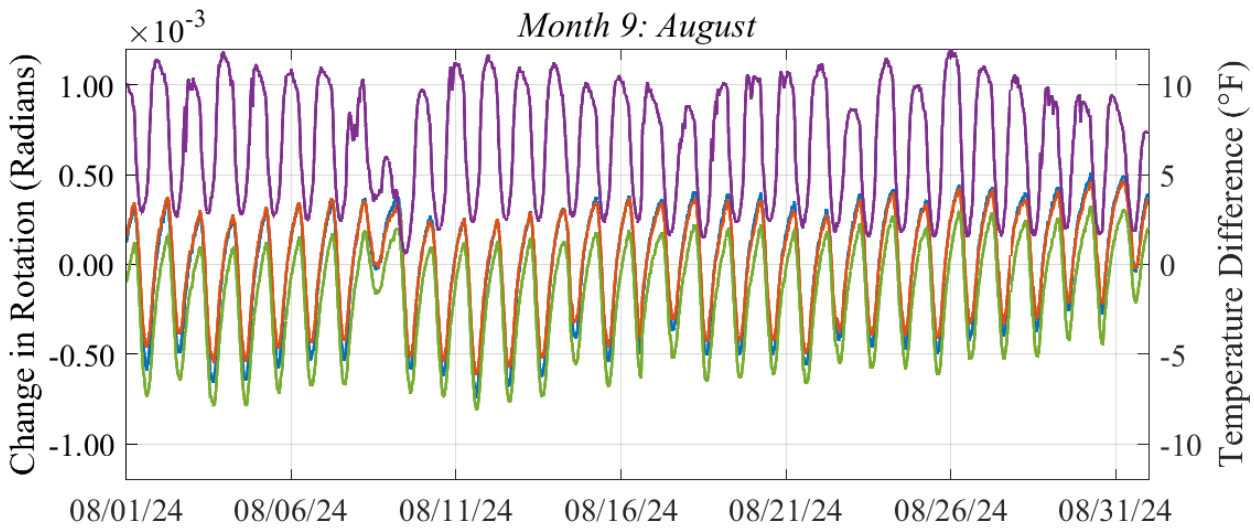

Figure D-9: Average rotation and temperature during August 2024

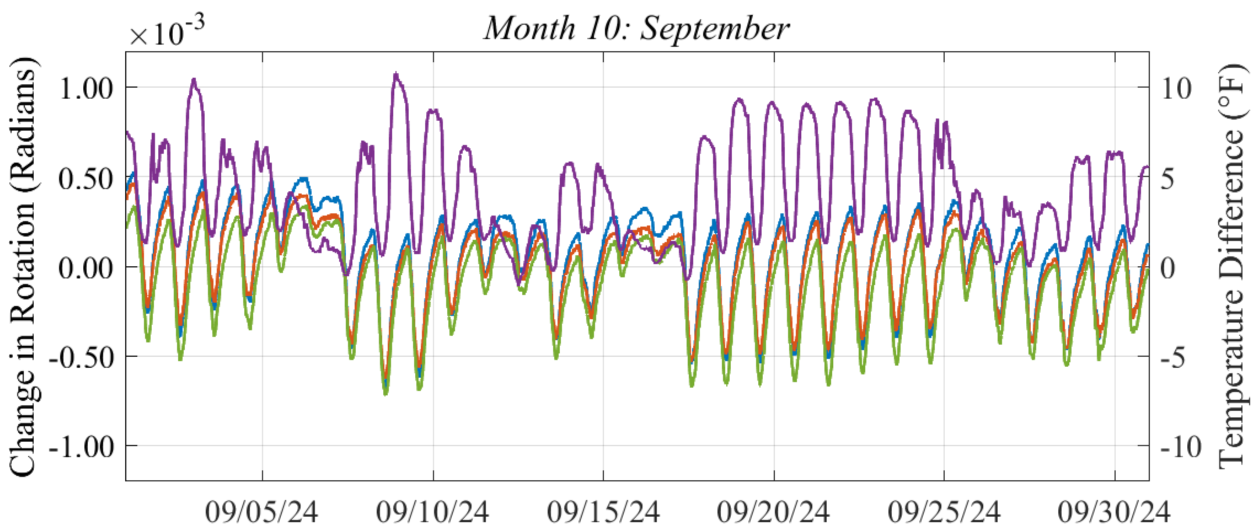

Figure D-10: Average rotation and temperature during September 2024

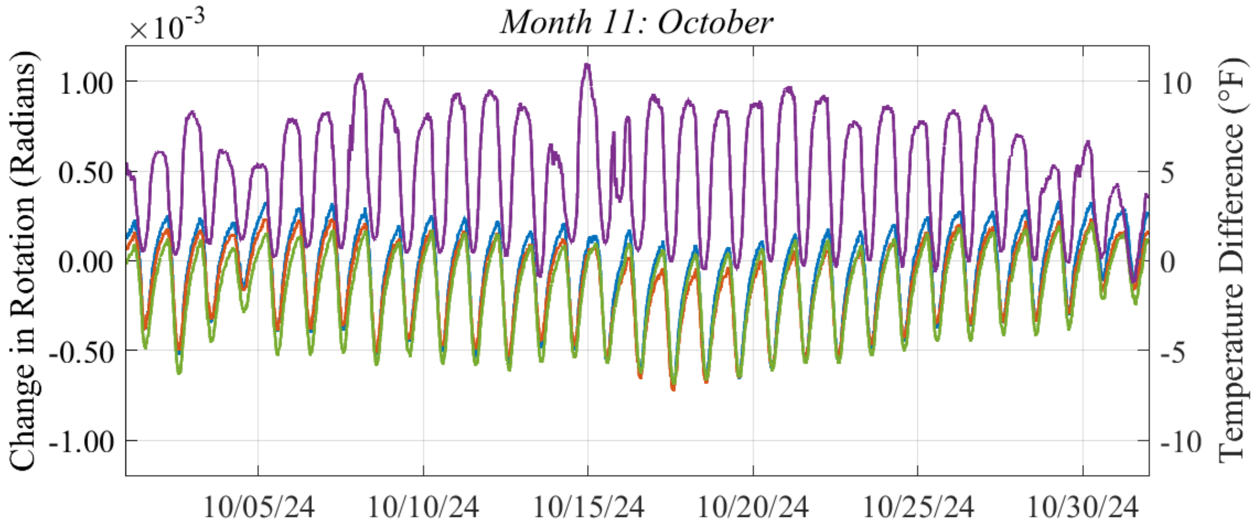

Figure D-11: Average rotation and temperature during October 2024

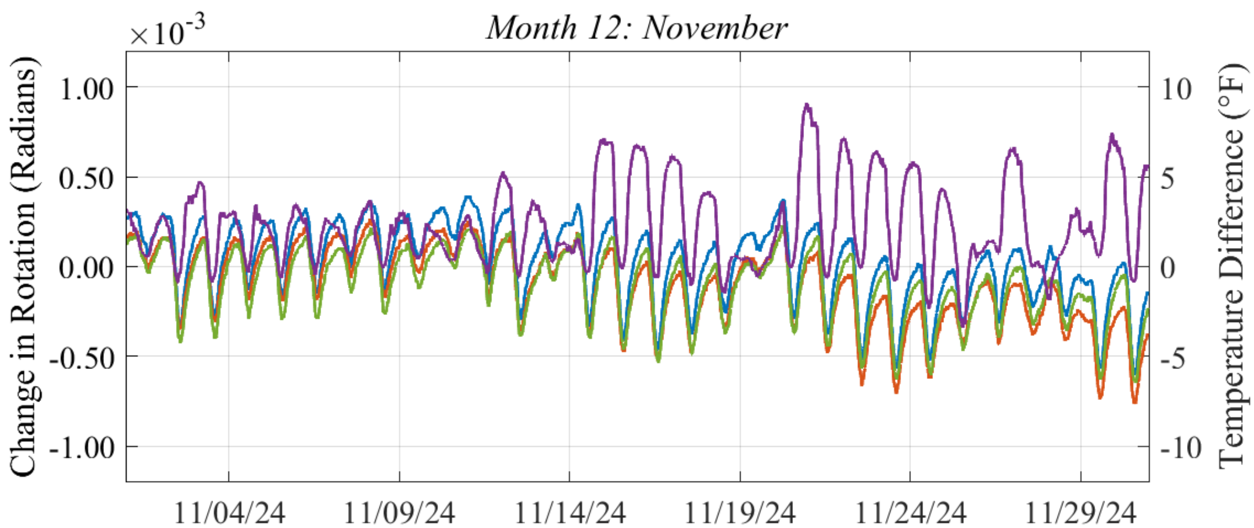

Figure D-12: Average rotation and temperature during November 2024

D.1.2. Total Rotation Across Joint

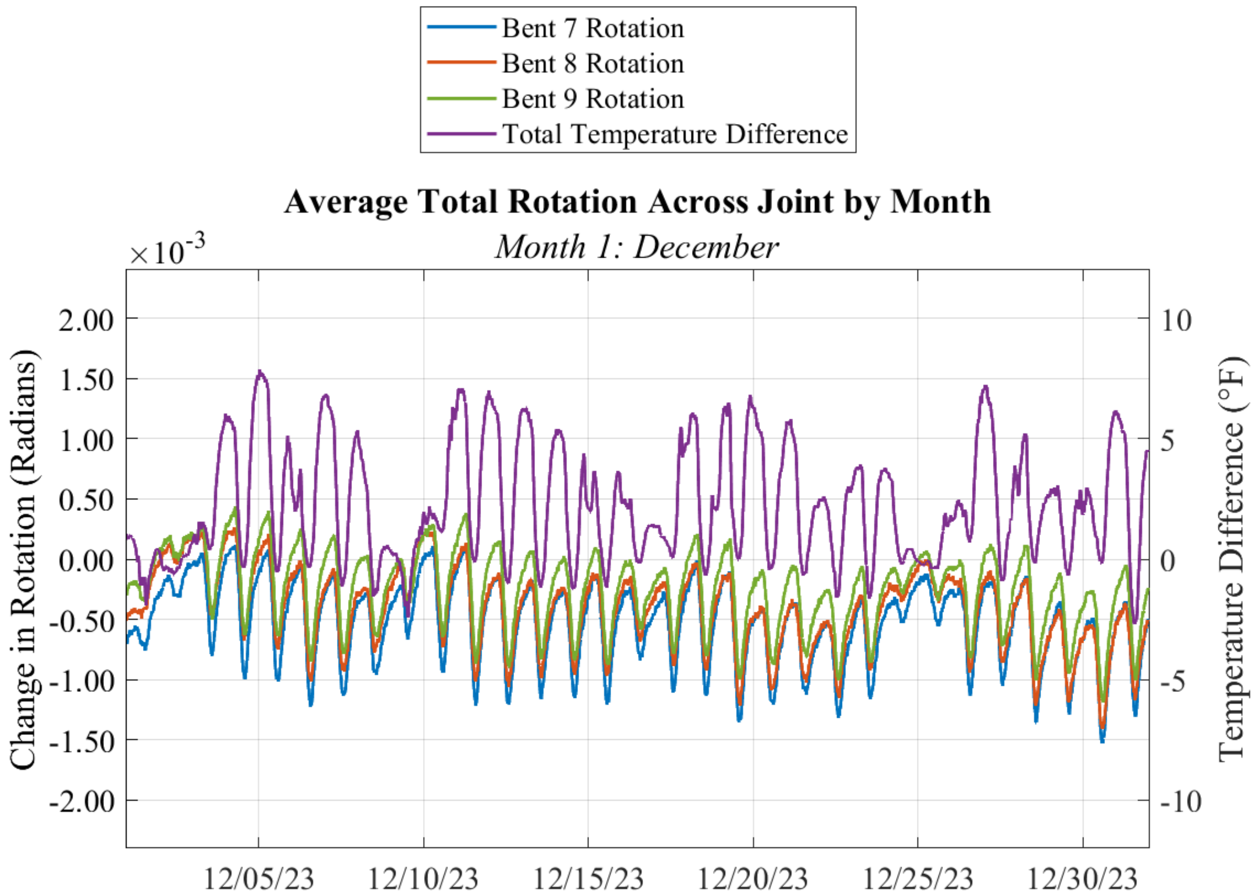

Figure D-13: Average total rotation across joint and temperature during December 2023

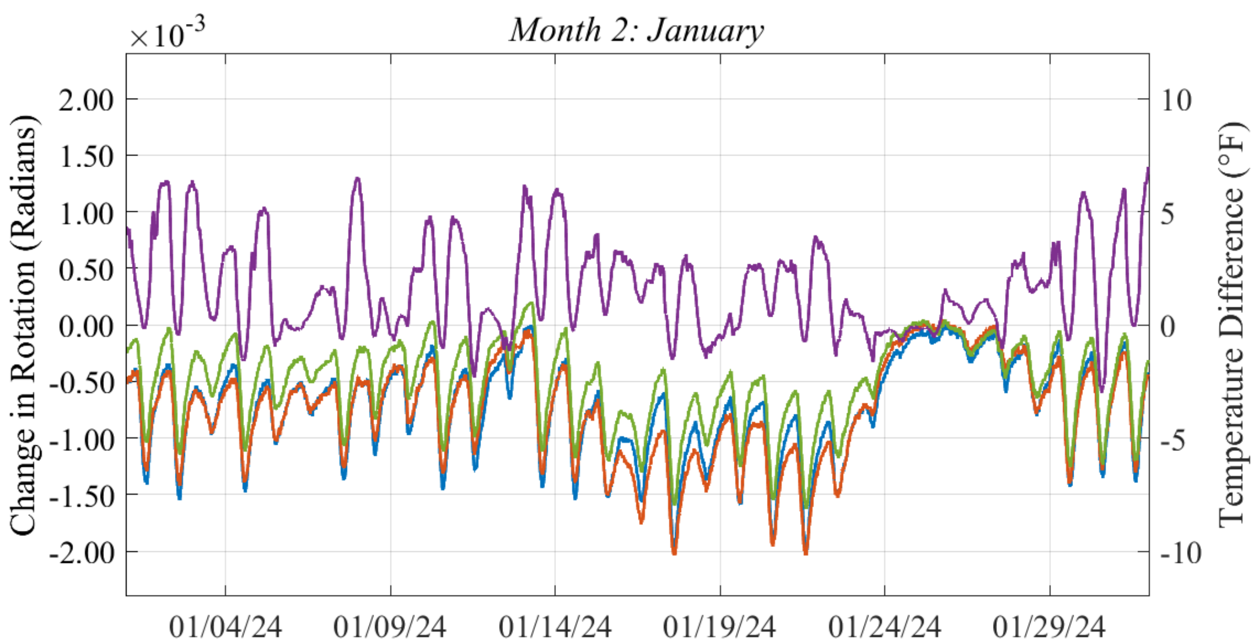

Figure D-14: Average total rotation across joint and temperature during January 2024

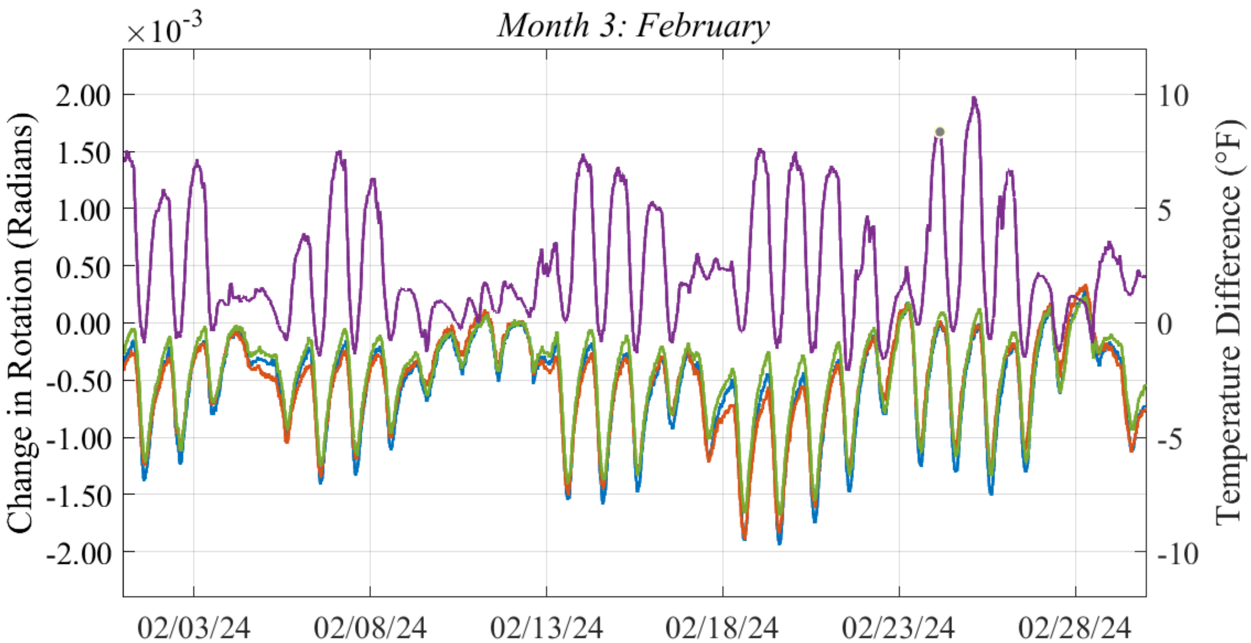

Figure D-15: Average total rotation across joint and temperature during February 2024

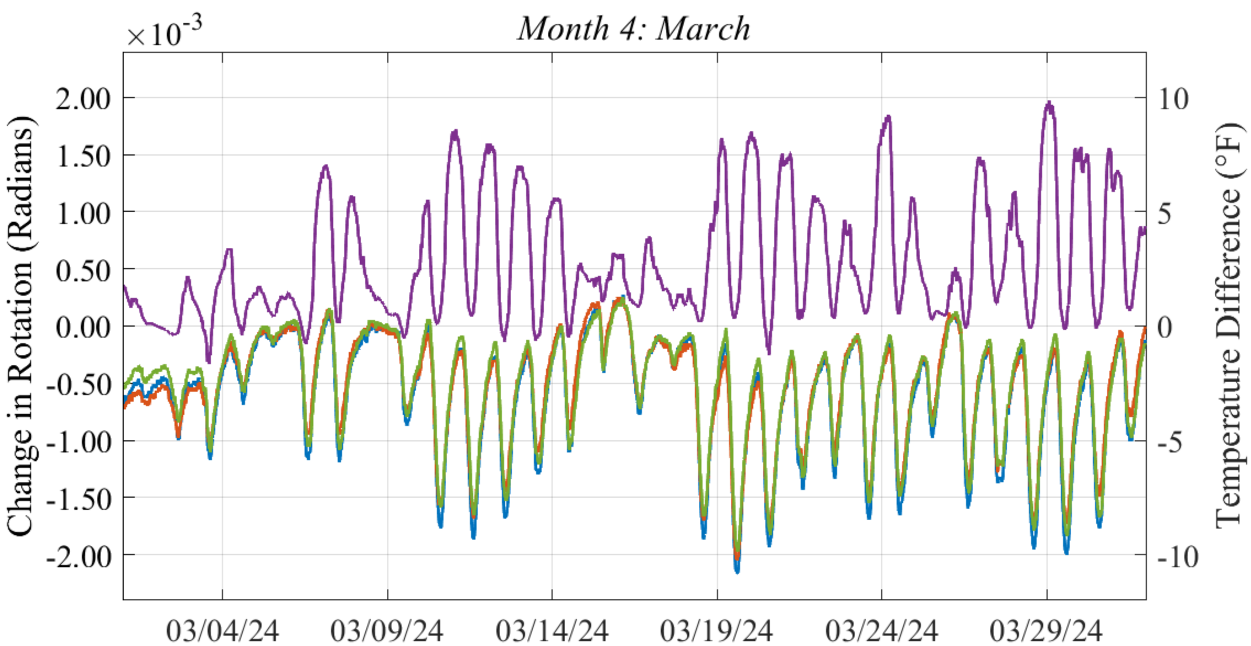

Figure D-16: Average total rotation across joint and temperature during March 2024

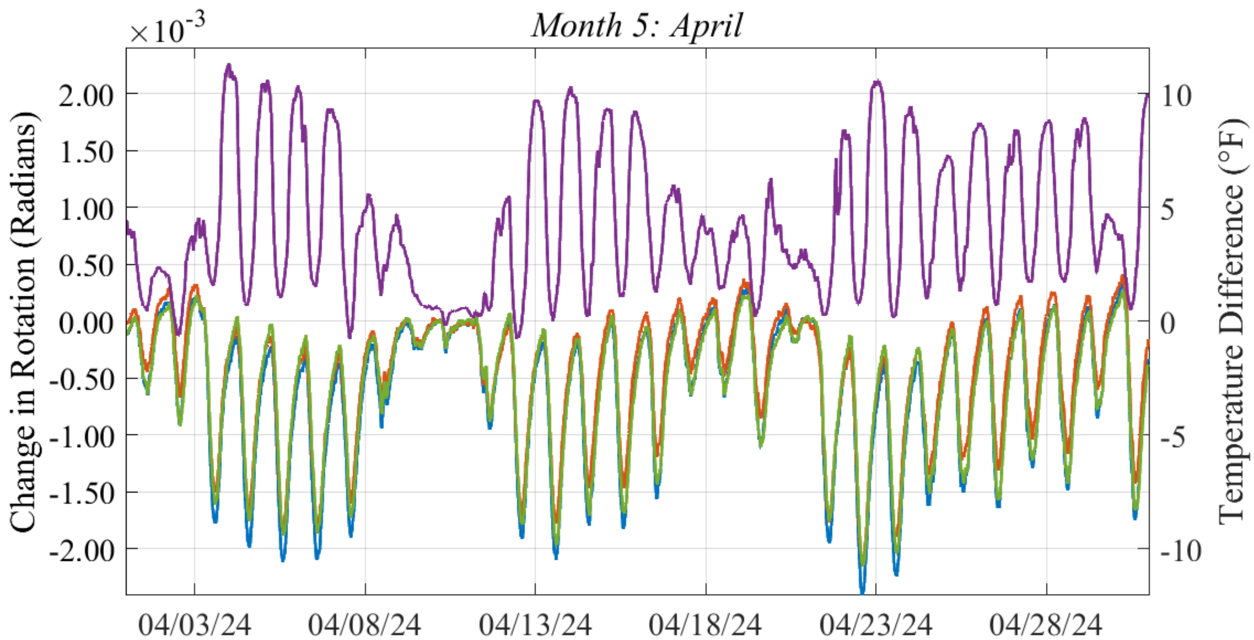

Figure D-17: Average total rotation across joint and temperature during April 2024

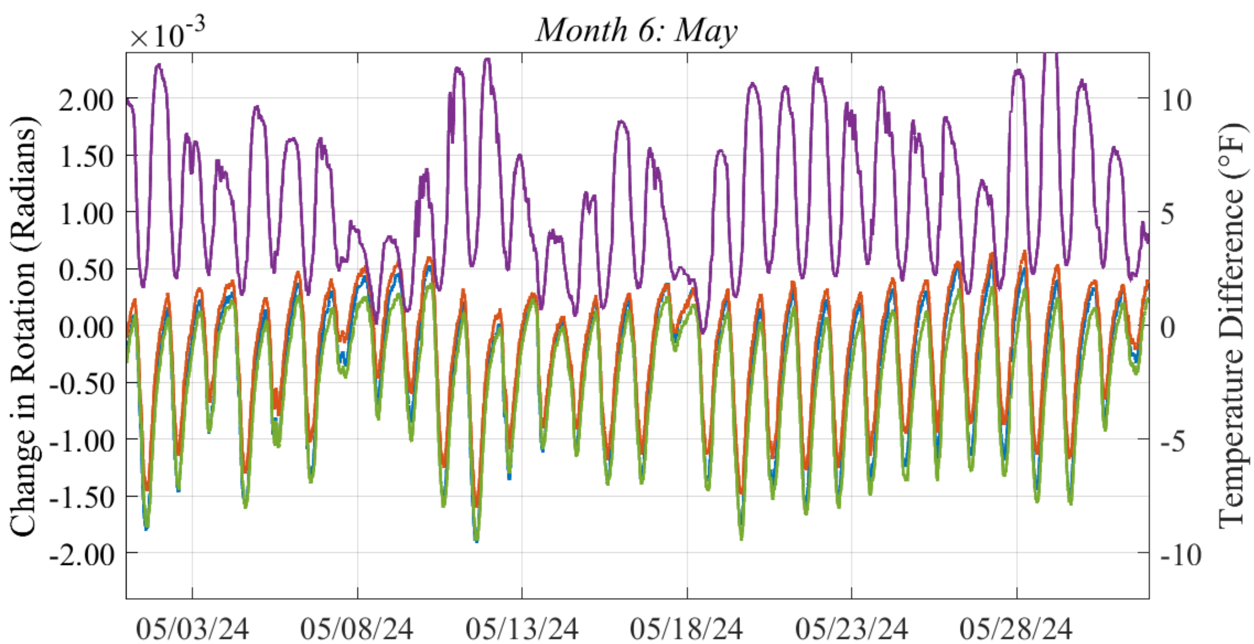

Figure D-18: Average total rotation across joint and temperature during May 2024

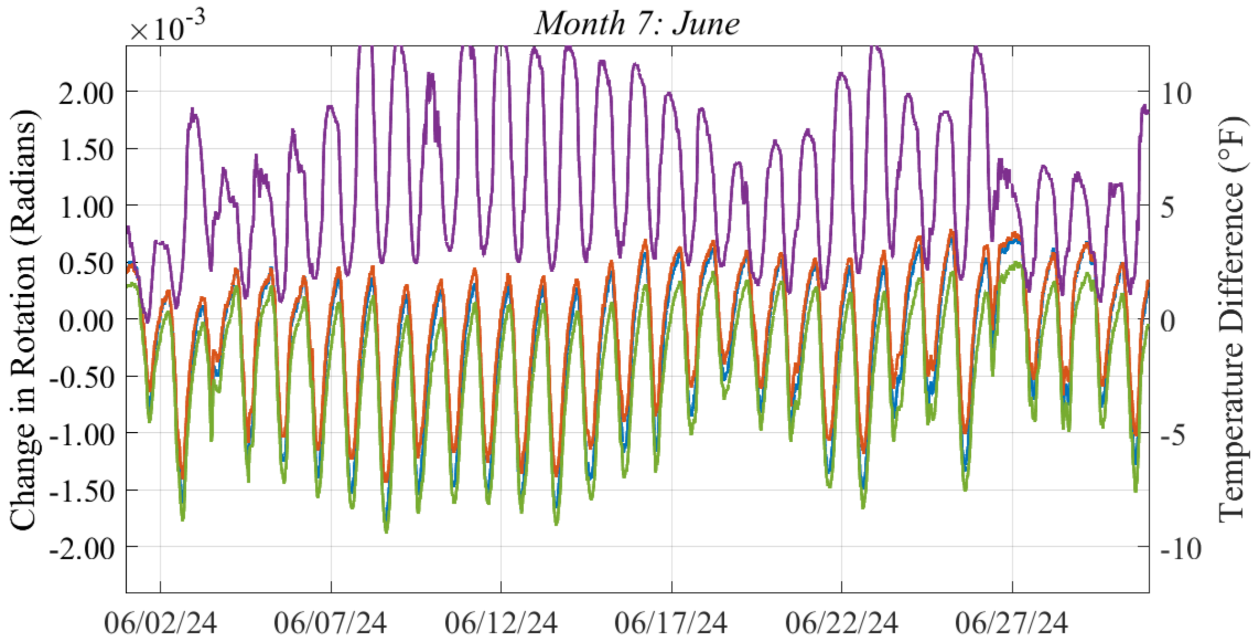

Figure D-19: Average total rotation across joint and temperature during June 2024

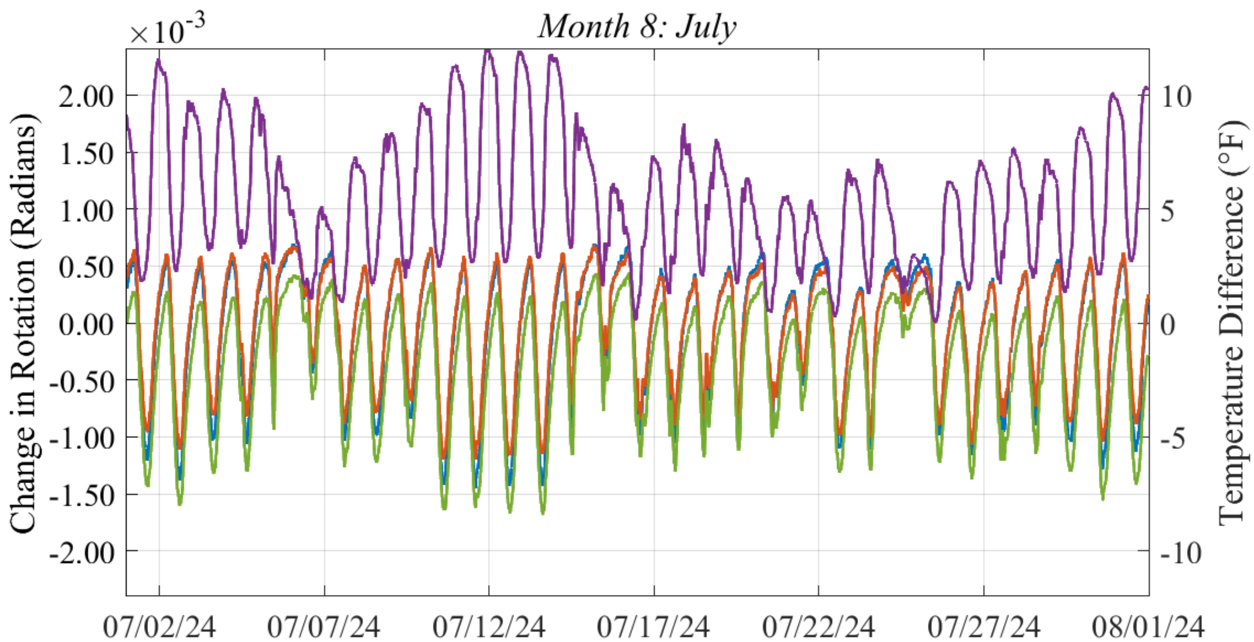

Figure D-20: Average total rotation across joint and temperature during July 2024

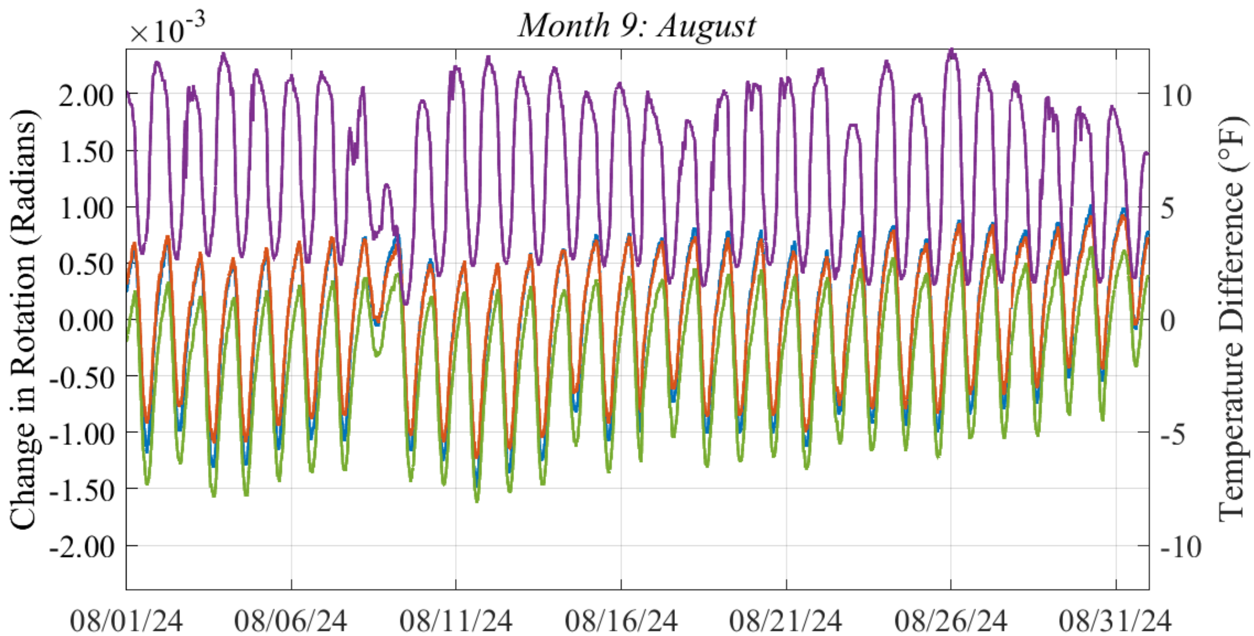

Figure D-21: Average total rotation across joint and temperature during August 2024

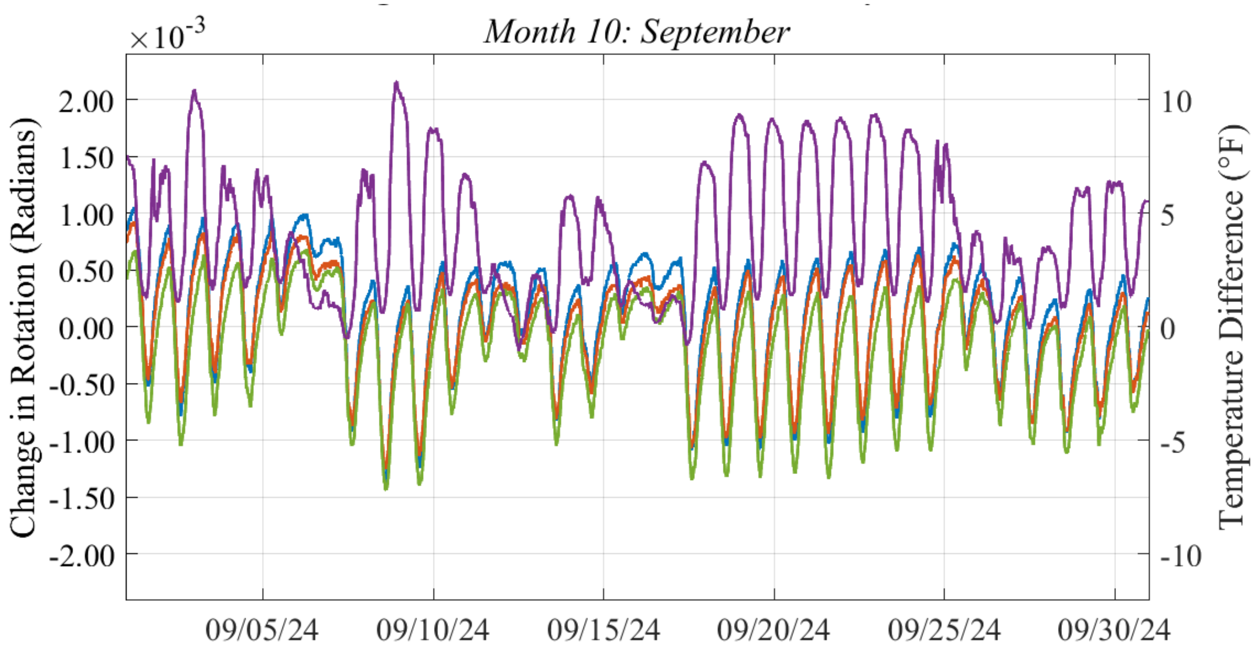

Figure D-22: Average total rotation across joint and temperature during September 2024

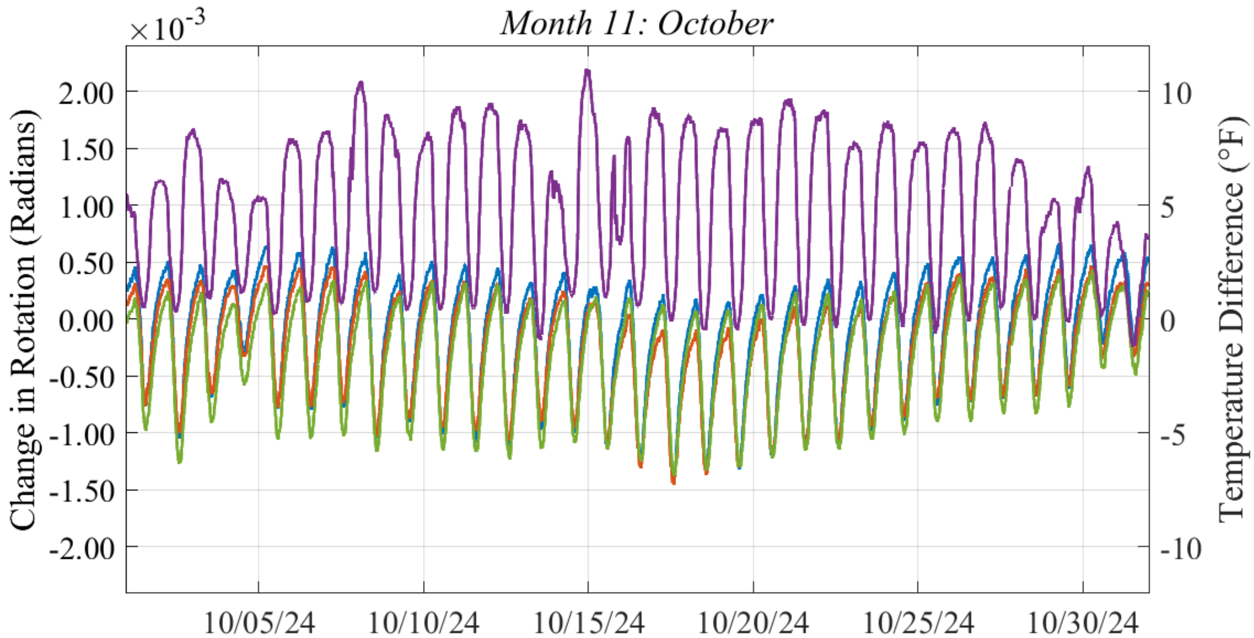

Figure D-23: Average total rotation across joint and temperature during October 2024

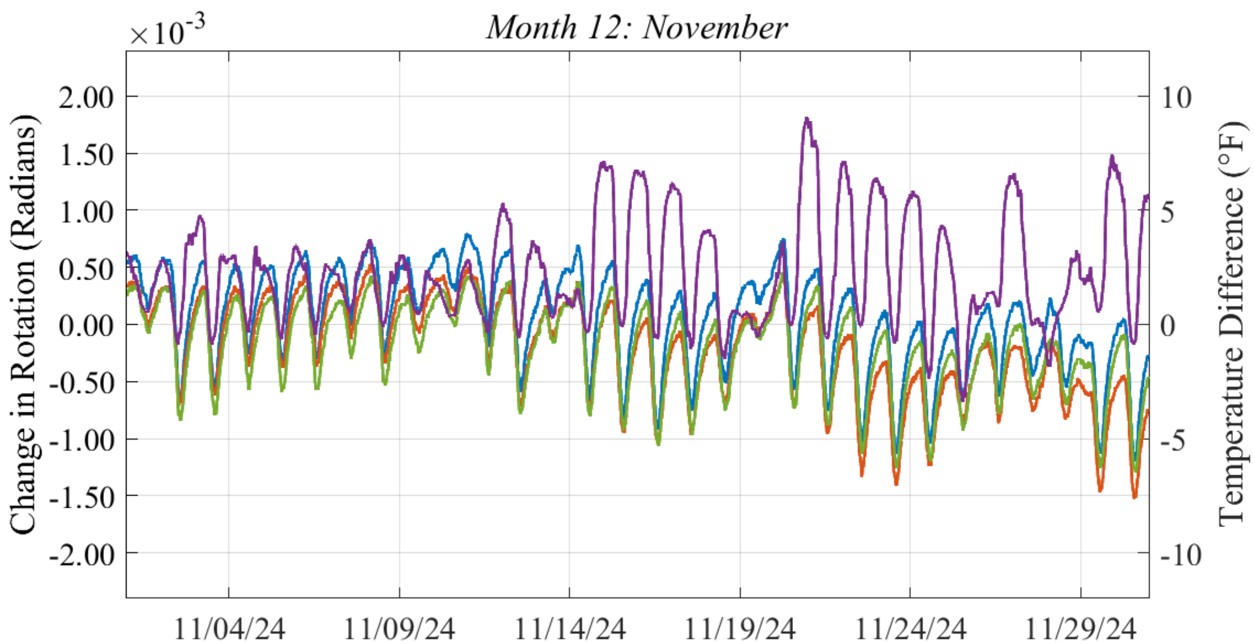

Figure D-24: Average total rotation across joint and temperature during November 2024

D.2. Girder-End Displacements

D.2.1. Open Joint (OJ)

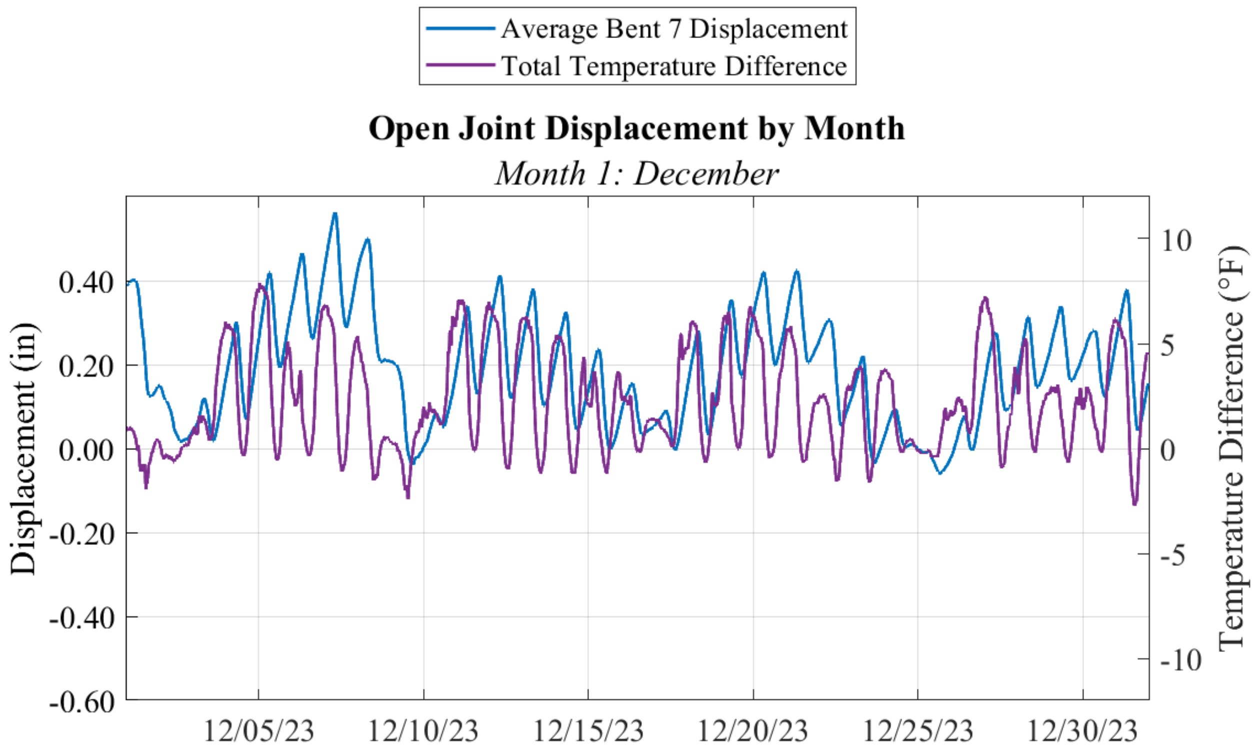

Figure D-25: Average OJ displacement and temperature during December 2023

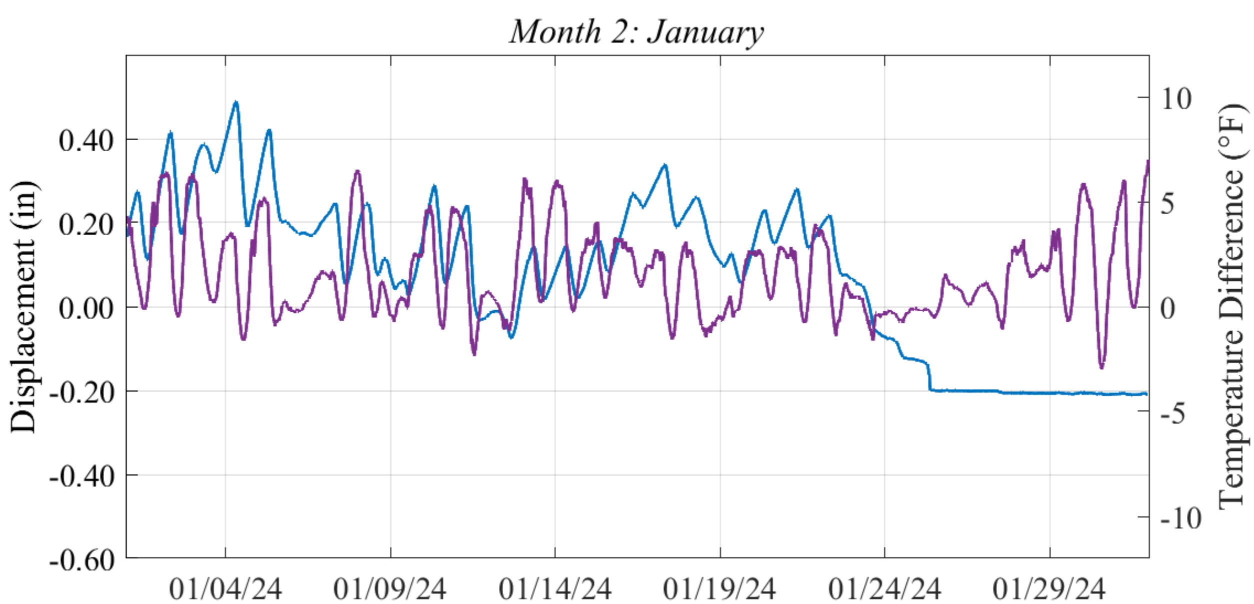

Figure D-26: Average OJ displacement and temperature during January 2024

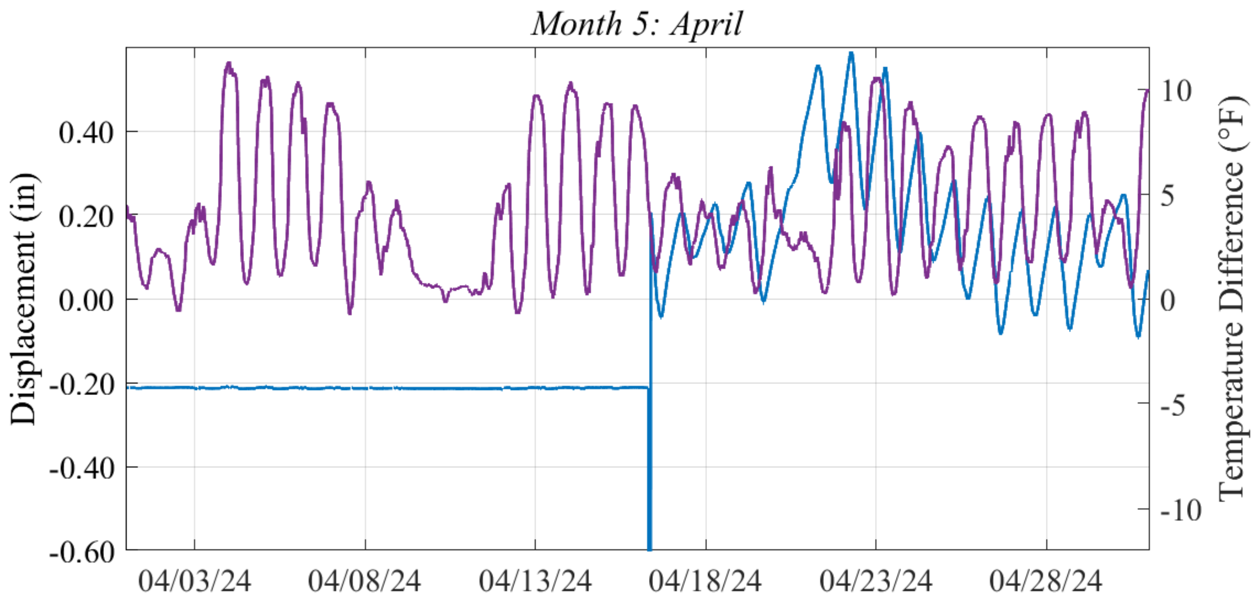

Figure D-27: Average OJ displacement and temperature during April 2024

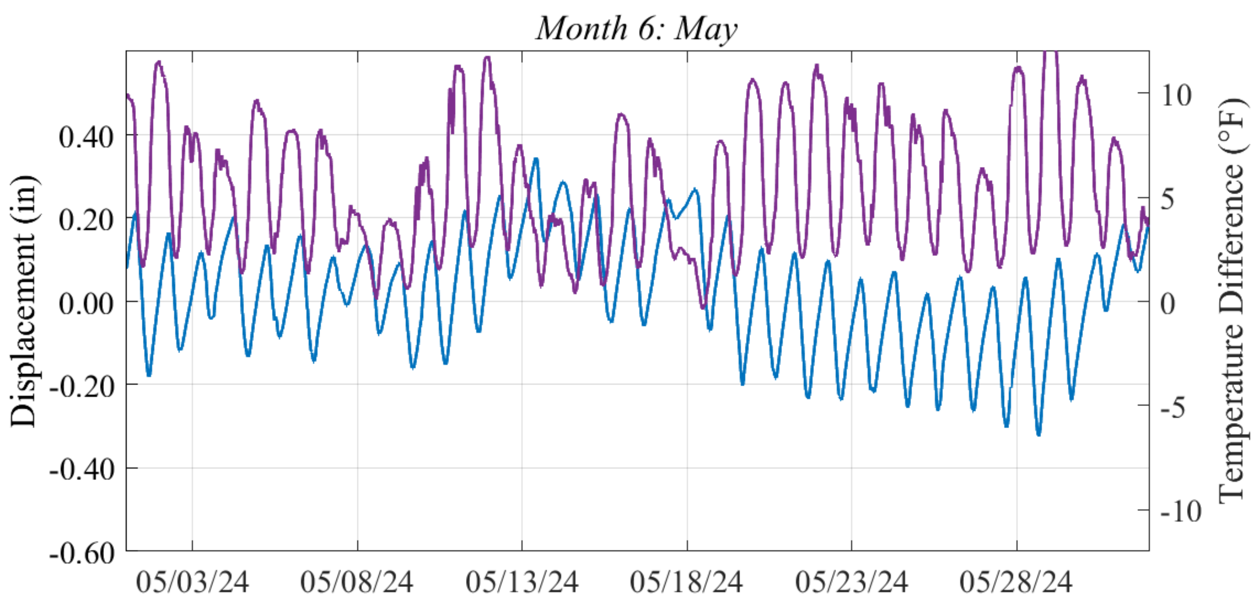

Figure D-28: Average OJ displacement and temperature during May 2024

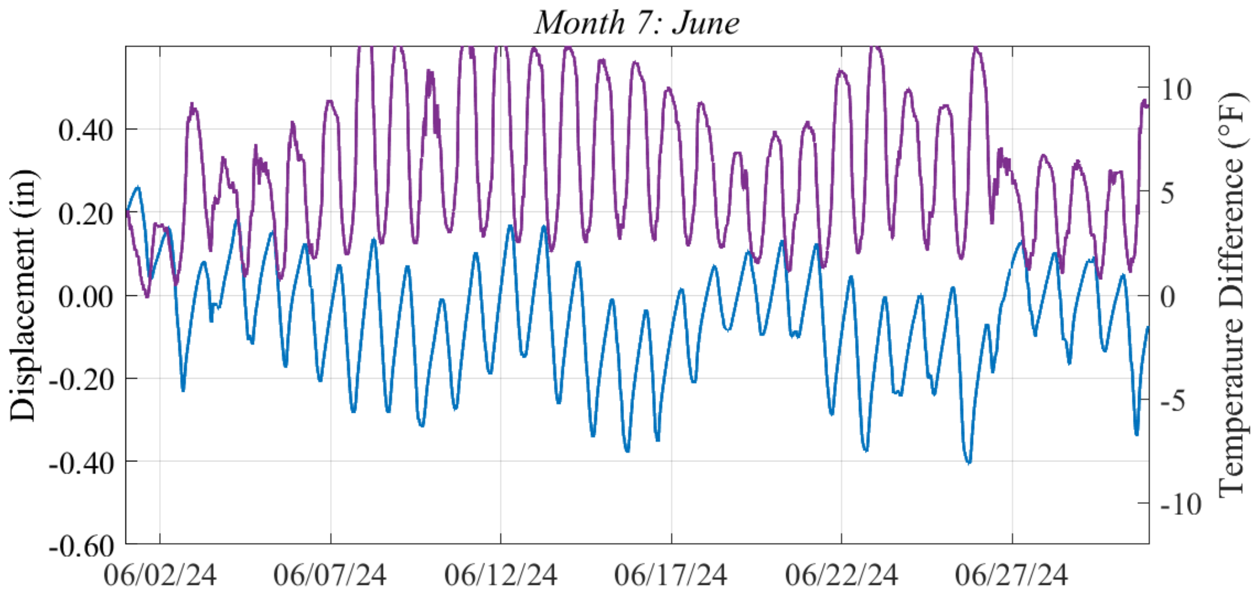

Figure D-29: Average OJ displacement and temperature during June 2024

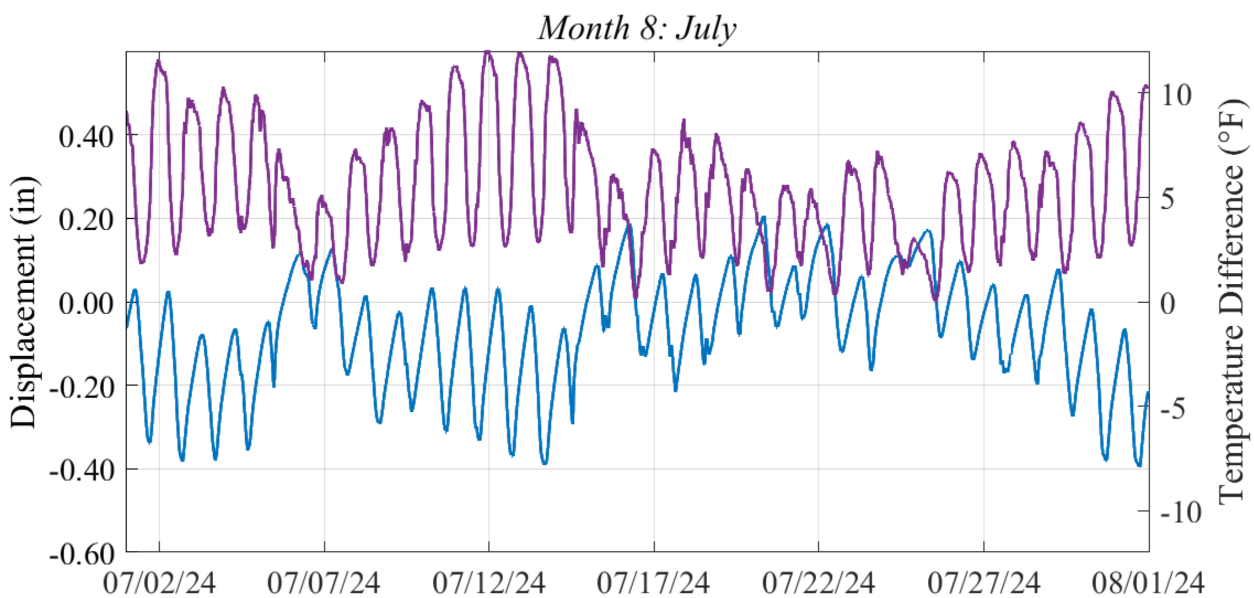

Figure D-30: Average OJ displacement and temperature during July 2024

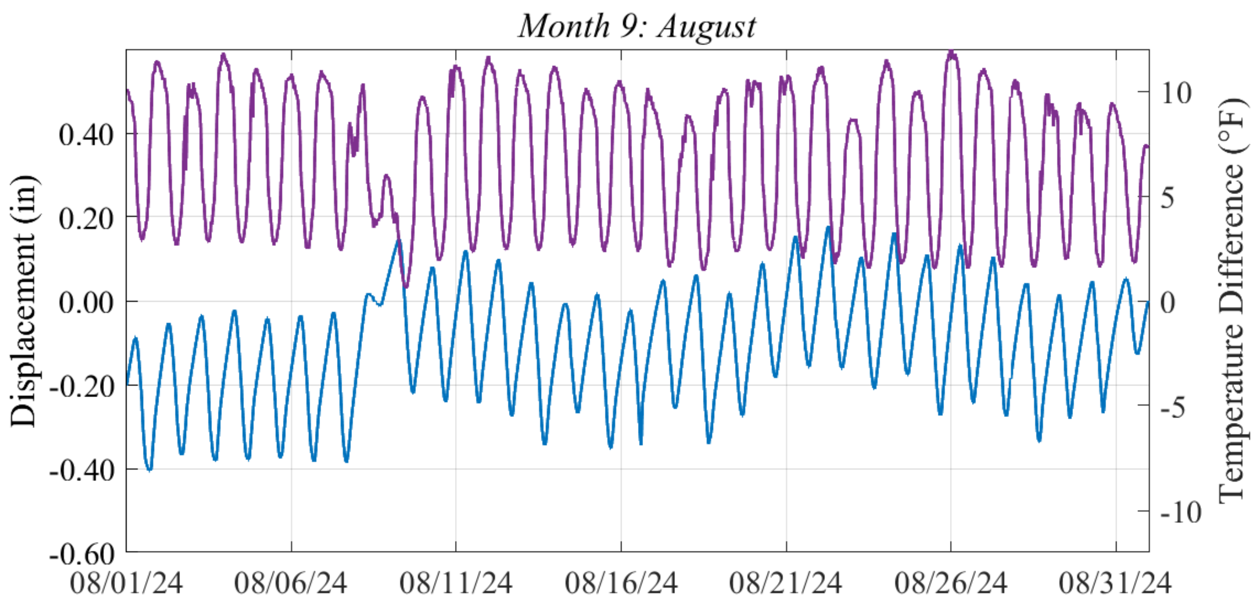

Figure D-31: Average OJ displacement and temperature during August 2024

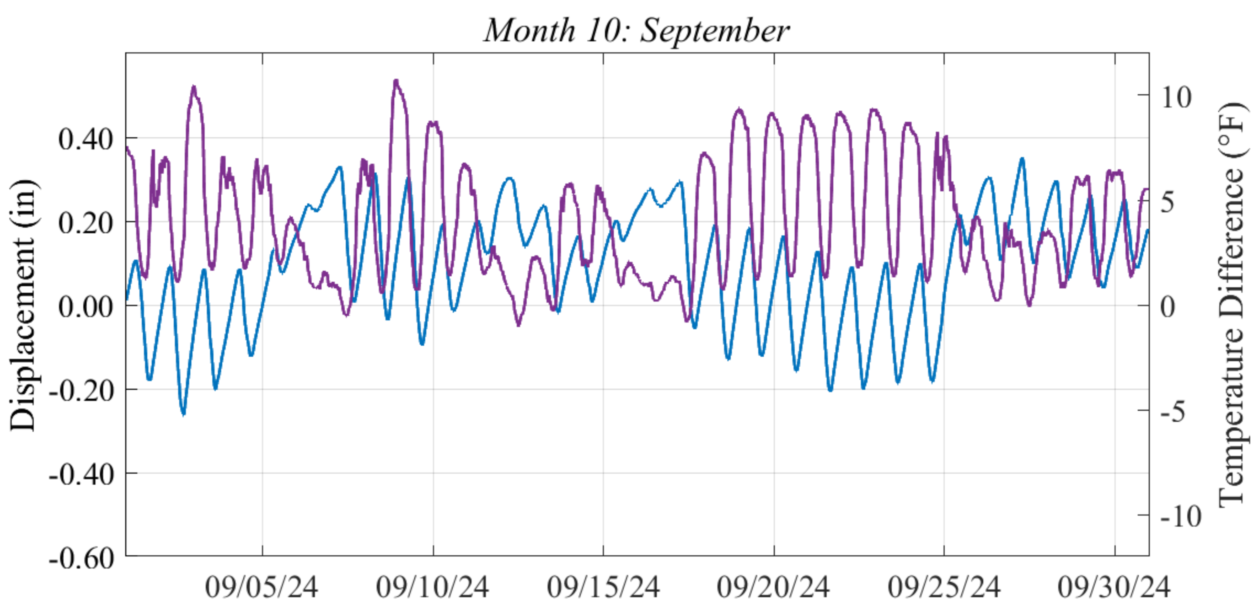

Figure D-32: Average OJ displacement and temperature during September 2024

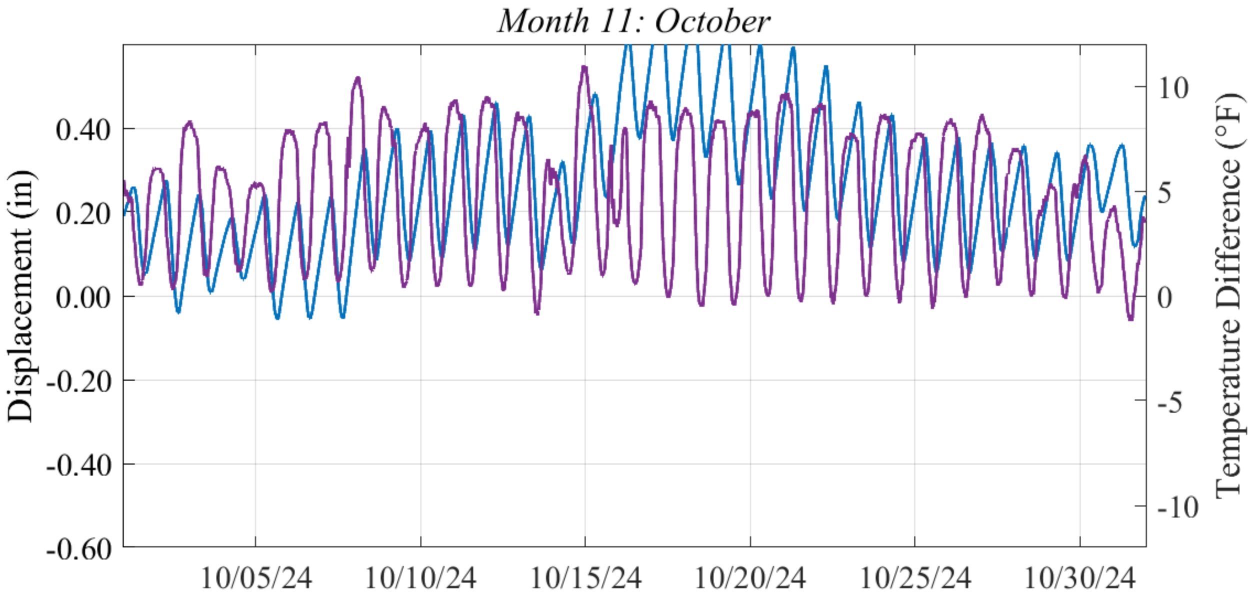

Figure D-33: Average OJ displacement and temperature during October 2024

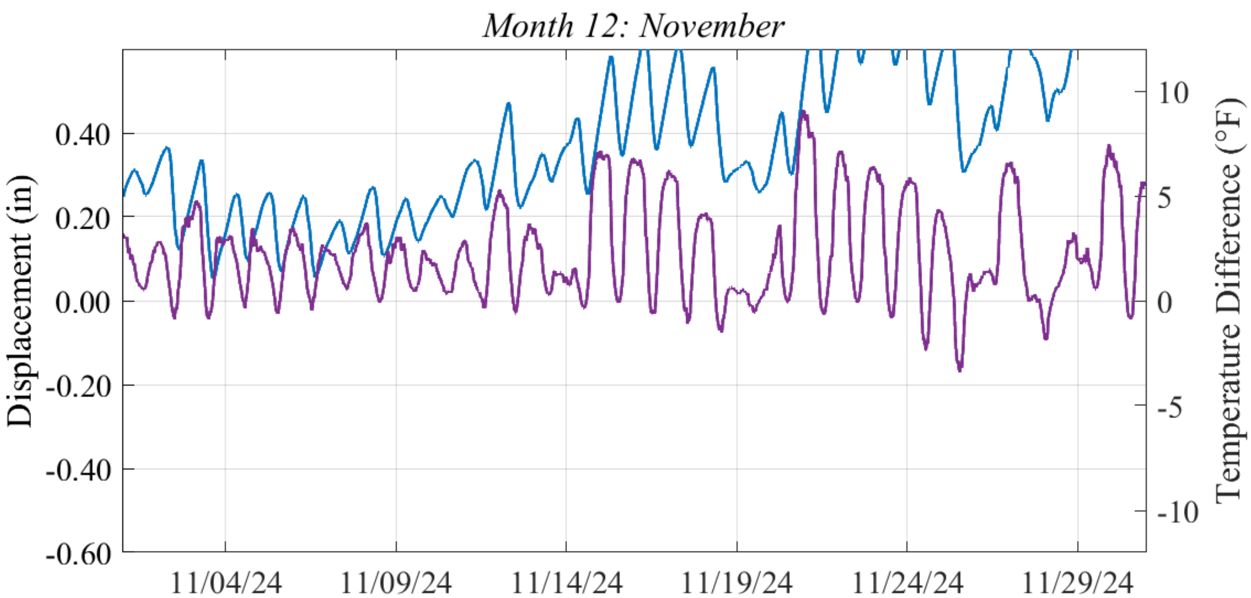

Figure D-34: Average OJ displacement and temperature during November 2024

D.2.2. Closed Joint (CJ)

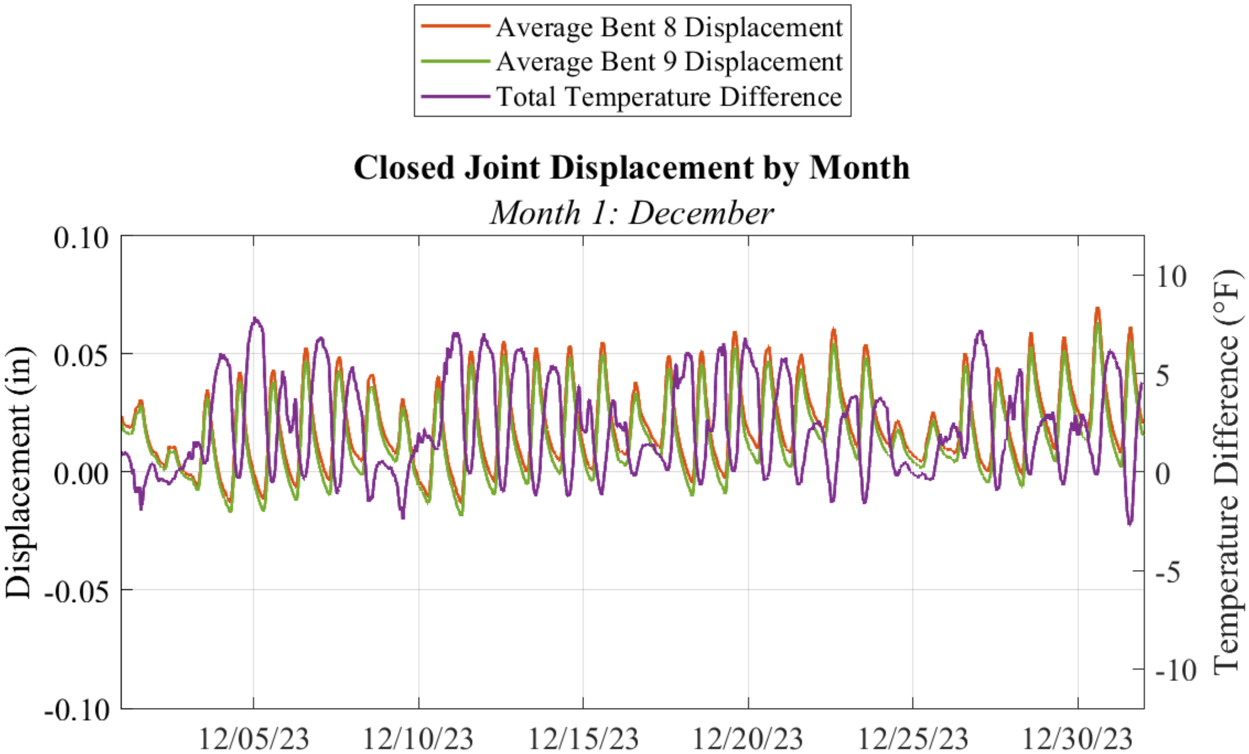

Figure D-35: Average CJ displacement and temperature during December 2023

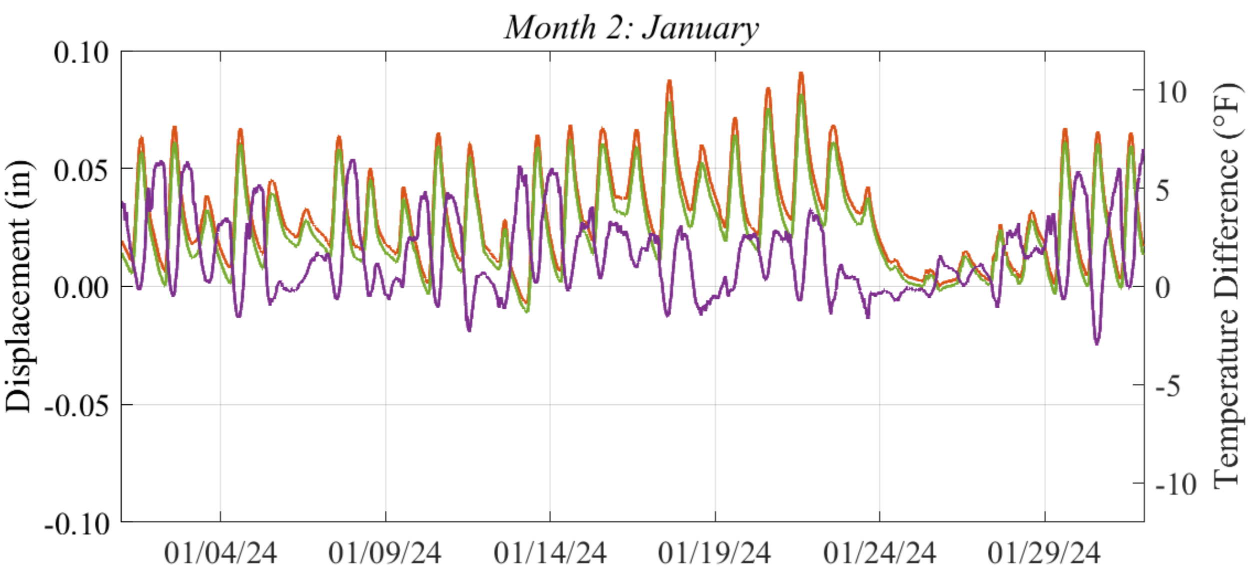

Figure D-36: Average CJ displacement and temperature during January 2024

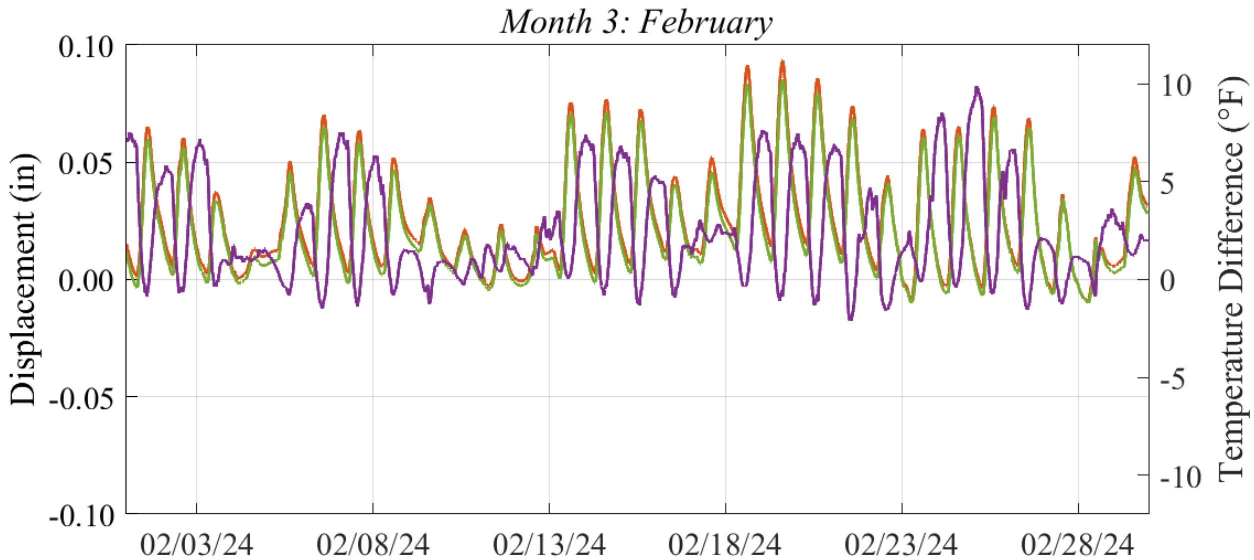

Figure D-37: Average CJ displacement and temperature during February 2024

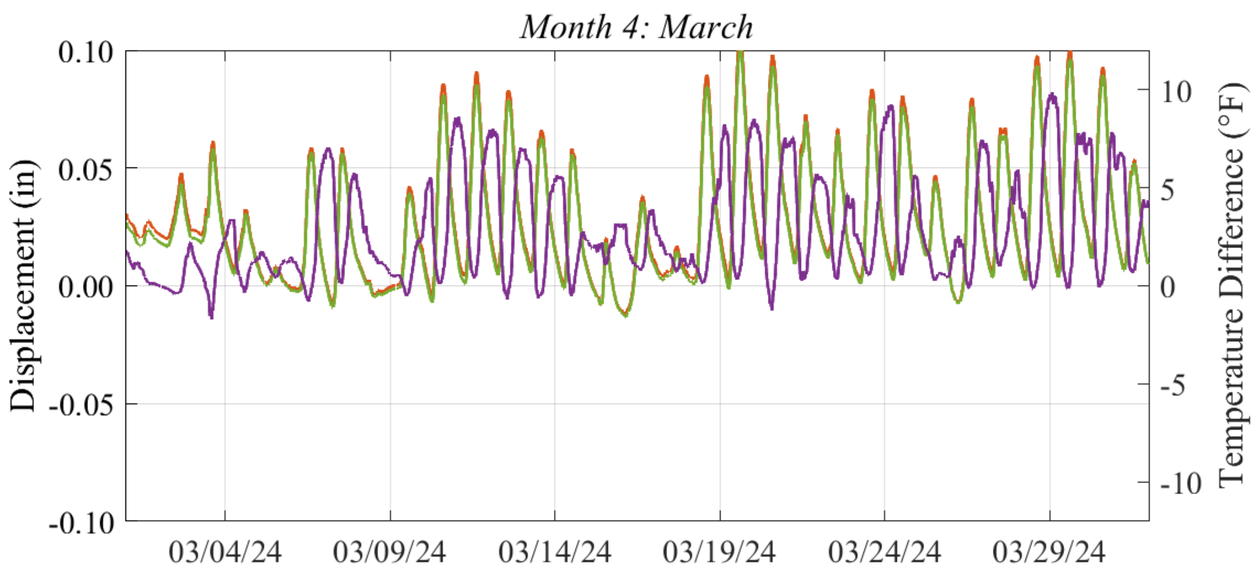

Figure D-38: Average CJ displacement and temperature during March 2024

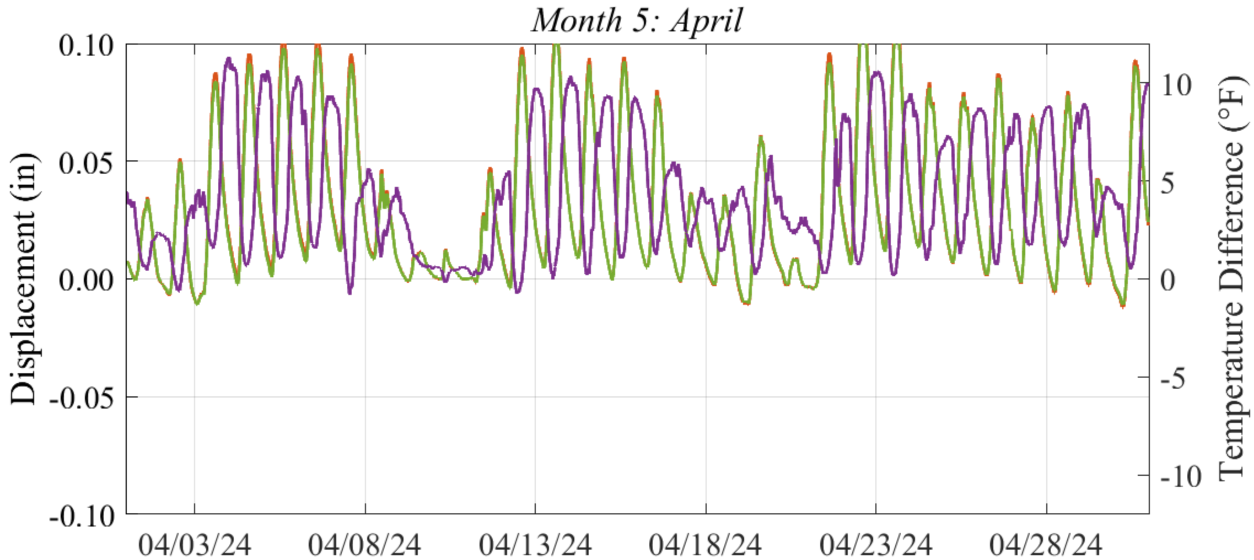

Figure D-39: Average CJ displacement and temperature during April 2024

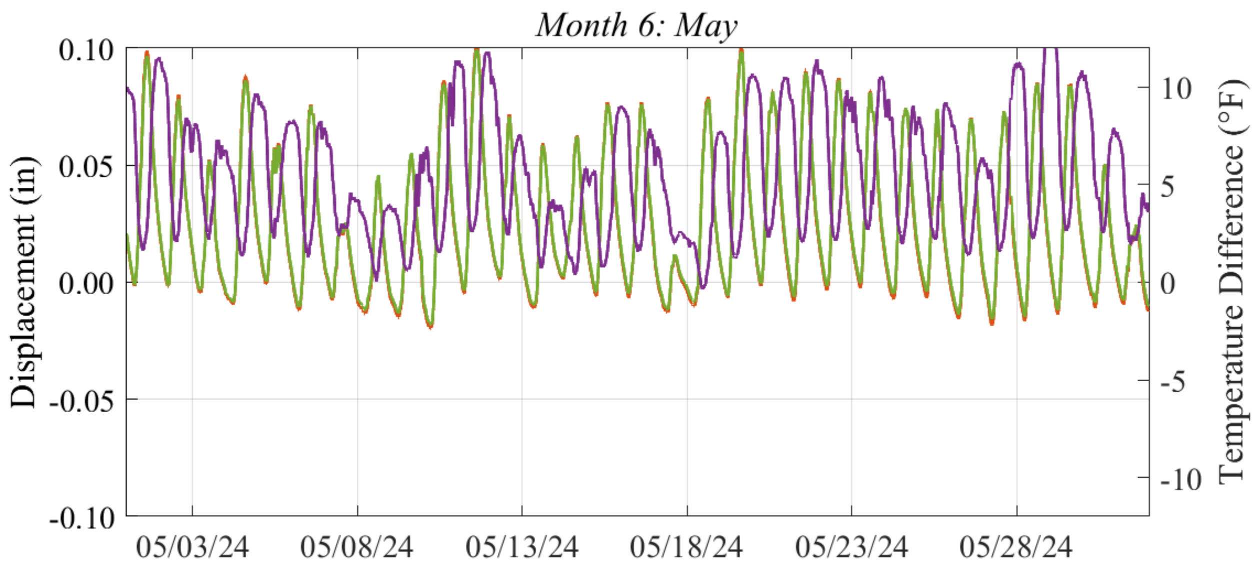

Figure D-40: Average CJ displacement and temperature during May 2024

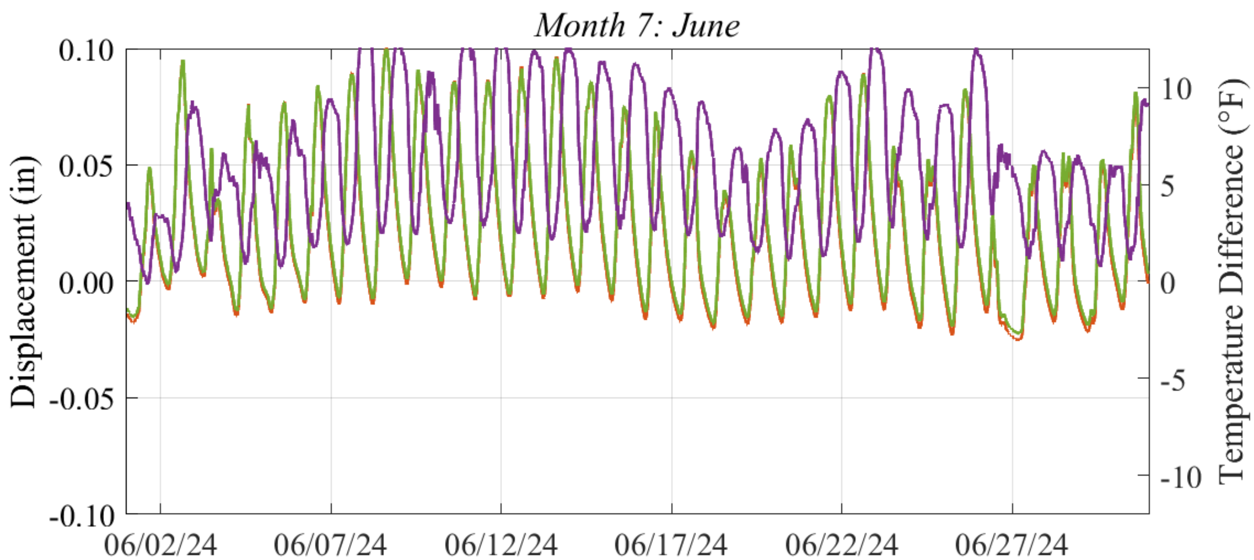

Figure D-41: Average CJ displacement and temperature during June 2024

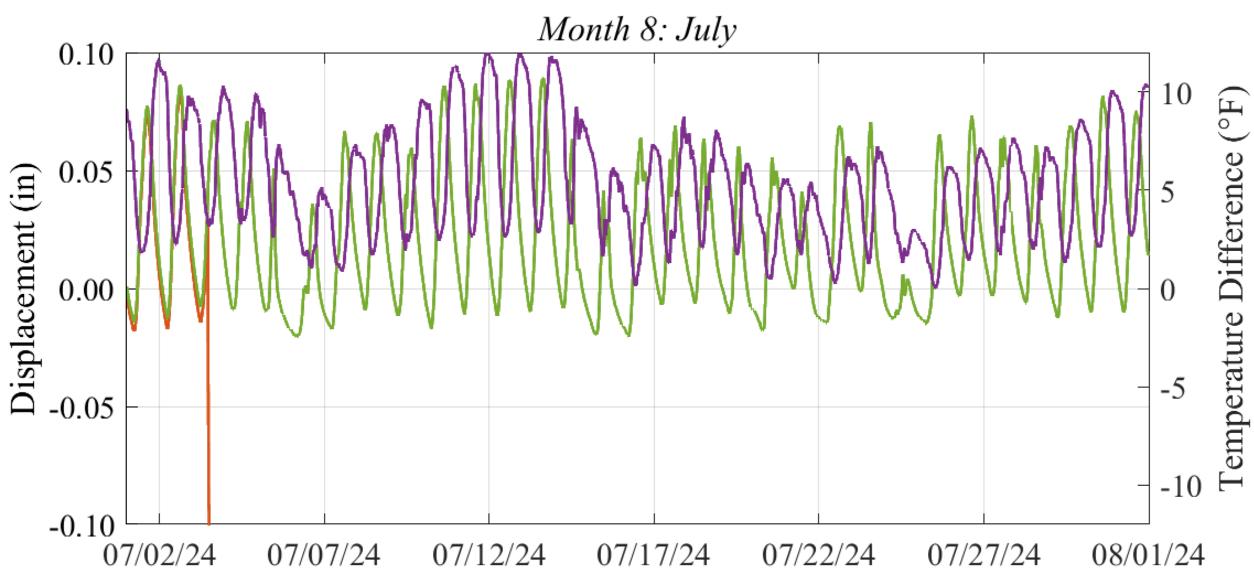

Figure D-42: Average CJ displacement and temperature during July 2024

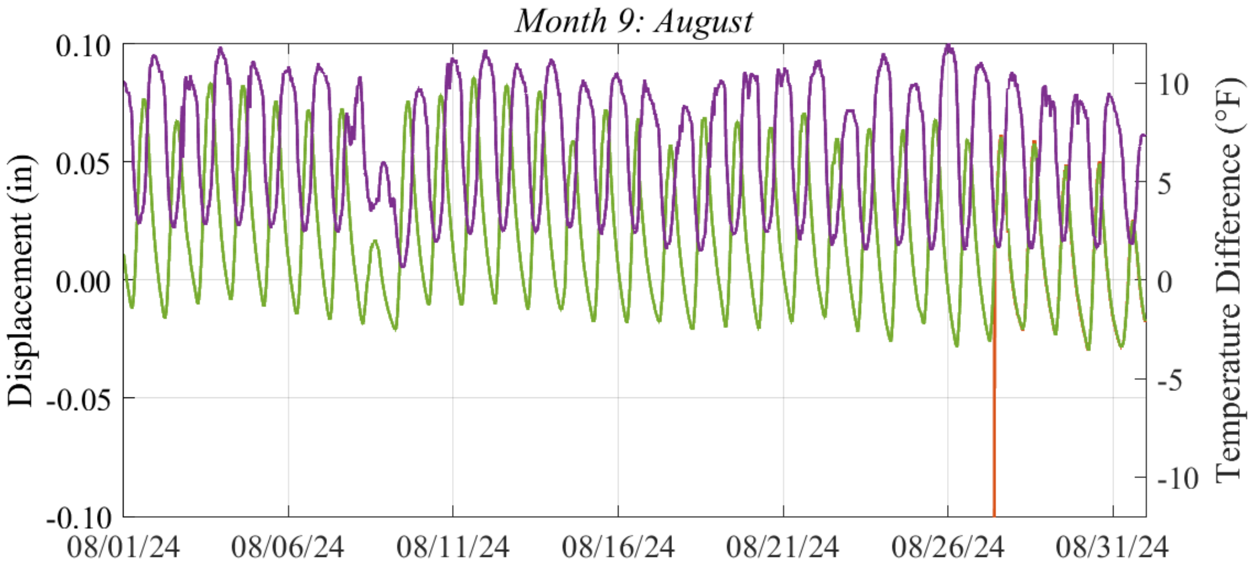

Figure D-43: Average CJ displacement and temperature during August 2024

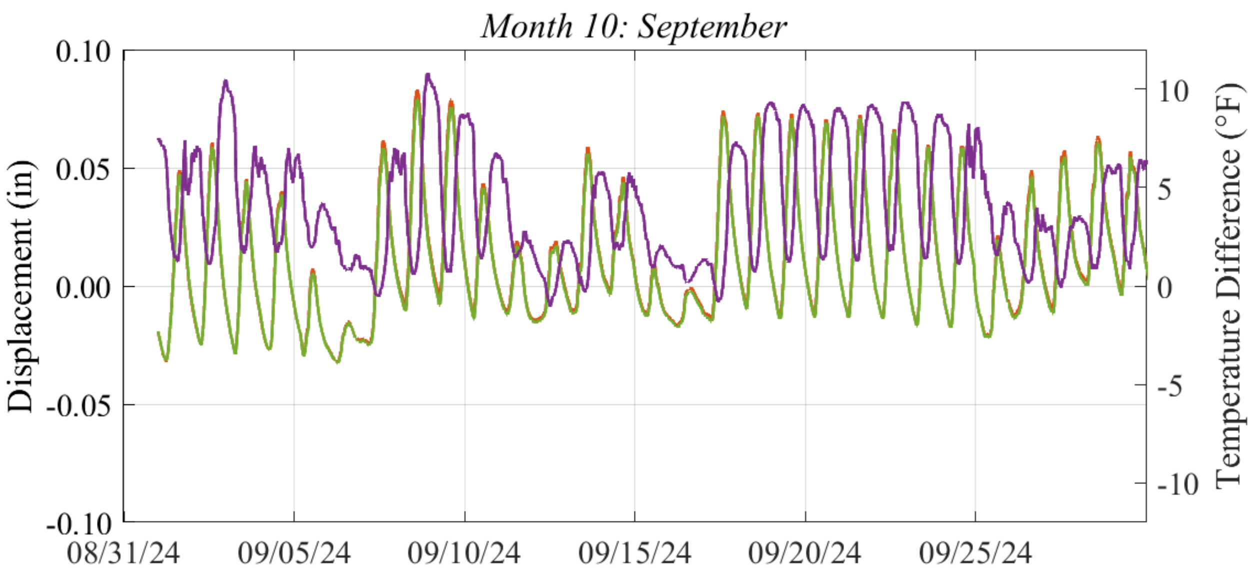

Figure D-44: Average CJ displacement and temperature during September 2024

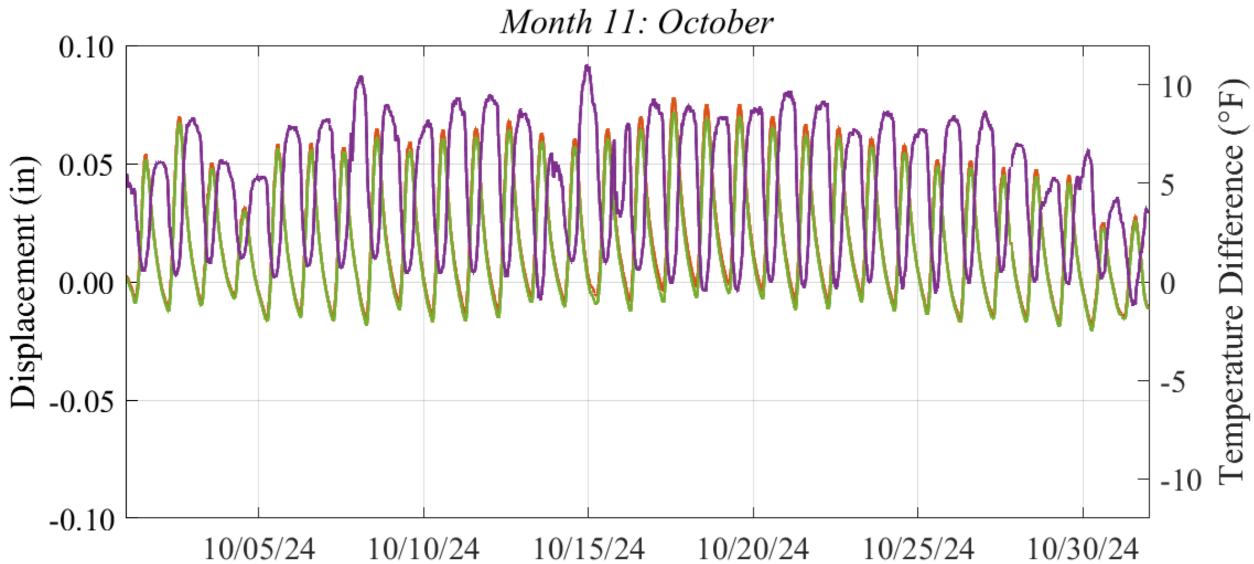

Figure D-45: Average CJ displacement and temperature during October 2024

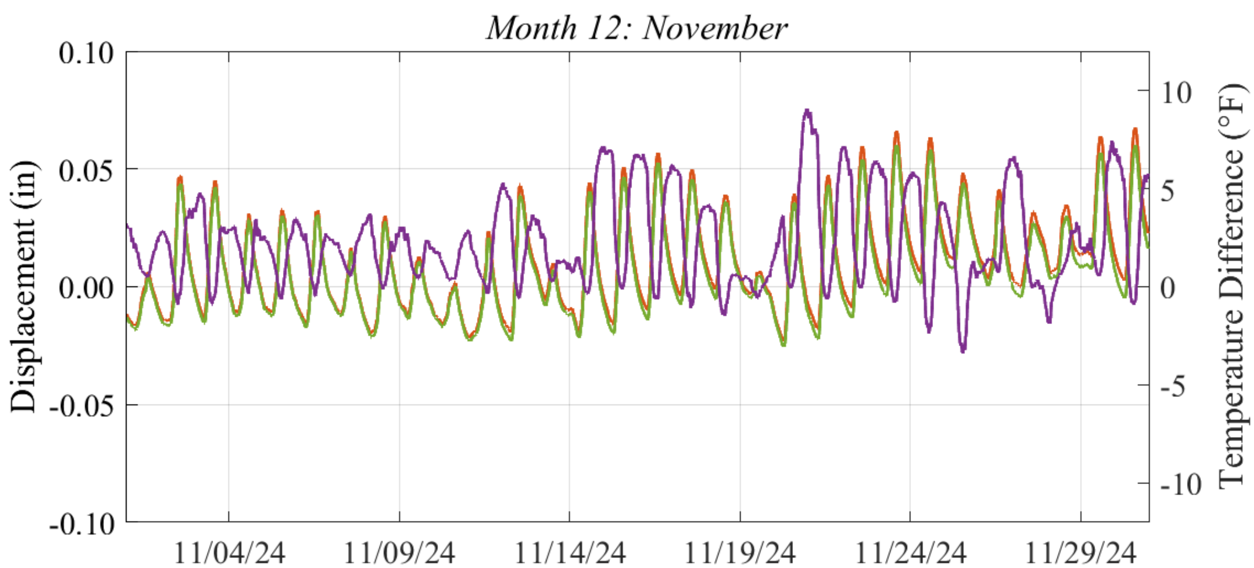

Figure D-46: Average CJ displacement and temperature during November 2024

D.3. End Temperatures (from Bent 8)

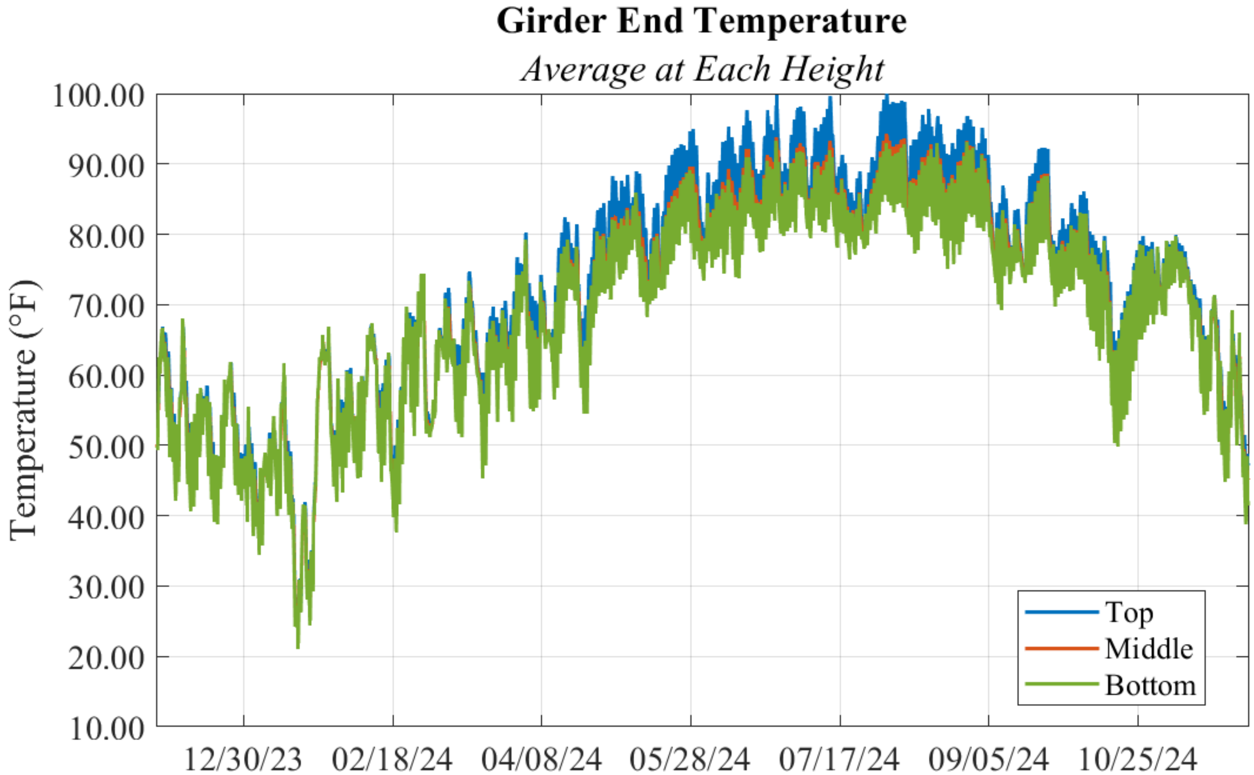

Figure D-47: Girder-end temperature over 12-month monitoring period

D.3.1. Temperature Gradient

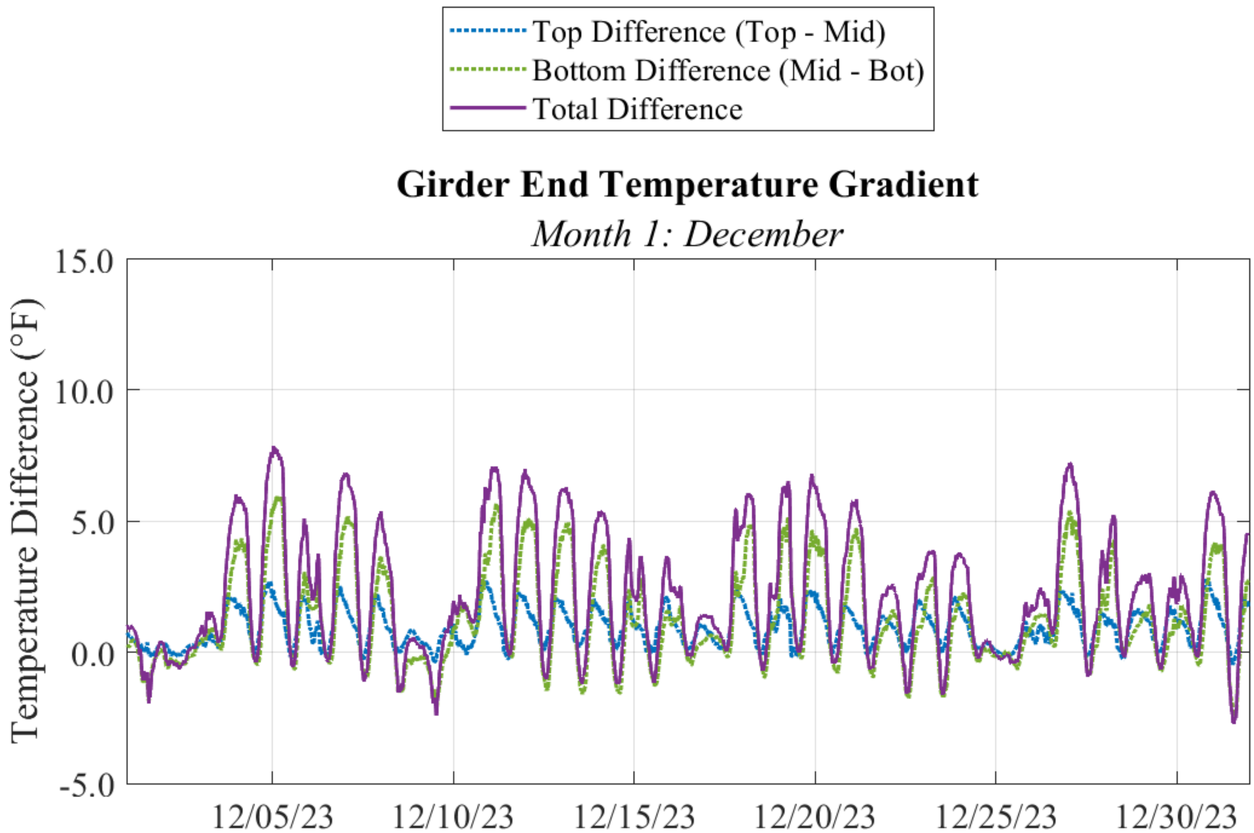

Figure D-48: Girder-end gradient during December 2023

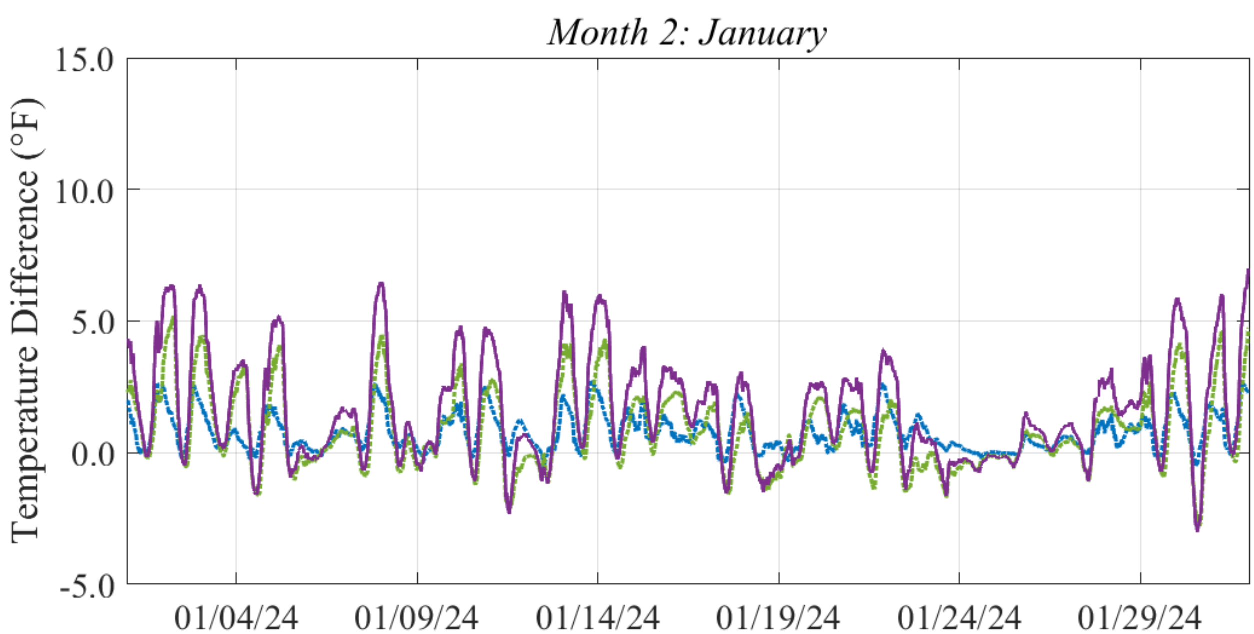

Figure D-49: Girder-end gradient during January 2024

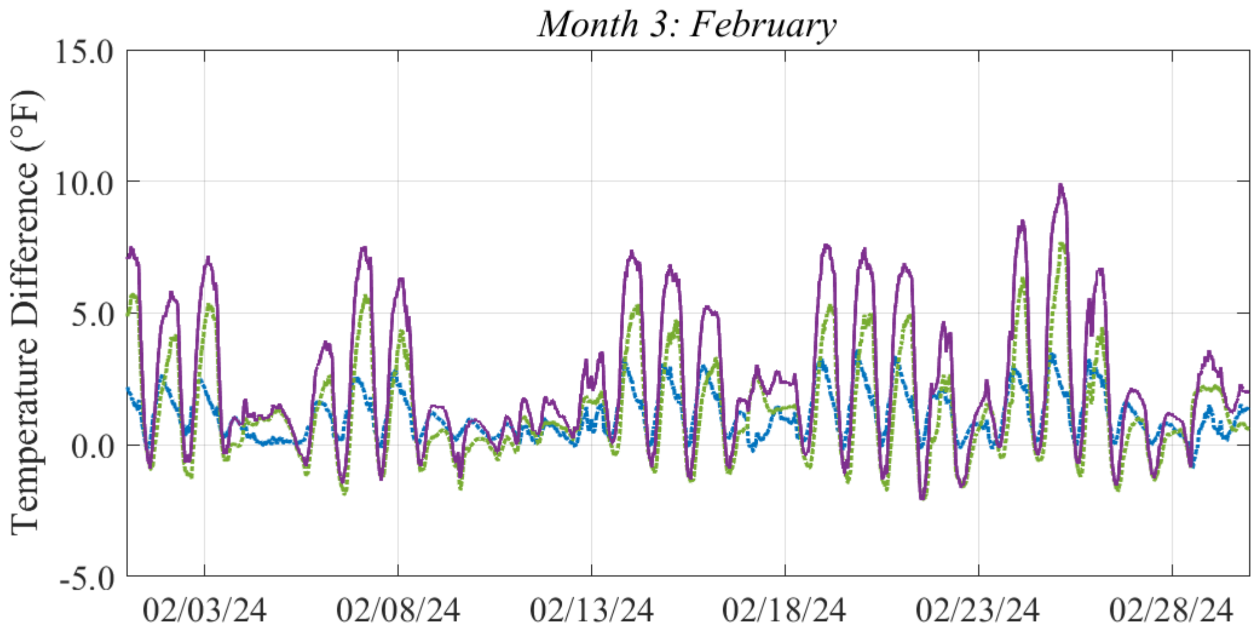

Figure D-50: Girder-end gradient during February 2024

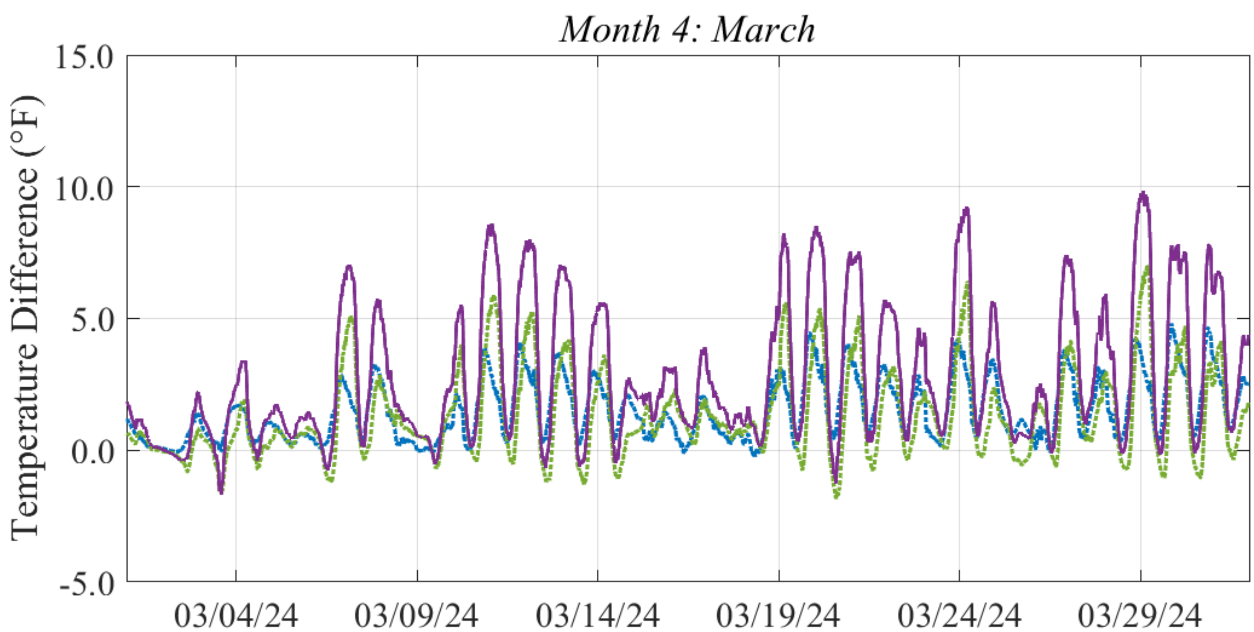

Figure D-51: Girder-end gradient during March 2024

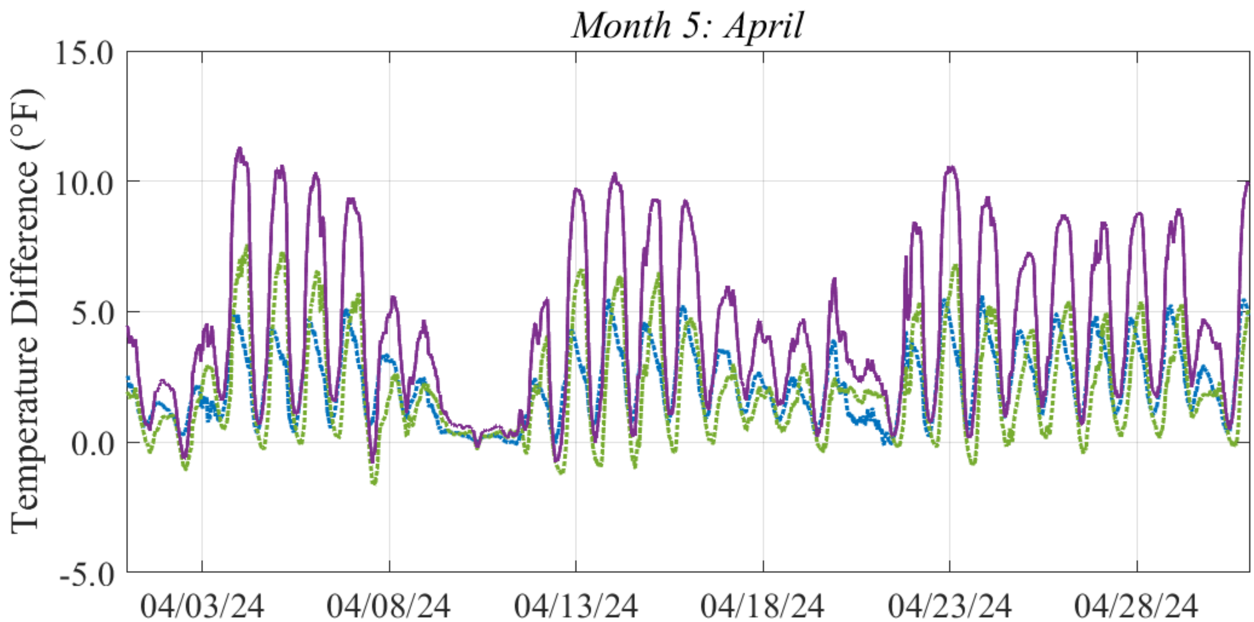

Figure D-52: Girder-end gradient during April 2024

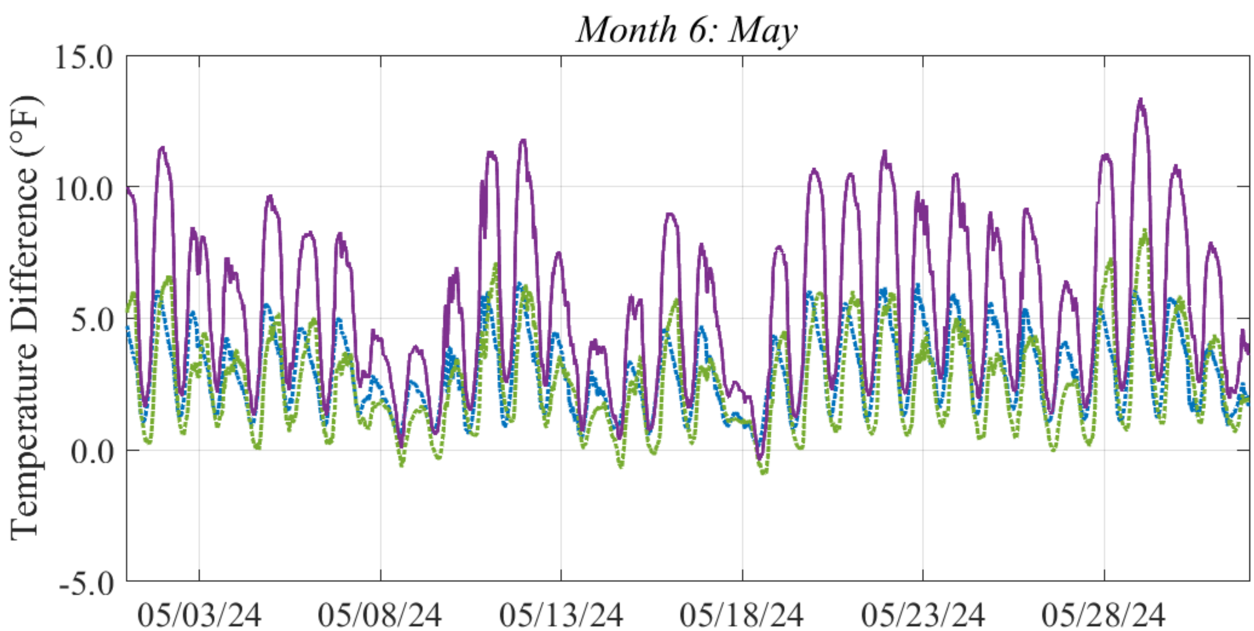

Figure D-53: Girder-end gradient during May 2024

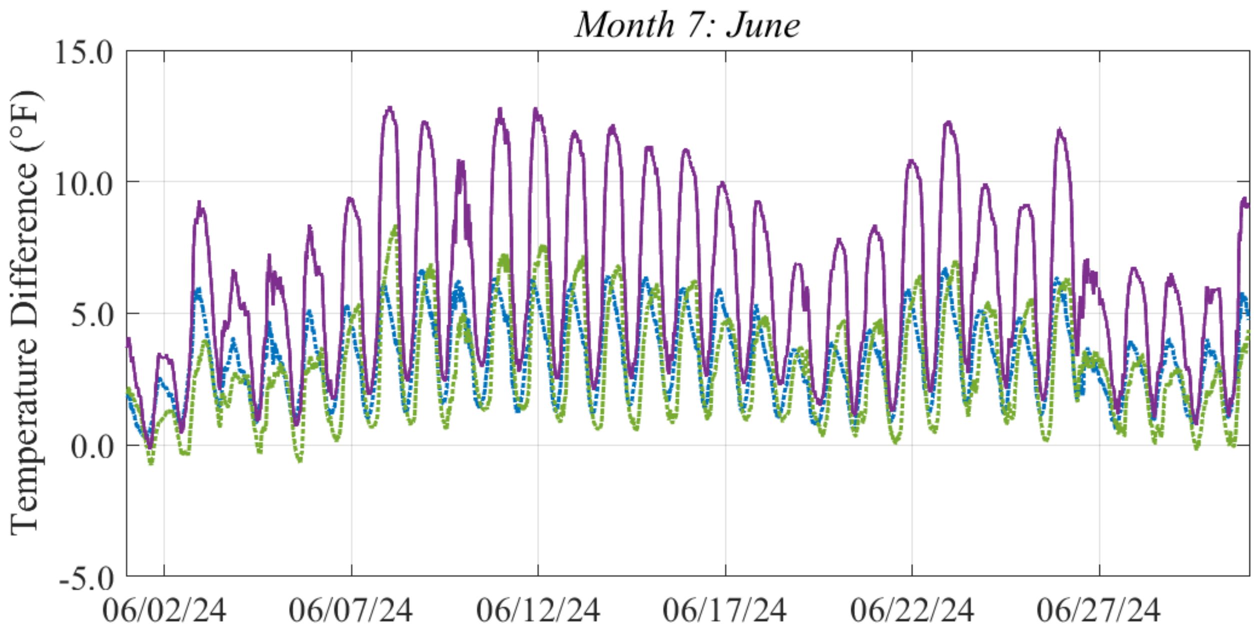

Figure D-54: Girder-end gradient during June 2024

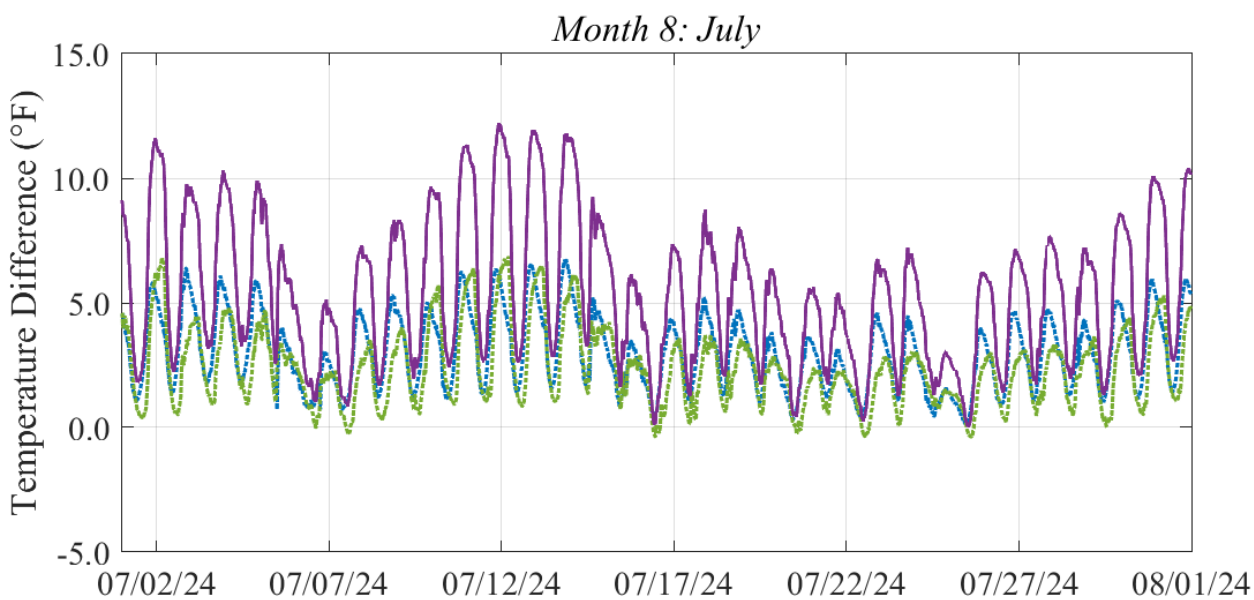

Figure D-55: Girder-end gradient during July 2024

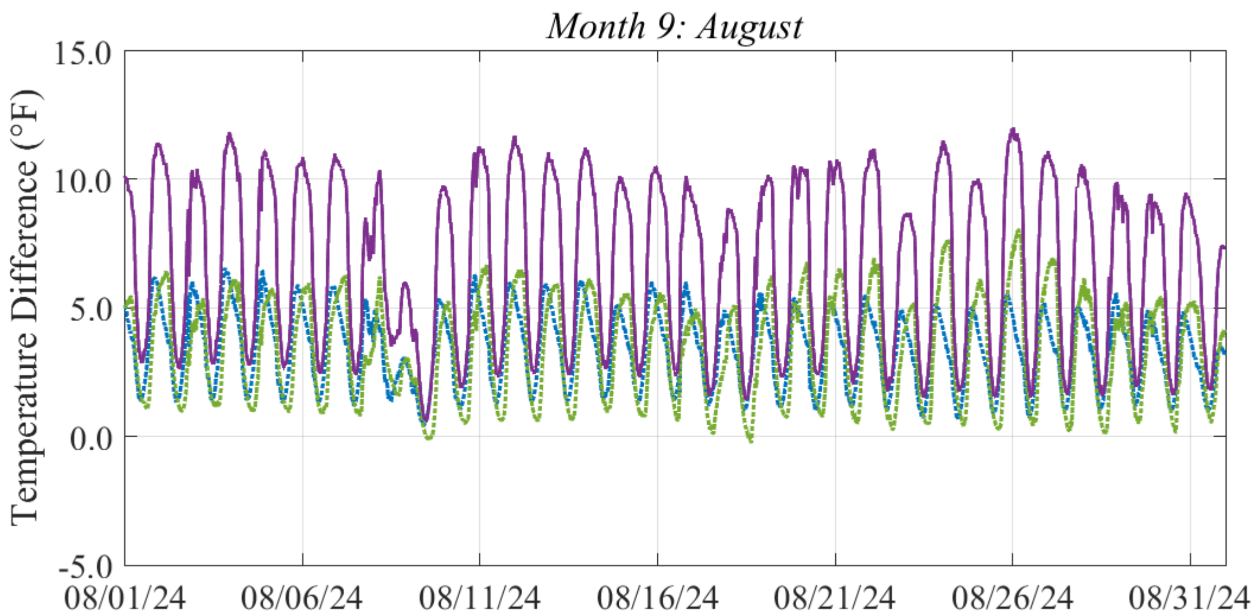

Figure D-56: Girder-end gradient during August 2024

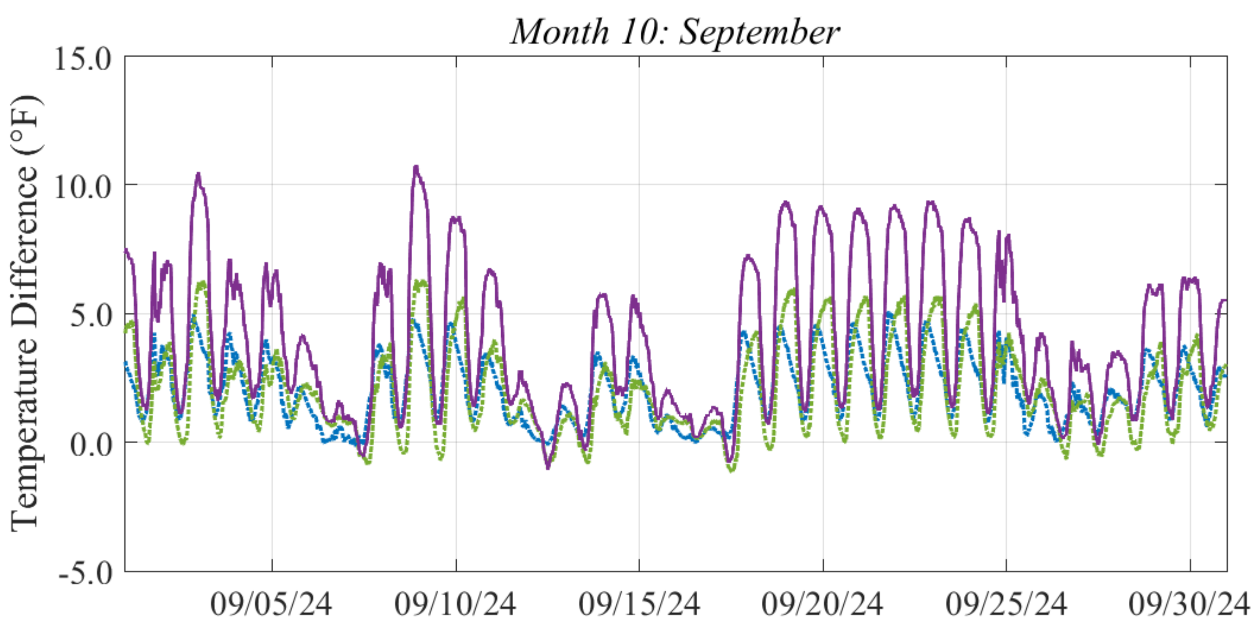

Figure D-57: Girder-end gradient during September 2024

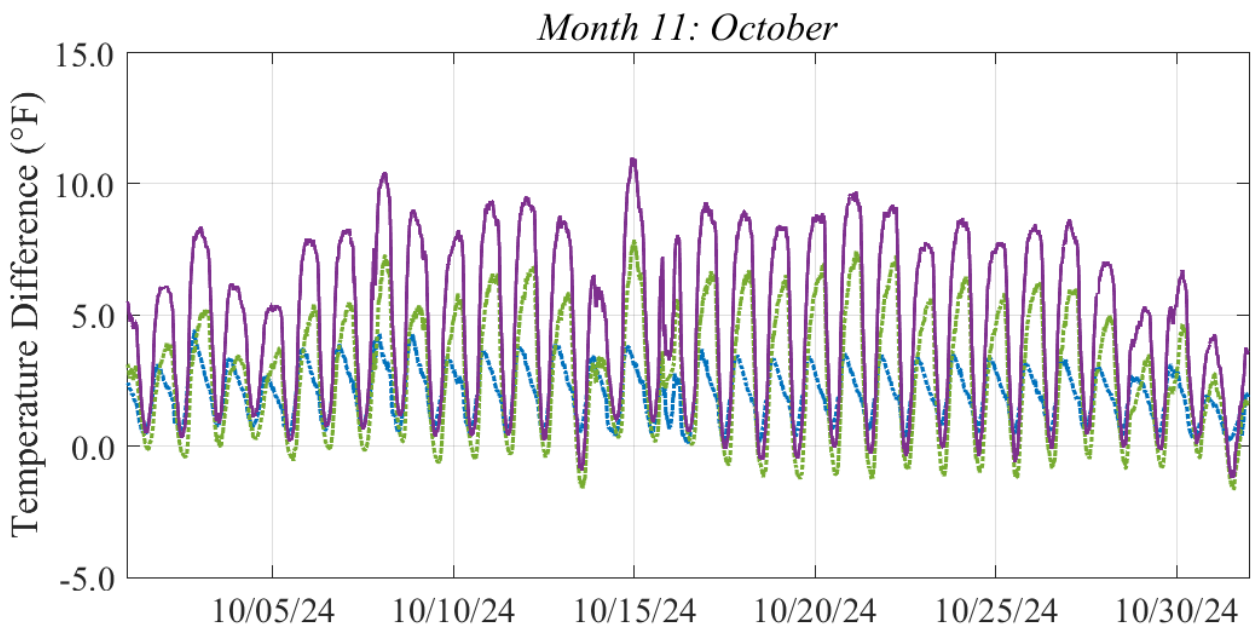

Figure D-58: Girder-end gradient during October 2024

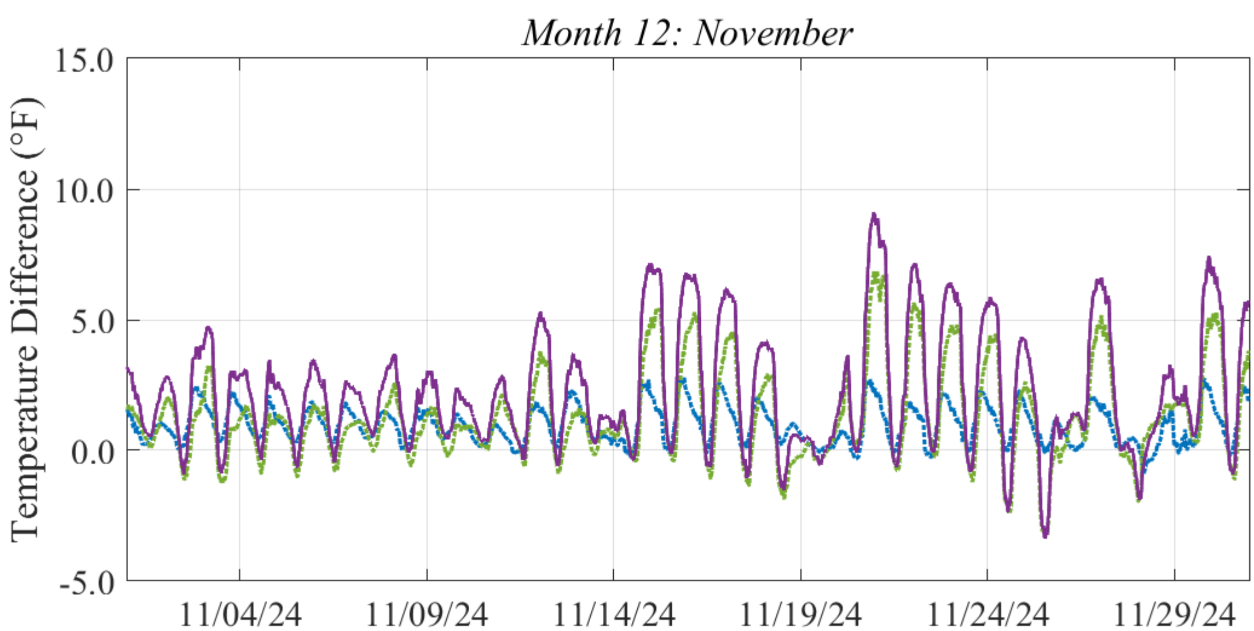

Figure D-59: Girder-end gradient during November 2024

Appendix E: Closed-Joint Demand Calculations

E.1. Geometries and Material Properties

GEOMETRIES & MATERIAL PROPERTIES

INPUTS OUTPUTS

Bridge Properties

$L := 80\ ft$ Span Length

$W := 42\ ft + 9\ in$ Total Deck Width

$N_g := 6$ Number of Girder Lines

$S := 7\ ft$ Spacing between Girders

$gap := 3\ in$ Build-up b/w deck and girder

Concrete Properties

$w_c := 150\ pcf$ Concrete Unit Weight

$f'_{c\_d} := 4\ ksi$ $K_1 := 1.0$ Deck Concrete Compressive Strength

$$E_{c\_d} := 120000 \cdot K_1 \cdot \left(\frac{w_c}{1000\ pcf}\right)^{2.0} \cdot \left(\frac{f'_{c\_d}}{ksi}\right)^{0.33} ksi = 4266\ ksi$$

AASHTO 2024 5.4.2.4
Deck Concrete Modulus of Elasticity

$f'_{ci} := 5\ ksi$ $f'_{c\_g} := 6\ ksi$ Deck compressive strength (initial and 28-day)

$$E_{c\_g} := 120000 \cdot K_1 \cdot \left(\frac{w_c}{1000\ pcf}\right)^{2.0} \cdot \left(\frac{f'_{c\_g}}{ksi}\right)^{0.33} ksi = 4877\ ksi$$

AASHTO 2024 5.4.2.4
Girder Concrete Modulus of Elasticity (28-day)

$$n := \frac{E_{c\_d}}{E_{c\_g}} = 0.875$$

Deck-to-Girder Concrete Modular Ratio

$\alpha := 6.0 \cdot 10^{-6}\ \Delta°F^{-1}$ Concrete Coefficient of Thermal Expansion (AASHTO 2024 5.4.2.2)

Girder Properties

$L_g := L - 2 \cdot (4 + 8)\ in = 78\ ft$ Girder Length (Bearing to Bearing)

Properties:

Type	Area in.²	y_{bottom} in.	Inertia in.⁴	Weight kip/ft
I	276	12.59	22,750	0.287
II	369	15.83	50,980	0.384
III	560	20.27	125,390	0.583
IV	789	24.73	260,730	0.822
V	1,013	31.96	521,180	1.055
VI	1,085	36.38	733,320	1.13

$A_g := 560\ in^2$ Girder Area

$y_g := 20.27\ in$ Girder Centroid (from bottom)

$I_g := 125390\ in^4$ Girder MoI

$w_g := 583\ plf$ Girder Unit Weight

Dimensions (inches)

Type	D1	D2	D3	D4	D5	D6	B1	B2	B3	B4	B5	B6
I	28	4	0	3	5	5	12	16	6	3	0	5
II	36	6	0	3	6	6	12	18	6	3	0	6
III	45	7	0	4.5	7.5	7	16	22	7	4.5	0	7.5
IV	54	8	0	6	9	8	20	26	8	6	0	9
V	63	5	3	4	10	8	42	28	8	4	13	10
VI	72	5	3	4	10	8	42	28	8	4	13	10

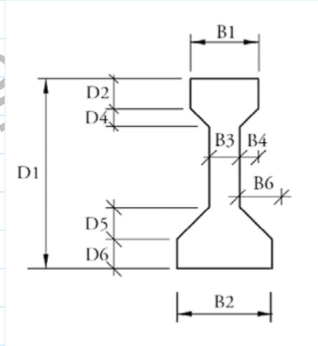

Type I-IV

$B_1 := 16\ in$ $B_2 := 22\ in$ $B_4 := 4.5\ in$ $B_6 := 7.5\ in$

$D_1 := 45\ in$ $D_2 := 7\ in$ $D_4 := 4.5\ in$ $D_5 := 7.5\ in$ $D_6 := 7\ in$

$$P_g := B_1 + 2 \cdot \left(D_2 + \sqrt{D_4^{\,2} + B_4^{\,2}} + \left(D_1 - \left(D_2 + D_4 + D_5 + D_6\right)\right) + \sqrt{D_5^{\,2} + B_6^{\,2}} + D_6\right) + B_2 = 137.941\ in$$

Girder Perimeter

$$VS_g := \frac{A_g}{P_g} = 4.06\ in$$

Girder Volume-to-Surface Ratio

Deck Properties (tributary width of girder)

$t_d := 7\ in$ $b_d := 7\ ft$ Deck Thickness and Tributary Width

$A_d := t_d \cdot b_d = 588\ in^2$ Deck Area

$A_{gap} := gap \cdot B_1 = 48\ in^2$ Area of Concrete Build-up b/w deck and girder

$$y_d := \frac{A_d \cdot \left(D_1 + gap + \frac{t_d}{2}\right) + A_{gap} \cdot \left(D_1 + \frac{gap}{2}\right)}{A_d + A_{gap}} = 51.123\ in$$ Deck Centroid (from bottom of girder)

$P_d := 2\ t_d + 2\ b_d + 2 \cdot gap = 188\ in$ Deck Perimeter

$VS_d := \frac{A_d + A_{gap}}{P_d} = 3.383\ in$ Deck Volume-to-Surface Ratio

$w_d := w_c \cdot \left(A_d + A_{gap}\right) = 662.5\ plf$ Deck Unit Weight

$I_d := \frac{1}{12} \cdot b_d \cdot t_d^{\ 3} = 2401\ in^4$ Deck MoI

$I_{gap} := \frac{1}{12} \cdot B_1 \cdot gap^3 = 36\ in^4$ Concrete Build-up MoI

Composite Properties

$H_c := D_1 + gap + t_d = 55\ in$ Composite Height

$A_c := n \cdot \left(A_d + A_{gap}\right) + A_g = 1116.349\ in^2$ Composite Area

$y_{bot} := \frac{n \cdot \left(y_d \cdot \left(A_d + A_{gap}\right)\right) + y_g \cdot A_g}{A_c} = 35.646\ in$ $y_{top} := H_c - y_{bot} = 19.354\ in$ Composite Centroids

$I_c := n \cdot \left(I_d + I_{gap}\right) + n \cdot \left(A_d + A_{gap}\right) \cdot \left(y_{bot} - y_d\right)^2 + I_g + A_g \cdot \left(y_{bot} - y_g\right)^2 = 393178\ in^4$ Composite MoI, from bottom of girder

Prestressing Steel Properties

$A_s := 0.153\ in^2$ Area of one strand

$N_{ps} := 30$ Number of strands

$A_{ps} := N_{ps} \cdot A_s = 4.59\ in^2$ Area of Prestressing Steel

$F_{si} := 33.818\ kip$ Initial Prestressing Force for one strand

$F_{pi} := N_{ps} \cdot F_{si} = 1015\ kip$ Initial Prestressing Force

$f_{pi} := \frac{F_{pi}}{A_{ps}} = 221.033\ ksi$ Initial Strand Prestress

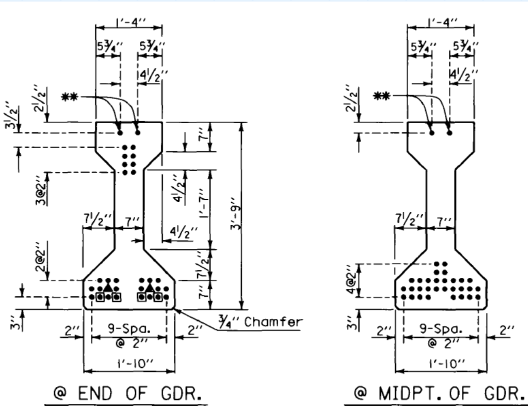

STRAND PATTERN
Scale: 3/4" = 1'-0"

$f_{pu} := 270\ ksi$ Steel Ultimate Stress AASHTTO 2024 5.4.4.1

$f_{py} := 0.9 \cdot f_{pu} = 243\ ksi$ Steel Yield Stress

$E_p := 28500\ ksi$ Steel MoE AASHTTO 2024 5.4.4.2

$$e_{pg} := y_g - \frac{8 \cdot 3\ in + 10 \cdot 5\ in + 8 \cdot 7\ in + 2 \cdot 9\ in + 2 \cdot 11\ in}{30} = 14.603\ in$$ Eccentricity relative to girder centroid

$e_{pc} := e_{pg} - y_g + y_{bot} = 29.979\ in$ Eccentricity relative to composite centroid

E.2. Rotations from Temperature Gradient using AASHTO 3.12.3 and 4.6.6

AASHTO Gradient Geometry

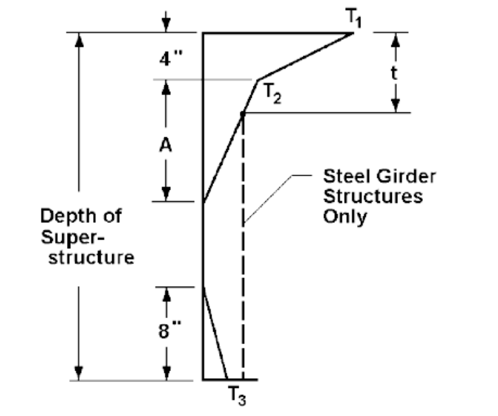

Figure 3.12.3-2—Positive Vertical Temperature Gradient in Concrete and Steel Superstructures

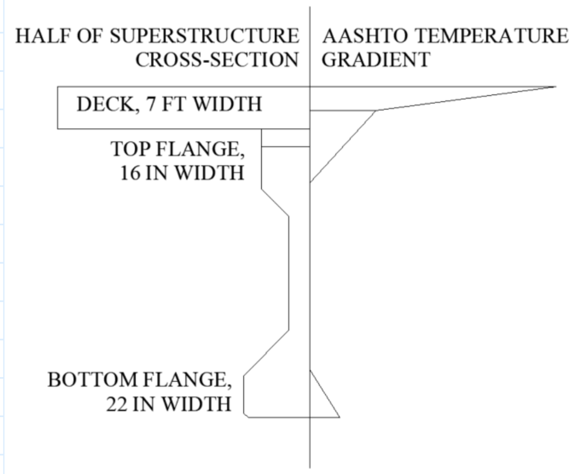

Distance from Bottom	Width
48 - 55 in (Deck):	$w_6 := 7\ ft$
38 - 48 in (Top Flange+Build-Up):	$w_5 := 16\ in$
14.5 - 33.5 in (Web):	$w_3 := 7\ in$
0 - 7 in (Bottom Flange):	$w_1 := 22\ in$

AASHTO Design Rotation

Positive Gradient - Negative Rotation

$L_{Tt} := 4\ in \qquad L_{Tb} := 8\ in \qquad A := 12\ in$

$T_1 := 41\ \Delta°F \qquad T_2 := 11\ \Delta°F \qquad T_3 := 0\ \Delta°F$

Using Eq. C4.6.6-3 from AASHTO (2020)

$$\phi_1 := \frac{\alpha}{I_c} \int_{(H_c - L_{Tt}) - y_{bot}}^{H_c - y_{bot}} \left(\frac{T_1 - T_2}{L_{Tt}} \cdot \left(z - \left(H_c - L_{Tt}\right) + y_{bot}\right) + T_2 \right) \cdot w_6 \cdot z \, \mathrm{d}z = \left(2.4 \cdot 10^{-6}\right) \frac{rad}{in}$$

$$\phi_2 := \frac{\alpha}{I_c} \int_{H_c - t_d - y_{bot}}^{H_c - L_{Tt} - y_{bot}} \left(\frac{T_2}{A} \cdot \left(z - \left(H_c - L_{Tt}\right) + A + y_{bot}\right) \right) \cdot w_6 \cdot z \, \mathrm{d}z = \left(515.4 \cdot 10^{-9}\right) \frac{rad}{in}$$

$$\phi_3 := \frac{\alpha}{I_c} \int_{H_c - L_{Tt} - A - y_{bot}}^{H_c - t_d - y_{bot}} \left(\frac{T_2}{A} \cdot \left(z - \left(H_c - L_{Tt}\right) + A + y_{bot}\right) \right) \cdot w_5 \cdot z \, \mathrm{d}z = \left(84.8 \cdot 10^{-9}\right) \frac{rad}{in}$$

$$\phi_4 := \frac{\alpha}{I_c} \int_{-y_{bot}}^{L_{Tb} - y_{bot}} \left(\frac{T_3}{-L_{Tb}} \left(z - L_{Tb} + y_{bot}\right) \right) \cdot w_1 \cdot z \, \mathrm{d}z = 0 \ \frac{rad}{in}$$

$$\phi := \phi_1 + \phi_2 + \phi_3 + \phi_4 = \left(2.97 \cdot 10^{-6}\right) \frac{rad}{in}$$

$$\theta_{T\_AASHTO\_neg} := -2 \left(\phi \cdot \frac{L_g}{2} \right) = -2.78 \cdot 10^{-3}\ rad$$

total due to rotation of adjacent girder ends (Assuming similar spans)

$$\theta_{T\_AASHTO\_pos} := -0.3 \cdot \theta_{T\_AASHTO\_neg} = \left(833 \cdot 10^{-6}\right)\ rad$$

New Zealand Design Rotation (Preistley, 1978)

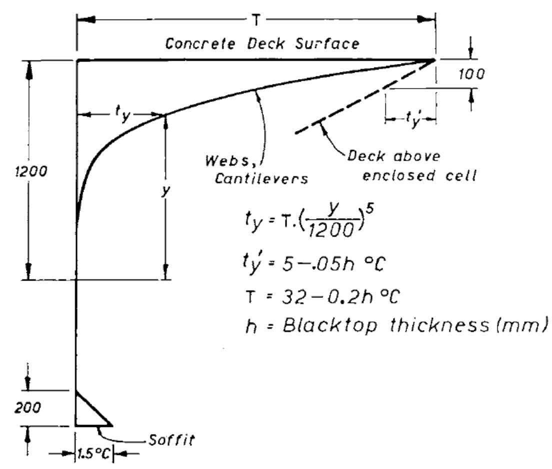

Fig. 9—New Zealand design thermal gradient

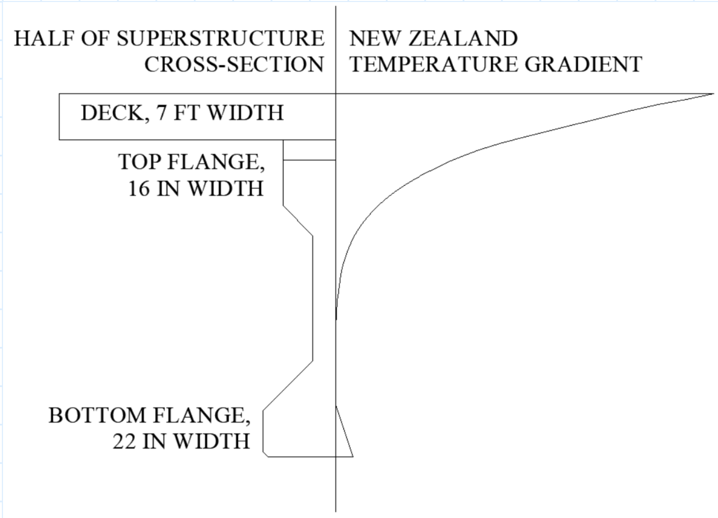

Neglect webs of cross section due to small widths and gradient values

Positive Gradient - Negative Rotation

$L_t := 1200\ mm = 47.244\ in$

$L_b := 200\ mm = 7.874\ in$

$T_0 := (32 - 0.2 \cdot 0)\ \Delta°C = 57.6\ \Delta°F$

$T_1 := 1.5\ \Delta°C = 2.7\ \Delta°F$

Using Eq. C4.6.6-3 from AASHTO (2020)

$$\phi_1 := \frac{\alpha}{I_c} \int_{H_c - t_d - y_{bot}}^{H_c - y_{bot}} \left(T_0 \cdot \left(\frac{z - (H_c - L_t - y_{bot})}{L_t} \right)^5 \right) \cdot w_6 \cdot z \, dz = (5.9 \cdot 10^{-6})\ \frac{rad}{in}$$

$$\phi_2 := \frac{\alpha}{I_c} \int_{H_c - t_d - gap - D_2 - y_{bot}}^{H_c - t_d - y_{bot}} \left(T_0 \cdot \left(\frac{z - (H_c - L_t - y_{bot})}{L_t} \right)^5 \right) \cdot w_5 \cdot z \, dz = (294.4 \cdot 10^{-9})\ \frac{rad}{in}$$

$$\phi_3 := \frac{\alpha}{I_c} \int_{-y_{bot}}^{D_6 - y_{bot}} \left(\frac{T_1}{L_b} (z + y_{bot}) \right) \cdot w_1 \cdot z \, dz = -8.738 \cdot 10^{-8}\ \frac{rad}{in}$$

$$\phi := \phi_1 + \phi_2 + \phi_3 = (6.1 \cdot 10^{-6})\ \frac{rad}{in}$$

$$\theta_{T\_NZ\_neg} := -2 \left(\phi \cdot \frac{L_g}{2} \right) = -5.68 \cdot 10^{-3}\ rad$$

total due to rotation of adjacent girder ends (Assuming similar spans)

$$\theta_{T\_NZ\_pos} := -0.3 \cdot \theta_{T\_NZ\_neg} = (1.70 \cdot 10^{-3})\ rad$$

New Zealand Gradient with AASHTO Design Values Rotation

Positive Gradient - Negative Rotation

$T_0 := 41 \cdot \Delta°F$ $T_1 := 0\ \Delta°F$

Using Eq. C4.6.6-3 from AASHTO (2020)

$$\phi_1 := \frac{\alpha}{I_c} \int_{H_c - t_d - y_{bot}}^{H_c - y_{bot}} \left(T_0 \cdot \left(\frac{z - (H_c - L_t - y_{bot})}{L_t} \right)^5 \right) \cdot w_6 \cdot z \, dz = \left(4.2 \cdot 10^{-6}\right) \frac{rad}{in}$$

$$\phi_2 := \frac{\alpha}{I_c} \int_{H_c - t_d - gap - D_2 - y_{bot}}^{H_c - t_d - y_{bot}} \left(T_0 \cdot \left(\frac{z - (H_c - L_t - y_{bot})}{L_t} \right)^5 \right) \cdot w_5 \cdot z \, dz = \left(209.6 \cdot 10^{-9}\right) \frac{rad}{in}$$

$$\phi_3 := \frac{\alpha}{I_c} \int_{-y_{bot}}^{D_6 - y_{bot}} \left(\frac{T_1}{L_b} \left(z + y_{bot}\right) \right) \cdot w_1 \cdot z \, dz = 0 \frac{rad}{in}$$

$$\phi := \phi_1 + \phi_2 + \phi_3 = \left(4.4 \cdot 10^{-6}\right) \frac{rad}{in}$$

$$\theta_{T\_NAASHTOZ\_neg} := -2 \left(\phi \cdot \frac{L_g}{2} \right) = -4.10 \cdot 10^{-3}\ rad$$

total due to rotation of adjacent girder ends (Assuming similar spans)

$$\theta_{T\_NAASHTOZ\_pos} := -0.3 \cdot \theta_{T\_NAASHTOZ\_neg} = \left(1.23 \cdot 10^{-3}\right) rad$$

E.3. Rotations from HL-93 Loading using AASHTO 3.6.1.2 and 3.6.1.3

LIVE LOAD DEMANDS

Section Properties

$L_g = 78\ ft$ Length of Girder

$S = 7\ ft$ Spacing between Girders

$N_g = 6$ Number of Girders

$E_{c\_g} = 4877\ ksi$ MoE of Girder Concrete (using deck transformed area)

$I_c = 393178\ in^4$ MoI of Girder+n*Deck (trib width)

Live Load Distribution Factor for Moment in Interior Beams (AASHTO 2024 Table 4.6.2.2.2b-1)

$$\left(\frac{K_g}{12.0\ L_g \cdot t_s^{\ 3}}\right)^{0.1} = 1.09$$ AASHTO 2024 Table 4.6.2.2.1-3

$$DF := 0.075 + \left(\frac{S}{9.5\ ft}\right)^{0.6} \left(\frac{S}{L_g}\right)^{0.2} (1.09) = 0.635$$ Two Design Lanes Loaded

3.6.2.1—General

Unless otherwise permitted in Articles 3.6.2.2 and 3.6.2.3, the static effects of the design truck or tandem, other than centrifugal and braking forces, shall be increased by the percentage specified in Table 3.6.2.1-1 for dynamic load allowance.

The factor to be applied to the static load shall be taken as: $(1 + IM/100)$.

The dynamic load allowance shall not be applied to pedestrian loads or to the design lane load.

Table 3.6.2.1-1—Dynamic Load Allowance, *IM*

Component	*IM*
Deck Joints—All Limit States	75%
All Other Components:	
• Fatigue and Fracture Limit State	15%
• All Other Limit States	33%

$IM := 1.33$

Design Truck

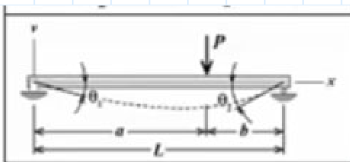	4 $\theta_1 = -\frac{Pb(L^2-b^2)}{6LEI}$ $\theta_2 = +\frac{Pa(L^2-a^2)}{6LEI}$	5 $v = -\frac{Pa^2b^2}{3LEI}$ at $x = a$	6 $v = -\frac{Pbx}{6LEI}(L^2-b^2-x^2)$ for $0 \le x \le a$

3.6.1.2.2—Design Truck

The weights and spacings of axles and wheels for the design truck shall be as specified in Figure 3.6.1.2.2-1. A dynamic load allowance shall be considered as specified in Article 3.6.2.

Except as specified in Articles 3.6.1.3.1 and 3.6.1.4.1, the spacing between the two 32.0-kip axles shall be varied between 14.0 ft and 30.0 ft to produce extreme force effects.

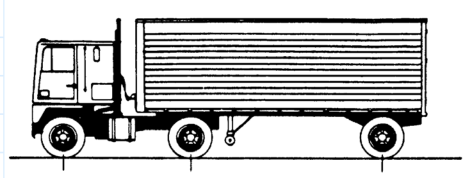

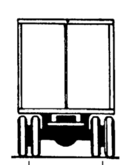

$P_1 := 8\ kip$ $P_2 := 32\ kip$

$S_1 := 14\ ft$ $S_2 := 14\ ft$

$a := 24\ ft$ $b := L_g - a = 54\ ft$

Truck facing towards joint

$l_{front} := a = 24\ ft$ $P_{front} := IM \cdot P_1 = 10.6\ kip$

$l_{mid} := a + S_1 = 38\ ft$ $P_{mid} := IM \cdot P_2 = 42.6\ kip$

$l_{back} := a + S_1 + S_2 = 52\ ft$ $P_{back} := IM \cdot P_2 = 42.6\ kip$

$$\theta_{front} := \frac{P_{front} \cdot l_{front} \cdot \left(L_g^{\ 2} - l_{front}^{\ 2}\right)}{6\ L_g \cdot E_{c\_g} \cdot I_c} = \left(225.7 \cdot 10^{-6}\right)\ rad$$

$$\theta_{mid} := \frac{P_{mid} \cdot l_{mid} \cdot \left(L_g^{\ 2} - l_{mid}^{\ 2}\right)}{6\ L_g \cdot E_{c\_g} \cdot I_c} = \left(1.2 \cdot 10^{-3}\right)\ rad$$

$$\theta_{back} := \frac{P_{back} \cdot l_{back} \cdot \left(L_g^{\ 2} - l_{back}^{\ 2}\right)}{6\ L_g \cdot E_{c\_g} \cdot I_c} = \left(1.2 \cdot 10^{-3}\right)\ rad$$

$$\theta_{g\_to} := \theta_{front} + \theta_{mid} + \theta_{back} = \left(2.63 \cdot 10^{-3}\right)\ rad$$

Truck facing towards beam end

Truck facing away from joint

$l_{front} := a + S_2 + S_1 = 52\ ft$ $\qquad P_{front} = 10.6\ kip$

$l_{mid} := a + S_2 = 38\ ft$ $\qquad P_{mid} = 42.6\ kip$

$l_{back} := a = 24\ ft$ $\qquad P_{back} = 42.6\ kip$

$$\theta_{front} := \frac{P_{front} \cdot l_{front} \cdot \left(L_g^{\ 2} - l_{front}^{\ 2}\right)}{6\ L_g \cdot E_{c\_g} \cdot I_c} = \left(300.1 \cdot 10^{-6}\right)\ rad$$

$$\theta_{mid} := \frac{P_{mid} \cdot l_{mid} \cdot \left(L_g^{\ 2} - l_{mid}^{\ 2}\right)}{6\ L_g \cdot E_{c\_g} \cdot I_c} = \left(1.2 \cdot 10^{-3}\right)\ rad$$

$$\theta_{back} := \frac{P_{back} \cdot l_{back} \cdot \left(L_g^{\ 2} - l_{back}^{\ 2}\right)}{6\ L_g \cdot E_{c\_g} \cdot I_c} = \left(902.8 \cdot 10^{-6}\right)\ rad$$

$$\theta_{g\_from} := \theta_{front} + \theta_{mid} + \theta_{back} = \left(137.91 \cdot 10^{-3}\right)\ deg$$

Truck facing away from beam end

Design Lane Load

	10	11	12
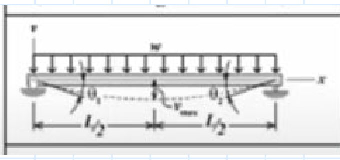	$\theta_1 = -\theta_2 = -\dfrac{wL^3}{24EI}$	$v_{max} = -\dfrac{5wL^4}{384EI}$	$v = -\dfrac{wx}{24EI}\left(L^3 - 2Lx^2 + x^3\right)$

$$w_{ll} := 0.64\ \frac{kip}{ft}$$

$$\theta_{g\_lane} := \frac{w_{ll} \cdot L_g^{\ 3}}{24\ E_{c\_g} \cdot I_c} = \left(54.45 \cdot 10^{-3}\right)\ deg$$

3.6.1.2.4—Design Lane Load

The design lane load shall consist of a load of 0.64 klf uniformly distributed in the longitudinal direction. Transversely, the design lane load shall be assumed to be uniformly distributed over a 10.0-ft width. The force effects from the design lane load shall not be subject to a dynamic load allowance.

Combinations

AASHTO 3.6.1.3.1

For negative moment between points of contraflexure under a uniform load on all spans, and reaction at interior piers only, 90 percent of the effect of two design trucks spaced a minimum of 50.0 ft between the lead axle of one truck and the rear axle of the other truck, combined with 90 percent of the effect of the design lane load. The distance between the 32.0-kip axles of each truck shall be taken as 14.0 ft. The two design trucks shall be placed in adjacent spans to produce maximum force effects.

$$\theta_{T\_LL} := DF \cdot 0.9 \cdot \left(\theta_{g\_to} + \theta_{g\_from} + 2 \cdot \theta_{g\_lane}\right) = \left(227.3 \cdot 10^{-3}\right)\ deg$$

E.4. Rotations from Time-Dependent Effects using AASHTO 5.9.3.4

LONG-TERM EFFECTS (AASHTO 2024 5.9.3.4)

Initial Properties from ALDOT Structural Design Manual (2020)

$t_f := 27500\ day$ $t_{id} := 120\ day$ $t_i := 0.75\ day$

$f'_{ci} = 5\ ksi$ $f'_{ci\_star} := f'_{ci} + 1.95\ ksi$

$$E_{ci} := 120000 \cdot K_1 \cdot \left(\frac{w_c}{1000\ pcf}\right)^{2.0} \cdot \left(\frac{f'_{ci\_star}}{ksi}\right)^{0.33} ksi = 5119\ ksi$$

$f'_{c\_star} := 1.3 \cdot f'_{ci} + 3.5\ ksi = 10\ ksi$

$$E_c := 120000 \cdot K_1 \cdot \left(\frac{w_c}{1000\ pcf}\right)^{2.0} \cdot \left(\frac{f'_{c\_star}}{ksi}\right)^{0.33} ksi = 5772\ ksi$$

Other Initial Properties

$VS_g = 4.06\ in$ Volume-to-Surface Ratio for Girder $E_p = 28500\ ksi$ Steel MoE

$VS_d = 3.383\ in$ Volume-to-Surface Ratio for Deck

$RH := 75$ Relative Humidity

Prestress Losses Between Transfer and Deck Placement

Creep

$M_g := \frac{1}{8} w_g L^2 = 5597\ kip \cdot in$ $F_{pi} = 1015\ kip$

$\frac{F_{pi}}{A_g} = 1.812\ ksi$ $\frac{(F_{pi} \cdot e_{pg}) \cdot e_{pg}}{I_g} = 1.725\ ksi$ $\frac{M_g \cdot e_{pg}}{I_g} = 0.652\ ksi$

$$f_{cgp} := \frac{F_{pi}}{A_g} + \frac{(F_{pi} \cdot e_{pg}) \cdot e_{pg}}{I_g} - \frac{M_g \cdot e_{pg}}{I_g} = 2.885\ ksi$$

$k_s := \max\left(1.45 - 0.13\left(\frac{VS_g}{in}\right), 1.0\right) = 1.000$ Eq. 5.4.2.3.2-2, Volume-to-Surface Ratio Factor

$k_{hc} := 1.56 - 0.008\ RH = 0.960$ Eq. 5.4.2.3.2-3, Humidity Factor for Creep

$k_f := \frac{5\ ksi}{1\ ksi + f'_{ci\_star}} = 0.629$ Eq. 5.4.2.3.2-4, Concrete Strength Factor

$$k_{td\_id} := \frac{\frac{t_{id}}{day}}{12\left(\frac{100\ ksi - 4\ f'_{ci\_star}}{f'_{ci\_star} + 20\ ksi}\right) + \frac{t_{id}}{day}} = 0.789$$

Eq. 5.4.2.3.2-5, Time Development Factor for time between transfer and deck placement

$$\psi_{b\_di} := 1.9 \cdot k_s \cdot k_{hc} \cdot k_f \cdot k_{td\_id} \cdot \left(\frac{t_i}{day}\right)^{-0.118} = 0.936$$

Eq. 5.4.2.3.2-1, Creep Coefficient for transfer to deck placement time

$$k_{td\_f} := \frac{\frac{t_f}{day}}{12\left(\frac{100\ ksi - 4\ f'_{ci\_star}}{f'_{ci\_star} + 20\ ksi}\right) + \frac{t_f}{day}} = 0.999$$

Eq. 5.4.2.3.2-5, Time Development Factor for time between transfer and final time

$$\psi_{b\_fi} := 1.9 \cdot k_s \cdot k_{hc} \cdot k_f \cdot k_{td\_f} \cdot \left(\frac{t_i}{day}\right)^{-0.118} = 1.185$$

Eq. 5.4.2.3.2-1, Creep Coefficient for transfer to final time

$$K_{id} := \frac{1}{1 + \frac{E_p}{E_{ci}} \cdot \frac{A_{ps}}{A_g} \cdot \left(1 + \frac{A_g \cdot e_{pg}^{\;2}}{I_g}\right) \cdot \left(1 + 0.7\ \psi_{b\_fi}\right)} = 0.86$$

Eq. 5.9.3.4.2a-2, Transformed Section Coefficient

$$\Delta f_{pCR} := \frac{E_p}{E_{ci}}\ f_{cgp} \cdot \psi_{b\_di} \cdot K_{id} = 12.93\ ksi$$

Eq. 5.9.3.4.2b-1, Prestress Loss Due to Concrete Creep before Deck Placement

Shrinkage

$k_s = 1.00$ Volume-to-Surface Ratio Factor

$k_{hs} := 2.00 - 0.014\ RH = 0.950$ Eq. 5.4.2.3.3-2, Humidity Factor for Shrinkage

$k_f = 0.629$ Concrete Strength Factor

$$k_{td\_id} := \frac{\frac{t_{id}}{day}}{12\left(\frac{100\ ksi - 4\ f'_{c\_star}}{f'_{ci\_star} + 20\ ksi}\right) + \frac{t_{id}}{day}} = 0.818$$

Eq. 5.4.2.3.2-5, Time Development Factor for time between transfer and deck placement

$$\varepsilon_{bid} := k_s \cdot k_{hs} \cdot k_f \cdot k_{td\_id} \cdot \left(0.48 \cdot 10^{-3}\right) = \left(2.346 \cdot 10^{-4}\right) \frac{in}{in}$$

Eq. 5.4.2.3.3-1, Concrete Shrinkage strain b/w transfer and deck placement

$K_{id} = 0.86$ Transformed Section Coefficient

$$\Delta f_{pSR} := \varepsilon_{bid} \cdot E_p \cdot K_{id} = 5.75\ ksi$$

Eq. 5.9.3.4.2a-1, Prestress Loss Due to Concrete Shrinkage before Deck Placement

Relaxation

$$\Delta f_{pR1} := 1.2\ ksi$$

5.9.3.4.2c, Prestress Loss Due to Steel Relaxation before Deck Placement

Total Prestress Losses b/w Transfer and Deck Placement:

$$\Delta f_{pTD} := \Delta f_{pSR} + \Delta f_{pCR} + \Delta f_{pR1} = 19.88\ ksi$$

Rotation due to Concrete Creep (b/w deck placement and final time)

$k_s = 1.00$ Volume-to-Surface Ratio Factor

$$k_f := \frac{5\ ksi}{1\ ksi + f'_{c\_star}} = 0.455$$

Eq. 5.4.2.3.2-4, Concrete Strength Factor

$k_{hc} = 0.96$ Humidity Factor for Creep

$$k_{td\_f} := \frac{\frac{t_f}{day}}{12\left(\frac{100\ ksi - 4\ f'_{c\_star}}{f'_{c\_star} + 20\ ksi}\right) + \frac{t_f}{day}} = 0.999$$

Eq. 5.4.2.3.2-5, Time Development Factor for time between transfer and final time

$$\psi_{b\_fd} := 1.9 \cdot k_s \cdot k_{hc} \cdot k_f \cdot k_{td\_f} \cdot \left(\frac{t_{id}}{day}\right)^{-0.118} = 0.471$$

Eq. 5.4.2.3.2-1, Creep Coefficient for deck placement to final time

$f_{pe} := f_{pi} - 19.67\ ksi = 201.363\ ksi$ Stress in Steel after Losses

$F_{pe} := f_{pe} \cdot A_{ps} = 924.255\ kip$ Force in Steel after Losses

$$\varepsilon_{elastic} := \frac{F_{pe}}{A_c \cdot E_c} = \left(1.434 \cdot 10^{-4}\right) \frac{in}{in}$$

$$\varepsilon_{creep} := \psi_{b\_fd} \cdot \varepsilon_{elastic} = \left(6.753 \cdot 10^{-5}\right) \frac{in}{in}$$

Strain due to Creep

$$\theta_{T\_CR} := 2\left(\frac{-\left(\varepsilon_{creep}\right) \cdot \frac{L_g}{2}}{H_c - y_g + e_{pg}}\right) = -1.281 \cdot 10^{-3}\ rad$$

Rotation due to Concrete Creep after Deck Placement (Assuming Similar Spans)

Rotation due to Differential Concrete Shrinkage (after deck placement)

$k_s = 1.00$ Volume-to-Surface Ratio Factor for Girder

$k_{hs} = 0.950$ Humidity Factor for Shrinkage

$k_f = 0.455$ Concrete Strength Factor

$k_{td\_f} = 0.999$ Time Development Factor for time after transfer

$$\varepsilon_{bdf} := k_s \cdot k_{hs} \cdot k_f \cdot k_{td\_f} \cdot \left(0.48 \cdot 10^{-3}\right) = \left(2.071 \cdot 10^{-4}\right) \frac{in}{in}$$

Eq. 5.4.2.3.3-1, Girder Concrete Shrinkage Strain

$$k_{s\_d} := \max\left(1.45 - 0.13 \left(\frac{VS_d}{in}\right), 1.0\right) = 1.010$$

Eq. 5.4.2.3.2-2, Volume-to-Surface Ratio Factor for Deck

$$\varepsilon_{ddf} := k_{s\_d} \cdot k_{hs} \cdot k_f \cdot k_{td\_f} \cdot \left(0.48 \cdot 10^{-3}\right) = \left(2.092 \cdot 10^{-4}\right) \frac{in}{in}$$

Eq. 5.4.2.3.3-1, Deck Concrete Shrinkage Strain

$$\theta_{T\_CS} := 2 \left(\frac{\left(\varepsilon_{ddf} - \varepsilon_{bdf}\right) \cdot \frac{L_g}{2}}{H_c - y_g - \frac{t_d}{2}} \right) = \left(63.389 \cdot 10^{-6}\right) rad$$

Rotation due to Differential Concrete Shrinkage after Deck Placement (Assuming Similar Spans)

Rotation due to Steel Relaxation (after deck placement)

Prestress Loss due to Steel Relaxation (after deck placement)

The relaxation loss, Δf_{pR1}, may be assumed equal to 1.2 ksi for low-relaxation strands.

$$\Delta f_{pR2} := \Delta f_{pR1} = 1.2\ ksi$$

Eq. 5.9.3.4.2c-1, Prestress Loss Due to Steel Relaxation after Deck Placement

Nawy (2009), Figure 7.6

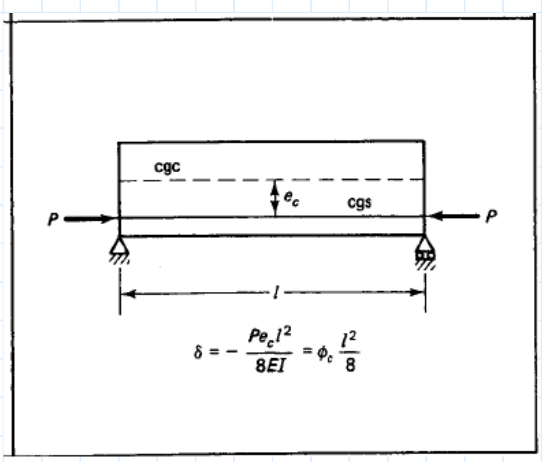

$$P := -\Delta f_{pR2} \cdot A_{ps} = -5.5\ kip$$

$$e_c := y_{bot} - \left(\frac{8 \cdot 3 + 8 \cdot 5 + 6 \cdot 7}{8 + 8 + 6}\right) in = 30.828\ in$$

$$E_{c\_g} = 4877\ ksi$$

$$I_c = 393178\ in^4$$

$$\theta_{T\_SR} := 2 \left(\frac{-P \cdot e_c}{E_{c\_g} \cdot I_c} \cdot \frac{L_g}{2}\right) = \left(82.883 \cdot 10^{-6}\right) rad$$